NORTHWESTERN UNIVERSITY

Chemical and Stimulus Driven Morphogenesis in Soft and Hybrid Materials: Structures for Energy Storage and Soft Robotics

A DISSERTATION

SUBMITTED TO THE GRADUATE SCHOOL

IN PARTIAL FULFILLMENT OF THE REQUIREMENTS

for the degree

DOCTOR OF PHILOSOPHY

Field of Materials Science and Engineering

By

Garrett C. Lau

EVANSTON, ILLINOIS

June 2020

ABSTRACT

Chemical and Stimulus Driven Morphogenesis in Soft and Hybrid Materials: Structures for Energy Storage and Soft Robotics

Garrett C. Lau

Living organisms undergo morphogenesis as they develop and change shape to fit their evolved niche in natural ecosystems. The biological processes underlying morphogenesis involve sophisticated feedback loops between spatiotemporal release of morphogenic molecules that diffuse and signal cell differentiation, as well as contextual interaction with the physical surroundings of the propagating cells. Analogous to biological morphogenesis, the development of morphology in synthetic materials influences many of the properties required for their function. Both synthetic pathways and external stimuli can be used to control the shape of structures in materials across scales. For example, designed molecular precursors and synthetic conditions such as temperature can enable morphogenesis in soft and hybrid materials across the nano- to micro-scale, impacting properties such as ionic and electronic conductivity and surface area that are critical to energy applications. Introducing external stimuli such as light and magnetic fields can induce morphogenesis at the macroscopic scale, resulting in geometries that allow locomotion and other robotic functions. In this work, morphogenesis is studied in several soft and hybrid materials, with structural evolution observed at the nanoscale in some systems and at macroscopic scales in others. First, the formation of hybrid nanostructures is studied for the synthesis of materials for energy storage materials. A conjugated aromatic surfactant molecule was found to template the

formation of oriented nanotubes consisting of concentric layers of cobalt hydroxide and organic surfactant. Energy storage electrodes made with electrodeposited films of these nanostructured hybrids exhibited enhanced charge storage capacity and lower electrochemical impedance due to their high surface area and oriented structure. A similar class of metal hydroxide/organic surfactant hybrid was used in another project to template metallic nanowires on macroporous nickel foam. The resulting hierarchical electronically conductive structures combine both the large surface area and bulk electronic conductivity important for electrochemical energy storage and conversion applications. The increased surface area provides the intimate contact with the surrounding liquid solution required for high rate of electrochemical reactions, while the bulk electronic conductivity contributed by the macroporous nickel foam reduces ohmic losses in high current applications. While the synthesized hierarchical electrodes exhibited high surface area, the long synthetic route and fragility of metallic nanowire networks limited extensive study of their use in catalysis and energy storage. The synthetic expertise in forming nanowires gained in this project was translated to scaling up production of nickel nanowires for use in soft artificial actuators that could exhibit stimulus driven morphogenesis at macroscopic scales using external magnetic fields. The ferromagnetic nickel nanowires were encapsulated within photoactive hydrogels to create hybrid materials that respond to both light and external magnetic fields. When nickel nanowires were aligned using external magnetic fields during polymerization of the hydrogel matrix, they formed a ferromagnetic skeleton with macroscopic nematic order. The photoactive spiropyran moieties within the hydrogel allow the material to macroscopically change shape in response to light as gradients of hydrophobicity and physical contraction are formed along the path of the photons. Flat cross-shaped films were found to bend into curved arches during this light-activated process and rotating external magnetic fields introduced torques that produced extension, contraction and rotation of the hydrogel objects. The synergistic response was found to enable fast walking motion of macroscopic objects in water and delivery of cargo through rolling motion and light-driven shape changes. The theoretical description and finite element simulation of the material's response to external energy input allowed for programming of specific trajectories of hydrogel objects that were verified experimentally, paving a path for fast and rational design of new geometries and material configurations for light and magnetic field activated robots with additional functionality and modes of locomotion. Finally, direct *in-situ* observation of nano- to micro-scale morphogenesis in supramolecular soft materials was enabled by coupling a custom-designed variable temperature sample stage with confocal laser scanning microscopy. The sub-micrometer resolution of this technique allowed for real-time observation of temperature-dependent morphogenic behavior of supramolecular peptide amphiphile nanofibers and supramolecular photocatalytic chromophore amphiphile nanoscale ribbons. The technique enabled direct monitoring and quantification of the kinetically-limited disassembly and breakdown of long peptide amphiphile nanofibers to short nanofibers, as well as the discovery of large microscale curl formation during thermally-driven crystallization of chromophore amphiphiles. The technique demonstrated in this work can sample large sample volumes and provides real-time information on thermally induced morphological changes in solution. Across this body of work, both synthetic inputs and external stimuli were studied as ways to control morphogenesis in soft and hybrid materials from the nano- to macroscale. These approaches are important for controlling the morphology and resulting materials properties that enable function and practical performance. Future studies expanding synthetic design inputs and additional external stimuli may enable morphogenesis of new materials and geometries for enhanced performance in energy storage applications and soft robotics.

To my family and my wife,

for their love and support that carried me through grad school.

ACKNOWLEDGEMENTS

- **Professor Samuel Stupp**, thank you for giving me the opportunity to work in your laboratory and conduct such a wide variety of exciting scientific research. When I decided to apply for graduate school, I was looking for opportunities to broaden my scientific training and expose myself to new areas of research outside of batteries and electrochemistry. I am forever grateful to you for enabling me to reach this goal through your guidance and the laboratory environment you created at Northwestern. I also thoroughly appreciate the training you provided in grantsmanship and how to formulate ambitious research projects with provoking scientific questions.
- **Professors Lincoln Lauhon, Joseph Hupp, Scott Barnett and Monica Olvera de la Cruz –** thank you for serving on my committee, providing feedback, and improving the scientific rigor of my research.
- **Professor Liam Palmer (or just Liam)**, thank you for making life better in the Stupp Group, whether that is providing feedback and guidance on how to develop research directions in uncharted territory, dealing with somewhat touchy conflicts of interest, or doing much of the unpraised administrative work like compiling grant progress reports and hounding facilities management about electrical work to get the big magnet powered.
- **Dr.! Nick Sather,** thank you for joining the group with me and working through that first project together. It was truly a struggle to work on energy storage initially

within the group, and I’m grateful that I had someone to work with everyday who was driven, communicated well, and not afraid of making selfless sacrifices for the team.

- **Dr. Hiroaki Sai,** thank you for inspiring me to be forever curious about the science behind strange physical phenomena, reminding me periodically to take a step back from engineering complex solutions and think about how my approach advances knowledge, and leading by example in never being afraid of learning new techniques/topics. You are the embodiment of what academia should strive towards.
- **Dr. Chuang Li**, thank you for collaborating with me on the magnetic photoactuator project. I apologize for not having faith in the project - thank you for patience in driving the project and motivating me to continue working on it until we had that amazing and surprising walking sample on our first (second?) try in November 2018.
- **Hang Yuan and Aaveg Aggarwal**, thank you for your theoretical work and simulations on the magnetic hydrogel project, it really pushed forward our understanding of the material and our ability to control and design robotic function.
- **Adam Dannenhoffer**, thank you for making so many molecules for me, for both failed and successful projects. I know that it takes enormous patience and faith to develop new synthetic routes for molecules with unproven utility, and I appreciate your efforts. Your fridge management was also amazing and appreciated.

- **Dr. Leonel Barreda,** thank you for making all those molecules for me and Nick, as well as providing color and personality to the lab. Outings with the lab were never a dull occasion with you around.
- **Dr. Victor Lopez Dominguez**, thank you for all your help with VSM measurements and understanding how magnets work.
- **Professor Pedram Khalili**¸ thank you for letting me use your VSM instrument with Victor.
- **Tyler Pearson**, thank you for your help and efforts with SQUID magnetometry.
- **Dr. Ashwin Narayanan**, thank you for livening up the office with food and conversation, and for dealing with MicroMagnetics, "Sensible Solutions".
- **Hussain Sangji**, thank you for taking care of the confocal microscope and tolerating the mess that Hiro and I leave whenever we do VT experiments.
- **Eric Earley**, thank you for creating and running SolidWorks workshops with the McCormick Graduate Leadership Council. Without your tutorial on how to use SolidWorks, I likely would have never considered taking on the variable-temperature stage design and fabrication discussed in Chapter 5.
- **McCormick School of Engineering**, thank you for providing amazing resources to graduate students, including funding for student groups, software packages like SolidWorks, and a brand new graduate student machine shop just in time for me to begin prototyping the variable-temperature stage.
- **Joe Kuechel**, thank you for always being willing and available to assist with machining at the Ford machine shop.

- **Salomon Rodriguez**, thank you for running the graduate student machine shop and giving such helpful suggestions for machining the VT stage and miscellaneous lab apparatuses.
- **Bruce Lindvall,** thank you for caring for all graduate students in McCormick and being such a great advisor for MGLC. I think you are one of the most vital parts of the administration underappreciated by the general student body, and I try to correct that every time your name comes up in conversation.
- **My undergrads**, **Elizabeth Waring, Emily Beeman, Elad Deiss-Yehiely, Ryan Zambrotta, and Isabel Albelo**, thank you for all your work on various project described here. It was a pleasure working with you and I hope that I was able to teach you as much as I learned mentoring you.
- **Professor David Dunand and Shannon Taylor**, thank you for enabling and assisting me with the hydrogen reduction experiments discussed in Chapter 3.
- **Professor Donald Sadoway,** thank you for introducing me to the field of materials science and engineering and providing the foundational lab experiences that led me to pursue a PhD.
- **Drs. Dane Boysen, Weifeng Wei, Kai Jiang, Kangli Wang and Ulrich Muecke**, thank you for tolerating me as I learned how to work in a lab and conduct science. The regimented data collection approach and hard-working spirit still stay with me today and helped me survive through grad school.

- **Dr. Mervin Zhao**, thank you for helping me apply to grad school and giving me a glimpse of what grad school life is one year ahead of me. Without you, I'm not sure I would have gotten into grad school and ended up where I am now.
- **Professor Warren Ruder**, thank you for your life advice and help with applying to grad school – you helped me become a better person at ADPhi and were one of the early influences that led me to apply to grad school.
- **Dr. Carla Shute**, thank you for managing the constantly malfunctioning TGA and helping troubleshoot thermal uniformity issues in the MatCI facility ovens.
- **Jerry Carsello and Dr. Sumit Kewalraman**, thank you for taking care of the XSW and making sure it still ran so Nick and I could finish the supercap project.
- **The Stupp Group super-admins – Laura, Maura, Dan, and Todd**, thank you for keeping the group running smoothly with the enormous volume of scheduling and supply/product ordering you deal with on a daily basis.
- **Mark Seniw,** thank you for all your amazing Cinema-4D graphics! They're an amazing tool for visualizing and explaining our research.
- **Tim Jager @ DMC Engineering**, thank you for your open-source project on cheap digital amplifiers and your help with sourcing components for it. People like you make the internet a wonderful place for learning how to engineer and hack projects.
- **Dr. D.J. Fairfield**, thank you for guiding me and Nick into the world of electrodeposition and mentoring us when we first joined the group.
- **Professor Zhilin Yu,** thank you for help synthesizing molecules and the really helpful suggestion for UV-vis spectroscopy to quantify PyBA concentration.

- **Professor Kohei Sato,** thank you for synthesizing that nightmare diene surfactant, it’s too bad it didn’t help keep our supercapacitors alive.
- **Dongxu Huang,** thank you for your help with trying to model the organic-cobalt hydroxide system and the delicious hot pot and home-cooked dinners!
- **Dr. Taner Aytun,** thank you for getting me addicted to good coffee and all the fun rides on the Taner express.
- **James Passarelli,** thank you for your realistic and helpful research suggestions, your patience in listening to all my crazy engineering ideas, and the geeking out over space and technology when I’m trying to procrastinate on work.
- My roommates, past and present: Dr. Seyoung Cook, Hayk Yegoryan, Dr. Shawn Chen, and Karen Derocher, thank you for making coming home something to look forward to every night and weekend.
- **The crew, Dr. Shawn Chen, Karen Derocher, and Dr. Ha-Kyung Kwon**, thanks for all the early sunrise workout and breakfast memories.
- **YouTube**, thanks for being such an accessible fountain of knowledge. I’ve learned how to solder, handle giant magnets safely, source and assemble electrical components, use Illustrator, troubleshoot an Agilent gas chromatography system, and edit videos by watching YouTube videos.
- **Amazon**, thanks for connecting me to the world of cost-effective unbranded electrical and mechanical components. The quick tests and experiments I did with these products gave me confidence to continue research projects and buy components that were orders of magnitude more expensive.

- **Digikey**, thanks for being such a reliable source of electrical components with actual product data sheets.
- **Dr. Joe Strzalka**, thank you for all your help with GIXS experiments at Northwestern.
- **Everyone I met through MGLC**, thank you for all the fun times running events and trying to make McCormick a better place.
- **My predecessors and successors at NETG**, thank you for continuing to provide an engaging community for students interested in learning about and entering the energy sector.
- **Vivian and Edwin,** thank you for welcoming me as part of your family and playing Overwatch with me, both before and after I married your sister.
- **Mom and dad,** thank you for always being supportive of my choice to go to grad school. The continual reminder that “grad school is hard, you don’t have to finish, and you can always come home” is both comforting and motivating at the same time.
- **Tiffany and Wendy**, thank you, my two wonderful sisters who support me in my personal life and remind me that there is life and success outside of science and research.
- **Christie,** thank you for being the best life partner I could ever ask for. Your infinite patience, love and wisdom has helped me become a better person and scientist.

LIST OF ABBREVIATIONS

AAO – Anodic alumina

CPP – Critical Packing Parameter

CLSM – Confocal laser scanning microscopy

DA – Decanoic Acid

EDL – electric double-layer

EDLC – electric double-layer capacitance

EIS – Electrochemical impedance spectroscopy

FRAP – Fluorescence recovery after photobleaching

FRET - Förster resonance energy transfer

GIXS – Grazing incidence x-ray scattering

GISAXS – Grazing incidence small-angle x-ray scattering

GIWAXS – Grazing incidence wide-angle x-ray scattering

HAADF – High angle annular dark-field

KOH – Potassium hydroxide

LC – Liquid crystalline

LCST – Lower critical solution temperature

MCH+ – Merocyanine

NBA – 1-naphthalenebutyric acid

NiNW – Nickel nanowire

PA – Peptide amphiphile

PMI-CA – Perylene monoimide chromophore amphiphile

PMI-CA-1 – 3-Pentylamino perylene monoimide

PyBA – 1-Pyrenebutyric acid

PyAA – 1-Pyreneacetic acid

PyHA – 1-Pyrenehexanoic acid

SEM – Scanning electron microscopy

SPIO – Superparamagnetic iron oxide

SP – Spiropyran

SP1 – Variant 1 of the Spiropyran molecule (*6-(3', 3'-dimethyl-8-methoxyspiro [chromene-2,2'-indolin]-1'-yl) hexyl methacrylate*)

SP2 – Variant 2 of the Spiropyran molecule (*6-(3', 3'-dimethyl-spiro[chromene-2,2'-indolin]-1'-yl) hexyl methacrylate*)

SQUID – Superconducting quantum interference device

STEM - Scanning transmission electron microscopy

TEM – Transmission electron microscopy

UHMR – Ultrahigh magnetic responsive(ness)

VSM – Vibrating sample magnetometry

VT – Variable-temperature

XRD – X-ray diffraction

5-ROX –5-carboxy X-rhodamine

CONTENTS

LIST OF TABLES

LIST OF FIGURES

1 INTRODUCTION

1.1 MORPHOLOGICAL DEVELOPMENT IN ORGANIC-INORGANIC HYBRID MATERIALS

The study of organic-inorganic hybrids has been a rich field for developing materials with emergent functional properties resulting from novel structures and interfaces. The “bottom-up” approach of molecular and macromolecular self-assembly has enabled the synthesis of hybrid materials exhibiting a high level of structural sophistication.[1,2] The use of self-assembling organic amphiphiles has been the keystone of this approach, drawing from nature for inspiration to template complex inorganic morphologies.[3] The field of supramolecular chemistry is critical to understanding how these morphological phases may be controlled. The term was first coined by Jean-Marie Lehn in 1978 to describe “chemistry beyond the molecule” – e.g. chemical interactions besides covalent bonds.[4] Examples of these non-covalent interactions include electrostatics, hydrogen bonding, van der waals forces, and π-π stacking, among others.

One of the most highly studied supramolecular systems is the family of amphiphilic surfactant molecules. In 1976, Jacob Israelachvili proposed the concept of a “critical packing parameter” (CPP), which provides general rules for how simple amphiphilic surfactants can pack into different structures based on the geometric constraints of the hydrophilic headgroup and length of the hydrophobic tail.[5] These rules have provided a baseline philosophy for how to approach creating structures ranging from spherical and cylindrical micelles to vesicles and bilayers. This knowledge translated to the use of cationic surfactants to template highly ordered nanostructured silicates in sol-gel processing at the beginning of the nineties.[6,7] These seminal works provided the foundation for designing ceramic materials with tailored mesopore size and crystalline order for use as catalyst supports and adsorbents. Following this, there was a natural progression to utilize block co-polymer amphiphiles to take advantage of larger molecular weight to further increase pore size, as well as access new inorganic structures such as lamellae and 3-dimensional gyroids.[8,9] In parallel, there were efforts to expand the number of inorganic compounds that can be templated with self-assembled organic phases, such as the development of lamellar CdS templated by polyol amphiphiles,[10] hexagonally-ordered superlattices of semiconducting CdSe and CdS templated by lyotropic non-ionic amphiphiles,[11] and mesoporous metal oxides templated by poly(alkylene oxide) block copolymers.[12]

In the aforementioned works, the organic component of the hybrid material generally only plays a structural templating role and is often removed to leave a pristine nano-/mesostructured inorganic phase. In these cases, one may question whether we should consider the resulting material a true functional hybrid. An early prominent example of a self-assembled hybrid material where both the inorganic and organic phases provide functionality is the synergistic self-assembly of a conjugated aromatic surfactant with zinc hydroxide to form lamellar photoconductors, as developed by Sofos and Goldberger in the Stupp laboratory.[13] (Figure 1.1) In this example, the organic phase provides the dual role of stabilizing the inorganic layers during thermal annealing and conversion to semiconducting zinc oxide, as well as acting as a photosensitizer to enable application as a photoconductor.

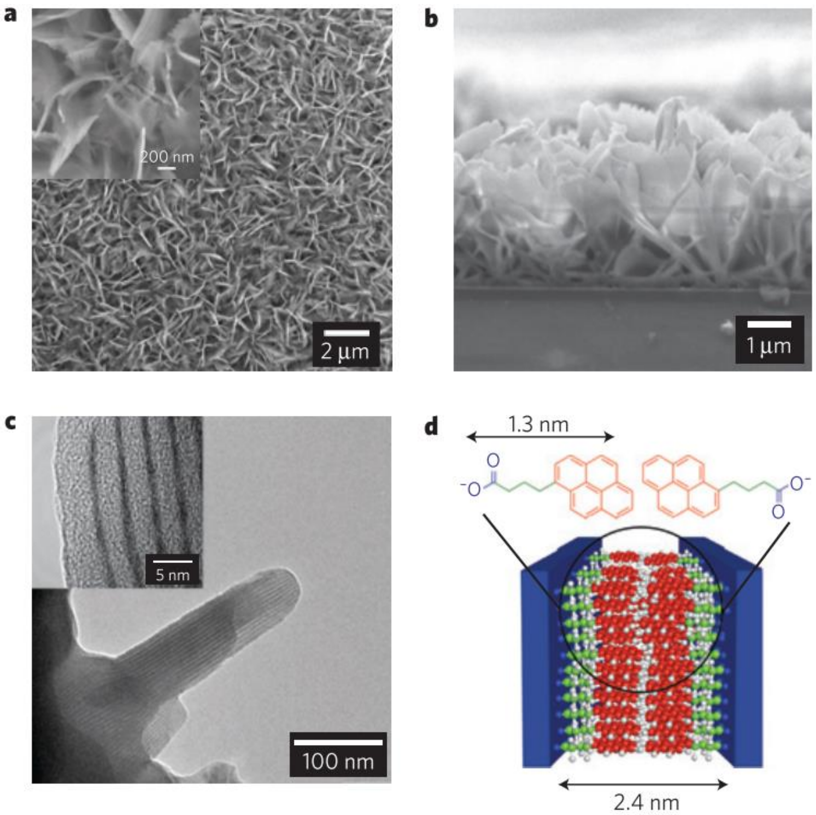

Figure 1.1 Overview of electrodeposited hybrid lamellar structures. a) Top-down SEM of electrodeposited flakes using 1-pyrenebutyric acid (PyBA) as a surfactant; b) cross-sectional SEM of the electrodeposited flakes; c) TEM image of lamellar flakes showing alternating organic-inorganic layers; d) schematic diagram of lamellar ordering showing zinc oxide inorganic sheets (blue) and organic bilayers of PyBA molecules. Reproduced from Sofos *et al*.[13]

Following this work, there have been many efforts within the Stupp group to understand how organic surfactants may be used to control the resulting morphology of organic-inorganic hybrids synthesized with them. Control over orientation of the hybrids as electrodeposited on conductive substrates was explored by Herman *et al*, since orienting the zinc oxide layers perpendicular to the substrate would facilitate electron transport and increase efficiency when used in organic photovoltaic cells.[14] Design rules for the molecular structures of conjugated organic amphiphiles to control their interactions with the underlying substrates for electrodeposition were also hypothesized as a way to control the final hybrid morphology.[15] (Figure 1.2) Furthermore, the use of oligothiophene-peptide conjugates as the organic phase for templating hybrids in solution with zinc oxide enabled more complex hybrid micro-/nano-structures such as multi-layered scrolls and tubes. However, such oligothiophene conjugates were unfortunately less stable to the thermal annealing processes required for increasing crystallinity of the inorganic zinc oxide phase, limiting performance as hybrid photoconductors.[16,17]

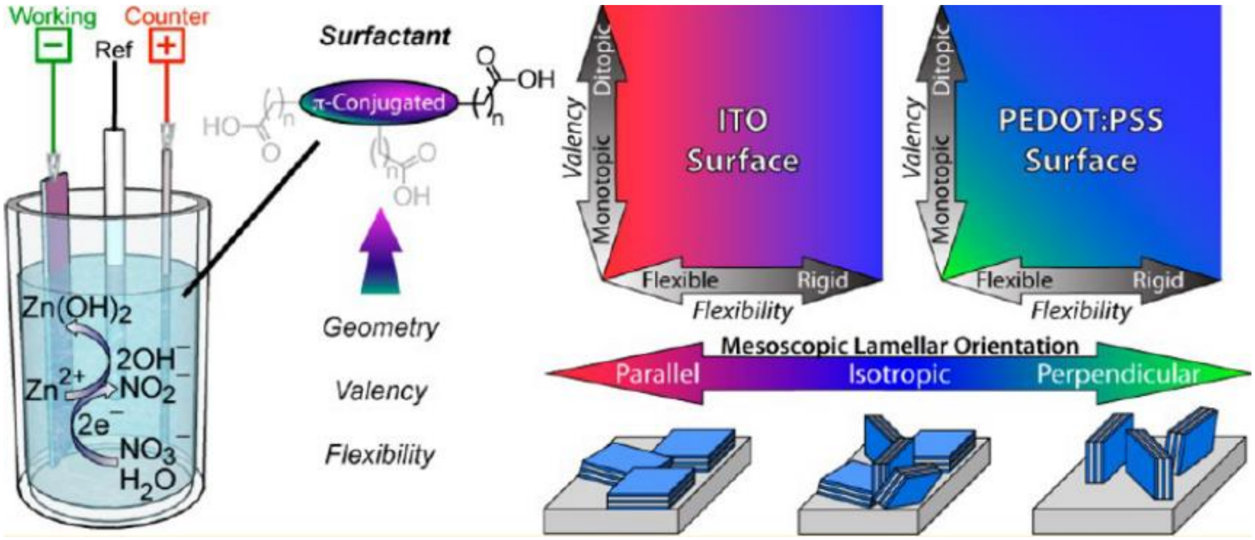

Figure 1.2 Schematic showing the dependence of surfactant molecular structure and underlying substrate on the orientation of hybrid lamellar flakes after electrodeposition. Reproduced from Bruns *et al*. [15]

In parallel to the investigation of organic-inorganic hybrids for photovoltaics and photoconductors, researchers working on asymmetric supercapacitors also took advantage the ability of layered transition metal hydroxides to intercalate anionic molecules during synthesis to tune the inorganic morphology, interlayer spacing and overall performance as a charge-storage material. One notable example is the formation of cobalt hydroxide ‘nanocones’ through hydrothermal synthesis in the presence of a sodium dodecyl sulfate surfactant. [18] These nanocones with large interlayer spacings were found to exhibit higher charge storage capacity and lower electrochemical impedance compared to nanocones exchanged with smaller anions to reduce the interlayer spacing. Other groups have also used ionic liquids and ethanolamine during synthesis of cobalt hydroxide, creating high surface area nanostructured flakes and single layers of cobalt hydroxide, respectively. How the organic phases mediate the resulting morphologies of the organic-$Co(OH)_2$ hybrids is still not thoroughly understood and will be discussed in Chapter 2.

1.2 SOFT ARTIFICIAL ACTUATORS

Soft artificial actuators are another active field of materials research inspired by nature, with scientists targeting materials that are capable of morphing shape and exerting force under external stimuli. Skeletal muscles provide an elegant example for researchers to emulate with artificial materials – the millions of aligned sarcomeres within muscle tissue contracting in concerto can exert large macroscopic forces, a lofty goal for artificial actuators designed for soft robotics. These sarcomeres consist of supramolecular actin and myosin polymers anchored on macromolecular titin backbones,[19] forming a blueprint for hierarchically-ordered actuators that researchers can mimic to produce unidirectional and programmable actuation. Recently in the Stupp Group, Chin *et al* have shown that hierarchically-ordered actuators can be formed by hybridizing supramolecular peptide amphiphile (PA) nanofibers with thermoresponsive covalent polymers. This hierarchical ordering enables anisotropic shrinkage during heating of the hybrid gel due to the mechanical reinforcement provided by the circumferentially-aligned PA nanofibers. (Figure 1.3) [20] Soft artificial actuators may be categorized by their responsiveness to the following external stimuli, as compiled by Hines *et al.*: electrical, magnetic, chemical, thermal, light, and hydraulic pressure. (Figure 1.4)[21] The categories of photoactive and magnetically active actuators are highlighted in the following subsections 1.2.1 and 1.2.2. Combining the dual stimuli of light and magnetic fields to create new actuation modes in a novel polymer-magnetic nanoparticle composite forms the basis for Chapter 4.

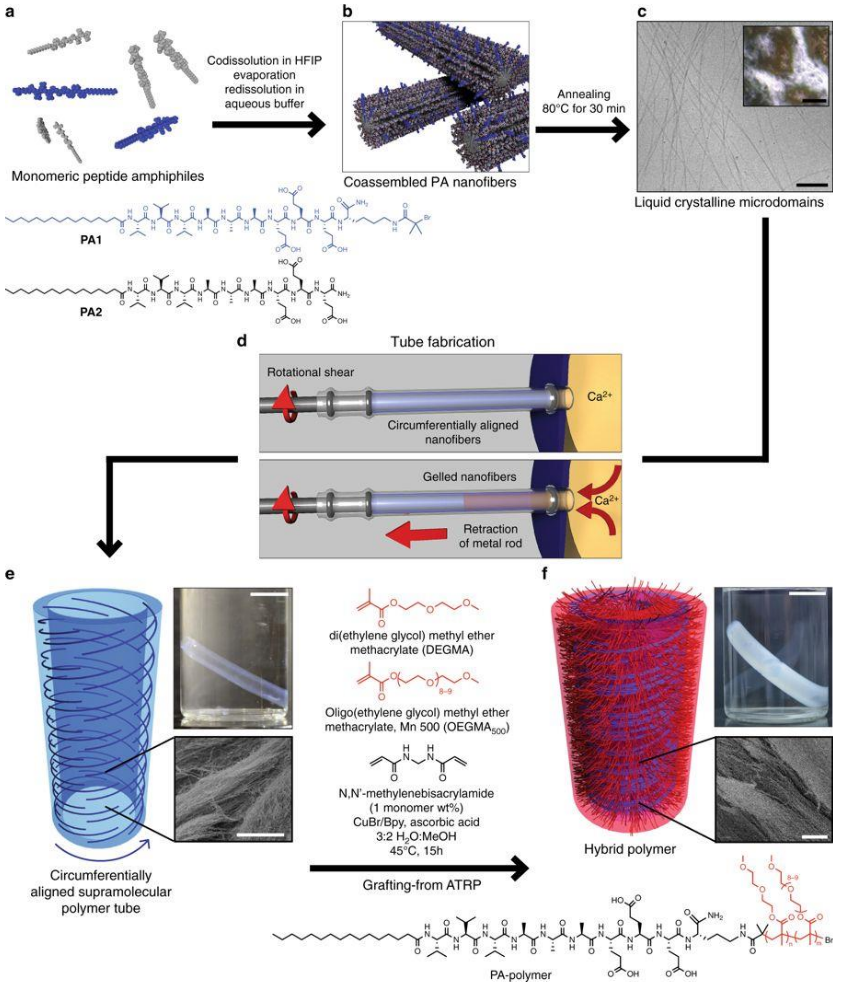

Figure 1.3 Overview of hybrid actuator synthesis. Scale bars are c) 200 nm in cryo-TEM, 200 μm in polarized optical microscopy; e,f) 1 cm in photographic insets, 10 μm in SEM insets. Reproduced from Chin *et al*. [20]

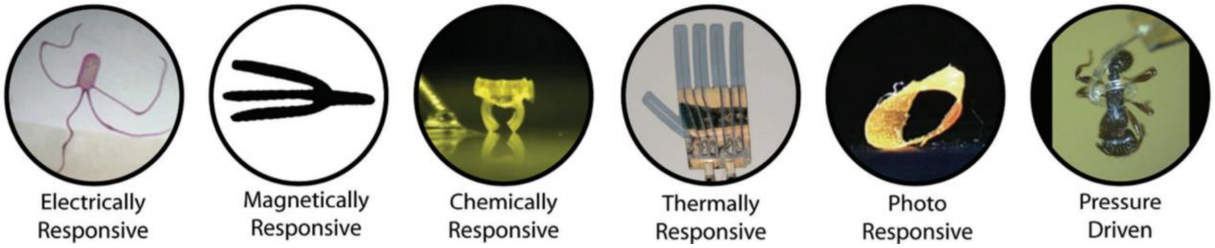

Figure 1.4 Examples of small soft robotic systems responsive to various stimuli. Reproduced from Hines *et al*. [21]

1.2.1 PHOTOACTUATION IN SOFT MATERIALS

Light is an attractive approach to actuating materials because of the ability to spatiotemporally control irradiation. This form of remote stimuli enables localized deformation in addition to modes of locomotion involving oscillation of light intensity and synchronous actuation. Two of the most explored materials classes for soft photoactuators are liquid-crystalline (LC) polymers and photoresponsive hydrogels.[21]

In photoresponsive LC polymer systems, the LC mesogens are typically aligned either through mold surface texturing pre-polymerization or mechanical stretching post-polymerization. Photo-switches – molecules that change isomers under irradiation of light – can be either incorporated as the LC mesogen or used as cross-linkers within the LC polymer network. When these switches absorb light, the isomerization results in a volumetric change in the polymer network due to the change in physical conformation of the molecule. The attenuation of light through the thickness of photoresponsive LC polymer systems is often quite high due to the large molar absorptivity of the photo-switches, resulting in local surface volume changes and bending of the macroscopic material. (Figure 1.5)[22] Complex shapes such as helices of varying pitch length[23] and fast oscillatory bending[24] can be achieved with control of mesogen alignment and polarization of the irradiating light source, respectively.

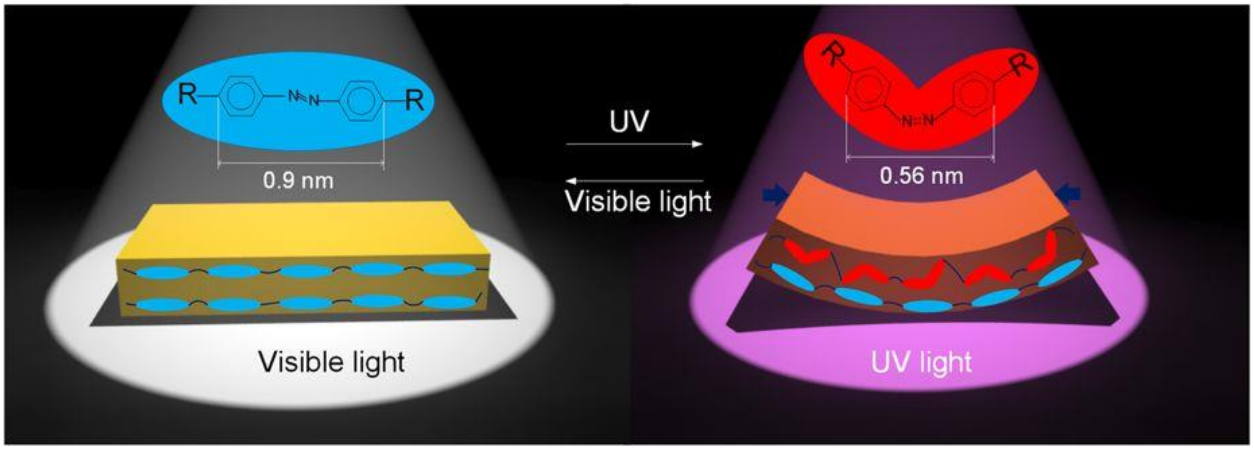

Figure 1.5 Example of actuation mechanism in LC polymers through photoisomerization. Reproduced from Huang et al.[22]

While LC polymer photoactuators are attractive due to their fast actuation speeds and high elastic modulus, they often require the use of harmful UV light for photoisomerization and present difficulties in achieving complex mesogen alignment patterns in bulk materials extending beyond thin films. Photoactive hydrogels are a promising alternative because of the potential for large deformations resulting from volumetric swelling/de-swelling behavior, as well as the possibility for biocompatible chemistry and use as drug delivery vehicles.[25,26] Hydrogels may be sensitized to light by incorporation of photoreactive moieties that act to contract the network either through physical changes in isomer conformation or through isomeric changes in ionicity and thus hydrophilicity. One family of photo-switches extensively studied for use in hydrogel actuators is the merocyanine-spiropyran class of chromophores, which switch from the ring-opened protonated merocyanine isomer to ring-closed hydrophobic spiropyran isomer under exposure to blue light. (Figure 1.6)[27] Bulk volumetric changes have enabled use of photoactuating hydrogels as light-controlled microfluidic valves,[28] while gradients in light transmission and thus degree of photoisomerization can result in macroscopic bending of rods and application as microconveyor belts.[27]

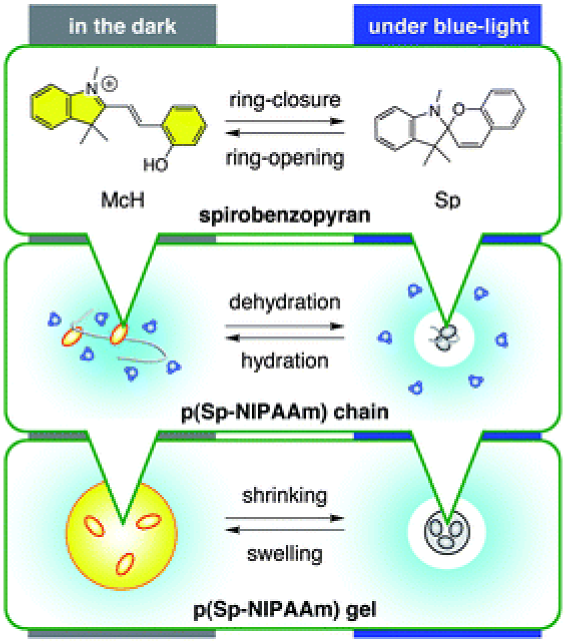

Figure 1.6 Schematic overview of the relationship between isomerization of the spiropyran class of chromophores and the hydration state of a spiropyran-functionalized hydrogel. Reproduced from Satoh *et al.* [27]

It is important to note that in both these systems, photothermal effects must be taken into consideration, as light absorption typically results in some heat generation that may influence or even overshadow actuation induced by photoisomerization. In LC polymers, heating the material can induce a phase transition from the ordered state to the isotropic state, accompanied by volumetric shrinkage. Hydrogels similarly can undergo thermally-induced shrinkage through a property known as a lower critical solution temperature (LCST), where water is driven out of the gel as the polymer entropically collapses at elevated temperatures.[25] While the actuation phenomenon may be similar to that induced by photoisomerization, higher light intensities and the associated heat generation may limit use in thermally sensitive biological applications. However, Gelebart *et al* were able to take advantage of photothermal effects to create oscillating physical waves in LC polymer films under constant angled light irradiation.[29] In this example, photothermal heating of the film was not large enough to induce transition from the ordered nematic LC phase to the isotropic phase. Instead, the elevated temperatures increased kinetics of the relaxation of the photoexcited azobenzene cis-isomer back to the trans-isomer. Along with self-shadowing of the angled light source by the buckled LC polymer film, this fast cis-trans relaxation created a fast feedback loop that manifests in physical traveling waves of the polymer film that increase in frequency as the intensity of light is amplified.

1.2.2 MAGNETIC MATERIALS FOR ANISOTROPIC REINFORCEMENT AND PROGRAMMABLE ACTUATION

Until the last two decades, the use of magnetic fields and magneto-responsive materials has remained relatively untapped for controlling mechanical properties and motion in artificial actuators. Magnetic control is a promising approach to manipulating soft matter because of the ability to remotely apply forces and torques with minimal interaction with surrounding non-magnetic media. This presents opportunities in assembling magnetic particles within soft matter for mechanical reinforcement, fabricating and actuating magnetically active soft composites, and controlling materials for biological applications.[30]

Magnetic fields can move magnetically active materials in two different ways – magnetic body force and magnetic torque. Magnetic body force is experienced by magnetized materials in the presence of magnetic field gradients, resulting in migration and aggregation towards regions of higher field strength. Magnetic body force is quite useful for concentrating and collecting magnetic particles, particularly for biological applications such as magnetic separation of cells and antibodies.[31] However, use of magnetic body forces requires feedback-intensive control to precisely manipulate materials and can easily result in non-uniform distributions when used to manipulate suspensions of magnetic particles.

Whereas magnetic body force is commonly used for translation of magnetic materials, magnetic torque is responsible for the alignment of magnetically anisotropic materials in magnetic fields. In uniform magnetic fields, no magnetic body force is applied and torque is the only interaction with a magnetic dipole, as the dipole aligns itself with the direction of the external magnetic field to reduce its magnetic potential energy. This can be used to great effect as a platform for massively parallel alignment of magnetic particles during fabrication of composite materials.[32] The different types of magnetic torque are summarized below in Figure 1.7.[30] It is important to note that for a material to experience magnetic torque, it first must exhibit magnetic anisotropy, forms of which include remanent magnetization from ferromagnetism, magnetocrystalline anisotropy, or geometric anisotropy.

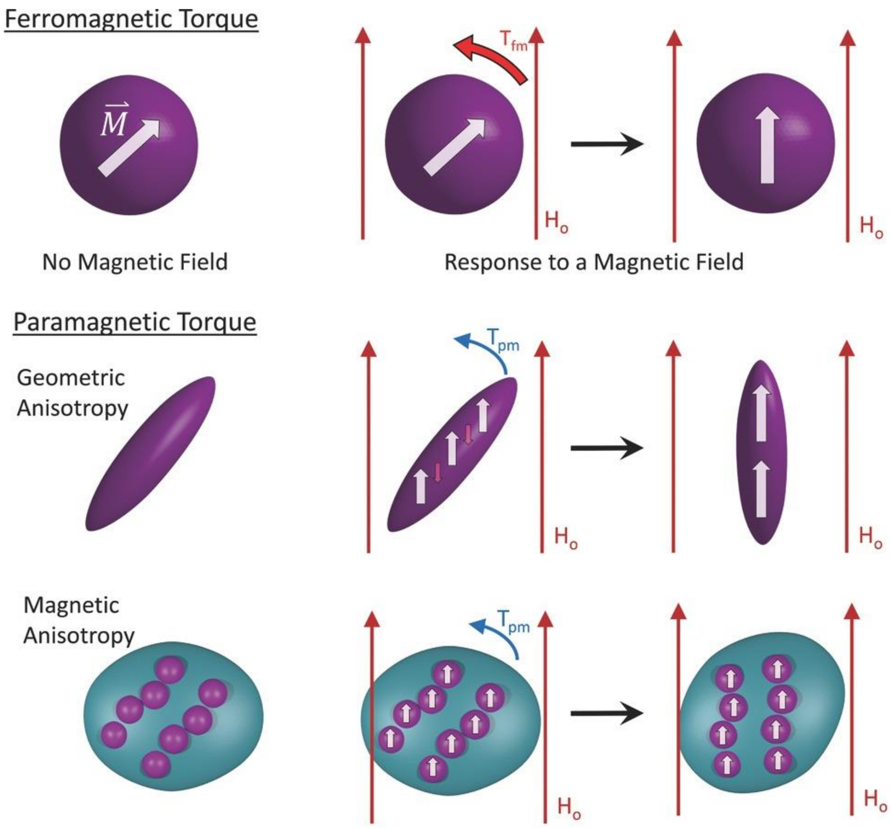

Figure 1.7 Overview of different types of magnetic torque. Adapted from Erb et al.[30]

Superparamagnetic iron oxide (SPIO) nanoparticles are one of the most commonly utilized magnetic particles across scientific fields due to their non-toxicity, tunability of surface chemistry, and insusceptibility to remanent magnetization-induced aggregation.[33] In the context of actuating soft materials, SPIO particles can be used to mechanical reinforce materials and impart anisotropic swelling.[34] Since SPIO particles are paramagnetic and do not retain remanent magnetization in the absence of an applied magnetic field, geometric anisotropy must be used to allow magnetic torque align mechanically reinforcing SPIO particles. In work pioneered by Erb *et al*, SPIO nanoparticles are used to impart ultrahigh magnetic responsiveness (UHMR) to geometrically anisotropic alumina plates when such microparticles are coated with SPIO by surface adsorption.[32] Under high-frequency low-amplitude magnetic fields, the long-axis of UHMR particles are easily aligned perpendicular to the axis of magnetic rotation due to "phase ejection" of plate rotation with respect to the magnetic field.[35] These UHMR particles were then used control swelling-deswelling behavior of hydrogels formed with alginate, gelatin and poly-(N-isopropylacrylamide), yielding helical deformation when bilayers with different directions of mechanical reinforcement were swollen.[34]

SPIO particles have also been used to directly control deformation of the soft actuators through paramagnetic torque. Kim *et al* showed that SPIO nanoparticles can be chained and aligned within photocurable polymer under the application of magnetic fields.[36] Different portions of the polymer composite contained SPIO chains with distinct orientations, as each section was separately cured with varying magnetic field directions. The resulting chains displayed shape anisotropy and could thus experience torque under the application of magnetic fields post-polymerization. This paramagnetic torque bent and twisted the microactuators as the patterned chains of SPIO nanoparticles aligned in the direction of the magnetic field. In related work, SPIO particles were randomly dispersed within an elastomeric matrix to form millimeter-scale swimmers propelled by paramagnetic torque.[37] The macroscopic shape of the swimmers as molded endowed geometric anisotropy to the composite and allowed the swimmer to rotate along its long axis under rotating applied fields. Finally, a combination of these two approaches was embodied in work by Huang *et al*, which utilized chains of SPIO particles as mechanical reinforcement to induce helical curling upon swelling of hydrogel bilayers.[38] The fabricated millimeter-scale "micromachines" with scrolled heads and helical flagella could swim under uniform rotating magnetic fields. Since hydrogels with LCST were used, thermally induced de-swelling of one layer could reduce the pitch length of the swimmer's flagella and tune the amount of propulsion produced. It is interesting to note that Huang *et al* were able to perform vibrating sample magnetometry (VSM) on SPIO/hydrogel composites as a function of SPIO particle alignment. Larger remanent magnetization was observed and a larger coercive field was required to demagnetize the composites with aligned SPIO chains, indicating that condensed geometrically anisotropic assemblies of SPIO particles can begin to exhibit ferromagnetic behavior.

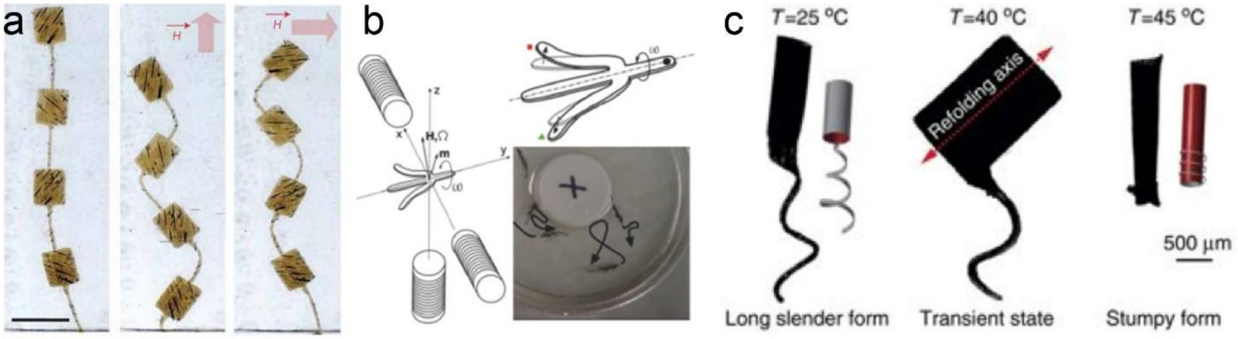

Figure 1.8 Examples of magnetic soft actuators. Adapted from a) Kim *et al*[36] b) Garstecki *et al* [37] and c) Huang *et al*.[38] Scale bar for a) is 100 μm.

While SPIO particles are attractive to use in soft magnetic actuators because of their nontoxicity and biocompatibility, ferromagnetic particles can often exert larger torques and result in faster actuation and/or deformation of materials with larger elastic moduli. Ferromagnetic torque for low applied magnetic fields (below the coercive field) scales linearly with the remanent magnetization of the material. A recent approach pioneered by the Sitti lab is creating soft ferromagnetic composites by polymerizing microparticles of NdFeB rare earth magnets within an elastomer. Non-uniform magnetization profiles are patterned within strips of these composites by wrapping them circumferentially around glass rods and applying a strong unidirectional magnetic field perpendicular to the long axis of the rods. (Figure 1.9)[39,40] The resulting harmonic magnetization profile enables accurate modeling and prediction of bending behavior, as well as precise control of complex actuation that allows the resulting robot to swim, crawl, walk, roll and jump. Simultaneously, Kim *et al* at the Zhao lab developed a novel approach to patterning ferromagnetic domains in NdFeB elastomeric composites by 3D printing with an electromagnet attached to the print nozzle to re-align NdFeB microparticles as they are extruded. (Figure 1.10)[41] While not as many modes of locomotion are explored for soft robots fabricated with this method, more complex actuation geometries are accessible through this innovative magnetic domain printing.

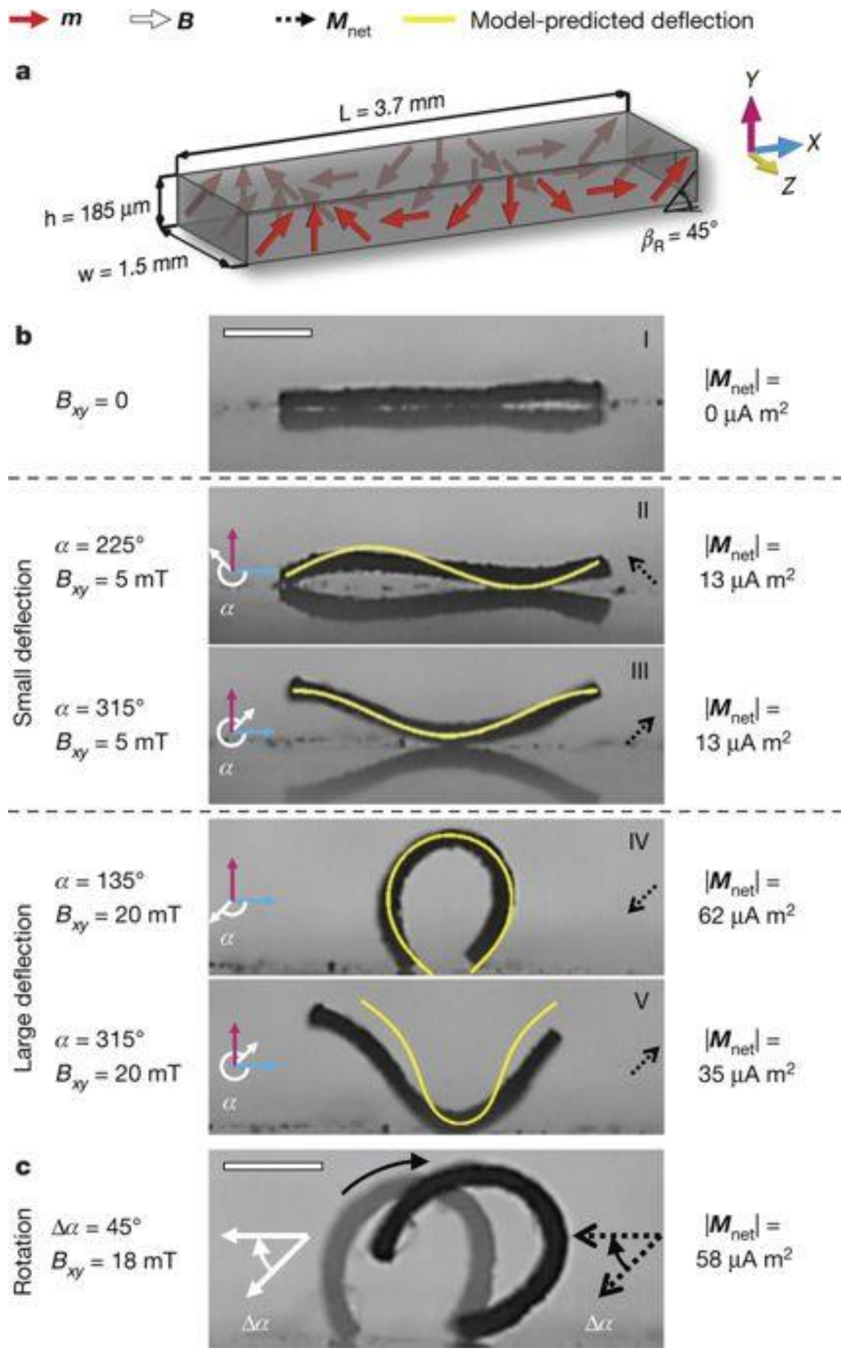

Figure 1.9 Magnetization profile and deflection under magnetic fields of a NdFeB/elastomer ferromagnetic composite soft robot. Reproduced from Hu *et al*.[40]

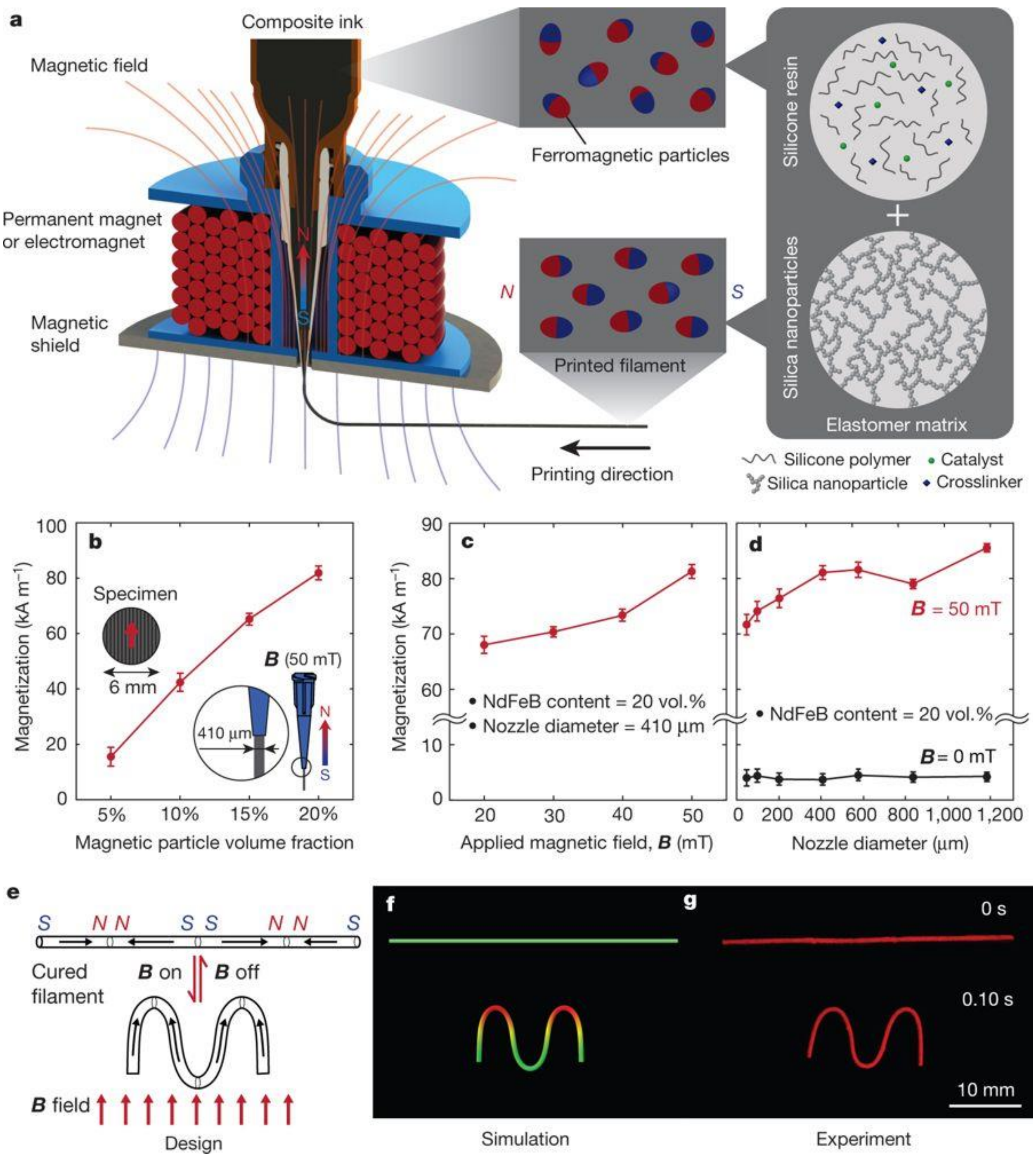

Figure 1.10 Printing of ferromagnetic domains in a NdFeB/elastomer ferromagnetic composite using extrusion printing with an on-board electromagnet. Reproduced from Kim *et al*.[41]

A fascinating intersection between ferromagnetic materials and shape anisotropy is the study of ferromagnetic metallic nanowires. The effect of shape anisotropy on the magnetic properties of ferromagnetic nanowires was first studied in 1993 by Whitney *et al*, where cobalt and nickel nanowires were deposited in track-etched polymer membranes.[42] They demonstrated that these nanowires displayed a preferred magnetization direction along their long axis and had enhanced coercivities and remanent magnetization as their diameters were decreased. This is perhaps the first example of increasing the "hardness" of a soft ferromagnetic material through nanostructuring. Further detailed magnetic studies on arrays of Co and Ni nanowires demonstrated that the relatively low magnetocrystalline anisotropy of Ni nanowires (NiNWs) allow NiNWs to exhibit magnetic shape anisotropy even at diameters exceeding the crystalline grain size.[43,44] In comparison, the shape anisotropy effect in polycrystalline Co nanowires of larger diameters (≥ 100 nm) is outcompeted by large magnetocrystalline anisotropy due to the lack of crystalline grain orientation, resulting in lower observed magnetic anisotropy. Because of their enhanced coercivity, relative stability to oxidation and corrosion, and ease of synthesis through commercially available anodic alumina membranes,[45,46] NiNWs have been used to study liquid crystal elastic interactions,[47,48] microscale rheology,[49–52] and magneto-active optical switches.[53] Their ease of alignment under magnetic fields also make them a promising candidate for mechanically reinforcing soft actuators and deforming them with magnetic torque, yet there have been no published reports of their use in such applications to date.

1.3 STRUCTURE MORPHING IN SUPRAMOLECULAR NANOSTRUCTURES

Supramolecular chemistry has also been studied as a way to understand and control the self-assembly of nanostructures that have great potential application in biological and electronic applications.[54] Inspired by the elegance of biological systems in their ability to form complex functional protein structures out of peptide building blocks, researchers have sought to understand the interplay between various supramolecular interactions and how they may be used in designing self-assembled structures.[55] The concept of thermodynamic energy landscapes have been highly investigated as a way of explaining the pathway dependence of observed self-assembled nanostructures. The Meijer group demonstrated in 2012 that helical supramolecular polymers of a thermodynamically unfavorable chirality may be accessed and kinetically trapped through addition and subsequent removal of a chiral auxiliary molecule.[56] Meanwhile, Tantakitti and Boekhoven *et al* in the Stupp group showed that PA concentration and solution ionic strength could be used to shift thermodynamic favorability of long and short PA nanofibers.[57] By using ionic strength to switch off electrostatic repulsion between PA molecules, long nanofibers at low dilutions were shifted from an energetically unfavorable kinetically trapped state to the preferred thermodynamic state. The trapping of the long PA nanofiber state was shown to have biological relevance, as short nanofibers were dramatically more cytotoxic than long nanofibers. These works demonstrated that pathways of formation and an understanding of energy landscapes, in addition to the traditional rational molecular design approach, are critical for determining final structure and function in supramolecular systems.

Thermal annealing of supramolecular assemblies is commonly used as a method of overcoming activation energy barriers and accelerating the morphing into thermodynamically preferred structures.[58–63] However, most of these studies heavily rely on ex-situ microscopy and imaging to characterize the formed thermodynamic structures. In-situ characterization of these structures at elevated temperatures is generally limited to bulk scattering and spectroscopic techniques such as x-ray scattering, dynamic light-scattering, circular dichroism, UV-vis absorption, and fluorescence. These techniques are often dominated by the majority structure or are limited by assumptions about scattering form factors. New techniques capable of in-situ imaging supramolecular nanostructures at elevated temperatures are required for capturing the structural diversity as well as providing quantitative kinetic data during shape transformations.

1.4 THESIS OVERVIEW

This thesis explores morphological development and shape changes in hybrid and soft materials across the nano- to macroscale. Morphogenesis is a term traditionally used within the field of developmental biology to describe the biological processes that cause organisms to develop and change shape. These processes include the spatiotemporal release and capture of morphogenic molecules that diffuse and signal cell differentiation, contextual buckling that results from growth within confinement, and mechanical forces such as blood flow.[64] Within the context of materials science, the term morphogenesis is used here to describe how materials develop their shape and morph with the input of reaction components or external stimuli such as light, magnetic fields or heat.

In chapter two, we first describe the unexpected formation and growth of multi-walled organic-inorganic nanotubes for energy storage applications. The use of conjugated organic amphiphiles allows for the formation of cobalt hydroxide-pyrenebutyric acid nanotubes instead of the more commonly observed layered lamellar hybrids. These nanotubes exhibit diameters of 30 nm and lengths of several micrometers, offering high surface area as well as macroscopic perpendicular orientation to allow for fast charge-discharge rates when used as supercapacitor electrodes.

In chapter three, we describe hierarchical metallic architectures that are enabled by metal hydroxide-amphiphile hybrid layered nanofibers as templates. These templates can be grown on top of macroporous nickel foam and processed by calcining and reduction under hydrogen to form hierarchical metallic structures. These materials may be used as electronically conductive current collectors that allow for spatially efficient loading of either charge storage or catalytic materials for energy applications. While the metallic nanowires formed from the hybrid templates exhibit high surface area, the slow multi-step synthetic process limits scalability of the material. Electroless deposition of nickel under magnetic fields is explored as an alternative method for growing metallic nanowires on nickel foam, and lead to an understanding of magnetic nanomaterials that fueled research into creating magnetically-controlled soft robots in the next chapter.

In chapter four, we discuss the use of magnetic fields to align ferromagnetic nickel nanowires within photoactive hydrogels. These hydrogels are exposed to directional lighting to morph their shapes with internal gradients of hydration induced by the conversion of covalently-bonded dyes from their hydrophilic to hydrophobic forms. The development of curved shapes under exposure to light creates complex magnetization profiles based on the orientation of magnetic nanowires locked within the hydrogel matrix. These 3-dimensional magnetization profiles are not easily achieved with traditional magnetization patterning techniques and enable actuation and locomotion of the hydrogels under directionally rotating uniform magnetic fields. The resulting macroscopic soft robots can walk, flip and roll underwater, as well as carry hydrogel cargoes.

In chapter five, the skills and insights derived from thermal processing of materials in chapter three are used to design and fabricate a variable-temperature stage for use with confocal laser scanning microscopy. The thermal uniformity and careful design of the stage enables heating of liquid samples in close proximity to the short working distance objective lenses required to achieve higher resolution in confocal microscopy. We study the thermal annealing of supramolecular nanostructures in-situ using this device, allowing for direct observation of shape changes and morphing as the assemblies reach their thermodynamically-favored structures.

Chapter 6 provides an overview of the research discussed in this dissertation and offers perspectives on where each project leaves the state of its respective field. Future outlooks and proposals for further experiments and study are provided. The chapter also offers a narrative of how each project was conceived and how each one of them was influenced by the surrounding research environment within the Stupp group and Northwestern University, describing morphogenesis at the metalevel of this PhD research experience.

2 ORIENTED MULTI-WALLED ORGANIC-$Co(OH)_2$ NANOTUBES FOR ENERGY STORAGE

2.1 OBJECTIVES AND SIGNIFICANCE

In energy storage materials, large surface areas and oriented structures are key architecture design features for improving performance through enhanced electrolyte access and efficient electron conduction pathways. Layered hydroxides provide a tunable materials platform with opportunities for achieving such nanostructures via bottom-up syntheses. These nanostructures, however, can degrade in the presence of the alkaline electrolytes required for their redox-based energy storage. We report here on a layered $Co(OH)_2$-organic hybrid material that forms a hierarchical structure consisting of micrometers-long, 30 nanometer diameter tubes with concentric curved layers of $Co(OH)_2$ and 1-pyrenebutyric acid. The nanotubular structure offers high surface area as well as macroscopic orientation perpendicular to the substrate for efficient electron transfer. Using a comparison with flat films of the same composition, we demonstrate that the superior performance of the nanotubular films is the result of a large accessible surface area for redox activity. We found that the organic molecules used to template nanotubular growth also impart stability to the hybrid when present in the alkaline environments necessary for redox function.

2.2 BACKGROUND

Over the past decade there has been great interest in energy storage materials partly motivated by consumer demand for portable electronics and electrified vehicles.[65–67] Supercapacitors are a promising class of electrochemical energy storage devices that can exhibit superior power capabilities and cycling lifetimes over traditional batteries.[68,69] However, conventional supercapacitors that store energy through electric double-layer capacitance (EDLC) in symmetric carbon-based electrodes have only limited energy density compared to currently used batteries. There has been growing interest recently in asymmetric supercapacitors that utilize high-performance EDLC anodes,[70,71] in conjunction with faradaic cathodes that undergo redox reactions and thus have much larger energy densities.[72–74] Among the materials investigated for cathodes, cobalt(II) hydroxide ($Co(OH)_2$) is a particularly promising candidate due to its high theoretical specific capacity and electrical conductivity.[75–77] This metal hydroxide is known to form a crystalline layered structure that facilitates ion transport, and in the presence of an oxidizing potential and hydroxide ions it will transform into a cobalt(III) oxyhydroxide (CoOOH) phase.[78] This charging transformation is easily reversible in a discharge process that reduces the oxyhydroxide back to the original cobalt hydroxide. This redox reaction offers the potential for high energy storage density and rapid charge/discharge cycles, the two attributes that define a supercapacitive material. While the operating voltage window for $Co(OH)_2$ electrodes is limited to ~ 0.5 V, solid-state asymmetric supercapacitor devices utilizing $Co(OH)_2$-based cathodes and EDLC anodes have demonstrated stable potential windows of 1.2 and 1.8 V.[79,80] This electrode pairing balances the high capacity and small voltage window of $Co(OH)_2$ with the low capacity and large voltage window of EDLC materials.

In an effort to increase the specific capacity of $Co(OH)_2$ electrodes, previous work has focused on the synthesis of high surface area nanostructures[80] and strategies to increase the interlayer spacing of $Co(OH)_2$ with various types of intercalated anions.[78] In addition to optimization of specific capacity, one of the critical challenges in the use of this material in supercapacitor devices is its inherent instability in alkaline electrolytes necessary for the redox reaction. Dissolution of layered cobalt hydroxide in the alkaline environment leads to re-precipitation of a different phase known as β-$Co(OH)_2$, which lacks intercalated anions, and to an accompanied change in microstructure that may compromise performance.[81–83] Direct observation of this degradation in nanostructured $Co(OH)_2$ electrodes is particularly challenging due to the common use of additives to create an electrically conductive network between energy storage particles and the current collection substrate. An important advance in this area would be to generate additive-free cobalt hydroxide electrodes with high capacity to conduct and store charge. The absence of additives is crucial to observe and understand mechanisms of degradation during charging and discharging cycles. In this work, we describe a one-pot electrodeposition process for the synthesis of hybrid organic-$Co(OH)_2$ electrodes without additives. In-situ synthesis of inorganic-organic hybrids has been an area of great interest as a strategy to generate unique morphologies, inspired by biomineralization processes.[2,7,8,11,84–87] Electrodeposition can lead to synthesis of high surface area hybrid nanostructures with tunable interlayer spacing and controllable orientation of the inorganic layers with respect to the substrate.[13–15,88,89] Applying this technique to $Co(OH)_2$ materials can yield high specific capacity electrodes with direct conduction pathways through the inorganic layers allowing for additive-free operation.

2.3 RESULTS AND DISCUSSION

2.3.1 ELECTRODEPOSITION MORPHOLOGIES

We first synthesized hybrid layered nanostructures on stainless steel substrates by electrodeposition in a water/dimethyl sulfoxide solution of cobalt nitrate ($Co(NO_3)_2$) and 1-pyrenebutyric acid (PyBA) surfactant. Cathodic reduction of nitrate ions increases the local pH near the surface of the steel working electrode, resulting in the deposition of $Co(OH)_2$. We selected PyBA as an amphiphile with a carboxylate group that could bind to the $Co(OH)_2$ layers and an aromatic core that could form attractive intermolecular interactions such as π-π stacking. We found that this synthetic procedure promotes the growth of nanotubular structures perpendicular to the substrate using cross-section scanning electron microscopy (SEM) (a). Analysis of transmission electron microscopy (TEM) images shows outer diameters of the tubes ranged from 22 to 46 nm with an average of 30 nm, while the inner diameters were measured to be 12 ± 2 nm. TEM further reveals that the nanotubes are composed of alternating layers of PyBA and cobalt hydroxide with a periodicity of about 3 nm (Figure 2.1b, left and top right). The cross-section for each tube shows equal number of layers on both sides, suggesting a concentric tube structure. High-angle annular dark-field scanning transmission electron microscopy (HAADF STEM) depicts the inorganic cobalt hydroxide layers as bright rings when viewed down the long axis of the hybrid tubes, further verifying the concentric arrangement (Figure 2.1b, bottom right). Subtracting the ~4.7 Å thickness of a single $Co(OH)_2$ sheet from the interlayer periodicity derived from x-ray scattering (*vide infra*), we calculate an interlayer gap width of 25.2 Å between $Co(OH)_2$ sheets.[80,90] Since the length of a single PyBA molecule is 1.3 nm,[13] we suggest that the PyBA molecules are not interdigitated and arrange instead in a bilayer structure. The bilayer structure would of course facilitate interactions between Co ions and carboxylate anions while still allowing π-π overlap among aromatic cores of the amphiphiles (Figure 2.1c and d). We observe the same nanotubular morphology for films deposited on lightweight and flexible substrates such as graphite foil and carbon fiber paper (Figure 2.2). While a solvothermal synthesis has been recently reported to homogeneously nucleate $Co(OH)_2$ nanotubes of similar diameters[91], our work is the first example of $Co(OH)_2$ nanotubes of high curvature heterogeneously nucleated on a substrate.

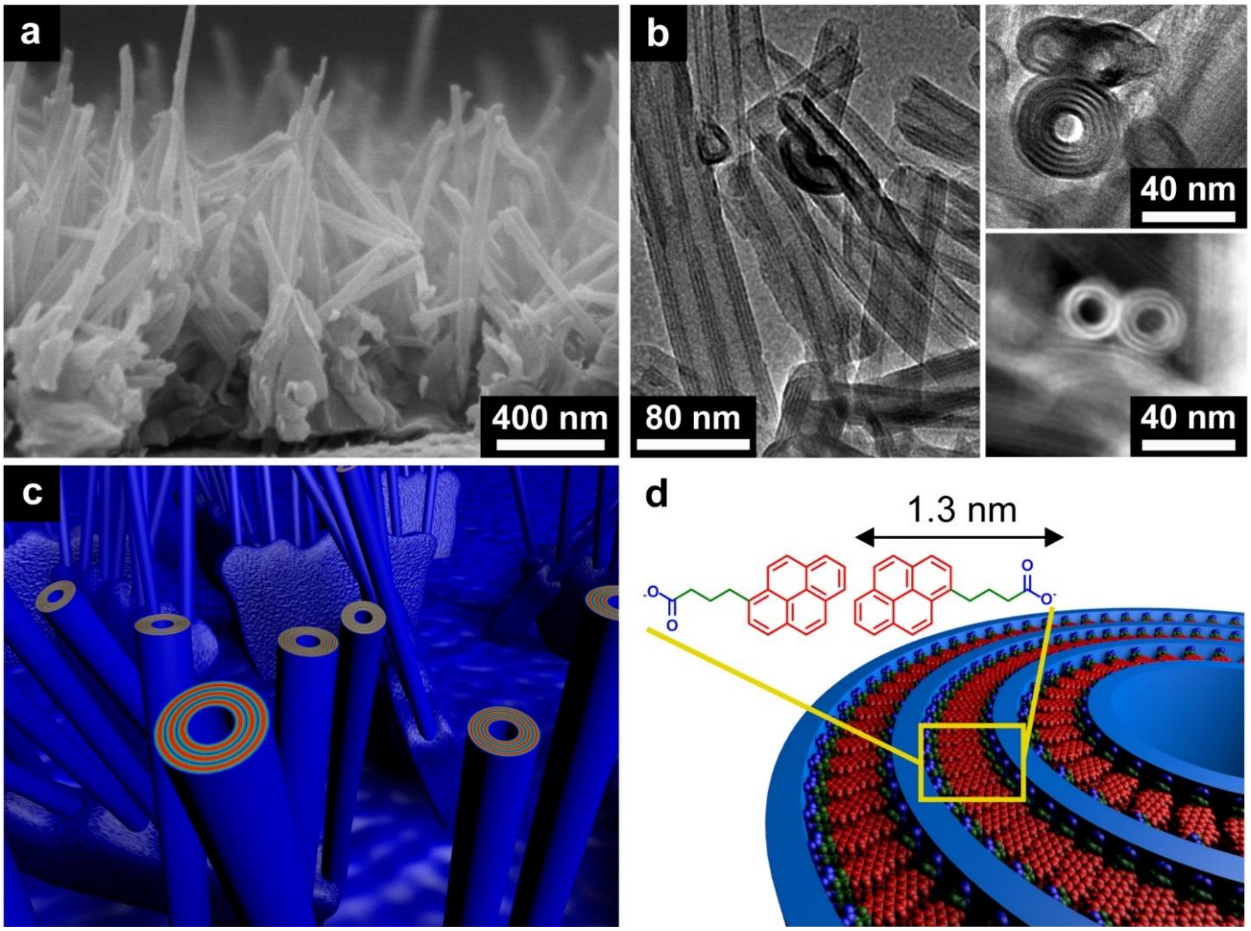

Figure 2.1 Structural characterization of layered hybrid nanostructure. (a) Cross-sectional SEM image of $Co(OH)_2$/PyBA nanotubes growing perpendicular to substrate. (b) Bright-field TEM images (left and top-right) and high angle annular dark field STEM image (bottom right) of $Co(OH)_2$/PyBA nanotubes. (c) Schematic of concentric nanotubes emerging from flakes. (d) Schematic of layered ordering within a nanotube composed of inorganic $Co(OH)_2$ tubes and bilayers of PyBA.

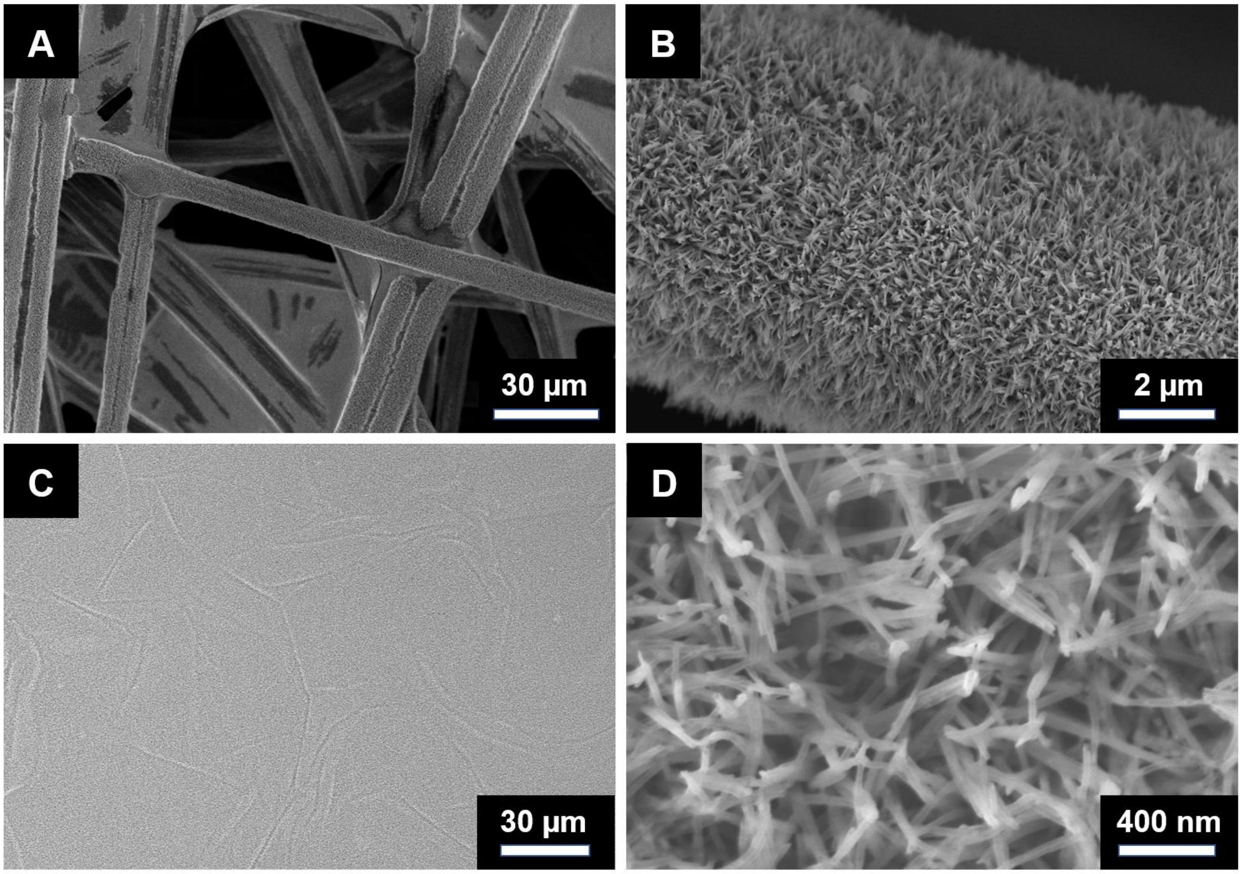

Figure 2.2 SEM images of $Co(OH)_2$/PyBA nanotubes electrodeposited on carbon fiber paper (a, b) and graphite foil (c, d).

To understand the nucleation and growth of the hierarchical tubular structure, we studied the changes in morphology using top-down and cross-sectional SEM as well as grazing incidence X-ray scattering (GIXS) (Figure 2.3). These techniques were used to characterize the structure at 5 minute intervals throughout the deposition. Three general stages of growth were observed: an initial flat dense film, a flake-like intermediate structure, and finally the perpendicularly oriented tubular structure. While small variations in reactant concentration and deposition bath pH affect the deposition time necessary for each growth stage to occur, the morphological transition from flat film to flakes to tubes was observed in all cases (see Figure 2.4, Table 2.1). Therefore, to normalize for variations in film area, we have divided the three growth stages in terms of film mass.

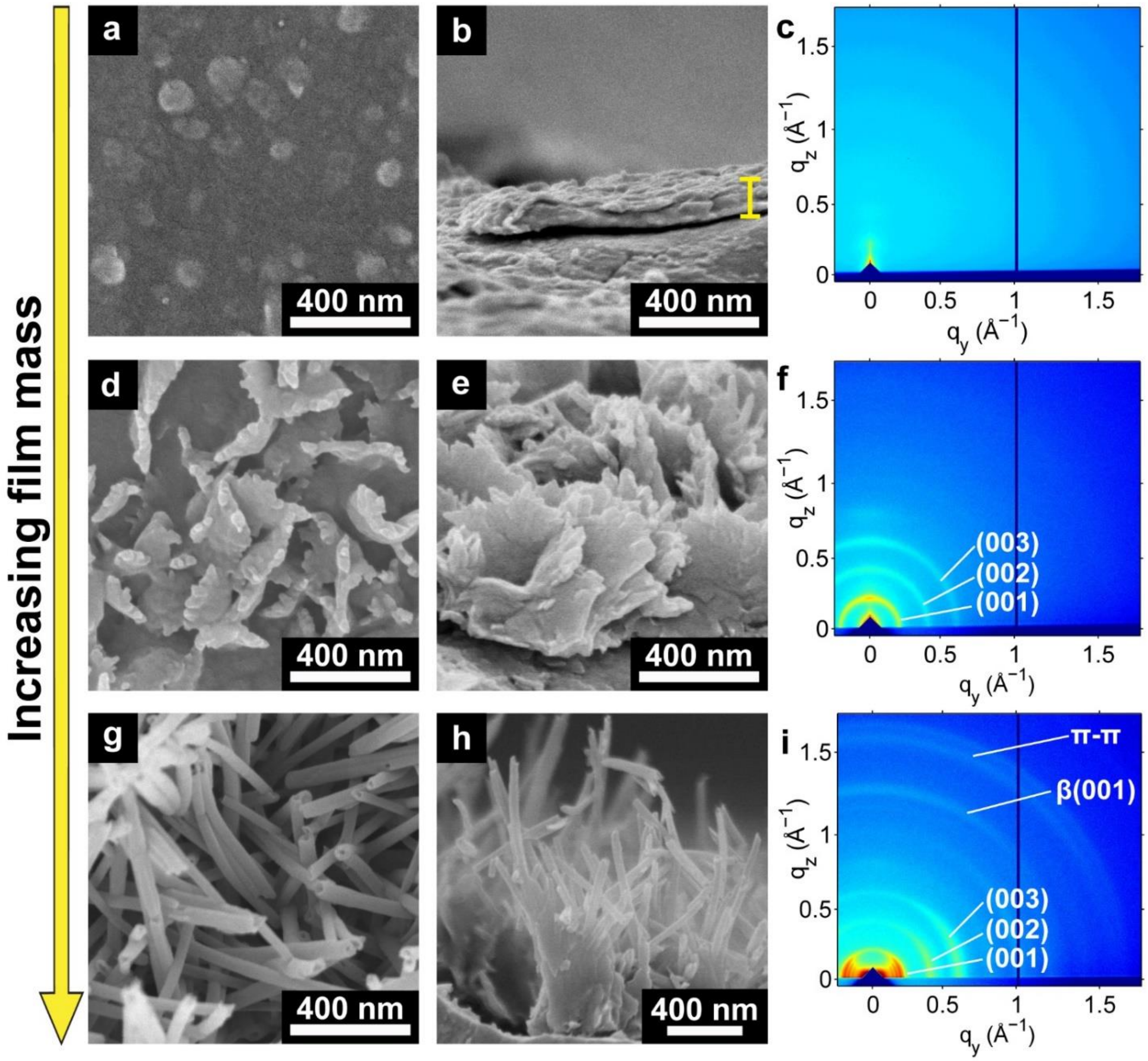

Figure 2.3 Structural evolution of the hybrid with increasing film mass. (a) Representative top-down SEM image, (b) cross-sectional SEM image and (c) 2D GIXS pattern of a 0-10 μg/cm^2 film. (d) Representative top-down SEM image, (e) cross-sectional SEM image and (f) 2D GIXS pattern of a 20-40 μg/cm^2 film. (g) Representative top-down SEM image, (h) cross-sectional SEM image and (i) 2D GIXS pattern of a 50-100 μg/cm^2 film. Emergence of π-π stacking is visible with preferential orientation parallel to the substrate. A small β-Co(OH)$_2$ impurity peak is also apparent (See **Figure 2.8**). All samples shown here were coated with 10 nm Au/Pd before imaging.

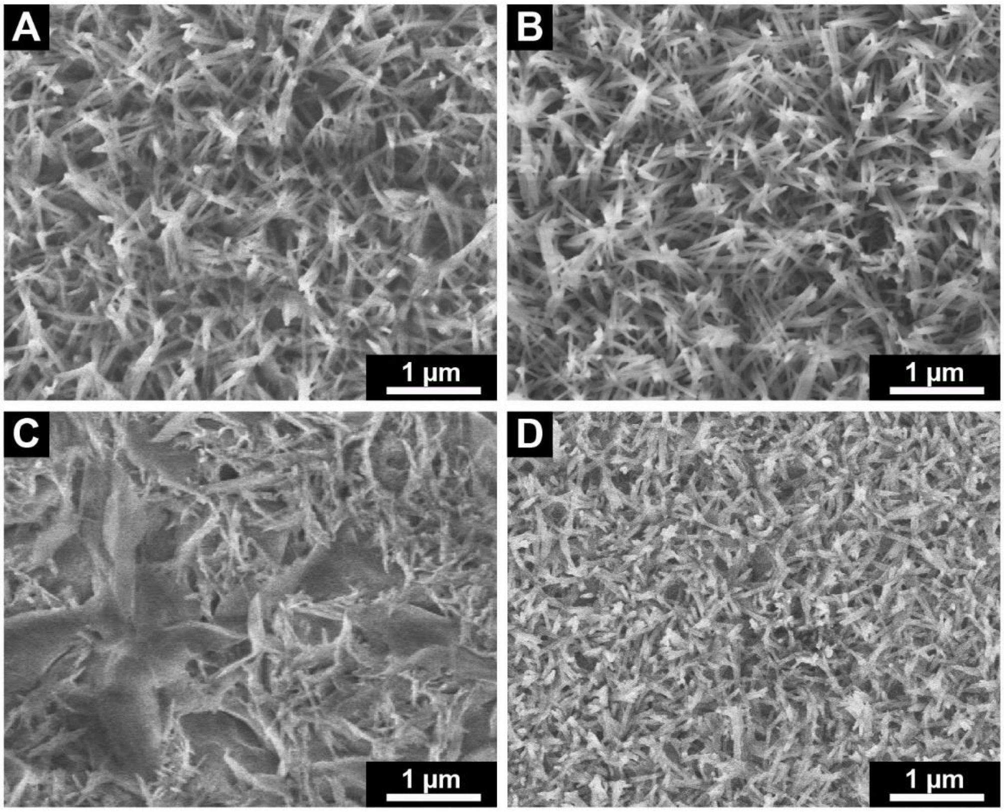

Figure 2.4 SEM images of $Co(OH)_2$/PyBA films at varying deposition bath concentrations. (a) 75% [NO_3^-] after 60 min, (b) 150% [NO_3^-] after 90 min, (c) 50% [PyBA] after 60 min, and (d) 150% [PyBA] after 120 min.

Table 2.1 Concentrations of reactants for samples in Figure 2.4.

Samples	[Co^{2+}]	[NO_3^-]	[PyBA]
A	0.1 M	0.15 M	1.25 mM
B	0.1 M	0.3 M	1.25 mM
C	0.1 M	0.2 M	0.625 mM
D	0.1 M	0.2 M	1.875 mM

The first stage of growth, in the 0-10 μg/cm^2 range, typically occurs within the first 5 minutes of deposition, and is comprised of a flat dense film of ~100 nm thickness (Figure 2.1a, b).

The GIXS pattern exhibits very weak lamellar ordering oriented parallel to the substrate, with a periodicity of ~2.9 nm (Figure 2.3c, Figure 2.5). Once the film grows to an areal density over 10 μg/cm^2, rounded protrusions begin to appear on top of the flat film. Between 20-40 μg/cm^2, discrete flakes grow vertically from these rounded structures on the flat dense base layer (Figure 2.3d,e). This is the typical structure for electrodeposited $Co(OH)_2$ thin films with organic surfactants previously reported in the literature[89] as well as in the $Zn(OH)_2$ studies from our group[13–15]. The GIXS pattern for the flake-dominant films shows a stronger lamellar ordering compared to dense films, with nearly isotropic (00*l*) rings corresponding to a d-spacing of 2.99 nm (Figure 2.3f, Figure 2.6). However, an interesting structure emerged during the final stage of growth consisting of tubes nucleated out of the ridges on top of the flakes (at film masses over 40 μg/cm^2). To our knowledge, our work is the first example of oriented metal hydroxide nanotubes grown on a substrate. At around 100 μg/cm^2 (~60 minutes of deposition time), the tubes were observed to grow to a few micrometers in length and 30 nm in diameter (Figure 2.3g and h). Since the Au/Pd coating process used for SEM imaging can result in mechanical damage of the film and partial fracture of the tubes, images of uncoated full-length tubes are provided in Figure 2.7. The lamellar d-spacing for the tubular films remains invariant at 2.99 nm, but the film transforms in time into a hierarchical structure with long range percolation of the electronically conductive redox-active phase parallel to the steel substrate normal (Figure 2.3i, Figure 2.6 and Figure 2.8). This is clearly shown by SEM and TEM images revealing radial lamellar ordering that is perpendicular to the long axes of the tubes (Figure 2.1b and Figure 2.3h). We also observed a reflection at q ~1.65 Å^{-1} with preferential orientation parallel to the substrate that does not correspond to lamellar ordering (Figure 2.9). Since this reflection corresponds to a spacing of 3.8

Å, consistent with a π-π stacking distance, we expect the PyBA molecules to be stacked with their face normal vectors perpendicular to the substrate and parallel to the long axes of the tubes (Figure 2.1d). Additionally, to get an ensemble measurement of tube diameters over the entire electrodeposited film we performed further analysis on the 2D GIXS profile. Upon close inspection of Figure 2.3i, new oscillations in the scattering profile are observed in the low *q* region (see Figure 2.10 for expanded view). These peaks correspond to form factor scattering associated with regular tube diameters across the substrate. Applying a solid cylinder form factor model with a first order Bessel function (Figure 2.11), we calculated an average tube diameter of 27.5 nm, in agreement with the average measurement from TEM imaging.

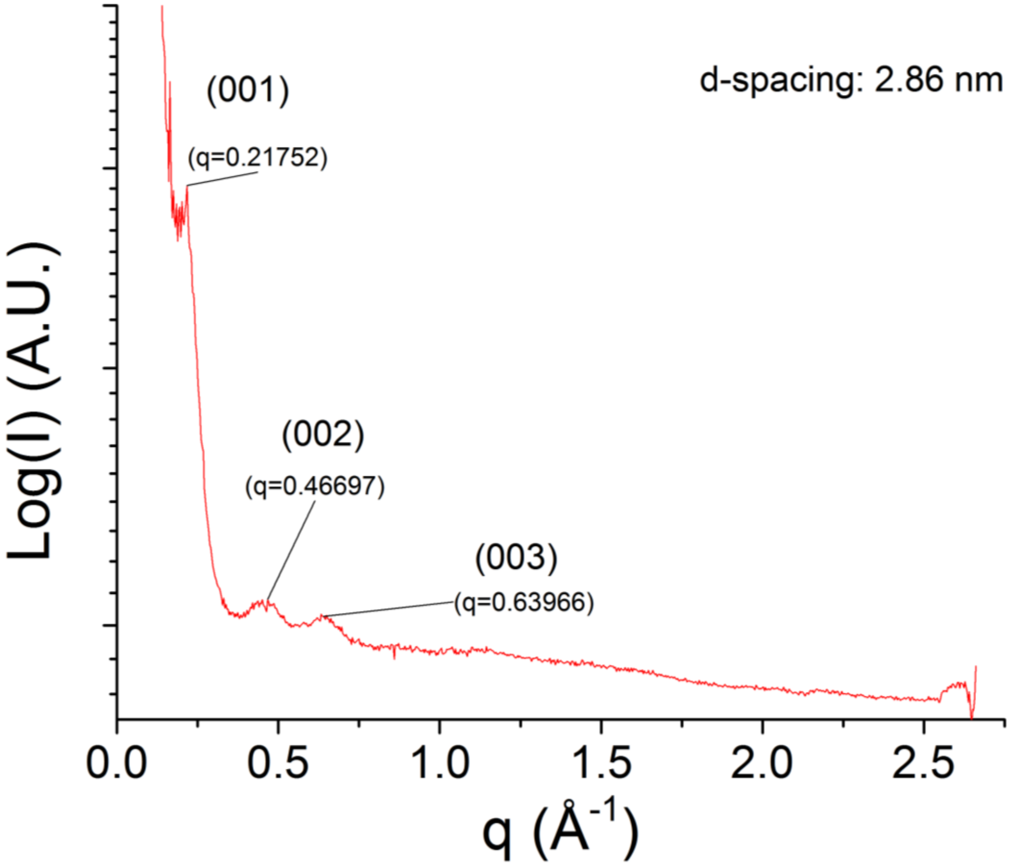

Figure 2.5 Line cut of the 2D-GIXS pattern depicted in Fig. 2C. A constrained mask on the GIXS pattern was set to Φ values of 70-90° to increase the signal-to-background ratio, since the majority of the (00L) ordering was parallel to the substrate at this growth stage and there was high fluorescence from the stainless steel substrates.

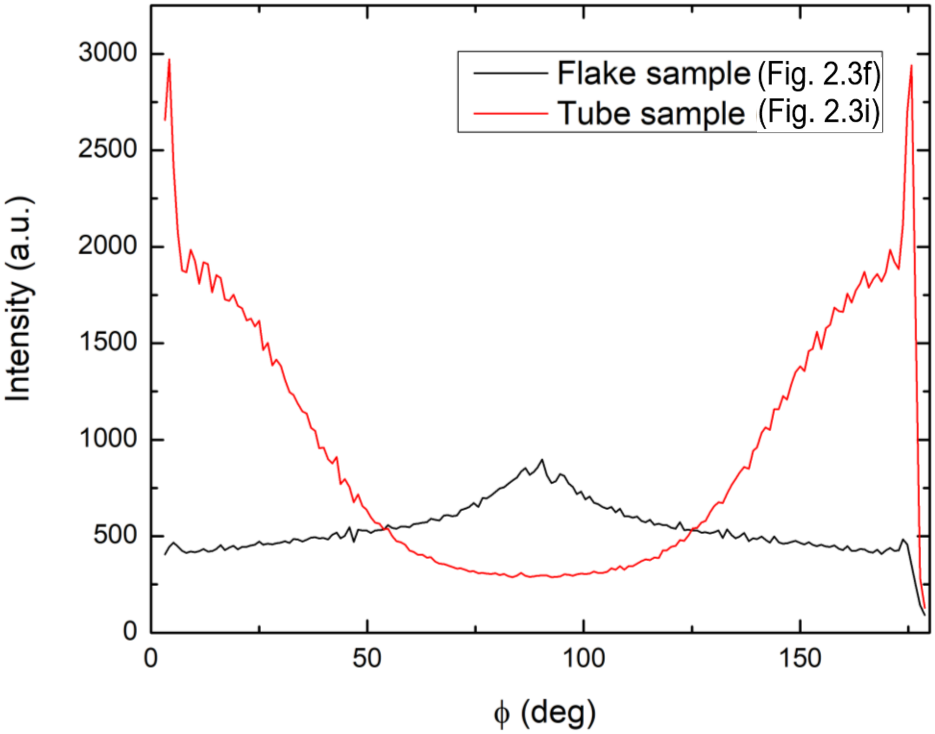

Figure 2.6 Line cut of the (001) peak in the 2D-GIXS pattern depicted in Fig. 2.3f and Fig. 2.3i, with a constraint of 0.18 Å-1 < q < 0.24 $Å^{-1}$. The larger intensity near Φ 0° and 180° clearly shows the preferential orientation of the concentric tubes perpendicular to the substrate, while the intensity for the flake sample is more isotropic with a slight preference for the (001) layers to lay parallel to the substrate (Φ = 90°).

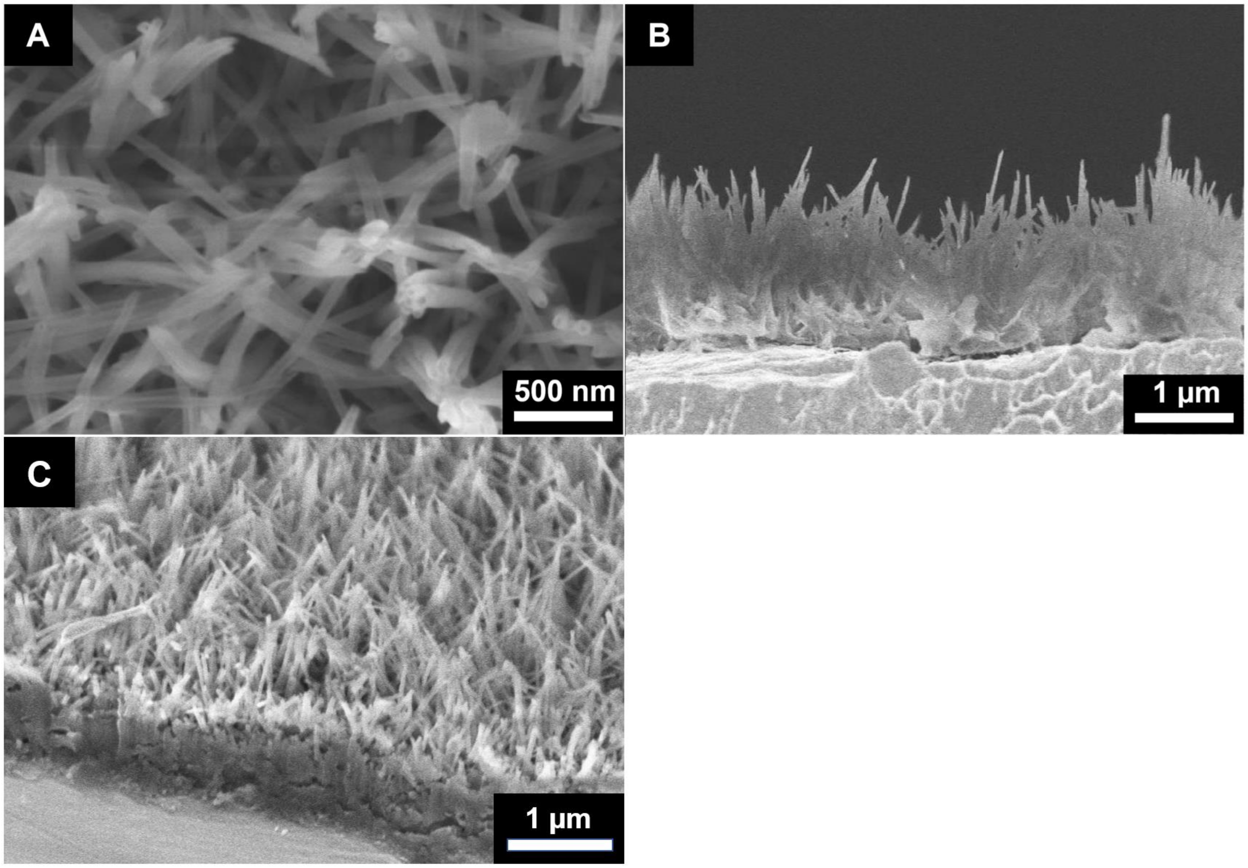

Figure 2.7 SEM images of an uncoated $Co(OH)_2$/PyBA nanotubular film from (a) a top-down view, (b) a cross-sectional view, and (c) a 30° view, showing the preferential nanotube orientation perpendicular to the substrate.

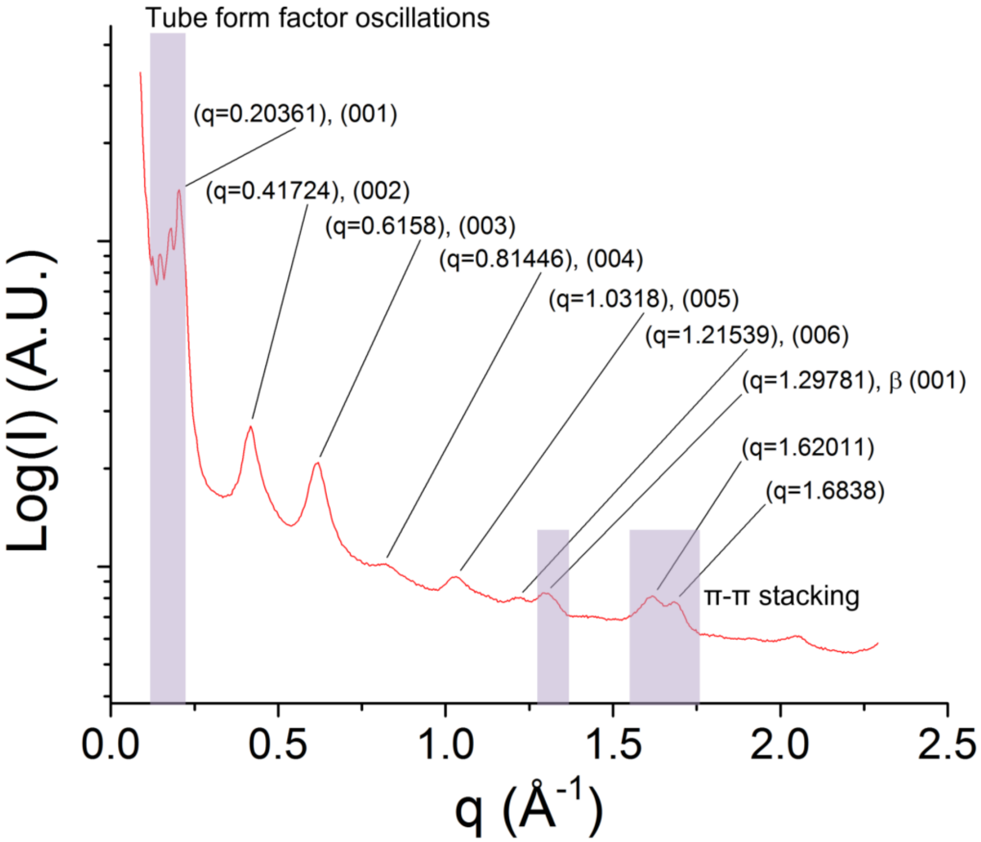

Figure 2.8 Line cut of the 2D-GIXS pattern depicted in Fig. 2.3i over Φ values of 0-90°. The tube form factor oscillations, the (001) peak for the impurity β-Co(OH)$_2$ phase and the π-π stacking peaks are highlighted in purple.

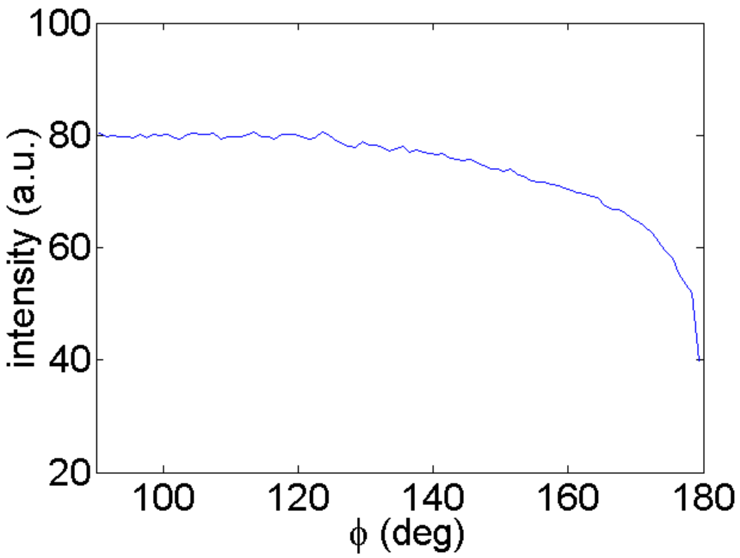

Figure 2.9 Line cut of the apparent π-π peaks in the 2D-GIXS pattern depicted in Fig. 2.3i, with a constraint of 1.55 Å^{-1}< q < 1.75 Å^{-1}. The decrease in signal intensity as Φ increases from 90° to 180° shows the preferential orientation of π-π stacking parallel to the substrate.

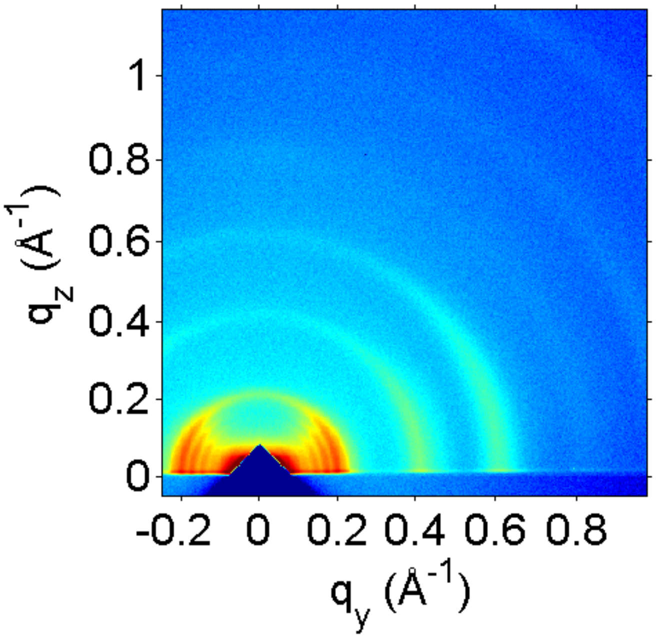

Figure 2.10 2D GIXS pattern from Fig. 2.3i. Enlarged to more clearly show the oscillations for q < ~0.2 Å^{-1} that are associated with the scattering form factor of tubes. A detailed analysis and description of this form factor is presented in section 2.6.2.

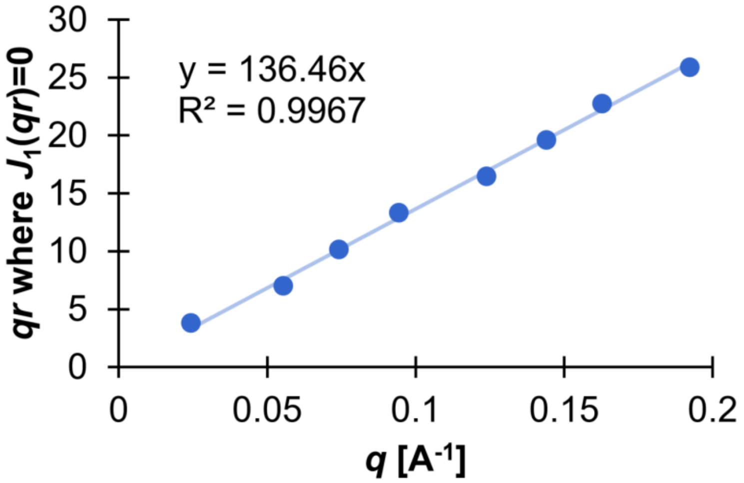

Figure 2.11 Correlation between the observed minima for the scattering intensity and the expected minima locations from the Bessel function of the first order. The first three points are derived from a GISAXS pattern, while the other five are from GIWAXS of the same sample.

To investigate the tube formation pathway in our system, we collected a series of high magnification electron micrographs on samples at different stages of tube growth (Figure 2.12). SEM images of samples at the initial stage of tube growth suggest that these tubes may be nucleated by curling of cobalt hydroxide sheets protruding from the ridges on the edge of the flakes (Figure 2.12a). The ridged flake edges are likely a result of non-uniform growth fronts during electrodeposition, similar to dendritic growth observed in electrodeposition of metals. HAADF STEM images of the same sample show the epitaxial relationship between the layered structures in the flake and the multilayer structure in the curled protrusion (Figure 2.12b). We observe in the STEM projection a line of low contrast that runs perpendicular to the flake layers and leads to the base of the curled protrusion, consistent with commonly observed projections of screw dislocations in layered materials.[92,93] We hypothesize that such screw dislocations may drive the nucleation of the nanotubes. Additionally, the curvature of the curled multilayered protrusions is similar to that of the final tubes, suggesting that the inner diameter of the tubes is defined at the initial nucleation step. One possible explanation for the induced curvature of the multilayered protrusions is internal mechanical stress between layers with different growth rates as described by Bavykin *et al*.[94] TEM and HAADF STEM images show that there are step edges along the tube axis in single layer increments (Figure 2.12c). Addition of concentric layers after initial tube formation would explain the variation in number of layers and tube outer diameters while maintaining the inner diameter. Our observations on the nanotube growth pathway reveal that screw dislocations in the layered flakes may result in epitaxial nucleation of curved multilayer sheets that close into concentric tubes.

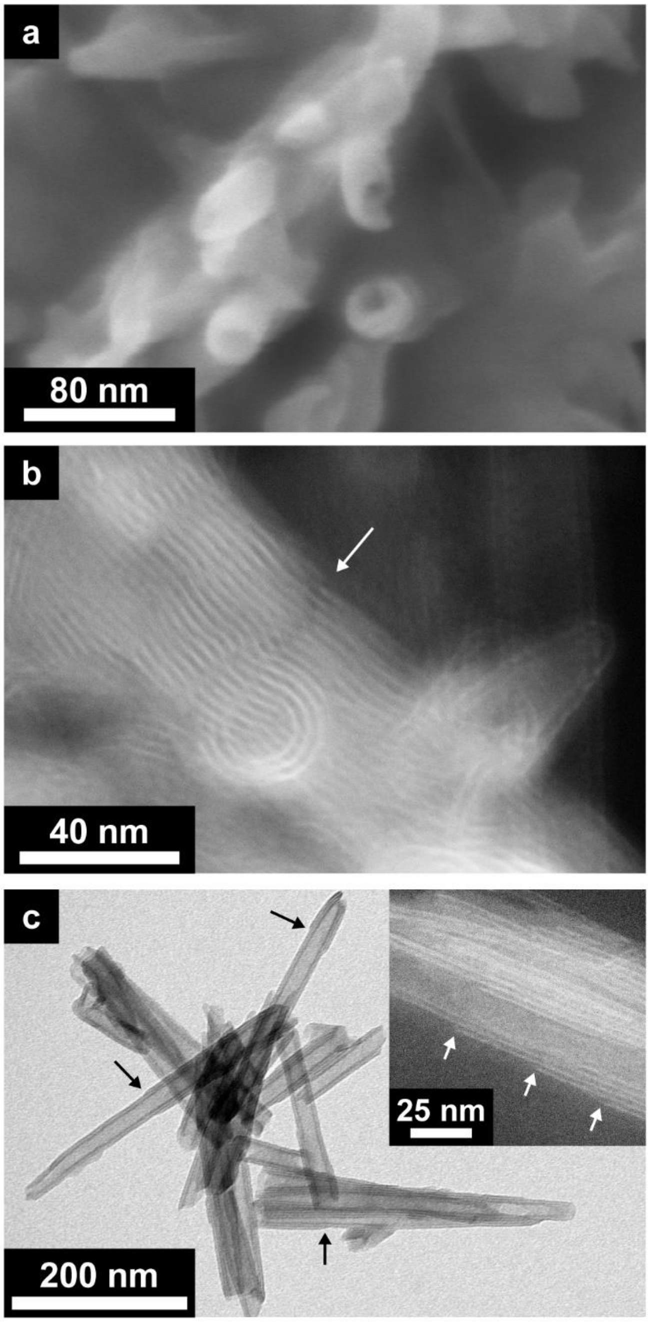

Figure 2.12 Growth pathway for hybrid nanotubes. (a) Top-down SEM image and (b) HAADF STEM image of nanotubes at the initial growth stage. Arrow in (b) marks the axis of a possible screw dislocation. (c) TEM and HAADF STEM images of full-length tubes. Arrows in (c) indicate the step edge of the $Co(OH)_2$ layers.

To understand the role of the pyrene surfactant in directing structure, we synthesized hybrid samples with other carboxylic acid containing amphiphiles. The molecular features changed include alkyl linker length, size of the aromatic core, and the use of only aliphatic chains (Figure 2.13). These molecules yielded layered hybrid materials with flat film or flake morphologies but failed to generate tubular structures across the range of electrodeposition parameters tested. This indicates that the molecular structure of PyBA plays a crucial role in driving the curvature for tubular growth with macroscopic order parameter. In particular, decanoic acid (DA) was further explored as a control amphiphile with similar molecular length to PyBA but without attractive intermolecular π-π interactions. When $Co(OH)_2$ is electrodeposited with DA, only flat films are observed even after 90 minutes of deposition time and similar film masses (Figure 2.13g). The lamellar nanostructure is still strongly apparent in the $Co(OH)_2$/DA GIXS patterns (Figure 2.14), with layer orientation parallel to the substrate and a d-spacing of 2.7 nm, consistent with previous reports from our group on $Zn(OH)_2$/DA hybrids.[13] When DA molecules intercalated in the hybrid are exchanged for PyBA, the resulting film has a flat morphology but the same d-spacing as the nanotubular films (Figure 2.15). As discussed later, this material is useful for isolating the effects of the tubular nanostructure versus a flat lamellar morphology on energy storage capacity.

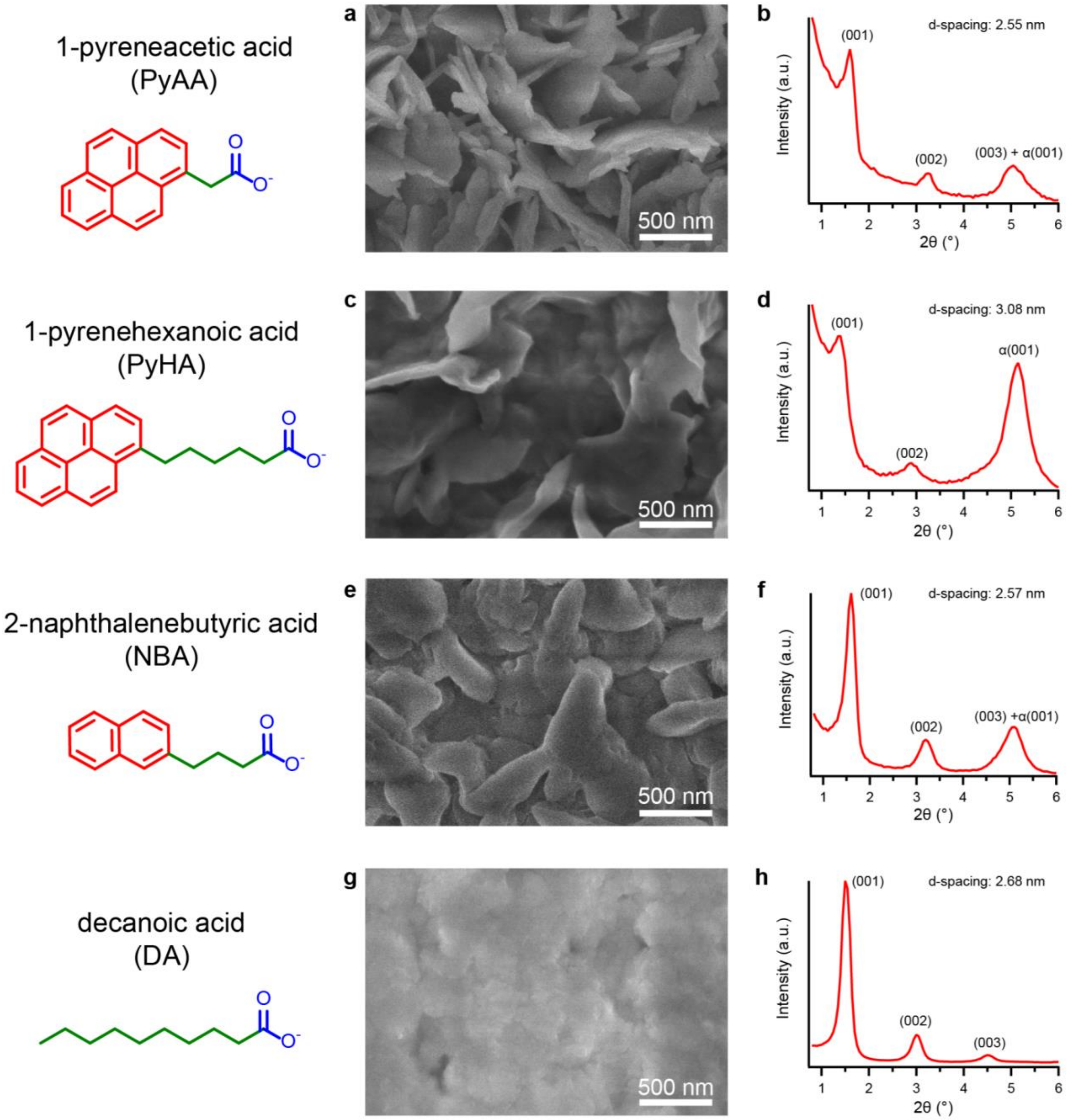

Figure 2.13 Electrodeposition of $Co(OH)_2$ hybrids with other surfactants. SEM images and XRD patterns for electrodeposited $Co(OH)_2$ films with PyAA (a, b), PyHA (c, d), NBA (e, f), and DA (g, h). Small impurity peaks from nitrate-intercalated α-$Co(OH)_2$ are observed at $2\theta = 5.2°$ for PyAA and NBA, with a larger α(001) peak for PyHA. These were observed across all samples and could not be reduced without decreasing the hybrid lamellar ordering simultaneously.

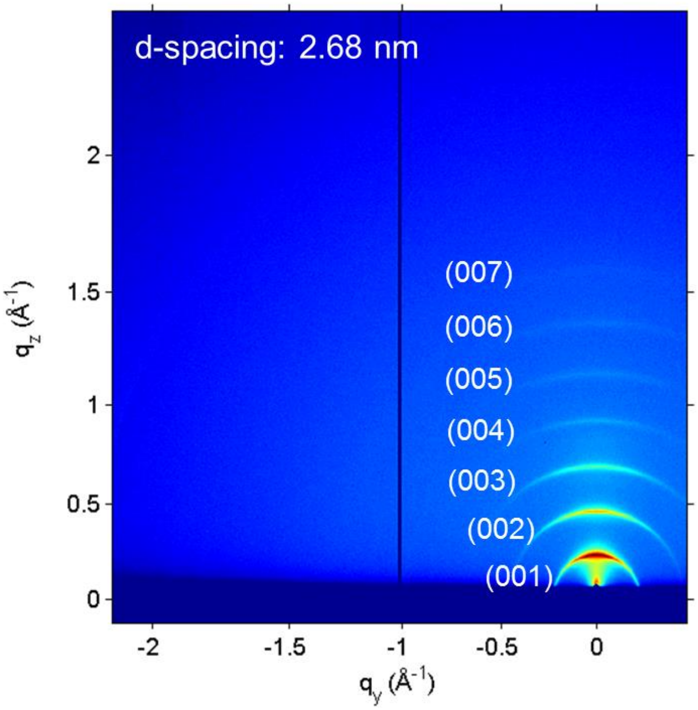

Figure 2.14 GIXS pattern of electrodeposited Co(OH)2/DA flat film. Strong lamellar orientation parallel to the substrate is observed.

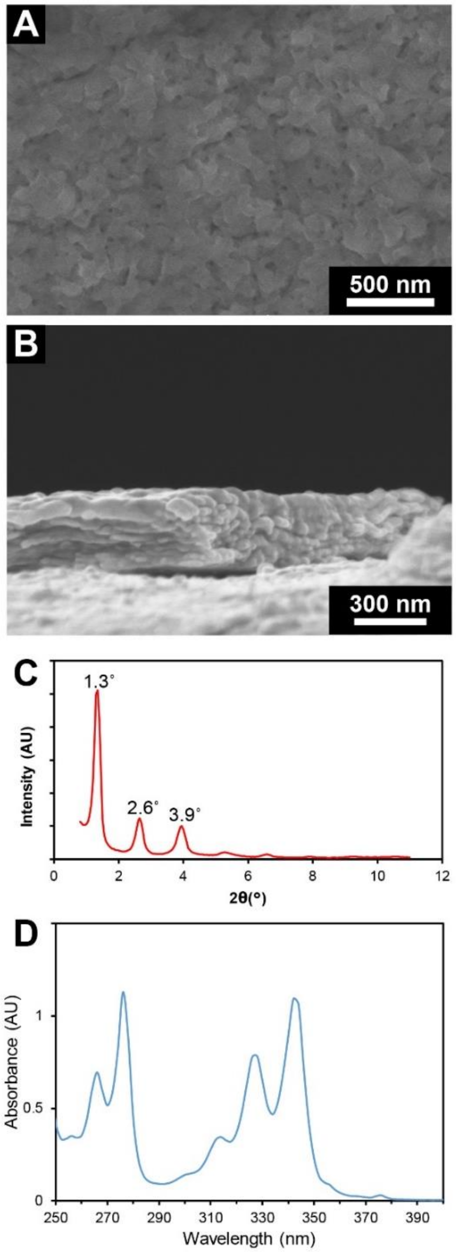

Figure 2.15 Characterization of PyBA-exchanged DA film. (a) SEM image of a DA film that has been exchanged with PyBA. (b) Cross-sectional SEM image of exchanged film. (c) XRD pattern of the film showing lamellar ordering with a d-spacing of 3.0 nm, the same d-spacing as hybrid films that were deposited with PyBA. (d) UV-vis absorbance spectrum of an aqueous 1 M KOH solution used for dissolving surfactants from a PyBA-exchanged DA film. Quantification of PyBA in this solution shows that 40% of the film mass can be attributed to PyBA, indicating that the majority of DA originally in the film has been exchanged with PyBA.

2.3.2 ELECTROCHEMICAL PERFORMANCE

To evaluate the electrochemical performance of the hybrid films, we performed galvanostatic charge/discharge measurements using a three-electrode setup in 1 M KOH electrolyte (Figure 2.16a,b). As commonly described in the literature, the faradaic reaction responsible for energy storage in $Co(OH)_2$ is the following:[75]

$$Co(OH)_2 + OH^- \leftrightarrow CoOOH + H_2O + e^-$$

We used specific capacity as the metric of energy storage capabilities which seems appropriate in the context of recent perspectives on performance assessment for redox-based supercapacitor materials.[72,95] The often-used specific capacitance metric is included as well to facilitate comparison to previous literature, but we note that it does not provide an accurate representation of energy storage capabilities for any nonlinear voltage profiles in galvanostatic charge-discharge testing. Galvanostatic charge/discharge on nanotubular $Co(OH)_2$/PyBA films was carried out at gravimetric current densities ranging from 2 A/g to 20 A/g (Figure 2.16a). We observe that the coulombic efficiency for galvanostatic cycling exceeds 94 percent after an initial 20 cycles at 2 A/g, indicating high reversibility of the redox charge storage reactions (Figure 2.17). The specific discharge capacity ranges from 63.4 mAh/g to 31.6 mAh/g at 2 A/g and 20 A/g, respectively (Figure 2.16b). When only the active material mass ($Co(OH)_2$ only) is considered, the specific capacity ranges from 137 mAh/g to 68.3 mAh/g (see Figure 2.18 and Table 2.2 for calculation of $Co(OH)_2$ mass). These values are comparable to $Co(OH)_2$ electrodes similarly deposited as thin films on non-porous substrates without conductive additives.[96–102] We note that many previous reports on $Co(OH)_2$ electrodes utilize nickel foam current collectors, which result in thinner layers of active material for the same mass loading and may also contribute to storage capacity due to the redox activity of $Ni(OH)_2$ formed from the current collector in alkaline conditions.[103,104]

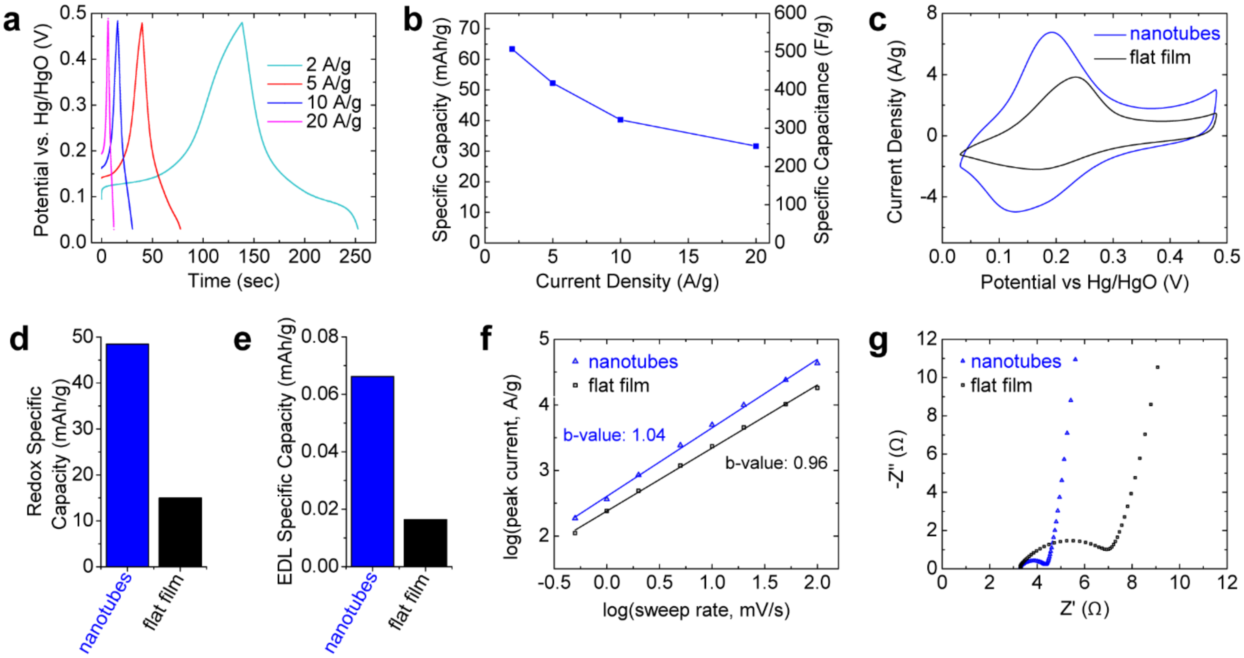

Figure 2.16 Electrochemical characterization of hybrid films. (a) Galvanostatic charge/discharge profiles for a tubular $Co(OH)_2$/PyBA film at different current densities. (b) Specific capacity and capacitance values for the charge/discharge curves in (a). (c) Cyclic voltammograms of a nanotubular $Co(OH)_2$/PyBA film and a flat $Co(OH)_2$/PyBA film in 1 M KOH at 10 mV/sec scan rate. (d, e) Specific charge capacity calculated from CV of nanotubular film compared to that of flat film in (d) 1 M KOH and in (e) 0.1 M TBAP/acetonitrile. (f) b-value analysis of nanotubular and flat films from CV in 1 M KOH. (g) Nyquist impedance plot of nanotubular and flat films in 1 M KOH.

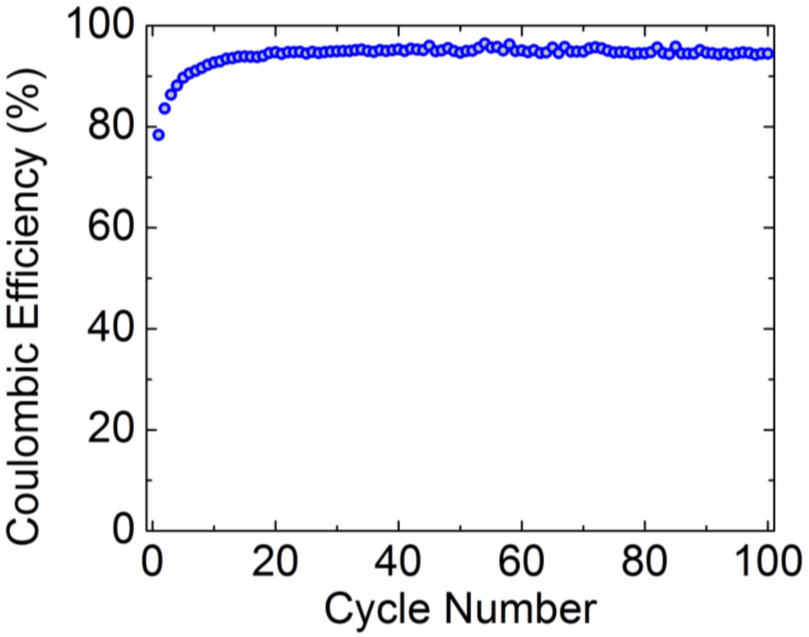

Figure 2.17 Coulombic efficiency of nanotubular film under galvanostatic charge/discharge cycling at 2 A/g in 1 M KOH.

Sample ID	Bare substrate mass (g)	Substrate + deposited film mass (g)	Substrate + deposited film mass post-calcination (g)	% film mass change
XG2 (PyBA)	1.1687760	1.1690200	1.168886	-54.9
XG3 (PyBA)	1.1694284	1.1696953	1.1695493	-54.7
XE5 (PyBA)	1.1708271	1.1710234	1.1709224	-51.4
XH6 (DA)	1.1664314	1.1667035	1.1665631	-51.6
XH8 (DA)	1.0944348	1.0945184	1.0944752	-51.7
XH9 (DA)	1.1265958	1.1267226	1.1266556	-52.8
			Average mass % loss ($Co(OH)_2$/PyBA film)	-53.7
			Average mass % loss ($Co(OH)_2$/DA film)	-52.0

Table 2.2 Sample masses before and after calcination

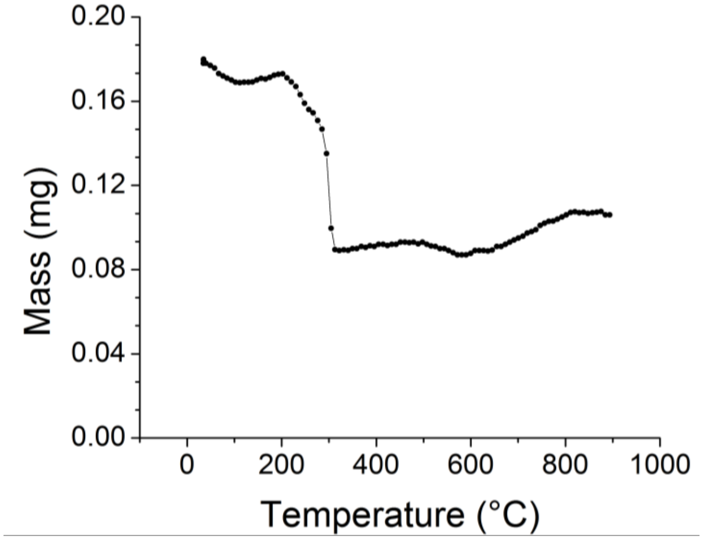

Figure 2.18 Thermogravimetric analysis (TGA) of $Co(OH)_2$/PyBA nanotubular films.

To investigate the effects of the hierarchical microstructure on performance while retaining the nanoscale interlayer spacing, we exchanged the intercalated DA molecules of a $Co(OH)_2$/DA flat film for PyBA and the resulting film was cycled for comparison with the nanotubular films. The exchanged flat film has the same interlayer spacing as the nanotubular films, but yields a peak specific capacity of 14.0 mAh/g versus the 40.6 mAh/g for nanotubular films at 10 A/g current density (Figure 2.19). We observe a decrease in capacity of the nanotubular film to 18.5 mAh/g over 10000 cycles, which we believe is linked to changes in surface area and morphology during charging and discharging (Figure 2.20). In comparison, the flat film only retains 1.5 mAh/g capacity over 10000 cycles. For reference, the as-deposited $Co(OH)_2$/DA films also reveal significantly lower specific capacity than that of the nanotubular films, which indicates that film morphology is the dominant factor in electrochemical performance (Figure 2.21). Future work needs to be focused on the stabilization of the nanostructure during charge/discharge cycles, which may be accomplished by incorporating a secondary electronically conductive phase that could minimize non-uniform charging and mitigate structural degradation. Additionally, to fabricate a full device with large energy and power density, a high-performance anode is necessary to match the capacity and rate capability of the $Co(OH)_2$ nanotubular electrode.[80,105]

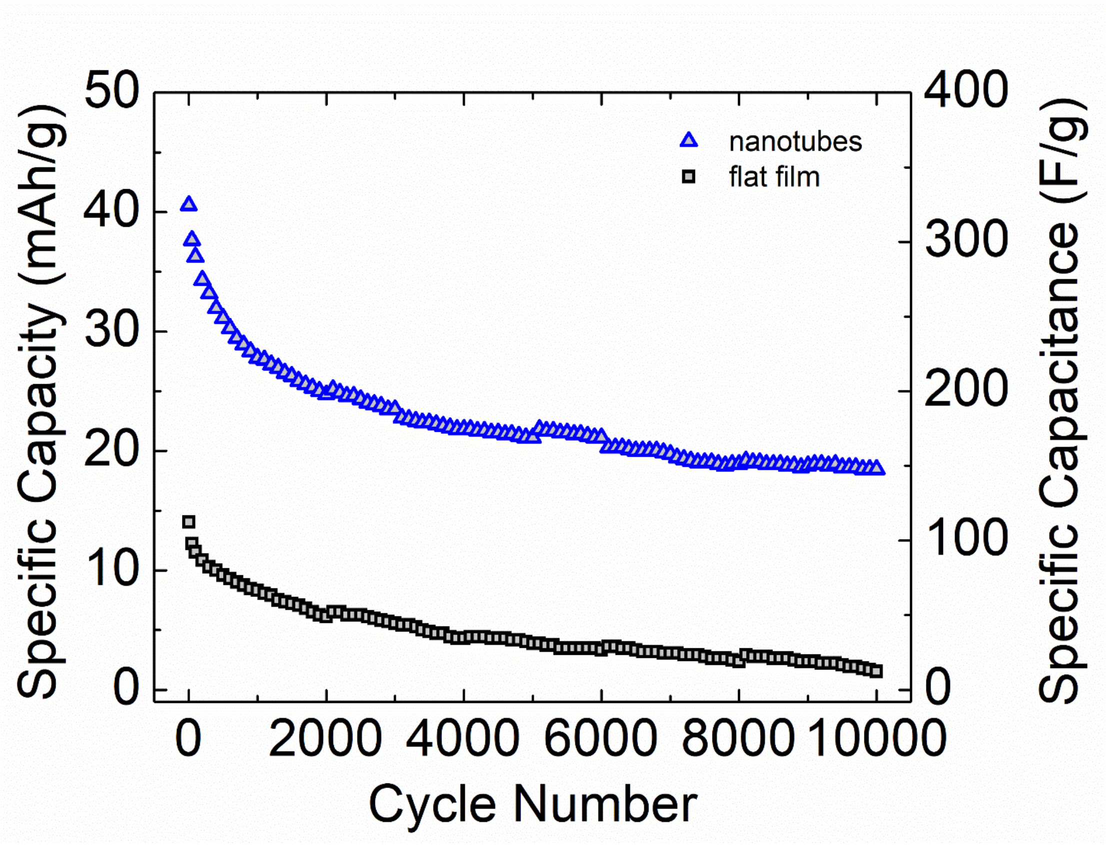

Figure 2.19 Specific capacity and capacitance over 10000 galvanostatic charge/discharge cycles at 10 A/g for a nanotubular $Co(OH)_{2s}$/PyBA film (blue) and a flat $Co(OH)_2$/PyBA film (black).

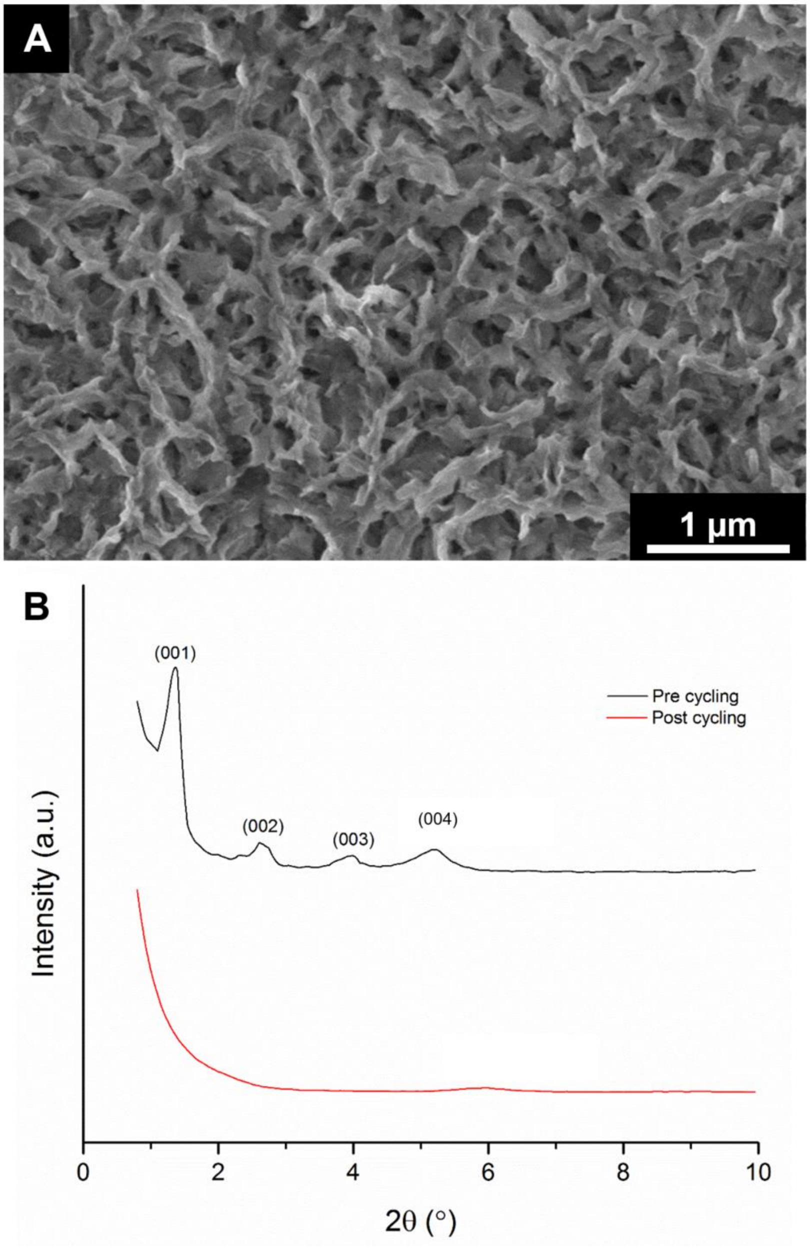

Figure 2.20 Structure of $Co(OH)_2$/PyBA films after 100 charge/discharge cycles in 1 M KOH. (a) SEM image of degraded nanotubular film after cycling. (b) XRD patterns of nanotubular film before cycling (black) and after cycling (red).

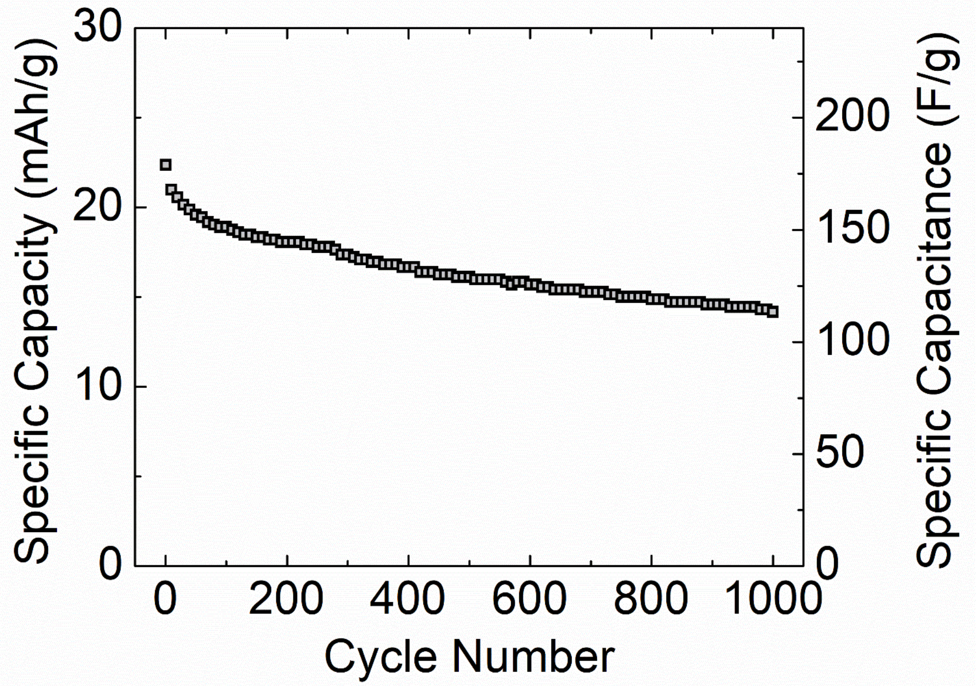

Figure 2.21 Specific capacity and capacitance over 1000 galvanostatic charge/discharge cycles at 10 A/g for a flat $Co(OH)_2$/DA film.

To probe the nature of the increased capacity of the nanotubular films, we performed potentiostatic and kinetic electrochemical characterization on both the nanotubular films and the $Co(OH)_2$/PyBA flat films (Figure 2.16c-g). Cyclic voltammetry (CV) performed on samples immersed in 1 M KOH shows redox peaks consistent with typical $Co(OH)_2$ materials (Figure 2.16c).[81,106] We measured the specific charge capacity of each film type with CV in both aqueous 1 M KOH and 0.1 M tetrabutylammonium perchlorate (TBAP) in acetonitrile to quantify the contribution of the electric double-layer (EDL) on the total specific capacity of each material (Figure 2.16d, e, Figure 2.22). Since the redox activity of $Co(OH)_2$ is limited in non-aqueous solutions such as acetonitrile, we expect only adsorption of the ClO_4^- anions to contribute to energy storage. The EDL contribution to specific capacity is less than 0.2 percent of the total charge storage measured in 1 M KOH for both nanotubular and flat films, demonstrating that the capacity measured in alkaline electrolytes is almost entirely due to redox reactions. We also observe that the capacity for nanotubular films is approximately three to four times higher than that of the flat films for both redox- and EDL-based storage. This indicates that the majority of the increased capacity of the nanotubular hybrid results from higher surface area accessible to the ions in solution required for redox and EDL storage. Furthermore, to investigate if the decrease in capacity is due to diffusion limitations in the flat film, we collected a series of cyclic voltammograms at different sweep rates. A power law relationship between the current and the sweep rate gives the equation:

$$i = av^b$$

where i is the measured current, v is the sweep rate, and a and b are adjustable parameters. For current response governed by semi-infinite diffusion limitation within the electrode, b approaches a value of 0.5, while capacitive current response would exhibit b values near 1.[95,105,107–109] The slopes of the log-log plots of the peak cathodic current versus the sweep rate give the b-values for nanotubular and flat films (Figure 2.16f). Both morphologies show linear behavior with b-values near 1 for sweep rates up to 100 mV/sec, corresponding to a charging time of 4.5 seconds. This indicates that the current response is predominately capacitive in nature and therefore diffusion limitation does not account for the lower capacity of the flat film. Thus, the EDL measurements and b-value analysis suggest that the increased capacity of the nanotubular film is a result of higher accessible surface area. Fittings of the Nyquist plot from electrochemical impedance spectroscopy (EIS) show similar series resistances (~3.3 Ω) but significantly larger resistance in the high frequency (HF) loop for the flat film (4.34 Ω) compared to that of the nanotubular film (1.35 Ω) (Figure 2.16g, Figure 2.23). We hypothesize that this larger HF loop is due to lower electronic conductivity perpendicular to the current collector in the flat film. The results of the EDL capacity measurements and the b-value analysis highlight the importance of high surface area morphologies, while EIS experiments demonstrate that the oriented tubes may facilitate more efficient electron transport parallel to the macroscopic normal of the electrode.

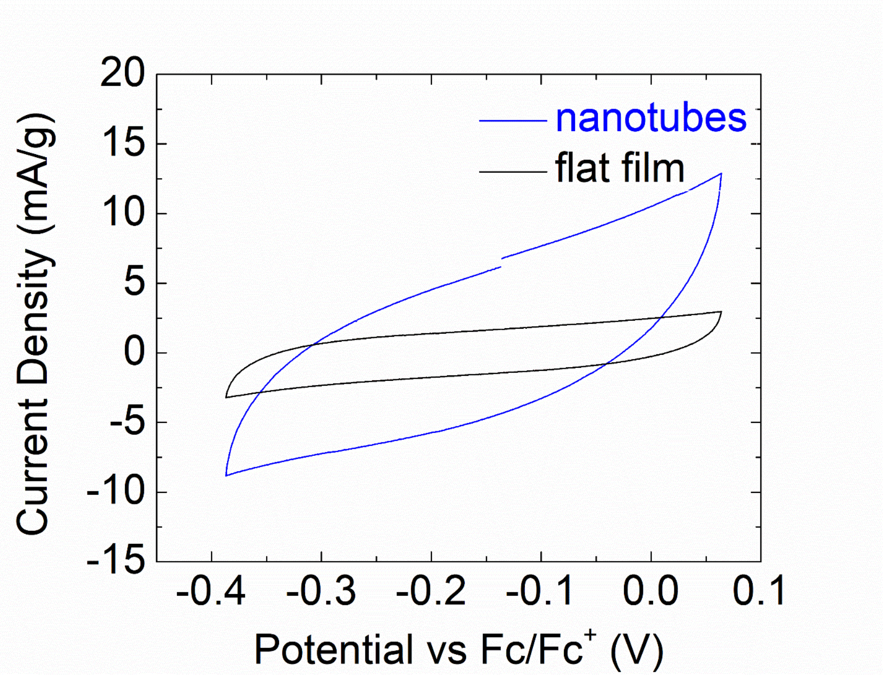

Figure 2.22 Cyclic voltammograms of nanotubular and $Co(OH)_2$/PyBA flat films in 0.1 M TBAP/acetonitrile electrolyte at a 10 mV/sec sweep rate. The potential is calibrated to the ferrocene redox couple.

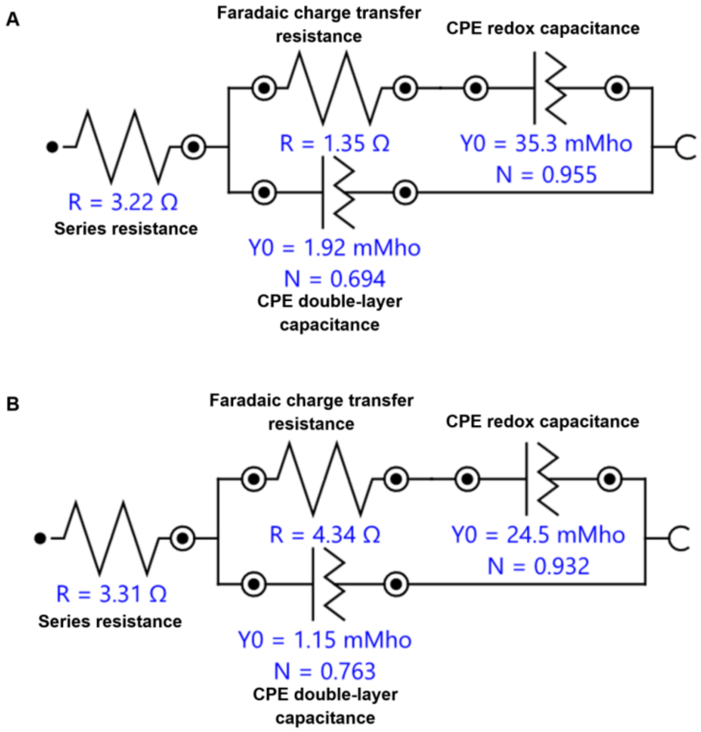

Figure 2.23 Modified Randles circuits used for fitting Nyquist impedance plots for (a) nanotubular films and (b) $Co(OH)_2$/PyBA flat films, consisting of resistors and constant phase elements (CPE). CPE are used for representing double-layer capacitance and redox capacitance in the films.

2.3.3 Stability During Immersion in Alkaline Electrolyte

One of the often-overlooked challenges in using $Co(OH)_2$ as an electrochemical energy storage material is the fundamental instability of this layered hydroxide phase in typical electrolyte conditions near pH 14. In the case of $Co(OH)_2$, it has long been understood that the anion-intercalated α-$Co(OH)_2$ polymorph undergoes dissolution and re-precipitation into the β-$Co(OH)_2$ phase, which we have also observed for electrodeposited nitrate-intercalated α-$Co(OH)_2$ films (Figure 2.25).[83,110] This phase and morphology change led to a ~88% loss of specific capacity (Figure 2.28). This demonstrates that the stability of electrode materials in their electrolytes is key to ensuring a reasonable “shelf life” of peak performance for energy storage devices.

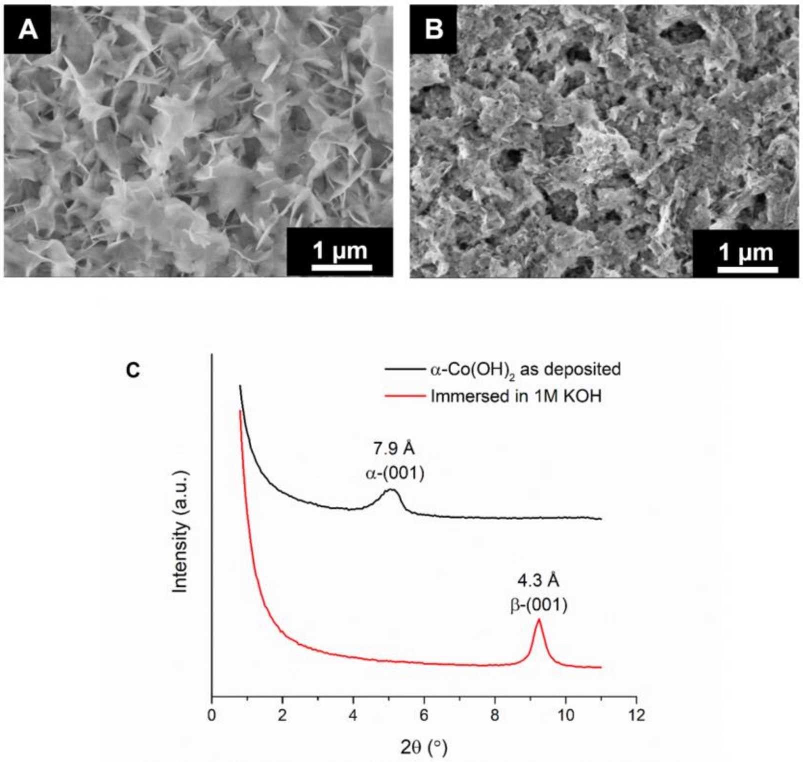

Figure 2.24 Degradation of nitrate-intercalated α-$Co(OH)_2$ films in 1M KOH electrolyte. (a) SEM image of electrodeposited α-$Co(OH)_2$ film with characteristic flake microstructure. (b) SEM image of the film in (a) after immersion in 1M KOH for 24 hours, resulting in platelet morphology. (c) XRD patterns of the samples in (a) and (b). We note that the primary (001) peak exhibited after immersion in 1 M KOH corresponds with a d-spacing of 4.3 Å and indicates the presence of β-CoOOH rather than β-$Co(OH)_2$.

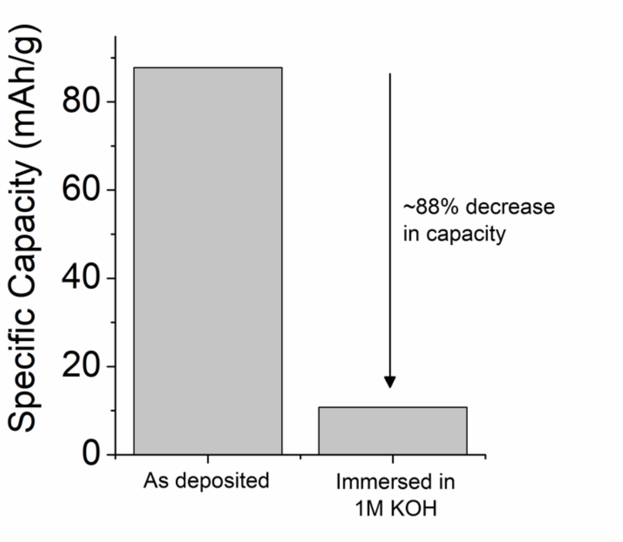

Figure 2.25 Specific capacity of nitrate-intercalated α-Co(OH)$_2$ films before and after immersion in 1 M KOH for 24 hours. The specific capacity was calculated from the first cycle discharge capacity during galvanostatic cycling at 2 A/g in 1 M KOH.

A similar dissolution and re-precipitation phenomenon occurs for our electrodeposited layered Co(OH)$_2$ films intercalated with organic anions. Upon immersion of Co(OH)$_2$/PyBA films in aqueous 1 M KOH, we observe dissolution of the nanotubes and re-precipitation to a platelet morphology within 24 hours (Figure 2.28a, b). The (001) peak of the resulting phase in the x-ray diffraction (XRD) pattern corresponds to a 4.3 Å d-spacing, indicating formation of oxidized β-CoOOH as opposed to β-Co(OH)$_2$ (Figure 2.28e).[90] This oxidation may be attributed to dissolved oxygen in the 1 M KOH solutions, as immersion in 1 M KOH sparged and sealed under inert Ar atmosphere results in formation of only β-Co(OH)$_2$ (Figure 2.26). The Co(OH)$_2$/DA films show an analogous decomposition, dissolving and reforming as β-CoOOH platelets within 24 hours (Figure 2.28f, g, j). We found that the intercalated PyBA and DA molecules are highly soluble in alkaline solutions as observed by mass decrease of hybrid films after immersion and by quantification of the dissolved molecules in the solutions (Section 2.6.5 and Figure 2.27). Therefore, we conclude that the change in morphology can be attributed to both the dissolution of the intercalated species and the Co(OH)$_2$ layers upon exposure to alkaline electrolytes.

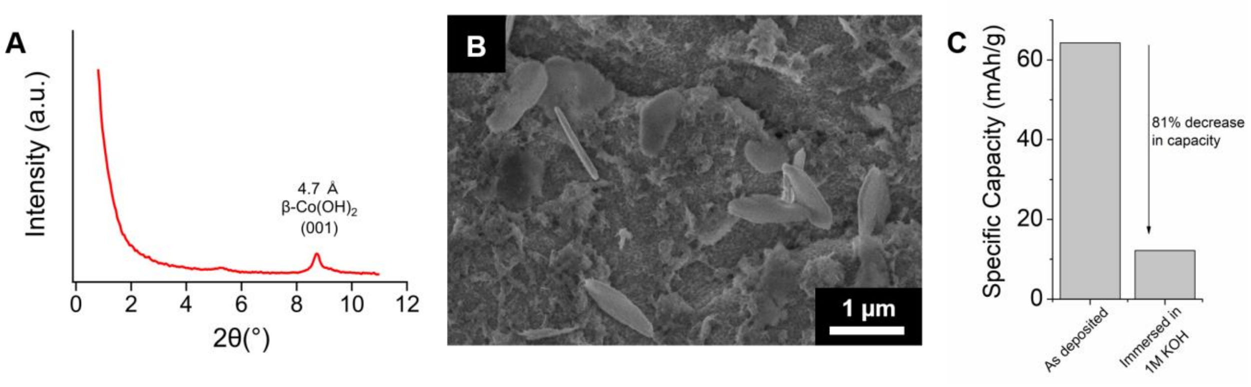

Figure 2.26 Stability of $Co(OH)_2$/PyBA films in Ar-sparged electrolyte. (a) XRD pattern, (b) SEM image, and (c) specific capacity of a nanotubular film after immersion for 5 days in Ar-sparged 1 M KOH. Large β-$Co(OH)_2$ platelets are present in the degraded film. The specific capacity of the immersed film was calculated from the first cycle discharge capacity during galvanostatic cycling at 2 A/g in 1 M KOH.

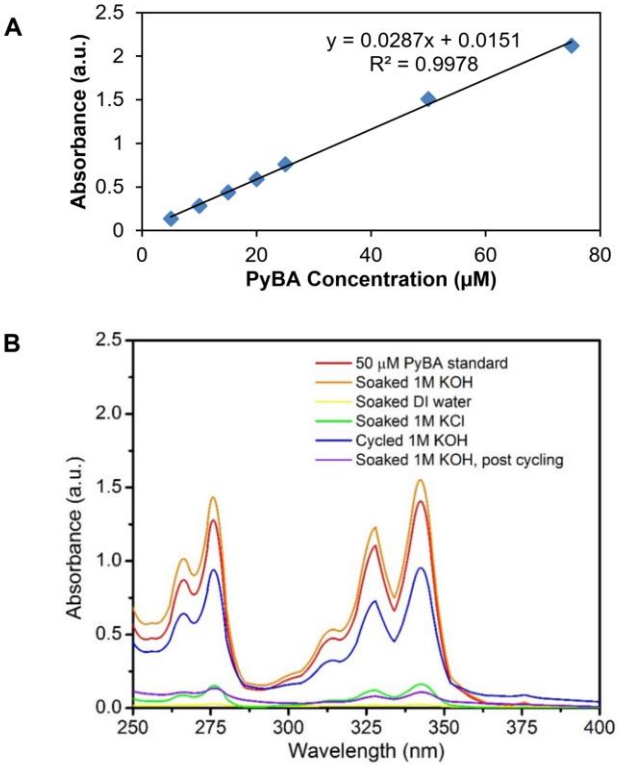

Figure 2.27 Absorbance spectroscopy on immersion and cycling electrolytes of $Co(OH)_2$/PyBA films. (a) Calibration curve for quantifying PyBA dissolved into various electrolytes. (b) Absorbance spectra for different electrolytes after immersion for at least 24 h.

To address the dissolution of organic moieties from the lamellar galleries, we used a high concentration (25 wt%) of deprotonated PyBA as an electrolyte additive. The high concentration of surfactant in the external electrolyte prevents the dissolution of the intercalated surfactants out of the hybrid film. This in turn slows the dissolution of the inorganic $Co(OH)_2$, increasing the overall stability of the hybrid. When immersing a $Co(OH)_2$/PyBA nanotube film into an aqueous solution of 1 M KOH with concentrated PyBA (1 M KOH/25 wt% PyBA) for five days, the film retained a nanotubular morphology as well as lamellar XRD peaks (Figure 2.28c, e). To prove that the stabilization effect is in fact due to suppression of PyBA intercalant dissolution, we immersed another $Co(OH)_2$/PyBA film in a 1 M KOH solution with similarly concentrated deprotonated DA (1M KOH/25 wt% DA) for five days. This resulted in dissolution of PyBA from the hybrid film and complete decomposition to β-CoOOH (Figure 2.28d, e). We also immersed $Co(OH)_2$/DA films in both PyBA and DA solutions to probe if suppression of intercalant dissolution is a general strategy for stabilization of Co(OH)2 hybrids. We found that immersion in the concentrated PyBA solution induces intercalant exchange, resulting in an expanded (001) d-spacing of 3.0 nm and stabilization of the hybrid over five days (Figure 2.28h, j). In contrast, immersion in a concentrated DA solution for five days resulted in complete decomposition to β-CoOOH (Figure 2.28i, j). These results indicate that simply concentrating the cycling electrolyte with the corresponding intercalated surfactant for a hybrid film is insufficient for stabilization and that only specific molecules provide stability to $Co(OH)_2$ hybrids in alkaline environments. We hypothesize that π-π interactions of the aromatic core of the surfactant contribute to the stability of the $Co(OH)_2$/PyBA hybrid over the $Co(OH)_2$/DA analogue.

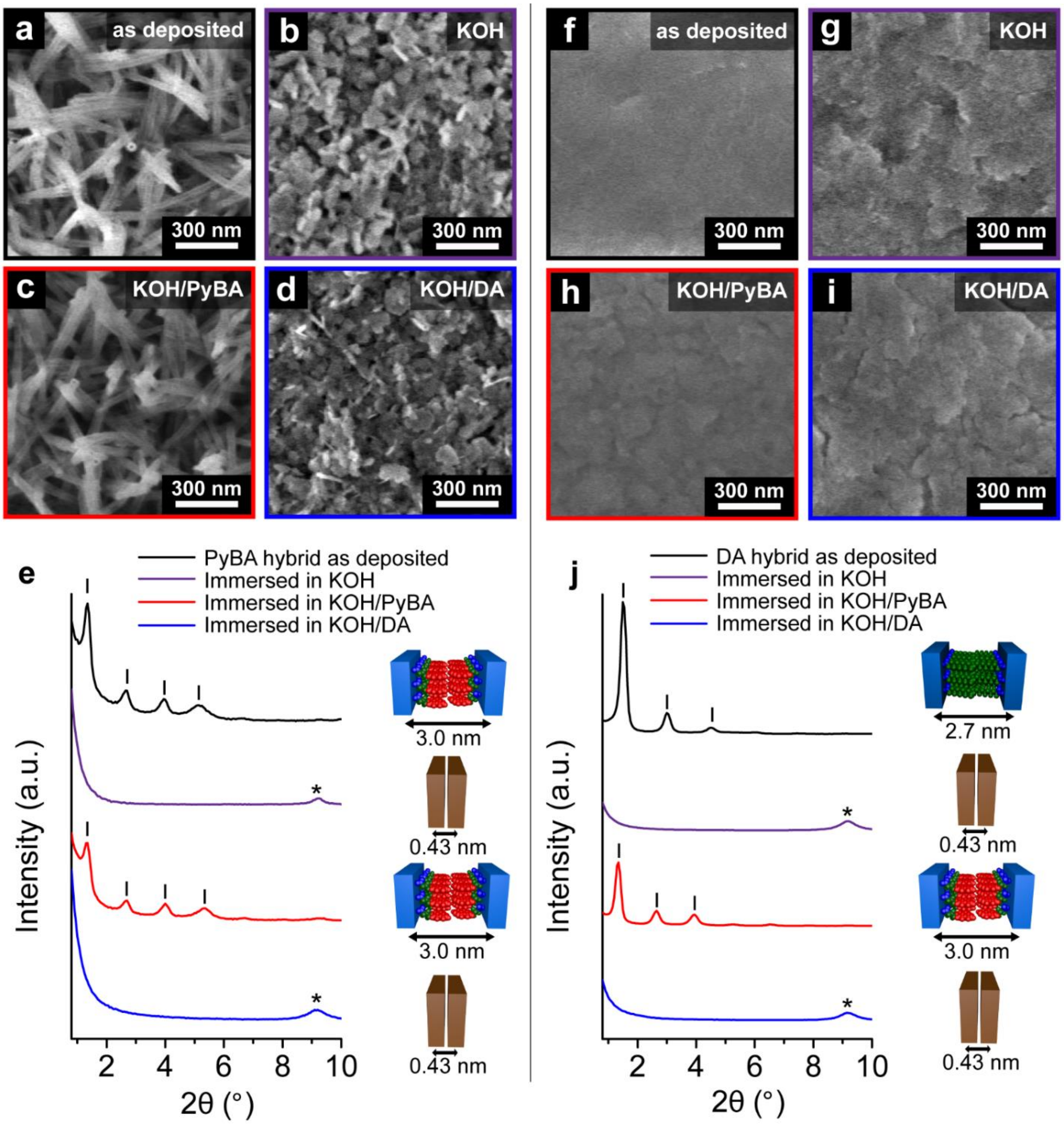

Figure 2.28 Stability of layered $Co(OH)_2$ materials in pH 14 solutions with concentrated surfactant electrolyte additives. SEM images of $Co(OH)_2$/PyBA films (a) as deposited, (b) after immersion in 1M KOH for 24 hours, (c) after immersion in 1M KOH/25 wt% PyBA for 5 days, and (d) after immersion in 1M KOH/25 wt% DA for 5 days. (e) XRD patterns of samples shown in (a)-(d). SEM images of $Co(OH)_2$/DA films (f) as deposited, (g) after immersion in 1 M KOH for 24 hours, (h) after immersion in 1M KOH/25 wt% PyBA for 5 days, and (i) after immersion in 1M KOH/25 wt% DA for 5 days. (h) XRD patterns of samples shown in (f)-(i). For (e) and (j), tick marks indicate (00L) peaks of the layered structures, while * denotes the (001) peak of the β-CoOOH degradation product.

To demonstrate the effectiveness of this stabilization method, we measured the first cycle discharge capacity of $Co(OH)_2$/PyBA nanotubular films as a function of time immersed in alkaline electrolytes with and without surfactant additives (Figure 2.29). Following immersion in 1 M KOH, 1 M KOH/25 wt% DA, and 1 M KOH/25 wt% PyBA, the films were galvanostatically cycled at 2 A/g in their respective electrolytes. Electrochemical measurements performed on as-deposited nanotubular films in these electrolytes indicate that the surfactant additives do not significantly affect the cycling behavior of the hybrid material (Figure 2.30). Consistent with the structural stabilization observed in Figure 5, only the alkaline electrolyte with concentrated PyBA successfully preserved the initial specific capacity of nanotubular films. In 1 M KOH and 1 M KOH/25 wt% DA, the nanotubular films lost more than 80 percent of the specific capacity of pristine nanotubular films after 24 hours of immersion. We attribute this loss in performance to the dissolution and reprecipitation of the nanotubular hybrid into β-CoOOH platelets (Figure 2.28b, d, e). Interestingly, the nanotubular film immersed for 120 hours in an electrolyte containing PyBA exhibited a specific capacity of 57.5 mAh/g, while the films immersed in electrolytes without PyBA exhibited specific capacities of ~4.5 mAh/g. These results suggest the possibility of stabilizing hybrid nanostructures, with their respective organic components in the electrolyte, prior to electrochemical cycling. Future experimental and computational work in this area could identify additional strategies to stabilize organic-inorganic electroactive hybrids in harsh chemical environments.

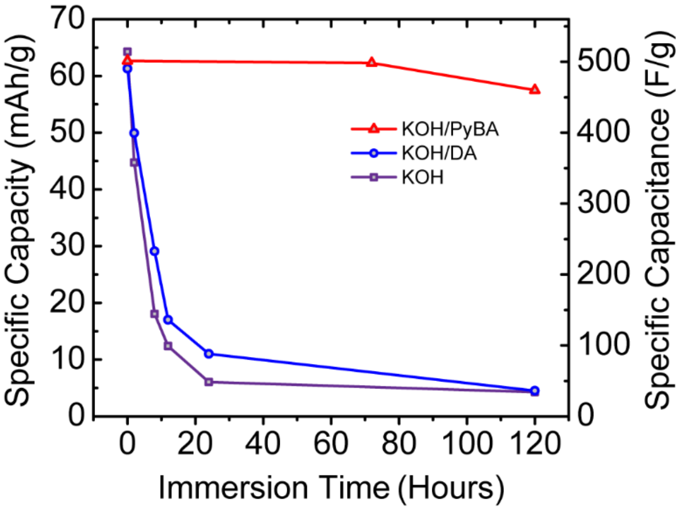

Figure 2.29 Specific capacity of nanotubular hybrid films after immersion in alkaline electrolytes for varying lengths of time. Samples were immersed in 1 M KOH (purple), 1 M KOH/25 wt% DA (blue), and 1 M KOH/25 wt% PyBA (red) prior to galvanostatic cycling at 2 A/g current density.

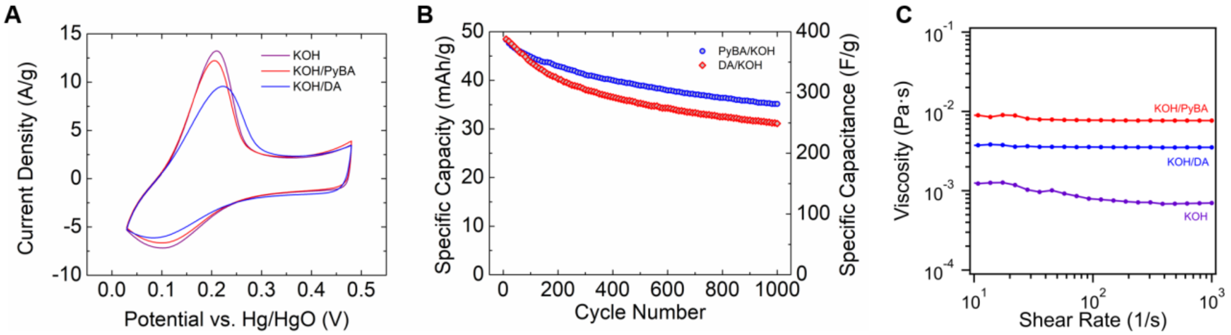

Figure 2.30 Electrochemistry of nanotubular $Co(OH)_2$/PyBA films in concentrated surfactant electrolytes. (a) CV at 10 mV/s and (b) galvanostatic cycling at 10 A/g in 1 M KOH/25 wt% PyBA electrolyte (blue) and in 1 M KOH/25 wt% DA (red). We note that there is an increase in the separation of the $Co(OH)_2$ redox peaks in KOH/DA. This may be due to a hydrophobic DA bilayer on the surface of the electrode resulting in slower diffusion kinetics. (c) Flow curves for 1M KOH and KOH/surfactant electrolytes. These viscosities are orders of magnitude below typical aqueous polymer electrolytes, which are allowed to dry to a solid-like gel. [79,80]

2.4 CONCLUSIONS

We synthesized concentric cobalt hydroxide-organic hybrid nanotubes perpendicular to a metallic substrate. We demonstrated that the superior electrochemical performance of the nanotubular films is the result of a large accessible surface area for redox activity and showed that diffusion limitations do not exist for charging times as fast as five seconds. Finally, we discovered a pathway to increase the stability of these hybrid architectures under the harsh conditions necessary to achieve high performance in energy storage devices or other potential electrochemical applications. Our work demonstrates that organic molecules in these hybrids can not only template complex architectures, but also stabilize materials at the solid-liquid interfaces critical to their functions.

2.5 MATERIALS AND METHODS

2.5.1 ELECTROCHEMICAL SYNTHESIS

Electrochemical synthesis of PyBA-$Co(OH)_2$ hybrid samples was carried out in 10 mL solutions (5:5 (v/v) DMSO/ultrapure H_2O, DMSO obtained from Sigma Aldrich) of 0.1 M $Co(NO_3)_2 \cdot 6H_2O$ (Alfa Aesar, 99.999% metals basis) and 1.25 mM 1-pyrenebutyric acid (Sigma Aldrich) in an undivided cell vial using a three-electrode set-up (Metrohm Autolab PGSTAT128N) with a Co counterelectrode (Alfa Aesar, 1 mm thick foil, 99.95% metals basis) and a Ag/AgCl reference electrode (BASi model RE-5B). Solutions were heated in an oil bath to 80° C, pH adjusted slowly with 0.1 M aqueous KOH to pH ~5.2 (Hanna HI 1131B pH electrode) and sparged for 20 min with Ar gas before depositions were started. Synthesis of the nitrate-intercalated α-$Co(OH)_2$ was carried out at room temperature with 10 mL aqueous solutions of 0.1 M $Co(NO_3)_2 \cdot 6H_2O$ in the same undivided vial with a three-electrode set-up with a Pt wire counterelectrode and a Ag/AgCl reference electrode.

Electrochemical synthesis of layered $Co(OH)_2$ materials with other organic surfactants were carried out in a similar electrodeposition procedure with a three-electrode set-up in 10 mL DMSO/H_2O solutions. The surfactants tested were 1-pyreneacetic acid (PyAA), 1-pyrenehexanoic acid (PyHA), 2-naphthalenebutyric acid (NBA), and decanoic acid (DA). The deposition conditions were systematically varied to tune the surfactant solubility and the deposition rate in an effort to enhance the synergistic self-assembly of the hybrid material. The surfactant concentrations ranged from 0.25 to 3 mM while the $Co(NO_3)_2$ concentrations were varied from 25 to 200 mM. The DMSO/H_2O ratio was varied from 5:5 to 7:3, depending on the solubility of the surfactant (e.g. 6:4 and 7:3 were used for lower solubility surfactants like PyHA). The solution temperature was tested between 70-80°C and pulsed depositions (-0.8 V vs Ag/AgCl Ref.) were carried out for 30-210 minutes. Representative SEM images and XRD patterns for the hybrid films of each surfactant with film masses near 100 $\mu g/cm^2$ are provided in Figure 2.13.

Freshly abraded 1 cm x 2 cm 304 stainless steel substrates (McMaster Carr) were used as working electrodes and positioned upright in the cell. Pyrolytic graphite foil (MTI) and carbon paper (Toray TGP-H-030, 5% waterproofed) were used as received for flexible working electrode substrates. A pulsed deposition procedure was used for hybrid samples, with alternating 30 second pulses of -0.8 V and 0 V vs. reference for 5 to 90 minutes. While pulsing is not required for tube growth, it allows for equilibration of pH and reactant concentrations which minimizes formation of undesired $Co(OH)_2$ phases (Figure 2.31). Nitrate-intercalated α-$Co(OH)_2$ samples were deposited at a constant potential of -1.0 V vs reference for 1 minute to achieve similar mass loadings as the hybrid films.

Deposited films were thoroughly rinsed with water and allowed to air dry at room temperature. Samples for the cross-sectional SEM images were deposited on 0.001” thick substrates, while samples for electrochemical and x-ray characterization, as well as all other SEM characterization were deposited on 0.031” thick substrates for more facile handling.

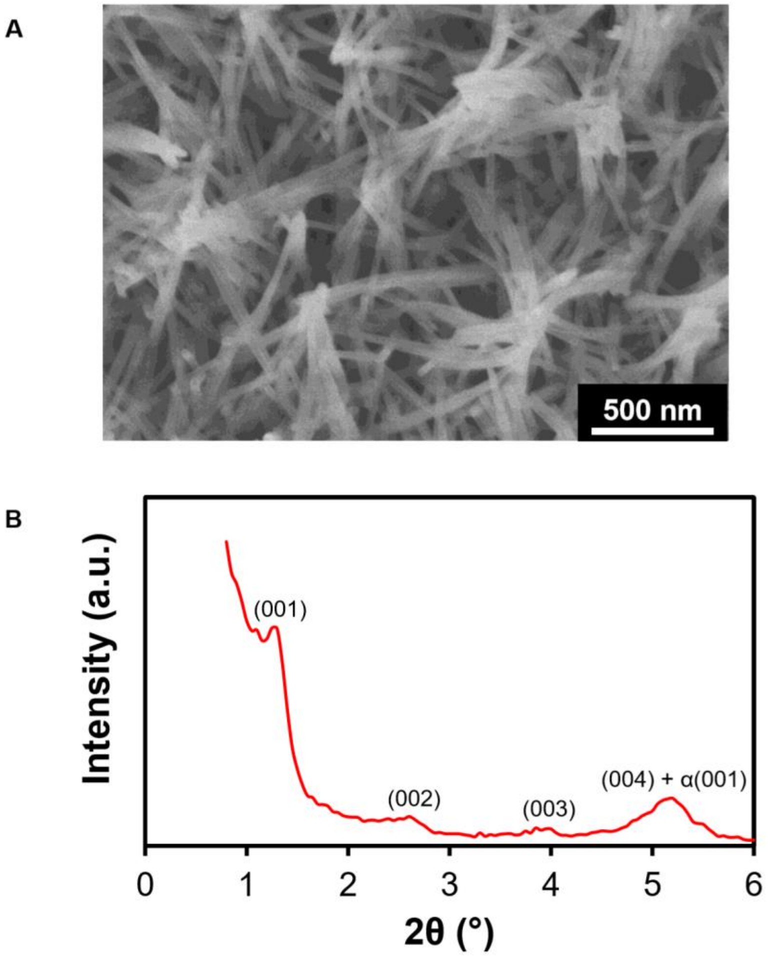

Figure 2.31 Characterization of a $Co(OH)_2$/PyBA film electrodeposited for 60 minutes with a constant potential of -0.8 V vs. Ag/AgCl (i.e. without 30 second pulses). (a) Representative SEM image of non-pulsed nanotubular films. (b) XRD pattern showing much weaker lamellar signal compared to pulsed samples shown previously. A significant α-$Co(OH)_2$ impurity peak is apparent, likely due to the higher pH at the electrode interface that arises without pulsing the deposition.

2.5.2 CHARACTERIZATION

SEM imaging was performed using a Hitachi SU8030 SEM. Au/Pd coated samples for SEM imaging were sputtered with 10 nm of Au/Pd using a Denton III Desk Sputter Coater. Bright-field TEM images were taken with a JEOL 2100F microscope at 200 kV and a Hitachi HT7700 microscope at 120 kV. Dark-field STEM images were taken with a Hitachi HD-2300 microscope at 200 kV. Samples were scraped off from the substrate with a razor blade and the powder was then applied on copper TEM grids. XRD data was obtained using Mo Kα x-rays from a two-circle diffractometer with a rotating anode generator and multilayer optic monochromator, using energy filters to exclude fluorescence signal from the stainless steel substrate and cobalt in the films. 2D-GIXS data was obtained at beamline 8-ID-E at the Advanced Photon Source, Argonne National Laboratory, using a photon energy of 7.35 KeV and an incident angle of 0.1 degrees.

All substrates were weighed before and after depositions, subtracting the pre-deposition mass from the post-deposition mass to obtain the film mass. All substrate masses were measured with a Mettler Toledo UMX2 microbalance. Surface areas of the deposited films were measured in ImageJ from photographs of the front and back of the electrodes. Typical mass loadings for samples used in electrochemical characterization ranged between 75 and 100 µg/cm^2.

All electrochemical characterization was performed in a three-electrode set-up with a Pt counterelectrode and a Hg/HgO reference electrode (CH Instruments, model CHI152). EDL measurement was performed using the same three-electrode setup with 0.1 M tetrabutylammonium perchlorate (TBAP) in acetonitrile as the electrolyte and a non-aqueous $AgNO_3$ reference electrode (BASi, MW-1085). CV, galvanostatic charge/discharge, and EIS measurements were carried out using a Metrohm Autolab PGSTAT128N equipped with a FRA32M module. Specific charge capacity measurements derived from CV were integrated from the total current passed in the negative voltage sweep direction at 10 mV/sec. EIS measurements were performed at 0.25V vs. Hg/HgO after a 10 minute potential equilibration step, with a 5 mV perturbation and frequencies ranging from 50 kHz to 10 mHz. For the immersion studies, the concentrated surfactant electrolytes were prepared as described in the Supplemental Methods. The storage capacities for the immersed films were normalized with the original hybrid film masses prior to immersion.

2.5.3 Exchange of PyBA into DA-intercalated hybrid

Flat $Co(OH)_2$/DA films with similar mass to that of the nanotubular films were produced with 60-90 minute pulsed depositions (30 second alternating pulses of 0V and -0.8V vs. Ag/AgCl). These films were immersed in 0.5 mL volume solutions of 1 M KOH/25 wt% PyBA for twelve hours. XRD and 2D-GIXS patterns of these films show that the d-spacing expands from the 2.7 nm characteristic of the original $Co(OH)_2$/DA films to the 3.0 nm that is observed for the $Co(OH)_2$/PyBA nanotubular films. To determine if any DA remains in these PyBA-exchanged films, the films were submerged into individually aliquoted aqueous 1 M KOH solutions. Subsequent quantification of their PyBA content by UV-vis absorbance spectroscopy of the KOH solutions and comparison to the measured mass loss after the KOH immersion indicates that nearly all mass loss can be attributed to PyBA dissolved out of the films. Since all intercalated surfactants are expected to dissolve out of the film into the KOH solution, we deduce that negligible DA remains with the PyBA-exchanged hybrid.

2.5.4 Preparation of 1 M KOH/25 wt% surfactant solutions

In order to prevent neutralization of the aqueous 1 M KOH solutions when adding large amounts of acidic surfactants, 0.75 g and 2 g of PyBA and DA powders respectively were added to separate conical tubes and neutralized with equimolar amounts of KOH using aqueous 1 M KOH solutions. ~30 mL of ultrapure water was added to each tube followed by mixing by vortexing and sonication. The resulting solutions were lyophilized to produce dry powders of deprotonated surfactants. 1 M KOH was then added to each tube in sufficient quantities to produce 1 M KOH/25 wt% surfactant solutions (approximately 1 molal PyBA and 1.6 molal DA).

2.5.5 VISCOSITY MEASUREMENTS ON SURFACTANT SOLUTIONS

Flow curves for each surfactant solution were measured with an MCR 302 rheometer (Anton Paar) operating in a cone-plate configuration with 50 mm diameter, 1° angle fixture (CP 50-1) and 0.1 mm gap. The viscosity was measured as a function of the applied shear rate from 1 to 1000 s^{-1}. All experiments were performed at 25°C.

2.5.6 SYNTHESIS OF 1-PYRENEHEXANOIC ACID AND 2-NAPHTHALENEBUTYRIC ACID

Unless otherwise specified, all reagents were used without further purification. Monomethyl adipate, triethylamine, pyrene, 2-bromonaphthalene, thionyl chloride, iodine and succinic anhydride were obtained from Sigma-Aldrich; diethyl ether, dichloromethane (DCM), hexanes, sodium hydroxide, hydrochloric acid (HCl), magnesium turnings, tetrahydrofuran (THF), and ethyl acetate (EtOAc) were obtained from Fisher Scientific; trifluoroacetic acid (TFA) was obtained from Alfa Aesar; triethylsilane was obtained from Acros Organics. Anhydrous solvents were degassed on a Vacuum Atmospheres 103991 system. Proton NMR spectra were performed on a Varian Inova 500 or Agilent DD MR-400 with working frequencies of 500 and 400 MHz, respectively. Carbon NMR spectra were obtained using a Bruker Avance III 500 spectrometer, with working frequency of 125.6 MHz for ^{13}C nuclei. Chemical shifts are reported in parts per million (ppm) and referenced to the residual nondeuterated solvent frequencies ($CDCl_3$: δ 7.26 ppm for ^{1}H, δ 77.36 ppm for ^{13}C, DMSO-D6: δ 2.62 for ^{1}H and 40.45 ppm for ^{13}C). High-resolution mass spectra were recorded on an Agilent Model 6210 LC-TOF multimode ionization (MMI).

The 1-pyrenehexanoic acid (PyHA) was synthesized using the scheme illustrated in Figure 2.32a.

1-Pyreneoxohexanoic methylester (PyCOHAMe). Monomethyl adipate (2.04 mL, 13.8 mmol) was dissolved in DCM (15 mL) and triethylamine (1.67 mL, 12.0 mmol) was added. The flask was put in an ice bath and thionyl chloride (0.872 mL, 12.0 mmol) was injected into the solution. The reaction was stirred for 10 minutes and the solvent was evaporated under vacuum. The crude material was dissolved in diethyl ether and the precipitate filtered. The ether washings were placed in a Schlenk flask and the ether was removed under vacuum. Pyrene (2.30 g, 9.99 mmol) was then added and the flask was degassed by three vacuum/nitrogen cycles before injecting anhydrous DCM (20 mL) under nitrogen. The flask was placed in an ice bath and immediately after, titanium (IV) chloride (1.32 mL, 12.0 mmol) was injected dropwise. The cooling bath was then removed and the reaction was left stirring for 30 minutes before quenching it by adding the solution to a solution of saturated sodium bicarbonate (100 mL) and filtering the entire mixture over celite, then washing the celite pad with DCM (250 mL). The DCM washings were placed in a separatory funnel to remove water. The solvent was then evaporated under vacuum and the product was purified by column chromatography (DCM) to give a yellow solid (2.52 g, 64%). ^{1}H NMR (400 MHz; $CDCl_3$): δ 8.88 (d, *J* = 9.4 Hz, 1H), 8.32 (d, *J* = 8.0 Hz, 1H), 8.26 (dd, *J* = 7.6, 1.8 Hz, 2H), 8.23-8.17 (m, 3H), 8.10-8.05 (m, 2H), 3.67 (s, 3H), 3.25 (t, *J* = 7.2 Hz, 2H), 2.42 (t, *J* = 7.3 Hz, 2H), 1.94-1.88 (m, 2H), 1.85-1.80 (m, 2H). ^{13}C NMR (126 MHz; $CDCl_3$): δ 204.9, 174.2, 134.1, 132.9, 131.5, 130.9, 129.94, 129.84, 129.66, 127.4, 126.76, 126.60, 126.4, 125.4, 125.1, 124.7, 124.4, 51.9, 42.5, 34.3, 25.0, 24.7. HRMS calc m/z 344.1412, found 344.1320.

1-Pyrenehexanoic methylester (PyHAMe). PyCOHAMe (1.23 g, 3.60 mmol) was dissolved in trifluoroacetic acid (6.00 mL, 78.4 mmol) and triethylsilane (1.50 mL, 9.00 mmol) was added dropwise before stirring the reaction for 1 h. The solvent was then removed under vacuum and the crude was washed with hexane (200 mL) to give a relatively pure yellow solid (0.792 g, 67%). ^{1}H NMR (400 MHz; $CDCl_3$): δ 8.27 (d, *J* = 9.3 Hz, 1H), 8.18-8.15 (m, 2H), 8.11 (dd, *J* = 8.5, 2.3 Hz, 2H), 8.02 (d, *J* = 2.3 Hz, 2H), 7.99 (dd, *J* = 9.8, 5.4 Hz, 1H), 7.86 (d, *J* = 7.8 Hz, 1H), 3.67 (s, 3H), 3.35 (t, *J* = 7.8 Hz, 2H), 2.34 (t, *J* = 7.5 Hz, 2H), 1.88 (dt, *J* = 15.4, 7.7 Hz, 2H), 1.74 (dd, *J* = 15.4, 7.6 Hz, 2H), 1.56-1.50 (m, 2H). ^{13}C NMR (126 MHz; $CDCl_3$): δ 174.5, 137.2, 131.8, 131.3, 130.1, 128.9, 127.8, 127.55, 127.51, 126.9, 126.1, 125.42, 125.38, 125.15, 125.11, 124.99, 123.7, 51.8, 34.4, 33.7, 31.8, 29.6, 25.2. HRMS calc m/z 330.1620, found 330.1630.

1-Pyrenehexanoic acid (PyHA). PyHAMe (1.00 g, 3.04 mmol) was dissolved in methanol (30 mL) and 6 M NaOH (5.00 mL, 30.0 mmol) was then added and the solution was refluxed for 6 h (or until TLC indicates full hydrolysis of methyl ester) before removing the solvent under vacuum. Acidification with 4 M HCl (10 mL) gave a yellow precipitate, which was filtered and washed with DCM (100 mL), collected and dried (0.600 g, 79%). ^{1}H NMR (499 MHz; THF): δ 8.36 (d, *J* = 9.3 Hz, 1H), 8.18 (t, *J* = 6.9 Hz, 2H), 8.15-8.13 (m, 2H), 8.07-8.03 (m, 2H), 7.99 (t, *J* = 7.6 Hz, 1H), 7.92 (d, *J* = 7.8 Hz, 1H), 3.61 (d, *J* = 19.9 Hz, 30H), 3.40 (t, *J* = 7.8 Hz, 2H), 2.29-2.26 (m, 2H), 1.92-1.88 (m, 2H), 1.76-1.68 (m, 20H), 1.60-1.55 (m, 2H). ^{13}C NMR (126 MHz; DMSO): δ 175.4, 137.9, 131.8, 131.3, 130.1, 128.9, 128.4, 128.1, 127.4, 127.0, 125.84, 125.66, 125.15, 125.10, 124.4, 34.6, 33.5, 32.2, 29.6, 25.4 HRMS calc m/z 316.1463, found 316.1472.

The 2-naphthalenebutyric acid (NBA) was synthesized using the scheme illustrated in Figure 2.32b.

2-Naphthaleneoxobutyric acid (NCOBA). A flask containing 2-bromonapthalene (5g, 24.2 mmol) and freshly polished magnesium (0.860 g, 36.0 mmol) was degassed by three vacuum/nitrogen cycles before injecting anhydrous THF (30 mL). Iodine (0.254 g, 1.00 mmol) was then added and the flask was heated until the color of iodine disappeared. The flask was placed in an ice-bath as necessary to prevent violent boiling of THF. Once cool to room temperature, the Grignard reagent was cannulated into a degassed solution of succinic anhydride (2.89 g, 28.9 mmol) in anhydrous THF (20 mL) and left stirring for 30 minutes. Aqueous NaOH (6 M, 1 mL) was then added and the reaction diluted in water (100 mL) and extracted with ethyl acetate (50 mL). The aqueous layer was collected and acidified with 4 M HCl (10 mL), then extracted with ethyl acetate (50 mL). The organic layer was collected and the solvent was removed under vacuum. The product was purified by column chromatography (10% MeOH/DCM) to afford a white solid (2.00 g, 36%). ^{1}H NMR (499 MHz; $CDCl_3$): δ 8.52 (d, *J* = 0.4 Hz, 1H), 8.05 (dd, *J* = 8.6, 1.7 Hz, 1H), 7.97 (d, *J* = 7.9 Hz, 1H), 7.92-7.88 (m, 2H), 7.63-7.55 (m, 2H), 3.49-3.46 (m, 2H), 2.90-2.88 (m, 2H). ^{13}C NMR (126 MHz; $CDCl_3$): δ 198.2, 176.6, 136.1, 134.1, 132.8, 130.2, 129.9, 128.95, 128.89, 128.2, 127.2, 124.1, 33.7, 28.1. HRMS calc m/z 228.0786, found 228.0789.

2-Naphthalenebutyric acid (NBA). NCOBA (0.560 g, 2.45 mmol) was dissolved in trifluoroacetic acid (3.00 mL, 39.2 mmol) and triethylsilane (0.980 mL, 6.12 mmol) was added dropwise before stirring the reaction for 1 h. The solvent was then removed under vacuum and the product was purified by column chromatography (10% MeOH/DCM) to afford a white solid

(0.430 g, 82%). ^{1}H NMR (499 MHz; $CDCl_3$): δ 7.80 (dd, *J* = 12.3, 8.0 Hz, 3H), 7.63 (s, 1H), 7.48-7.42 (m, 2H), 7.34 (dd, *J* = 8.4, 1.4 Hz, 1H), 2.85 (t, *J* = 7.6 Hz, 2H), 2.42 (t, *J* = 7.4 Hz, 2H), 2.11-2.05 (m, 2H). ^{13}C NMR (126 MHz; $CDCl_3$): δ 180.0, 139.0, 133.9, 132.4, 128.4, 127.95, 127.79, 127.5, 127.0, 126.3, 125.6, 35.5, 33.6, 26.4. HRMS calc m/z 214.0994, found 214.0989.

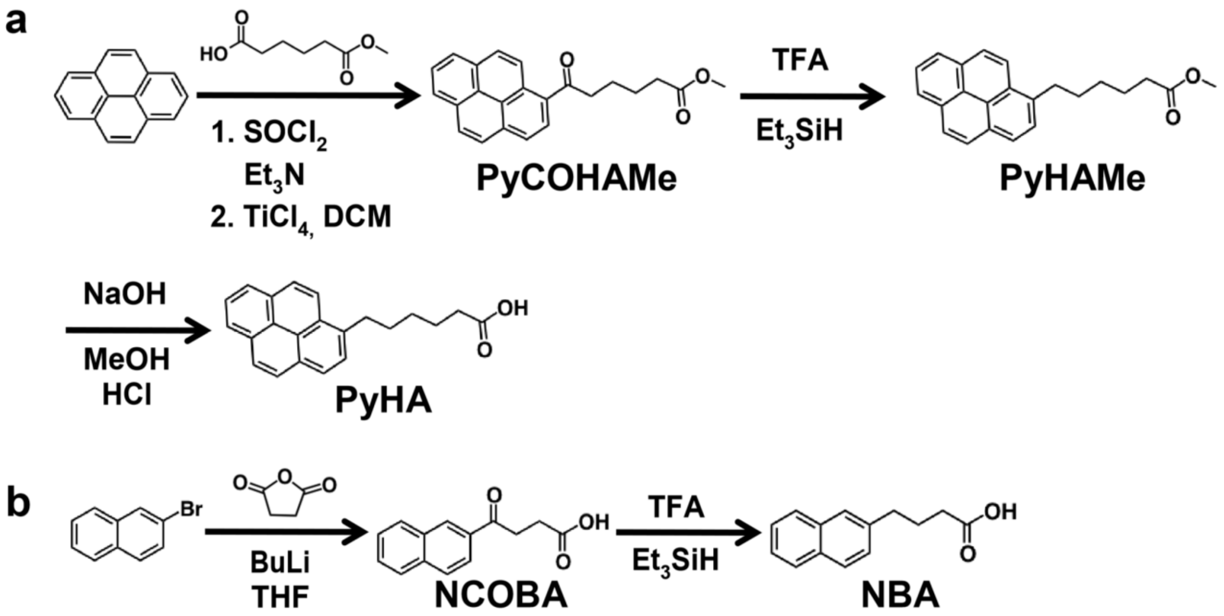

Figure 2.32 Synthesis of (a) 1-pyrenehexanoic acid and (b) 2-naphthalenebutyric acid.

2.6 SUPPORTING DISCUSSION

2.6.1 RELATIVE CONCENTRATION INDEPENDENCE OF TUBE FORMATION

We conducted a series of time-resolved morphological studies described in Figure 2 at different initial deposition bath concentrations to explore the range of compositional window for the nanotubular growth. We found that moderate changes to the precursor composition does not greatly affect the ability of nanotubes to form, but rather the amount of deposition time it takes to nucleate the tubes. Table 2.1 shows the compositions we have tested. For example, nanotubes were observed after 60 minutes at both 75% and 150% of the original nitrate concentration (Figure 2.4a and b, respectively). To maintain a constant Co^{2+} concentration, $CoCl_2$ was substituted to reduce nitrate concentration while KNO_3 was added to raise nitrate concentration. Raising the nitrate concentration accelerates the deposition, because more hydroxide ions are being produced at the surface of the working electrode leading to more rapid precipitation of the hybrid $Co(OH)_2$ structure. For PyBA concentrations between 50% and 150% of the original 1.25 mM, all films had at least partial nanotube formation after 90 minutes. At lower concentrations of PyBA, some pure flake structures were formed, presumably because there was insufficient PyBA intercalation to induce nanotube formation (Figure 2.4c). At higher concentrations, nanotube formation was observed after about 120 minutes (Figure 2.4d). This may be due to the increased concentration of PyBA molecules inhibiting nitrate reduction at the electrode surface, effectively acting as a passivating layer.

2.6.2 2D-GIXS AZIMUTHAL ANGLE (Φ) ANALYSIS

For the 2D-GIXS analysis referenced in this work, the angle Φ refers to the azimuthal angle in the q_{yz} plane of the detector. This angle determines the orientation of crystalline order with respect to the film's substrate. For peaks localized at $\Phi = 90^\circ$, the associated lattice planes are oriented parallel to the substrate. Peaks localized at $\Phi = 0^\circ$ or 180° are associated with lattice planes oriented parallel to the substrate normal and thus perpendicular to the substrate. Line cuts in this work refer to integrated signal intensities of 2D-GIXS data, and may be plotted with respect to q or Φ.

The small oscillations at $q < 0.2$ Å^{-1} are a result of the nanotubular scattering form factor, as later described in Figure 2.14 and Figure 2.11. A small β-$Co(OH)_2$ (001) peak is observed at q

= 1.30 Å^{-1}, which indicates the presence of non-intercalated $Co(OH)_2$ as a minor impurity phase. We expect that this impurity phase is a result of high pH localized at the substrate-film interface, which can convert PyBA-intercalated $Co(OH)_2$ to β-$Co(OH)_2$. This β-$Co(OH)_2$ is the more stable $Co(OH)_2$ phase at higher pH values. Two peaks are observed at q = 1.62 Å^{-1} and 1.68 Å^{-1}, which correspond to d-spacings of 3.88 Å and 3.73 Å respectively and are expected to be the result of π-π stacking of the PyBA (see Figure 2.9 for orientation of this π-π stacking).

2.6.3 SCATTERING ANALYSIS ON THE TUBE SIZE

We used the lateral intensity profiles from the grazing incidence X-ray scattering patterns to estimate the average diameter of the nanotubes. The measured scattering profiles have significant background from substrate fluorescence – therefore we identified the minima in the scattering profiles and compared against the theoretical form factor minima from a cylindrical model instead of fitting the entire curve to the core-shell cylindrical model.

The scattering form factor of an infinitely long cylindrical object is described as:

$$F = 4\pi r^2(\Delta\rho) \cdot \left(\frac{J_1(qr)}{qr}\right)$$

Here r denotes the radius of the cylinder, $\Delta\rho$ the electron density difference, q the scattering vector magnitude defined as $q = (4\pi \sin\theta)/\lambda$ where θ is half of the total scattering angle and λ is the wavelength, and J_1 the Bessel function of order 1. As the scattering intensity is proportional to the square of the form factor, minima for the scattering intensities occur where $J_1 = 0$.

Figure 2.11 shows the correlation between the observed minima of the scattering patterns and the roots of J_1. The lateral intensity profiles for both GISAXS and GIWAXS were laterally averaged over 100 pixels above the sample horizon. The linear fit of the correlation provides the average radius of the nanotubes, which is estimated to be 13.6 nm, giving 27.3 nm for the diameter.

2.6.4 DETERMINATION OF ACTIVE MATERIAL MASS BY THERMOGRAVIMETRIC ANALYSIS

To determine the mass of $Co(OH)_2$ active material deposited on each film, the mass percentage of $Co(OH)_2$ in the $Co(OH)_2$/PyBA hybrid films must first be determined. Thermogravimetric analysis was performed to determine the organic content of hybrid films, with the assumption that there is negligible mass loss by the inorganic $Co(OH)_2$ material during heating to moderate temperatures (Figure 2.18). Several films were scraped from their substrates and collected for analysis using a Mettler-Toledo TGA/SDTA 851 instrument. TGA was performed in air with a 5℃/min ramp rate. The TGA curve presented in Figure 2.18 has been subtracted with a blank curve collected under identical conditions with an empty pan to correct for buoyancy effects. A ~50% mass loss is observed in the 200-300℃ range, which is attributed to PyBA combustion. $Co(OH)_2$ active material mass percentage is thus estimated to be ~50% in the hybrid material.

Due to the difficulty of collecting enough material for accurate mass quantification with TGA, several films were left on their substrates and calcined for more accurate mass determination. Films of $Co(OH)_2$/PyBA and $Co(OH)_2$/DA hybrids were deposited on stainless steel substrates, heated to 310℃ with a 5℃/minute ramp rate, and held at 310℃ for 10 minutes before cooling to room temperature. The masses of these substrates before and after calcination are summarized in Table 2.2.

Assuming that any mass change of the underlying substrate is negligible compared to the mass changes of the deposited films, the mass percentage losses of the $Co(OH)_2$/PyBA and $Co(OH)_2$/DA films are -53.7 and -52.0 percent respectively. The $Co(OH)_2$ active material mass percentages for $Co(OH)_2$/PyBA and $Co(OH)_2$/DA films are thus calculated to be 46.3 and 48.0 percent respectively.

2.6.5 ABSORBANCE SPECTROSCOPY ON IMMERSION AND CYCLING ELECTROLYTES

UV-vis absorbance spectroscopy was used to characterize the extent of PyBA dissolution out of the nanotubular films during soaking or cycling in 1 M KOH. The PyBA concentration was calibrated using standards of known concentration and applying Beer-Lambert's law (Figure 2.27a). In Figure 2.27b, absorbance spectra of various electrolytes used for soaking and cycling are plotted along with a 50 µM PyBA standard curve. After normalizing the spectra of each film for electrolyte volume, we determined the PyBA mass in the electrolyte and compared to the total film weight. For immersion or cycling of a nanotubular film in 1 M KOH for 24 hours, we found the PyBA mass constitutes roughly half of an average film and concluded that approximately all of the organic content dissolves out, corroborating the data in Table 2.2. We further confirmed the mass change calculated from UV-vis by weighing the films after immersion. We found that the mass change can be solely attributed to the dissolution of the PyBA, and thus conclude that any dissolved $Co(OH)_2$ species reprecipitate as β-CoOOH.

To verify complete dissolution of PyBA, we immersed a cycled sample in fresh 1 M KOH after cycling in 1 M KOH and observed neglible PyBA absorbance. Furthermore, we deduced that it is the bascity of the KOH rather than the ionic strength or liquid phase of the electrolyte that dissolves the PyBA out of the structure when comparing to 1 M KCl and pure deionized water controls.

3 HIERARCHICAL METALLIC ARCHITECTURES ENABLED BY HYBRID LAYERED NANOFIBER TEMPLATES AND MAGNETIC ASSEMBLY

3.1 OBJECTIVE AND SIGNIFICANCE

In large living organisms, hierarchical vasculatures are omnipresent as branching networks are required to efficiently transport nutrients through fast fluid flow to small diameter high surface area tubules where they may diffuse out to surrounding tissue. Analogously, electrochemical energy storage devices such as batteries and supercapacitors require hierarchical architectures to efficiently conduct electrons to and from electrochemically active material where energy storage takes place. Inspired by the branched vasculature found in plants and animals, here we report on two approaches to synthesizing metallic nanowires on nickel foam substrates to form hierarchical current collectors for electrochemical energy storage. The first approach involves hydrothermally synthesis of hybrid layered nanofibers on nickel foam as metal-rich templates. Subsequent calcination and hydrogen reduction of these nanofibers yields metallic nanowires, albeit with loss of the initial fiber network structure and fragility. The second approach utilizes electroless deposition of nickel under magnetic fields to assemble nickel nanowires onto nickel foam substrates. This approach is much faster and more scalable but results in poor filling of the nickel foam with nanowires due to shielding of the magnetic field within the pore structure.

3.2 BACKGROUND

Nanostructuring is an important approach for achieving high surface areas and enabling fast charge-discharge operation of energy storage electrodes. Due to their high surface areas and accompanying fast surface-redox reactions, these materials can exhibit extraordinary power density while maintaining near-theoretical specific energy density. However, much of published supercapacitor work has been limited from practical applications by the low “mass loading” compared to commercial energy storage devices.[77,80,81,111] Mass loading refers to the mass of active material coated per area of current collector. Since electrochemical energy storage devices are conventionally fabricated as planar stacks or cylindrical rolls of alternating anodes/cathodes supported by metal foil current collectors and separated by polymer separators, low mass loading reduces the ratio of active material to other cell components, reducing the overall energy density of the device.[112,113]

While low mass loading prohibits translation to medium- and large-format devices, forming only thin coatings of active materials on current collectors is an important strategy for improving rate capabilities by reducing ion and electron conduction path lengths in low conductivity active materials. To address issues of low mass loading while still maintaining thin active material layers, many researchers have directed efforts towards creating three-dimensional electrode architectures.[114,115] A great deal of attention has been placed on carbon-based three-dimensional scaffolds due to their high electrochemical stability and the inherently high surface area of low-dimensional carbons (e.g. carbon nanotubes and graphene). However, these scaffolds can suffer from issues such as low electrolyte wettability, low density and high contact resistance between carbon components. Metal scaffolds can also be utilized when constructed from corrosion-resistant metals such as nickel and gold. A nanoporous gold current collector was fabricated by de-alloying a silver-gold film. When loaded with manganese oxide, there was an enhancement in the pseudocapacitive behavior of the manganese oxide due to the high electrical/ionic conductivity of the overall electrode.[116] Another high-profile example of metallic scaffolds was the templation of a bicontinuous inverse opal nickel current collector by self-assembled polystyrene beads. This current collector was used as a scaffold for nickel hydroxide and manganese oxide deposition, which allowed for full discharge of the resulting nickel metal hydride and lithium ion battery electrodes on the order of seconds.[117] However, the reported thicknesses of these electrodes are on the order of ~100 nm and ~10 microns respectively, limiting mass loading and full device energy/power density. Increasing the thickness of these electrodes is technically challenging from a fabrication standpoint. Additionally, rate capabilities may be reduced for thicker electrodes because of limitations in long-range electrolyte transport and electrical conductivity in finely nanostructured ion and electron pathways. A new electrode architecture is required that can be fabricated to macroscopic dimensions while maintaining high surface area and bulk conductivity. Introducing multiple length scale porosity and electron conduction pathways with a hierarchical structure should provide a large surface area for high mass loading of active materials and simultaneously reduce bulk ion and electron transport resistances.

Biological structures have also been used as templates for three-dimensional electrodes because of the natural hierarchical vasculatures and mineralized skeletons.[118–120] However, when using biological materials as templates, one is limited to the existing structures found in nature and parameters such as porosity, tortuosity and strut thicknesses may not be finely optimized. In this work, we propose utilizing commercial nickel foam substrates to support the growth of an internal nickel nanowire (NiNW) network. The nickel foam provides bulk structural support and electrical conductivity, while the nanowires provide additional surface area for increasing the loading capacity of the electrode. Two methods of synthesizing NiNWs are demonstrated, the first using a hybrid nanofiber template that is converted to NiNWs with subsequent calcination and hydrogen reduction, and the second using magnetic fields to direct the growth of NiNWs during electroless deposition.

3.3 RESULTS AND DISCUSSION

3.3.1 GROWTH OF ORGANIC-NICKEL HYDROXIDE HYBRIDS

We base our synthesis of hybrid nanowires on a recently reported hydrothermal synthesis of hybrid organic-cobalt hydroxide nanofibers. The authors reported growth of ~100 nm wide nanofibers with lengths up to hundreds of micrometers upon heating of an aqueous cobalt nitrate and sodium benzoate solution.[121] The nanofibers have a layered internal structure, with the intercalated benzoate molecules presumably directing the anisotropy of the nanostructure and π-π stacking possibly providing mechanical stability. We apply a similar synthesis using a nickel nitrate and sodium benzoate solution into which we immerse a nickel foam substrate to allow internal growth of nickel hydroxide hybrid nanofibers. Subsequent heat treatment is used to thermally decompose the organic phase and leave nickel oxide nanofibers. A simultaneous reducing and sintering process in hydrogen is performed to produce nickel metal and sinter the nanofibers together to reduce junction resistances within the network. (Figure 3.1)

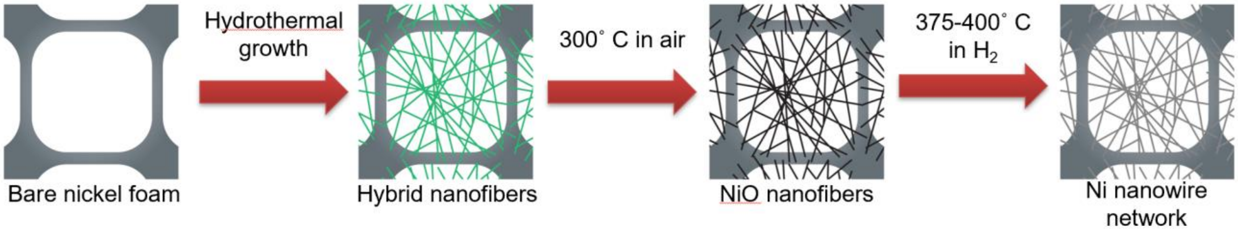

Figure 3.1 Schematic describing synthesis of nickel nanowires templated by hybrid nanofibers.

Immediately, we discovered that organic-nickel hydroxide nanofibers exhibited spherulitic nucleation behavior, with fibers growing radially from discrete nucleation points within the reaction solution as opposed to nucleating from the nickel foam surface. This results in most of the hybrid material growing outside of the foam, with the material that is grown within the foam only being trapped by weak physical entanglement instead of having strong adhesion to the nickel surface. (Figure 3.2) Filtration of the reaction solution with 200 nm nylon syringe filters did not mitigate this behavior, indicating that solid contaminants were not the cause of spherulitic growth.

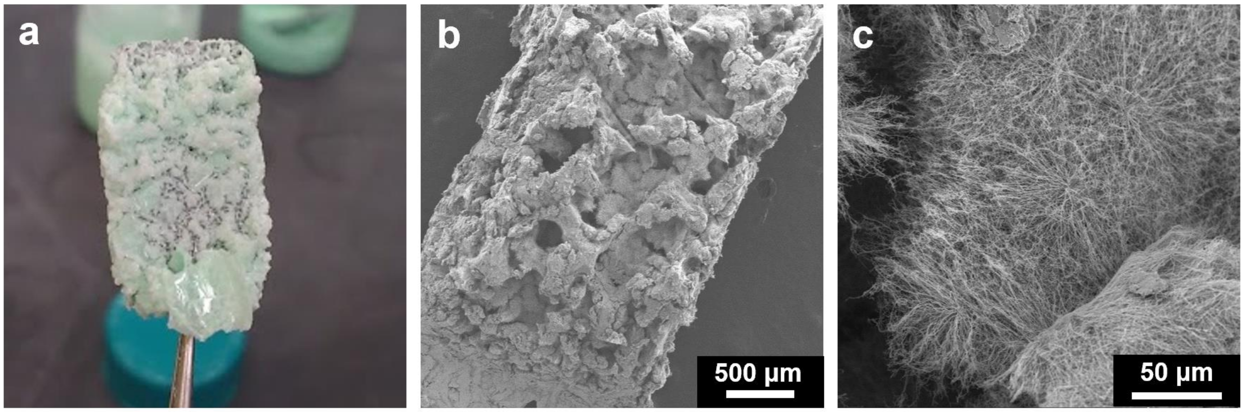

Figure 3.2 Spherulitic nucleation morphology in unagitated solutions. a) Photograph and b,c) SEM images of hybrid nanofibers as grown within nickel foam.

In an attempt to make nucleation more energetically favorable on surface of the nickel foam, foam substrates were coated with nickel hydroxide by oxidative etching of the nickel in potassium hydroxide following a similar synthesis described by Kung *et al*.[122] The etching in alkaline solution results in a thin layer of nickel hydroxide flakes on the foam, (Figure 3.3a) which was washed and dried before placed in the nanofiber reaction solution. While some nanofibers were observed to grow from the nickel hydroxide flakes, (Figure 3.3c) the majority of nanofiber growth was still dominated by spherulitic nucleation away from the nickel foam surface. (Figure 3.3b)

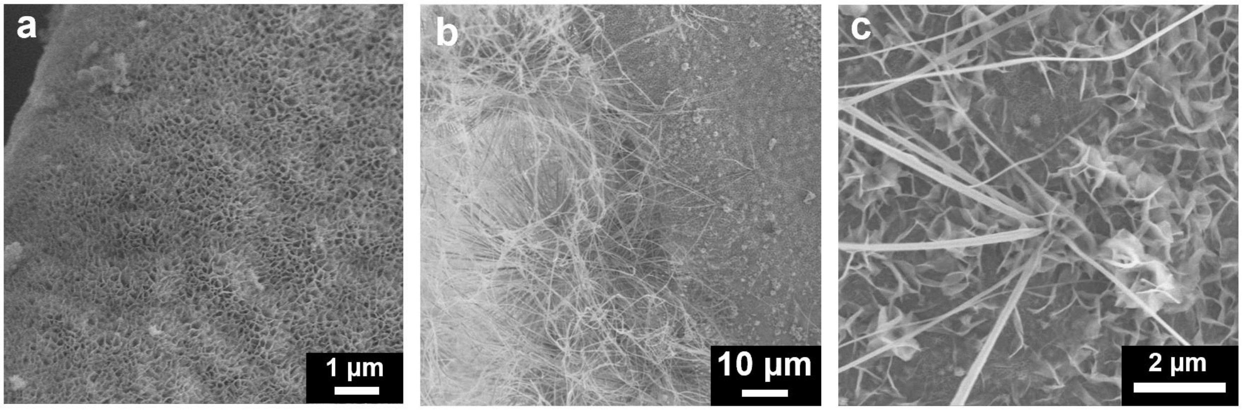

Figure 3.3 a) SEM image of nickel hydroxide as deposited on nickel foam. b,c) SEM images of hybrid nanofibers grown within nickel foam coated with nickel hydroxide.

In an alternative approach, nanofibers were grown under continuous stirring. The shear forces of the stirring reaction solution were observed to shear excess material from the nickel foam, while the continuous rotation of the nickel foam substrates in the solution trapped the growing nucleates within its porous structure. (Figure 3.4) Samples synthesized with this method were used for the following section on optimization of conversion to metallic nanowires.

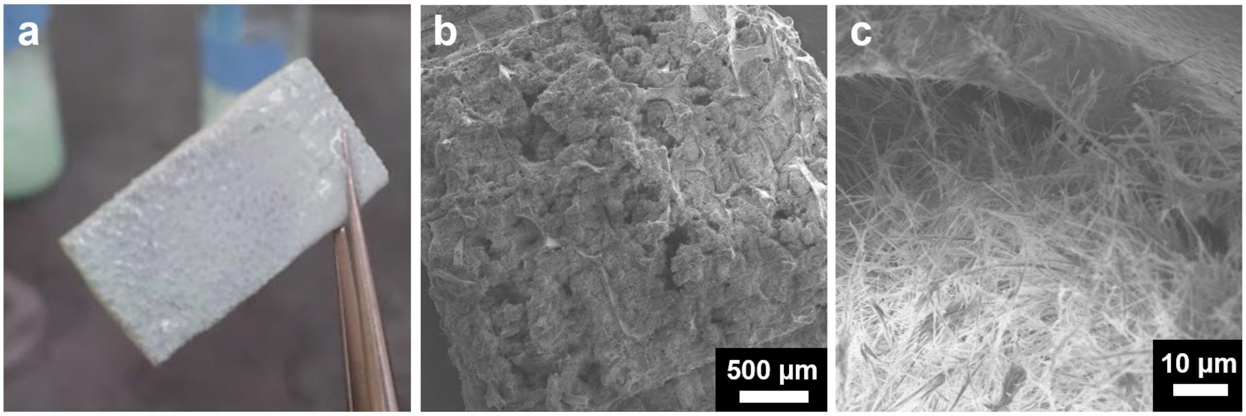

Figure 3.4 Hybrid nanofibers grown within nickel foam with magnetic stirring of hydrothermal bath. a) Photograph and b,c) SEM images of nickel foam with nanofibers grown within.

3.3.2 CONVERSION TO METALLIC NANOWIRES

The calcination of the hybrid nanofibers was first studied using thermogravimetric analysis (TGA). Heating nanofibers in air to 800 °C resulted in a 66 percent loss of mass, a combination of dehydration and oxidation of the nickel hydroxide layers and the combustion of the benzoate surfactants. (Figure 3.5)

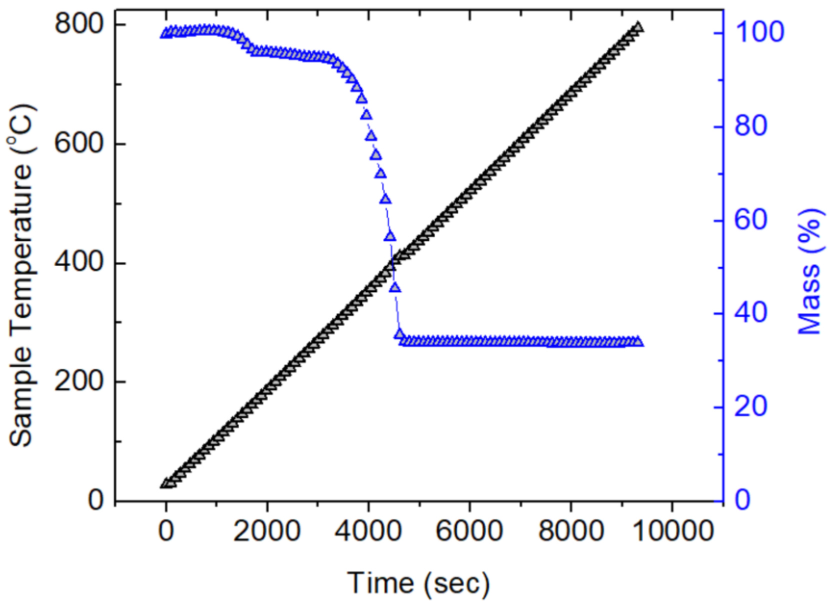

Figure 3.5 TGA trace of hybrid nanofibers decomposed under air.

In order to slowly remove the organic phase and preserve the morphology of the hybrid nanofibers, samples were heated in air for 16 hours in a small muffle furnace set to 300 °C. It was quickly determined with carefully positioned thermocouples that small thermal gradients existed within the furnace. A small increase in sample height of a few centimeters resulted in a 7.5 °C rise in temperature. (Figure 3.6a,c) This increase also resulted in a significant change in the calcined morphology, with the higher temperature treatment resulting in chained round particulates as the nickel oxide presumably sintered. (Figure 3.6b) In comparison, calcination at 301 °C retained the nanofibrous structure, with only small internal porosity displayed within each nanofiber. (Figure

3.6d) The mass changes of both of these samples post-calcination corresponded well with the TGA data, indicating that there was complete removal of the benzoate from the hybrid nanofibers.

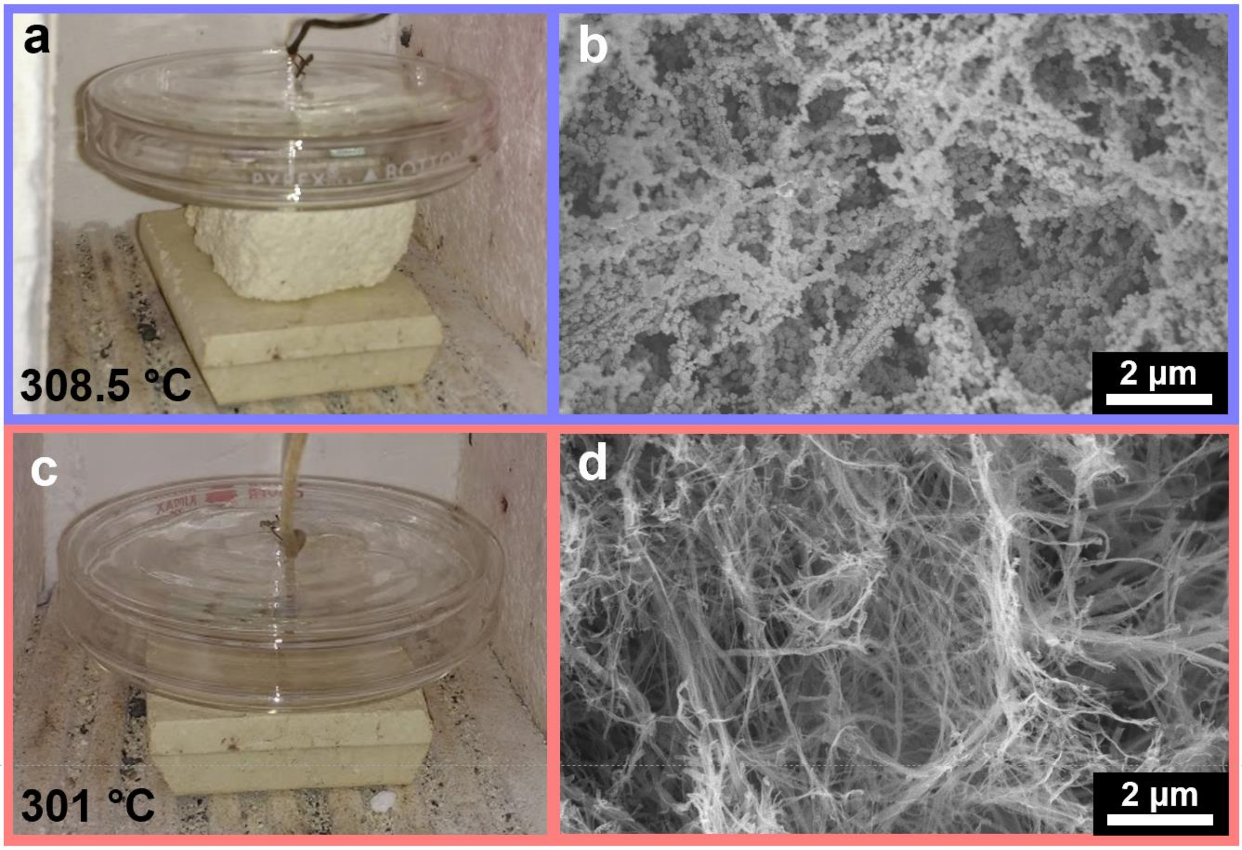

Figure 3.6 Comparison of calcination of hybrid nanofibers at different positions of a muffle furnace with a set point temperature of 300 °C. a) Photograph of calcination position and b) SEM image of nanofibers post-calcination when elevated within the furnace. c) Photograph of calcination position and d) SEM image of nanofibers post-calcination when positioned lower within the furnace.

In order to better control the temperature of calcination batch-to-batch, an aluminum heating block was designed and machined, with slots located inside the block for placement of samples. (Figure 3.7a) The combination of the high thermal conductivity of aluminum and large thermal mass of the block would ensure spatially-uniform and stable temperatures during calcination. (Figure 3.7b) However, calcination at 300 °C in the heating block only yielded a 36 percent loss of mass as well as a non-uniform gray and white appearance of the sample, indicating incomplete removal of the organic phase. (Figure 3.7c) Literature references on thermal decomposition of similar composition nickel benzoate salts indicate that benzoate may sublimate at temperatures near 300 °C instead of combusting.[123] As a result, use of a closed heating block may result in slower sublimation kinetics despite the controlled thermal environment. All samples used for hydrogen reduction were thus calcined in closed petri dishes that contained more headspace and allowed escape of benzoate vapors. (Figure 3.7d)

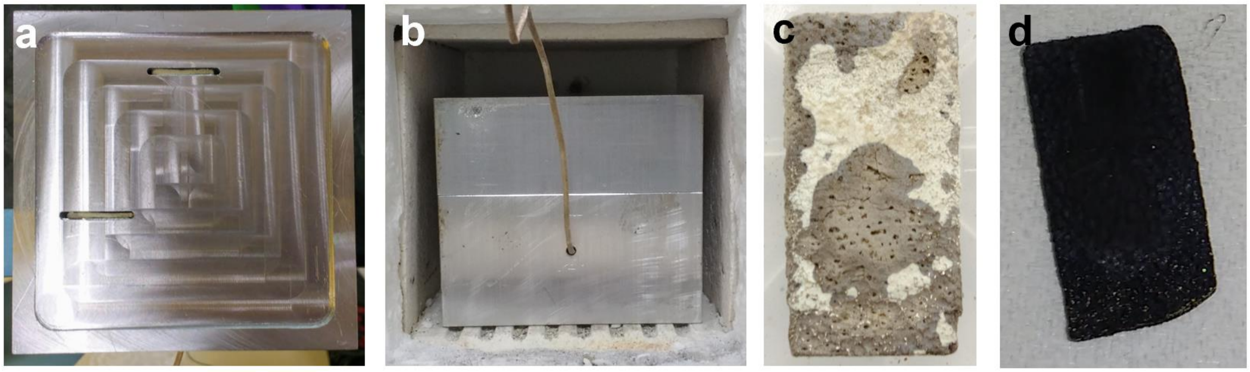

Figure 3.7 Attempts to use an aluminum heating block to ensure thermal uniformity. a) Photograph of slots inside heating block with nanofiber/nickel foam samples inserted. b) Photograph of heating block with closed lid and thermocouple inserted into furnace. c) Photograph of nanofiber/nickel foam sample incompletely calcined within the heating block. d) Photograph of nanofiber/nickel foam sample calcined completely within glass petri dish.

Hydrogen reduction of calcined samples was conducted at 375 °C, as in-situ environmental TEM studies indicate that Ni metal begins to nucleate from NiO at 370 °C under flow of pure hydrogen.[124] The change in morphology to full-density connected globular structures indicated reduction and sintering to Ni metal. However, the resulting metallic nanostructures exhibited large volumetric shrinkage after reduction and sintering and were fragile and easily dislodged from the nickel foam support. This indicates poor sintering to the nickel foam and likely poor electrical contact.

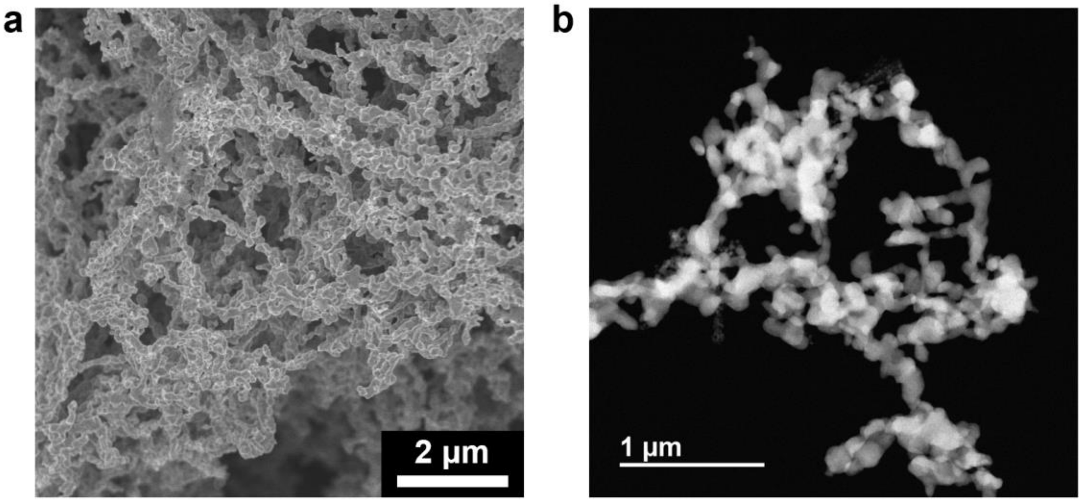

Figure 3.8 a) SEM image and b) HAADF STEM image of nickel nanowires after hydrogen reduction.

3.3.3 MAGNETIC ASSEMBLY OF NICKEL NANOWIRES

As an alternative approach to forming nickel nanowires on nickel foam supports, electroless deposition under magnetic fields were explored. First reported by the Matsubara lab in 2011,[125] nickel nanowires formed by assembly of nucleated nickel nanoparticles under magnetic fields were utilized as current collectors in electrochemical energy storage devices both as free-standing nanowire networks and as grown on titanium foil. [126,127] Nickel foam was suspended within the electroless deposition bath and held upright against the reaction beaker by the magnetic field gradient of the NdFeB rare earth magnets attached outside the beakers. Nickel nanowires were observed to attach and grow from the edges of struts in the nickel foam, presumably due to channeling and concentration of the magnetic field at these points. However, no nanowire growth was observed inside the pores because of magnetic shielding effects of the ferromagnetic foam scaffold. (Figure 3.9)

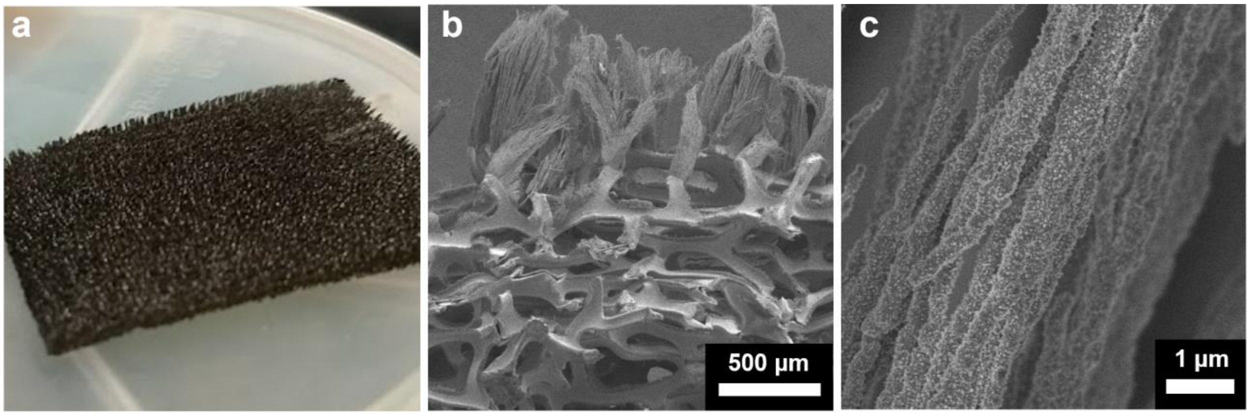

Figure 3.9 a) Photograph and b,c) SEM images of nickel nanowires grown on nickel foam using electroless deposition under magnetic fields.

3.4 CONCLUSIONS

Two separate approaches to forming nickel nanowires within nickel foam substrates were explored in this work. The first utilized hybrid nanofiber templates that could be converted to nickel nanostructures through subsequent calcination and hydrogen reduction steps. While this method allows for better in-filling of the pores in the nickel foam, the resulting nanostructured nickel did not fully retain the original structure of the hybrid nanofibers and were physically delicate, indicating poor connectivity and sintering to the foam scaffold. Additionally, this process was slow and unscalable with the long hydrothermal synthesis and slow calcining and reduction steps. The second method was based on published methods of forming nickel nanowires through electroless nickel deposition under magnetic fields. While this method was much faster than the hybrid template approach, nanowires could not be grown inside of the nickel foam structure because of the magnetic shielding effect of the ferromagnetic foam. This limits the coverage of the nickel nanowires on the foam and the potential applications of the resulting hierarchical structure for current collectors in energy storage devices.

3.5 MATERIALS AND METHODS

3.5.1 PREPARATION OF NICKEL FOAM SUBSTRATES

Nickel foam substrates (MTI corporation, EQ-bcnf-16m) were cut to rectangular 1x2 cm strips using a razor blade. They were cleaned with sonication under isopropanol and water, then dried overnight in a vacuum oven at 60 °C. Bare substrates were made more hydrophilic and less susceptible to air bubble trapping by plasma cleaning for 30 seconds. Nickel hydroxide coated foam substrates were prepared with this same process, followed by 100 CV sweeps from 0 to 0.8V vs. Hg/HgO in 1 M KOH at 25 mV/sec, using an Autolab PGSTAT128N, a Pt wire counter electrode, and a CH instruments CHI152 Hg/HgO reference electrode. The resulting foam substrates were immersed and shaken in milli-Q water, replacing the water three times to ensure full removal of KOH. Samples were then dried overnight in a vacuum oven at 60 °C.

3.5.2 GROWTH OF ORGANIC-NICKEL HYDROXIDE HYBRID NANOFIBERS

An aqueous solution of 0.12 M sodium benzoate and 60 mM nickel (II) nitrate was prepared and degassed by sonication under house vacuum. Unagitated foam samples were sealed in separate 4 dram glass vials with 5 mL of solution in each and heated to 95 °C for 48 hours in an aluminum heating block. Stirred foam samples were placed in a 100 mL round-bottom flask with 25 mL of reaction solution, a magnetic stir bar and 7 foam substrates per batch. The round-bottom flask was then sealed with a rubber septum and heated in a 95 °C oil bath with 150 RPM stir rate. Post-growth, samples were immersed in milli-Q water, changing the water every 10 minutes for 3 wash cycles. Samples were then frozen under liquid nitrogen and lyophilized to preserve the porous structure.

3.5.3 CALCINATION OF HYBRID NANOFIBERS

Calcination was performed with a small muffle furnace, ramping to 300 °C at 5 °C/min and holding for 16 hours before shutting off. The setpoint for the calcination experiments with the aluminum heating block was adjusted upwards to allow the equilibrium internal temperature of the heating block to reach 300 °C.

3.5.4 HYDROGEN REDUCTION OF CALCINED NANOFIBERS

Calcined samples were placed on an alumina dish and put into a tube furnace purged with Ar. 150 mL/min flow of hydrogen was started after purging and samples were heated to 375 °C at a ramp rate of 10 °C/minute, held at 30 minutes, then allowed to cool to room temperature slowly with the power shut off (several hours).

3.5.5 ELECTROLESS DEPOSITION OF NINWS UNDER MAGNETIC FIELDS

25 mL of an aqueous solution of 0.100 M $NiCl_2$, 37.5 mM $Na_3C_6H_5O_7$ and 0.20 mM H_2PtCl_6 was prepared. 25 mL of an aqueous solution of 1.00 M N_2H_4 was prepared separately. The pH of both solutions was adjusted to 12.5 under constant stirring using a 6 M NaOH solution. We note that the nickel-based solution will form solid precipitates that re-dissolve after exceeding pH 12. Both solutions were heated separately to 80 °C in a water bath in a fume hood due to the volatility and carcinogenic properties of the N_2H_4 solution. A beaker was prepared with two parallel ¼” thick 1.5” diameter disk-shaped neodymium rare earth magnets (McMaster-Carr, #5862K15) secured to the outer diameter with Kapton tape to create a linear field gradient across the beaker. 2 bare nickel foam substrates were placed inside the beaker, sticking to the sides of the beaker due to the gradient in magnetic field. The two solutions were mixed into this beaker and the beaker was placed inside the water bath for 15 minutes until the solution becomes clear and

the nickel has become fully reduced. Samples were thoroughly rinsed 3x with milli-Q water and dried overnight in a vacuum oven at 60 °C.

3.5.6 ELECTRON MICROSCOPY

SEM was performed on uncoated samples adhered to sample stubs using carbon tape. Hitachi S-3400N-II and SU8030 SEM instruments were used. HAADF STEM was performed using a Hitachi HD-2300 STEM.

3.5.7 THERMOGRAVIMETRIC ANALYSIS

TGA was performed using a Mettler-Toledo TGA/SDTA 851 instrument. Samples were packed into alumina crucibles for analysis.

4 FAST AND PROGRAMMABLE LOCOMOTION OF HYDROGEL-METAL HYBRIDS UNDER LIGHT AND MAGNETIC FIELDS

4.1 OBJECTIVE AND SIGNIFICANCE

An enormous challenge for science is the design of soft matter in which internal fuels or an external energy input can generate locomotion and shape transformations observed in living organisms. Such materials could assist in productive functions that may range from robotics to smart management of chemical reactions and communication with cells. In this context, hydrated matter that can function in aqueous media would be of great interest. We report here on the design of hydrogels containing a skeleton of ferromagnetic nanowires with nematic order dispersed in a polymer network that change shape in response to light and experience torques in rotating magnetic fields. The synergistic response enables fast walking motion of macroscopic objects in water on either flat or inclined surfaces and also guides delivery of cargo through rolling motion and light-driven shape changes. The theoretical description of the response to the external energy input allowed us to program specific trajectories of hydrogel objects that were verified experimentally.

4.2 BACKGROUND

The design of hydrated soft matter that responds to external stimuli in ways that mimic the motion and shape changes of living organisms remains an enormous scientific challenge. Design of hydrated structures and mechanisms to achieve this objective may be eventually useful for the development of materials with locomotive capacity for novel aqueous chemistry or to augment the functions of living systems.[128–130] Pursuing this objective with magnetically actuated soft matter is particularly attractive since magnetic fields can safely penetrate most materials, including biological matter. In previous work it has been shown that magnetic fields can remotely activate locomotion of elastic filaments[131] and elastomeric materials that contain ferromagnetic components.[40,41,132–134] In these examples, specific patterns of magnetization and object geometry were generated by various fabrication techniques. However, once these samples have been prepared, the responsive magnetization profile cannot be reconfigured in the absence of a magnetic field. Moreover, the magnetic components were either embedded in a solid hydrophobic elastomer or supported on a rigid silicon nitride membrane. Hydrogels offer the possibility to function in water and also have the capacity to exchange fluids with aqueous environments. Previous work on hydrogels has shown walking or swimming behavior activated by light[135,136], thermal[137], chemical [138] or electrochemical stimuli[139], but all of these systems display slow actuation kinetics on the order of tens of seconds per step. We report here on the development of hydrogel–metal hybrid materials that are actuated by magnetic fields after exposure to light and also remain reconfigurable by light to alter their magnetic response. We theoretically predict the response of the hybrid objects to light and magnetic fields enabling the programming of their trajectories under water and gait on the fly.

Light as a stimulus is useful since it can be delivered to synthetic matter remotely and potentially in localized fashion. Recent examples of light responsive materials include polymer films containing *cis-trans* azobenzene switches[29] and hydrogels based on spiropyran chemistry[136,140] or molecular motors[141,142]. Soft materials capable of responding to both light and magnetic fields can initiate the exploration in soft matter of the multisensory interactions we observe in living organisms. In this work, we designed and synthesized hydrogel objects that perform distinct tasks with remote control over geometry, stiffness, and magnetization using a combination of light and magnetic fields. The samples are prepared by incorporating aligned ferromagnetic nanowires into a photoactive hydrogel matrix that is capable of changing shape in response to light. Macroscopic deformations of the hydrogel upon light irradiation generate complex three-dimensional magnetization profiles that lead to programmable actuation. These hydrogels can perform functions such as walking, steering, climbing, and delivering cargo under the control of an external magnetic field and light. Furthermore, small changes in the chemical structure of these systems change the kinetics of light response and thus provide access to a broader range of actuating behaviors.

4.3 RESULTS AND DISCUSSION

To synthesize the hydrogel–metal samples, nickel (Ni) nanowires (Figure 4.1) were added to a solution containing monomers, crosslinking agents, initiators and polymerizable molecular photoswitches (SP1, Scheme S1) in order to create a light-responsive crosslinked network (Figure 4.2a, see Section 4.5.3 for synthetic details). Under dark conditions, the photoswitch contains a hydrophilic merocyanine (MCH+) moiety that isomerizes to a hydrophobic spiropyran (SP) form upon exposure to visible light. This isomerization with light exposure results in contraction of the hydrogel due to dehydration, followed by expansion under dark conditions. The ferromagnetic nanowires were aligned under a static magnetic field and then fixed in this configuration by free-radical photopolymerization of the light-responsive hydrogel (Figure 4.2a,b and Figure 4.3). Small angle x-ray scattering (SAXS) confirmed the alignment of the nanowires, as shown by the radial integration of a 2D scattering intensity plot (Figure 4.2c). We measured a remanent magnetization of 260 emu/cm^3 parallel to the alignment of the nanowires and the coercive magnetic field required to reverse the magnetization of the sample was found to be 25 mT (Figure 4.2d). This is a 1.9-fold enhancement in the coercivity over bulk nickel (13 mT)[143], highlighting the utility of the shape anisotropy derived from the nanowire architecture (~8 μm long on average and 200 nm in diameter). In comparison, magnetization loops measured perpendicular to the alignment direction were noisy and exhibited a much lower magnetization, demonstrating the magnetic anisotropy of the composite material. Samples with randomly oriented Ni nanowires did not show any macroscopic magnetic anisotropy (Figure 4.4). Also, when spherical Ni nanoparticles formed chained clusters during photopolymerization under a magnetic field we did not detect any anisotropy since each individual particle can rotate to align its magnetization with the field (Figure 4.5). The magnetic anisotropy of the Ni nanowires was also confirmed by SQUID magnetometry with a rotating stage (Figure 4.6). This indicates that the shape of Ni nanowires is a critical structural feature responsible for the anisotropic magnetic properties of the Ni-hydrogel composites.

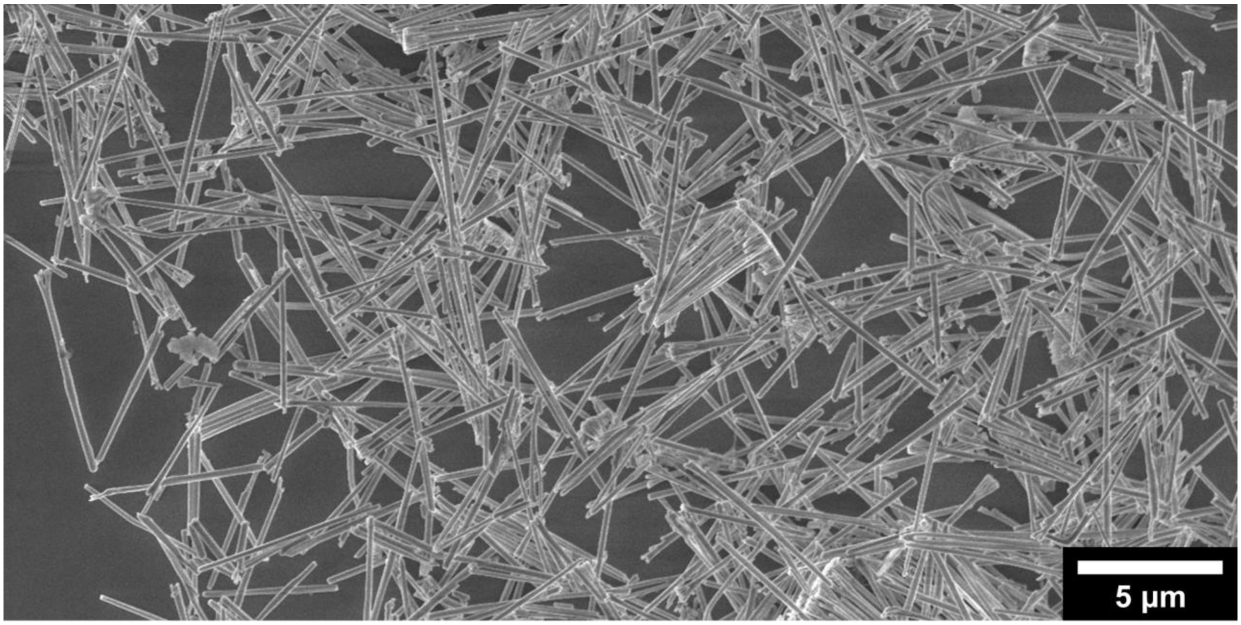

Figure 4.1 Scanning electron microscopy (SEM) image of Ni nanowires, 200 nm in diameter and 8-10 µm in length.

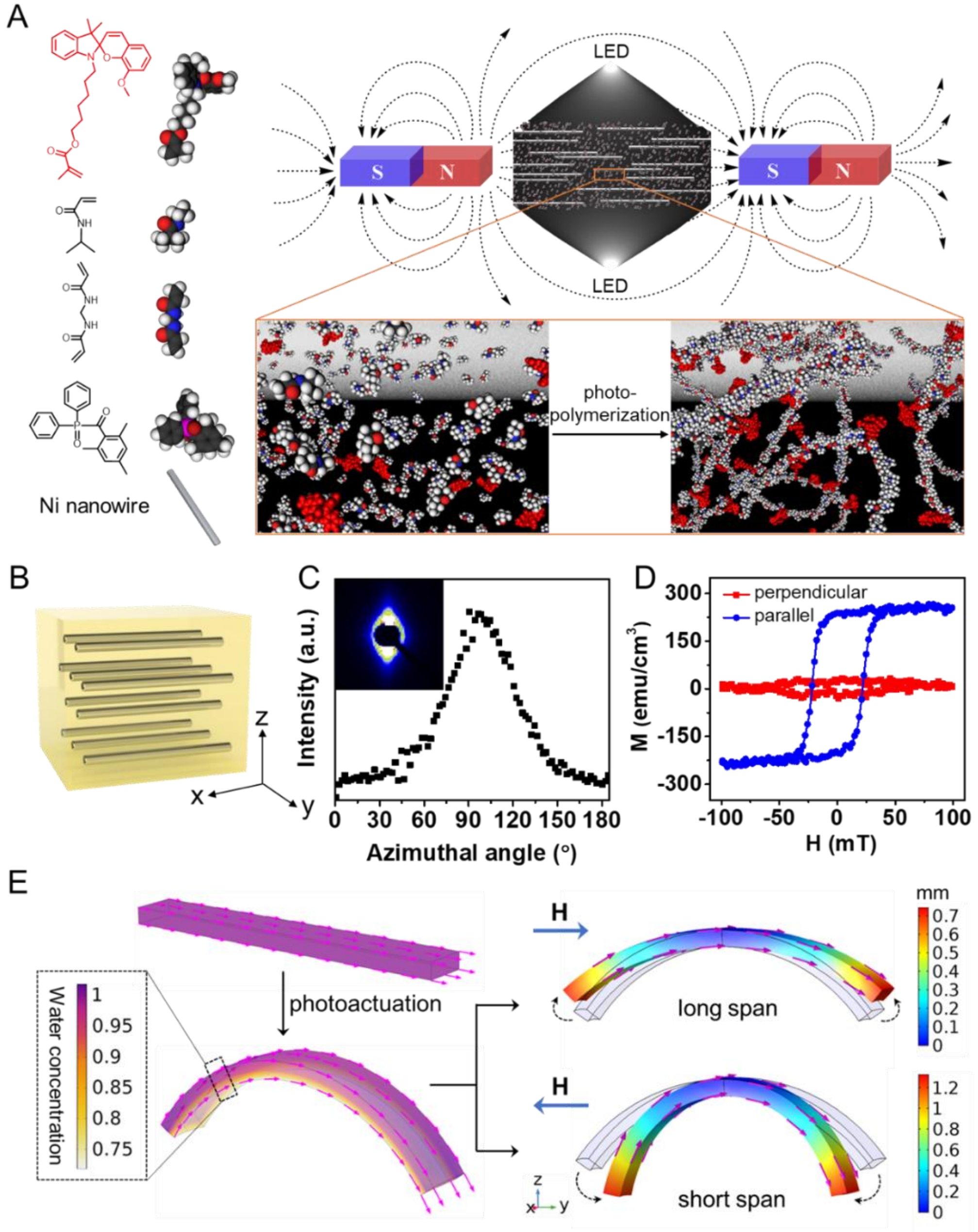

Figure 4.2 Hydrogels designed for coupled response to light and magnetic fields. (a) Schematic showing Ni nanowires aligned and fixed within a hydrogel network containing photoactive spiropyran moieties using a uniform magnetic field during free radical photopolymerization. (b) Schematic representation of aligned Ni nanowires (grey) immobilized in a hydrogel network (yellow). (c) Radial integration of 2D SAXS pattern revealing the macroscopic alignment of Ni nanowires within the hydrogel. (d) Magnetization loops parallel and perpendicular to the alignment axis of the nanowires. (e) Finite element calculation of the water concentration gradient and

deformation in a slab of hydrogel exposed to light (left); finite element calculation of deformation as a result of magnetic field exposure in a hydrogel slab previously bent by light (right). Magenta arrows denote the magnetization of Ni nanowires; blue arrows indicate the direction of the external magnetic fields; dashed arrows represent the movement of both ends after applying magnetic fields; rainbow surface colors represent the deformations relative to its initial configurations (shaded regions).

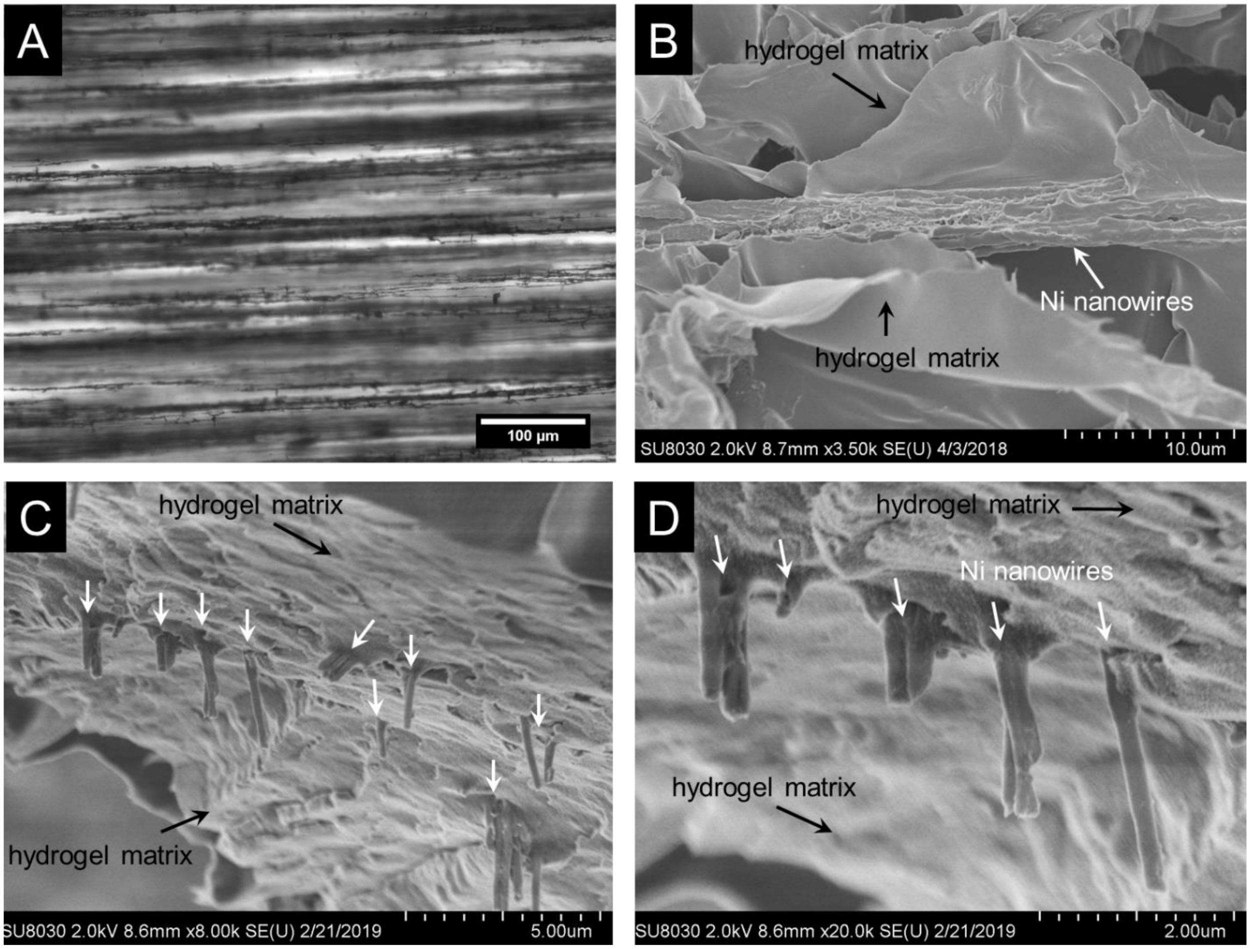

Figure 4.3 (a) Optical microscopy image of parallelly aligned Ni nanowires embedded in the hydrogel matrix by the free-radical photopolymerization. (b) Scanning electron microscopy (SEM) image of aligned Ni nanowires embedded in the hydrogel matrix after the hydrogel was lyophilized. (c) and (d) cross-section SEM images of lyophilized hydrogel thin film with different amplifications with aligned Ni nanowires embedded inside. White arrows indicate the aligned Ni nanowires embedded in the hydrogel matrix. Black arrows indicate the hydrogel matrix.

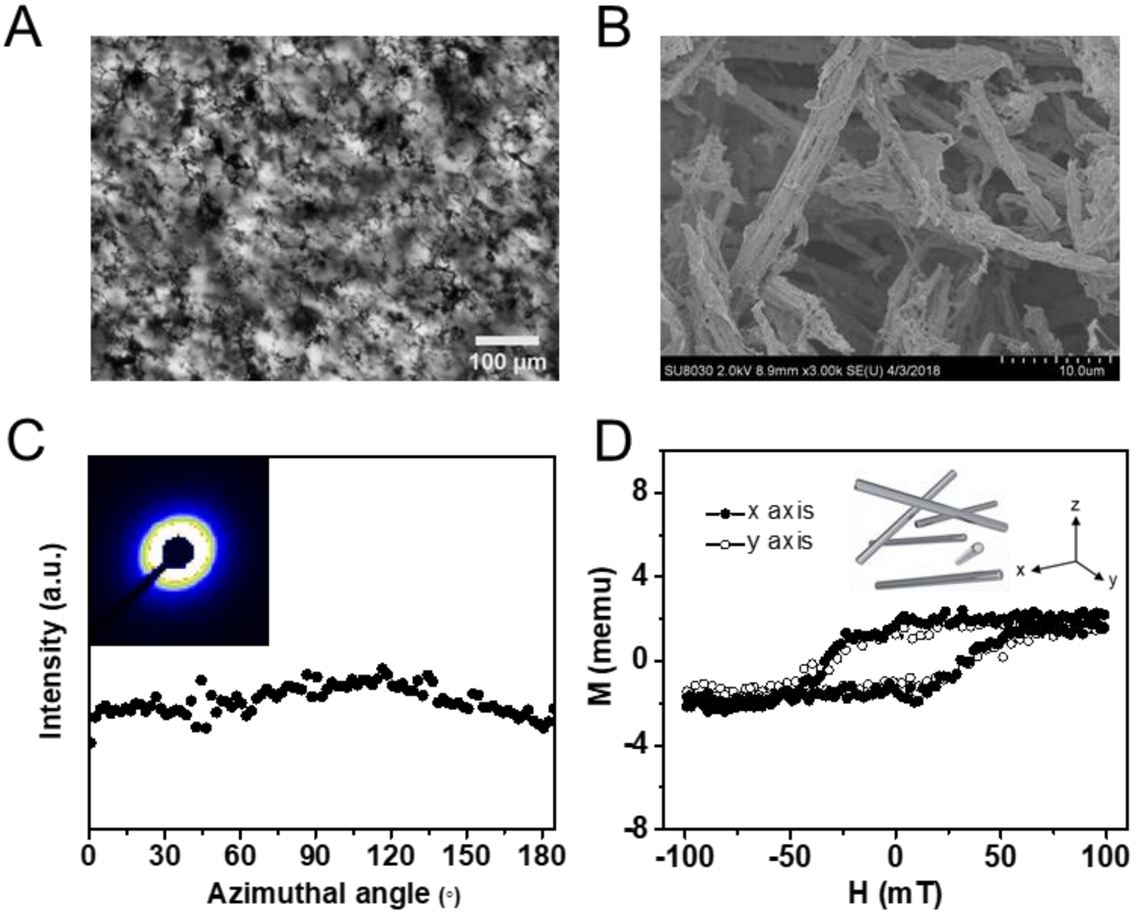

Figure 4.4 (a) Optical microscopy image of non-aligned Ni nanowires embedded in the hydrogel matrix by the free-radical photopolymerization. (b) Scanning electron microscopy (SEM) image of non-aligned Ni nanowires embedded in the hydrogel matrix after the hydrogel was lyophilized. (c) Radial integration of 2D SAXS pattern (inset) of non-aligned Ni nanowires within the hydrogel. (d) Magnetization loops of random oriented Ni nanowires (0.25 mg) did not show any magnetic anisotropy. Inset, schematic representation of randomly oriented Ni nanowires.

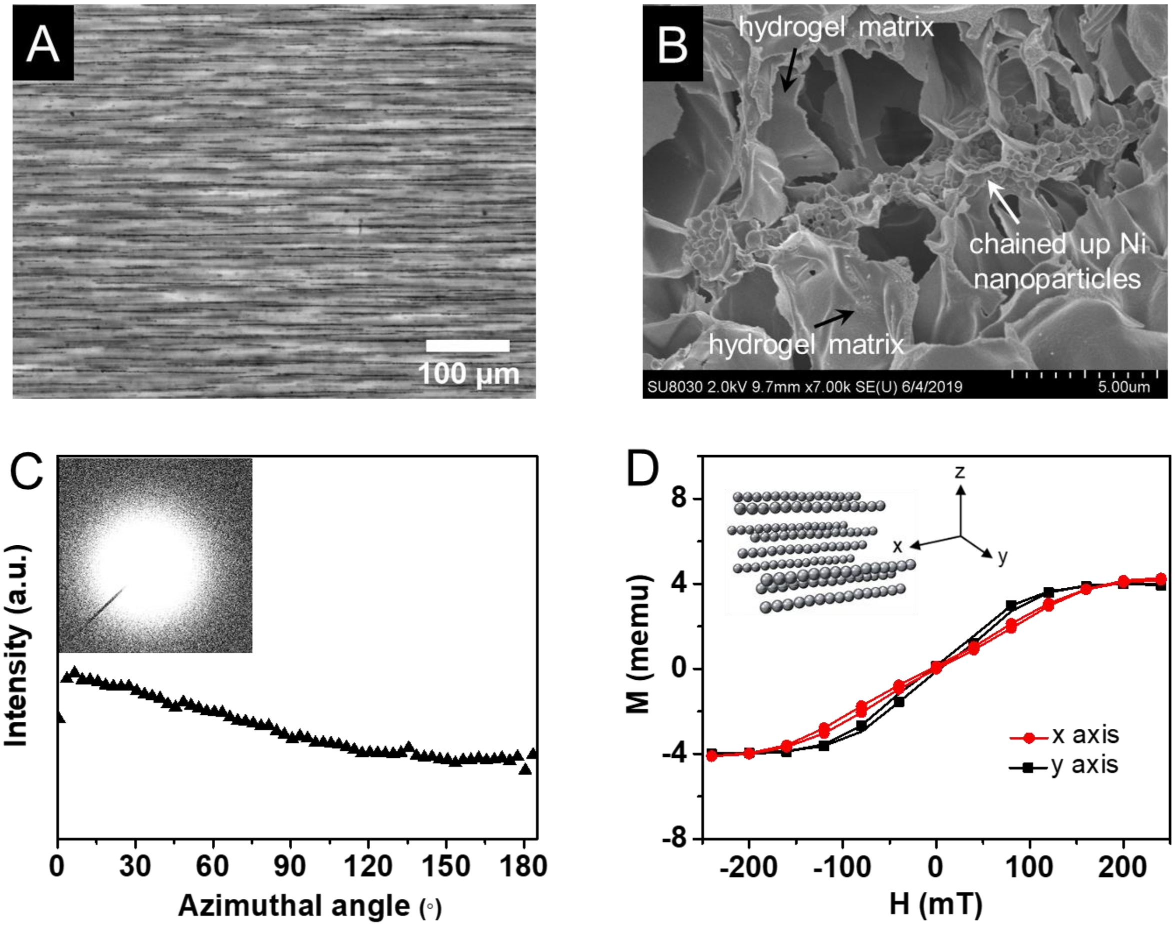

Figure 4.5 (a) Optical microscopy image of chained up Ni nanoparticles embedded in the hydrogel matrix by the free-radical photopolymerization. (b) Scanning electron microscopy (SEM) image of chained up Ni nanoparticles embedded in the hydrogel matrix after the hydrogel was lyophilized. (c) Radial integration of 2D SAXS pattern (inset) of chained Ni nanoparticles within the hydrogel. (d) Magnetization loops of chained up Ni nanoparticles (0.25 mg) did not show any magnetic anisotropy. Inset, schematic representation of chained up Ni nanoparticles.

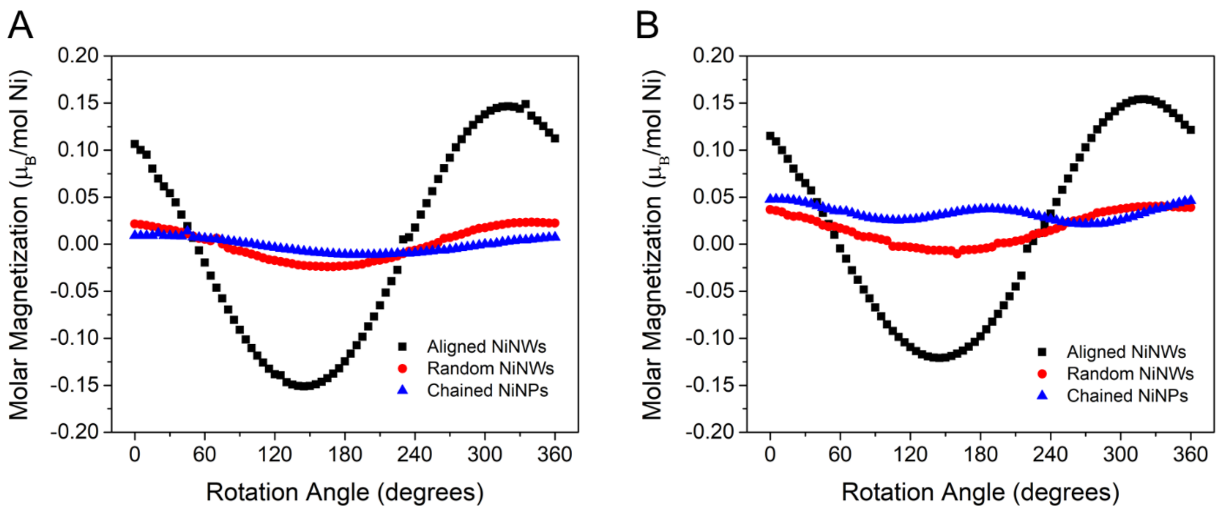

Figure 4.6 SQUID measurement of molar magnetization at 300 K under 0 Oe of magnetic field (a) and 160 Oe of magnetic field (b) with a rotating stage for random Ni nanowires (black), aligned Ni nanowires (red) and chains of aligned Ni nanoparticles (blue).

The fundamental mechanism of deformation under the action of light in the materials investigated is rooted in the creation of a spatial gradient in the population of hydrophilic and hydrophobic moieties within the hydrogel (MCH^+ versus SP segments). This should result in the decrease of water concentration within the material as a function of increasing SP unit density, which in turn leads to a mechanical deformation. A phenomenological model[144] has been developed to describe such photoinduced hydrophobicity in gels with an additional contribution to the free energy proportional to $r_{sp}(1-\phi)$, where ϕ is the monomer volume fraction and r_{sp} is the fraction of chromophores in the SP configuration. Here we derived the additional contribution to be $\alpha\phi(1-\phi)$, where α is given by

$$\alpha = \frac{zf}{k_B T}(u_{sw} - u_{mw})r_{sp}$$

where u_{sw} and u_{mw} are the interaction energies of the SP and MCH$^+$ moieties with water, respectively, z is the coordination number of the lattice, and f is the fraction of monomers containing a chromophore. Moreover, r_{sp} is described by the kinetics of the chemical reaction, $MCH^+ \leftrightarrow SP$ and can be calculated by computing the light intensity as a function of the spatial coordinates of the hydrogel objects (see Section 4.5.8 for details). Figure 4.2e (left) shows the calculated water concentration gradient within a hydrogel slab using this methodology and the resultant deformation. The deformed geometry leads to a nonuniform 3D magnetization profile (indicated by the magenta arrows), enabling the control of the arch-shaped hydrogel by an external magnetic field $\mathbf{H}$. Thus, the span of the arch-shaped hydrogel can be increased or decreased by simply applying a static magnetic field parallel or anti-parallel to the nanowires' alignment direction (Figure 4.2e, right). To quantitatively characterize deformations of the hydrogel, we developed a continuum model of fiber-reinforced magnetoelastic materials. An external magnetic field induces local torques since Ni nanowires prefer to align with the field. Given that the nanowires are immobilized by the hydrogel, these magnetic torques transmit stresses that collectively result in macroscopic deformation of the material. Since the interaction between the field and magnetized material is orientation dependent, strain tensors are not enough to fully describe the state of the system. Instead, we used here the deformation gradient tensor $\boldsymbol{F}$, which takes into account the rotational deformation to develop a free energy density function of fiber-reinforced magnetoelastic materials, W, given by,

$$W = \frac{1}{2}\mu(\overline{I_1} - 3) + \frac{1}{2}\mu\gamma(\overline{I_4} - 1)^2 + \frac{\kappa}{2}(J - 1)^2 - (\boldsymbol{FM}) \cdot \boldsymbol{B}$$

where μ and κ are the shear and bulk modulus, respectively; γ is a stiffness parameter resulting from mechanical reinforcement by the aligned nanowires[145]; $J = \det\boldsymbol{F}$ characterizes volumetric changes with respect to the initial state; $\overline{I_1}$ describes shape changes and $\overline{I_4}$ describes the deformation along the direction of nanowires; $\boldsymbol{B}$ is the magnetic flux density; and $\boldsymbol{M}$ is the magnetization field in the reference configuration (see Section 4.5.9 for details). In this model, the nickel nanowires move with the hydrogel without slipping and the higher order energy contributions in $\boldsymbol{B}$ to the free energy density W are ignored[41]. This continuum model was solved using finite element methods that provide a quantitative analysis for the dynamic behavior of the hydrogels in magnetic fields.

To develop robotic functions, we prepared cross-shaped hydrogel films containing aligned Ni nanowires (Figure 4.7a). After light irradiation, the flat sample bends up as an object with two walking legs (w1, w2) and two stabilizing arms (s1, s2) (Figure 4.7b). The alignment of the wires within the object creates an anisotropic mechanical response and therefore the span between w1 and w2 (see front view) is larger than that between s1 and s2 (see side view). We calculated photoactuation of these samples using the model described before and generated the green wireframes shown in Figure 4.7b. There is clear agreement between the calculated and actual light-induced deformation observed in photographs of the hydrogels. It is therefore possible to exploit this mechanical anisotropy (Figure 4.8) caused by the aligned Ni nanowires to modulate photoactuation in hydrogel samples with simple geometries such as squares (Figure 4.9). We found that when the hybrid hydrogel-metal hybrids are illuminated and bent by the light, a 3D magnetization profile is established that enables walking under the influence of an external rotating magnetic field (Figure 4.7c, Video 4.1). As a control, samples containing unaligned Ni nanowires or aligned chains of Ni nanoparticles exhibited minimal movement under the same magnetic field and were not capable of walking (Figure 4.10). The average magnetization (purple arrow) and the external magnetic field (blue arrow) lie within the y-z plane and the magnetic torque density is given by $\boldsymbol{\tau_m} = \mathbf{FM}/\mathrm{J} \times \boldsymbol{B}$. Therefore, only the x-component of the magnetic torque is a nonzero quantity. The rotating magnetic field in the y-z plane generates an oscillatory x-component of the magnetic torque that causes the objects to rotate alternately clockwise and counterclockwise around the x-axis (perpendicular to the walking direction) (Figure 4.7d). Because of the combination of magnetic torque and gravity, the object lands on its front and back legs in alternating fashion (Figure 4.7c). Our model assumes friction between the legs and the floor is large enough to avoid slippage during walking (see Section 4.5.10.2 for details). Magnetoelastic coupling results in a periodic change in the hydrogel's leg span (distance between w1 and w2) (Figure 4.7d,e), which enables the net displacement of the hydrogel along the y-axis. Furthermore, longer side arms were found to be important in stabilizing the hydrogel's movement and optimizing its lift during walking (Video 4.2**,** Figure 4.11). Also, the walking speed was found to be faster with higher frequencies (0.3–0.7 Hz) or stronger magnetic fields (115–160 Oe) (Figure 4.7f, Video 4.3). With a fixed frequency and field strength, it was possible to achieve walking over macroscopic distances (Figure 4.7g) and reduction of the hydrogels to millimeter size scales did not change the mechanism of motion (Video 4.4). Finally, we found that the objects did not only walk on a flat plane but can also climb inclined surfaces (see Section 4.5.11, Video 4.5, Figure 4.12).

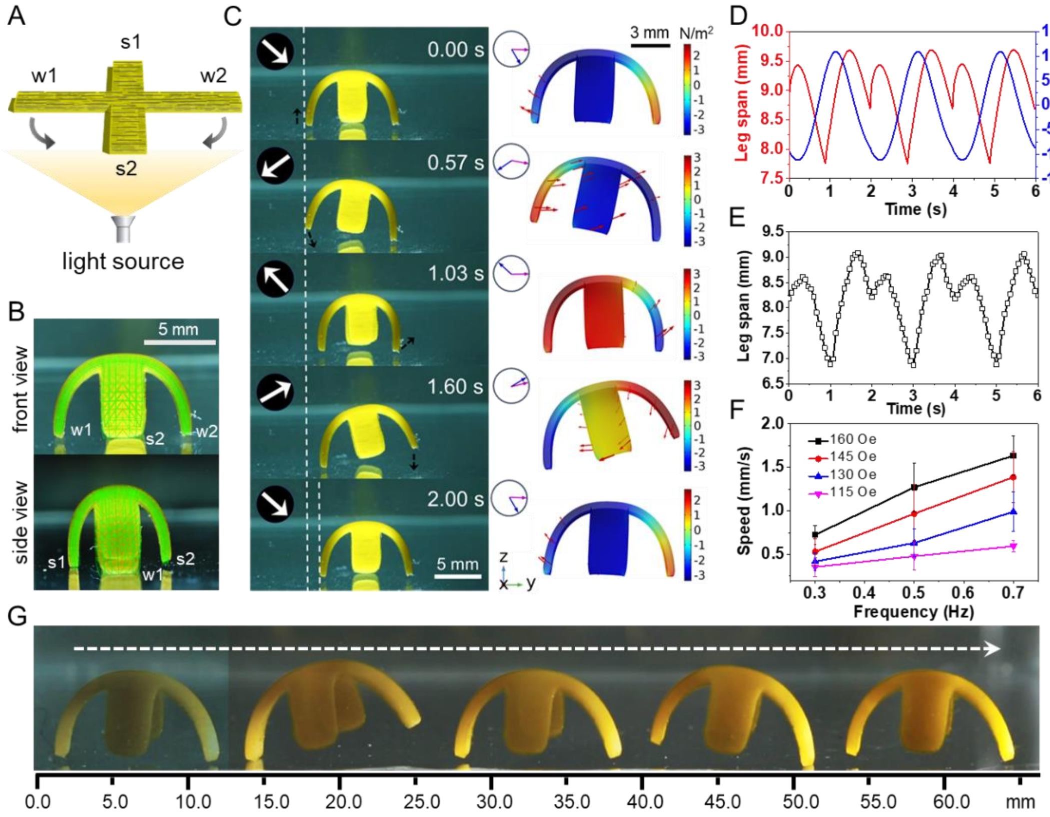

Figure 4.7 Light triggered walking under rotating magnetic fields. (a) Schematic of a cross-shaped hydrogel film containing aligned Ni nanowires irradiated from below. (b) Photographs of the bent hydrogels (front and side views) superimposed with green wireframe representations of the calculated photoactuation using a finite element method. (c) (Left) Photographs of the hydrogel walking from left to right for one cycle (white arrows indicate direction of the magnetic fields). (Right) Calculated snapshots from a finite element simulation of the walking motion (color scale used on the object's surface represents the x-component of the magnetic torque density). Red arrows indicate the instantaneous velocity field, blue arrows indicate the direction of the external magnetic field, and magenta arrows indicate the direction of the average magnetization. (d) Plot of the x-component of the magnetic torque (blue) and leg span (red) obtained from the simulation. (e) Plot of the experimental leg span of samples as a function of time over multiple walking cycles. (f) Plot of the walking speed of samples as a function of rotating frequency at various magnetic field strengths. (g) Time-lapsed photographs of hydrogel walking (collected every four cycles, ~8.3 s) over macroscopic distances under a rotating magnetic field (145 Oe, 0.7 Hz).

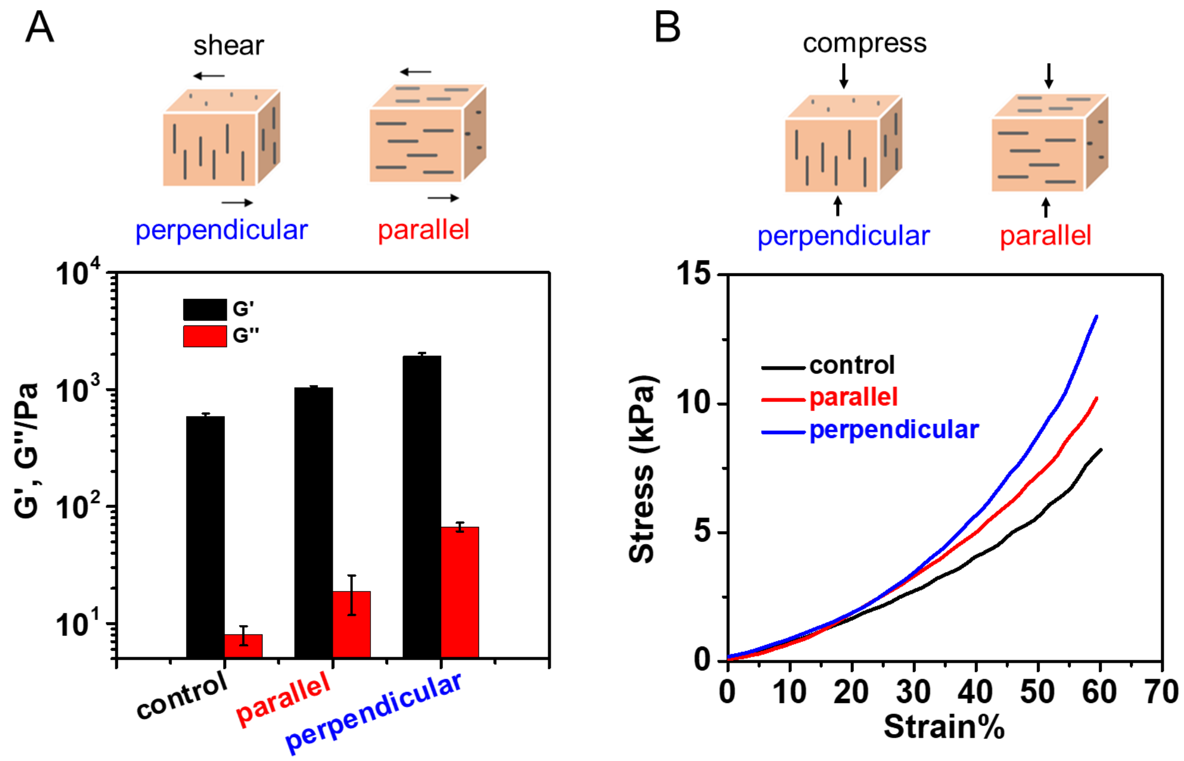

Figure 4.8 Characterization of mechanical properties for hydrogel film samples with Ni nanowires (0.5 wt%) aligned parallel or perpendicular to the plane of the films. Control sample is hydrogel without Ni nanowires. (a) Rheological experiments were performed on parallel and perpendicular samples at a fixed angular frequency of 10 rad/s and strain of 1%, respectively, at 25 ºC. (b) Stress–strain curves were obtained using dynamic mechanical analysis. Samples were tested in 8 mm parallel-plate geometry using compression mold with a compression rate of 0.48 mm/min.

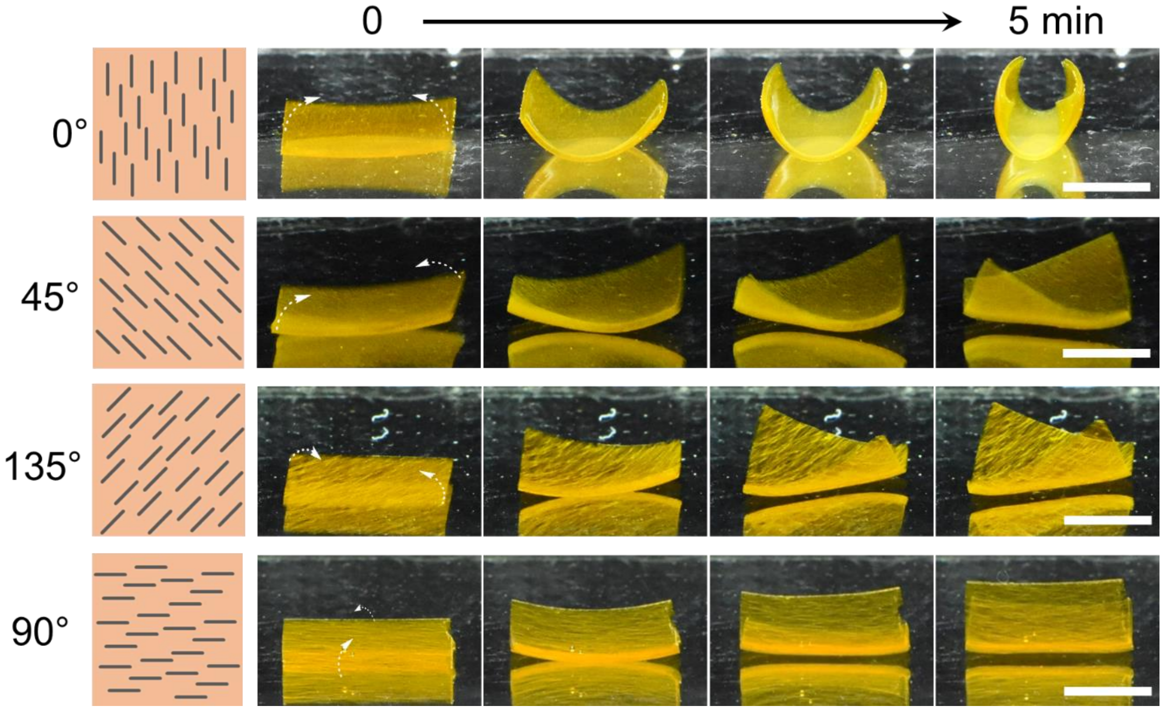

Figure 4.9 Light-induced bending directions of the hydrogel squares (10×10×0.5 mm, L×W×T) containing aligned Ni nanowires (0.5 wt%) were affected by the mechanical anisotropy caused by the aligned Ni nanowires. Scale bar is 5 mm.

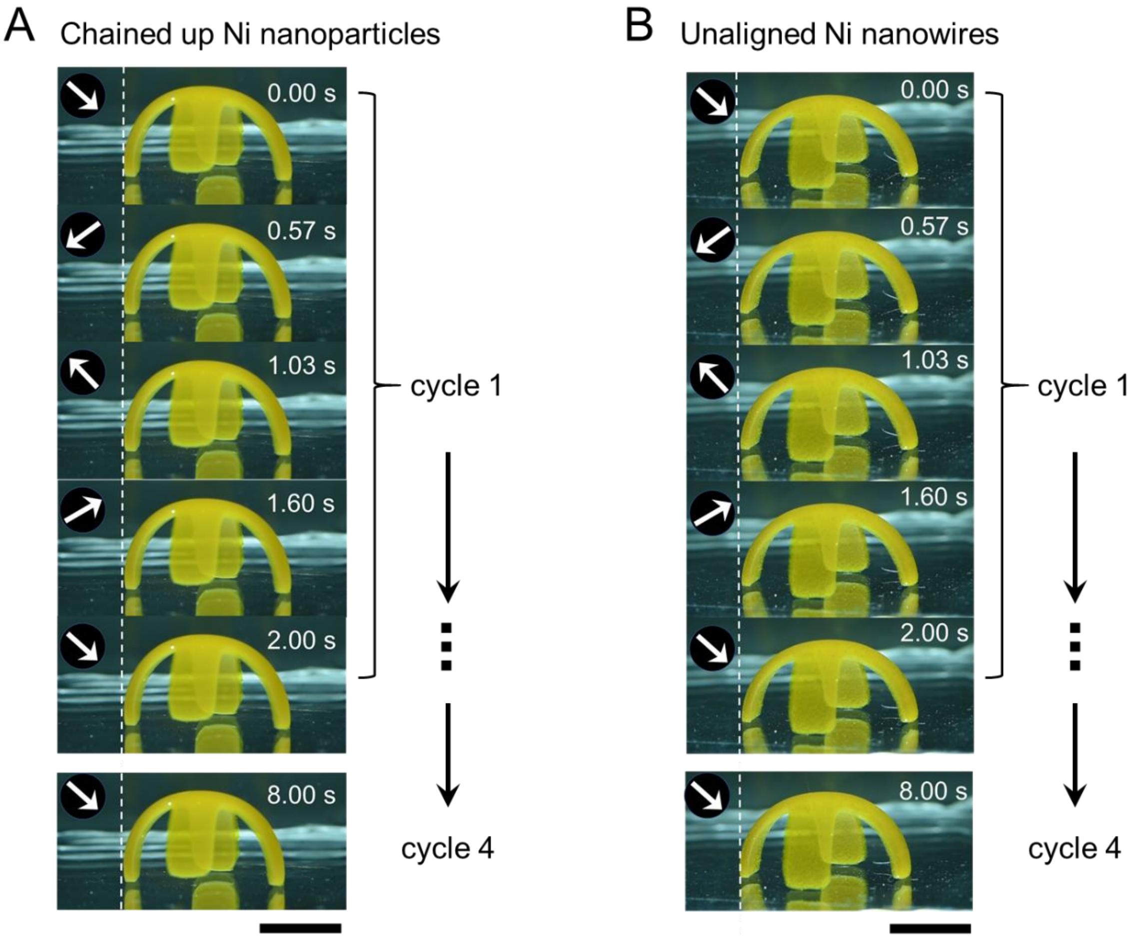

Figure 4.10 (a) Photographs of the hydrogel objects containing aligned chains of Ni nanoparticles (diameter 200 nm, 0.5 wt%) exhibited minimal movement under the same magnetic field for multiple cycles and were not capable of walking. (b) Photographs of the hydrogel objects containing unaligned Ni nanowires (diameter 200 nm, 0.5 wt%) exhibited minimal movement under the same magnetic field for multiple cycles and were not capable of walking. White arrows indicate direction of the magnetic fields. Scale bars are 5 mm.

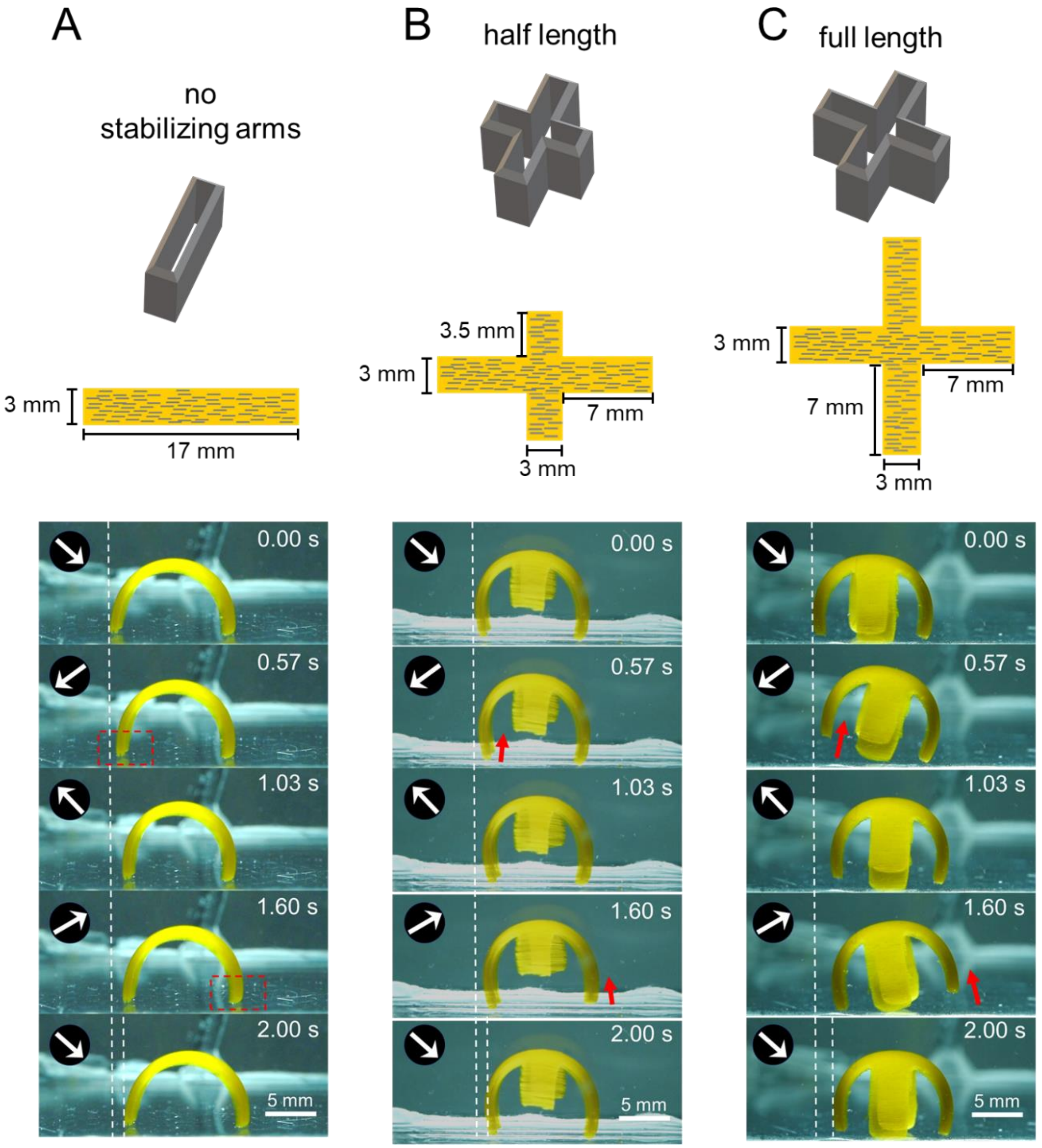

Figure 4.11 Optimization of the length of stabilizing arms. (a) Photographs of the hydrogel objects containing aligned chains of Ni nanowires without stabilizing arms exhibited no lifting of the walking legs during the motion. The legs are dragging on the floor by the magnetic field. Red rectangles indicate no lifting was observed during walking. (b) Photographs of the hydrogel objects containing aligned chains of Ni nanowires with half length of the stabilizing arms exhibited small lifting of the walking legs during the motion. Red arrows indicate the lift of walking legs. (c) Photographs of the hydrogel objects containing aligned chains of Ni nanowires with full length of the stabilizing arms exhibited big lifting of the walking legs during the motion. Red arrows indicate the lift of walking legs.

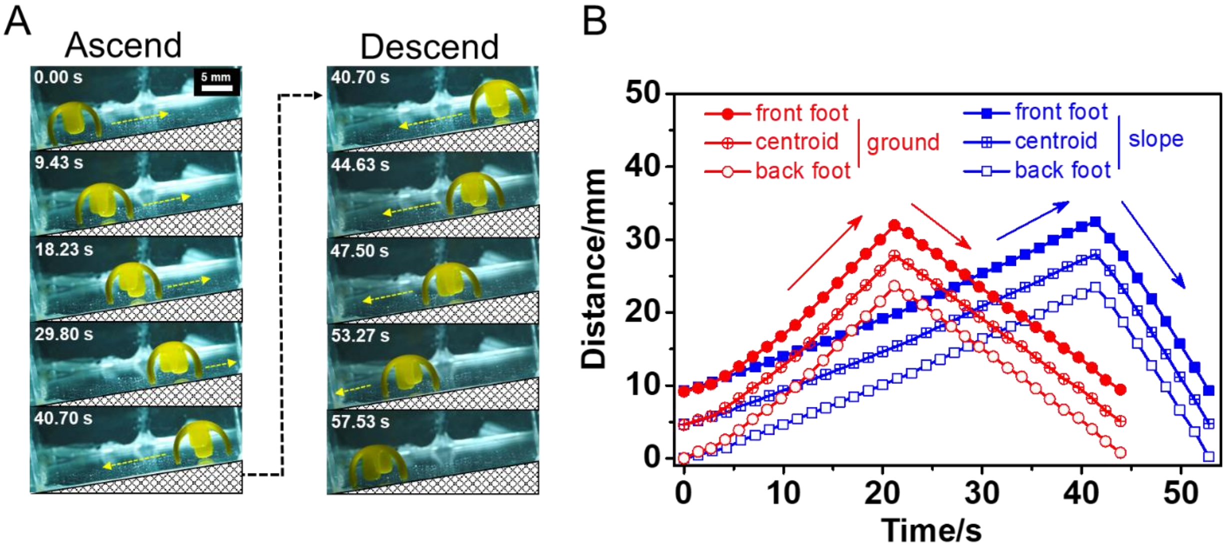

Figure 4.12 Hydrogel object containing SP1 moiety walks on a glass surface with an inclined angle of 9° under a magnetic field rotating in y-z plane. (a) Ascend (left) and descend (right) process. (b) Plotting of front and front feet, centroid vs time walking on an inclined surface (blue) and a flat surface (red).

The hybrid hydrogels can also achieve steering motion in arbitrary directions while walking by controlling the applied magnetic field to produce an additional torque in the z direction (i.e. normal to the walking plane). Using simulations we predicted that the objects could turn 90° in 30° increments (Figure 4.13a, Video 4.6) by programming the applied field in the x, y, and z directions to achieve the required torque (Figure 4.13b,c). The predicted motion using simulations was in fact observed experimentally as shown in Figure 4.13a. Figure 4.13d shows a designed arbitrary path with multiple turns and Figure 4.13e its corresponding experimental realization (Video 4.7). We therefore conclude that the experimental samples of these materials can have robotic functions, which in this case involve following continuous paths over macroscopic distances.

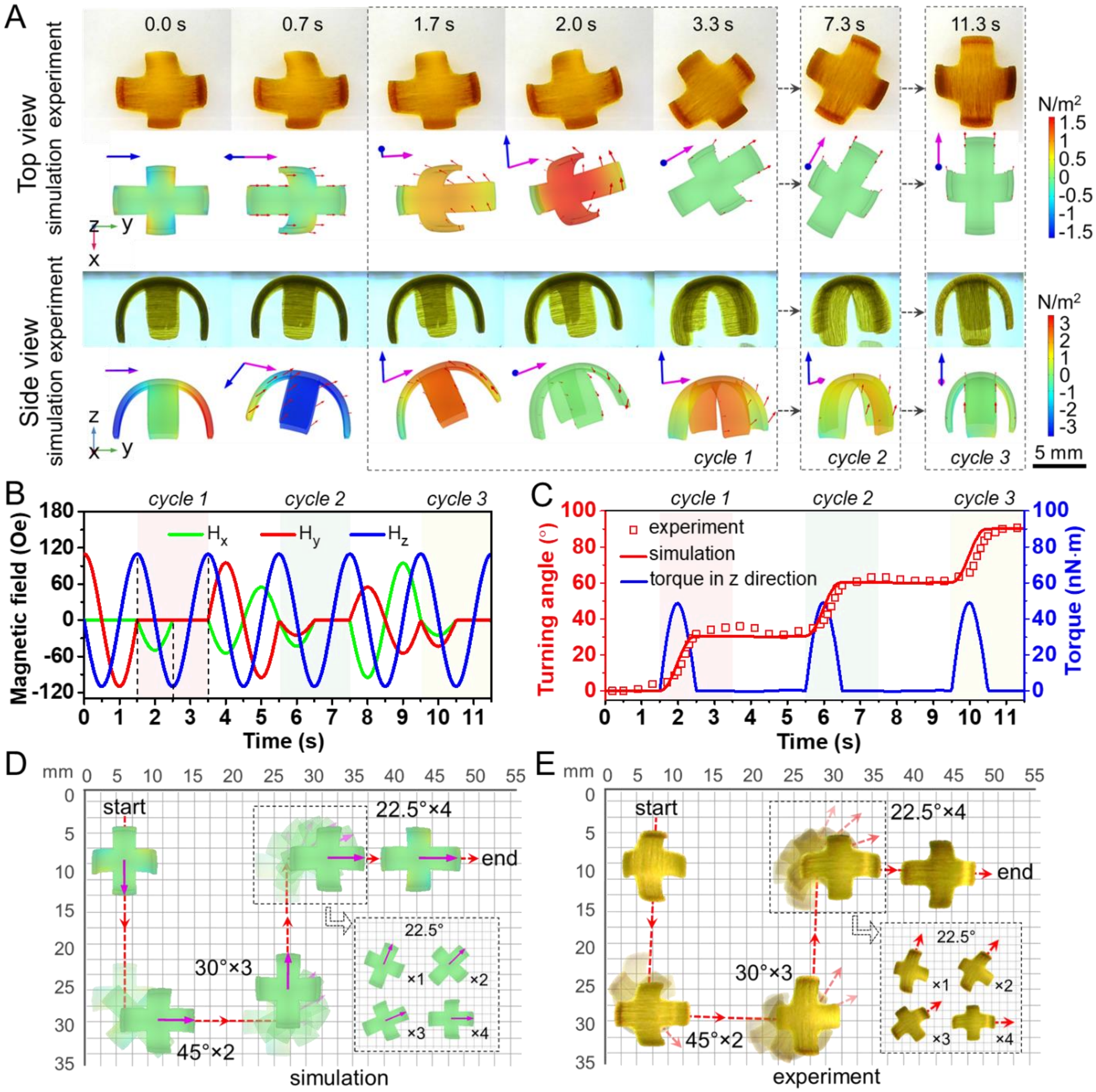

Figure 4.13 . Steering motion and path followed by samples under rotating magnetic fields. (a) Snapshots of three periods of steering motion from both experiment and simulation shown in the top view (top) and side view (bottom). Red arrows depict the instantaneous velocity field, blue arrows depict the direction of external rotating magnetic fields, purple arrows depict the direction of the average magnetization and surface colors represent the z- and x-components of the magnetic torque density in the top and side views, respectively. (b) The x, y and z components of the external rotating magnetic fields as functions of time. (c) Turning angle of the hydrogel robot from the experiment (red square) and the simulation (red line) and the z component of the total magnetic

torque (blue line). Arbitrary path of the hydrogel from simulations (d) and experiment (e). The surface colors represent the z-component of the magnetic torque density; dashed red line indicates the motion trajectory; magenta arrows indicate the direction of the average magnetization. Insets show a 90° turn in four 22.5° increments.

To develop more complex robotic functions, we synthesized hydrogels with different molecular photoswitches (see Section 4.5.3 for synthetic details) to tune the kinetics of photoactuation. Hydrogels made of SP1 can maintain their bending curvature under variable light intensities (96-190 mW/cm^2) through the duration of our experiments (Figure 4.14a), confirmed by the change of leg span (Figure 4.14c, black). We also synthesized a photoswitch (SP2) that could be covalently incorporated in the polymeric network, which lacks the methoxy group and displays faster photoisomerization to the ring closed form (Figure 4.15 and Figure 4.16). The hydrogel component of the hybrid samples made of SP2 bend and then flatten in response to relatively low light intensities (23.5-33.0 mW/cm^2) (Figure 4.14b,c , red), since the light destroys the gradient of hydrophobicity in the material. Therefore, a permanent walker made of SP1 walks with a constant speed while a transient walker made of SP2 gradually loses its walking ability with continuous irradiation (Figure 4.14d**,** Figure 4.17**,** Video 4.8). The walking speed can be controlled by programmed sequences of light intensity. As shown in Figure 4.14e,f, samples containing SP1 hydrogel were found to bend and walk faster as the light intensity increases. We also demonstrate the use of localized light to selectively accelerate walking along a path, allowing another avenue for adaptive response to the surrounding environment (Video 4.8). This permanent walker gradually stops walking when light is turned off (Figure 4.18). However, increasing the light intensity did not cause samples containing SP2 to walk faster, but instead accelerated the flattening of the bent sample (Figure 4.19). We also found that we can create objects with different walking modes by controlling the alignment direction of the nanowires during preparation of the Ni-hydrogel composites (Figure 4.20, Figure 4.21 and Video 4.9).

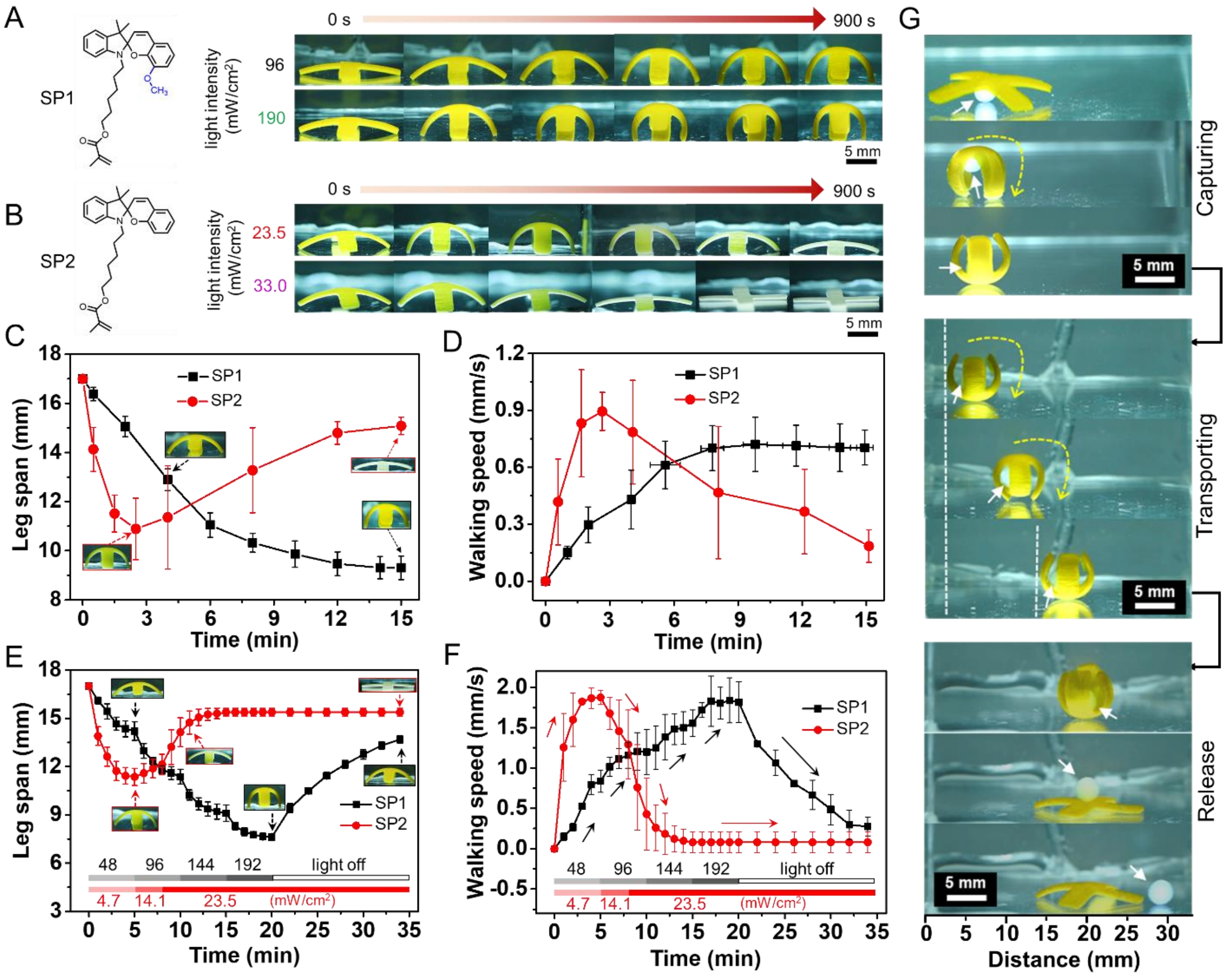

Figure 4.14 Chemical design and bimodal control of the hydrogel robots. (a, b) Molecular structures of SP1 and SP2 and snapshots of the corresponding hydrogel robots under constant light irradiation over 900 s. (c) Leg span and (d) walking speed under irradiation with 96 mW/cm^2 for SP1 and 23.5 mW/cm^2 SP2. (e, f) Variable light intensity applied over 2100 s to program leg span and walking speed, respectively. (g) Alginate bead captured underneath a flat walker upon irradiation with strong white light from below, transported by rolling under magnetic fields and released by irradiation to invert the sample curvature.

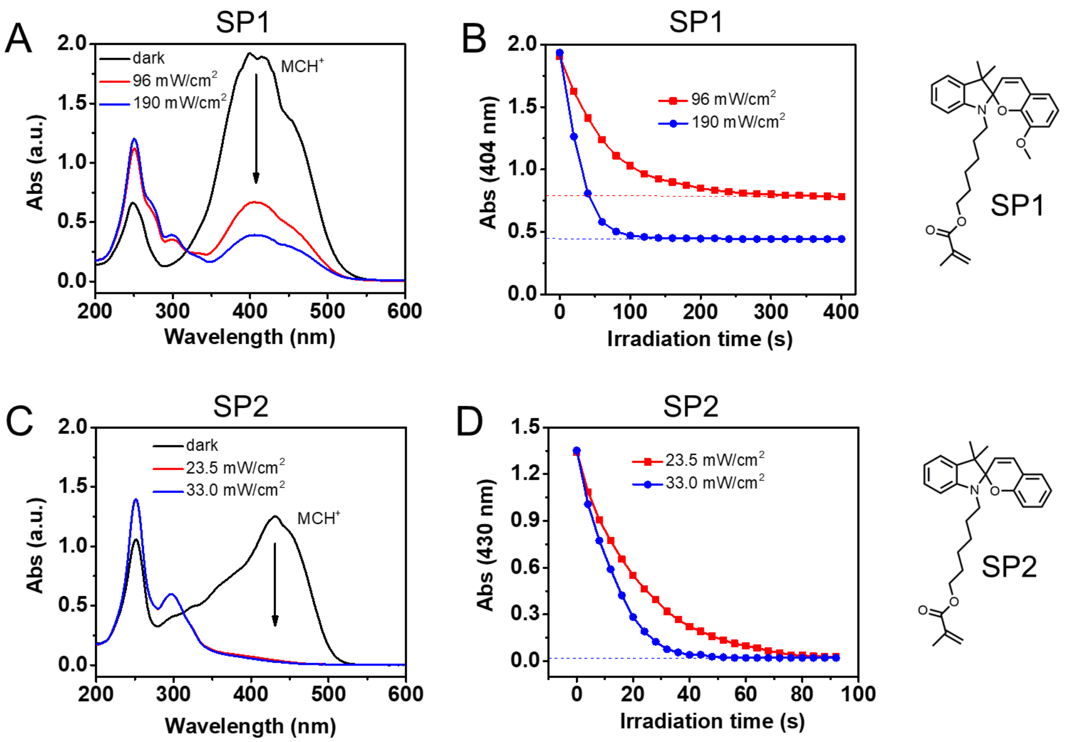

Figure 4.15 (a) Absorbance spectra of SP1 (0.1 mM) in the dark (black), after irradiation white light for 30 min with an intensity of 96 mW/cm^2 (red) and 190 mW/cm^2 (blue). (b) Plotting of the absorbance at 404 nm for SP1 vs light irradiation time. The absorbance reached equilibrium state at 0.78 and 0.44 under irradiation of 96 and 190 mW/cm^2, respectively. (c) Absorbance spectra of SP2 (0.1 mM) in the dark (black), after irradiation white light for 30 min with an intensity of 23.5 mW/cm^2 (red) and 33.0 mW/cm^2 (blue). (d) Plotting of the absorbance at 430 nm for SP2 vs light irradiation time. The absorbance both became 0 under irradiation of 23.5 and 33.0 mW/cm^2, respectively.

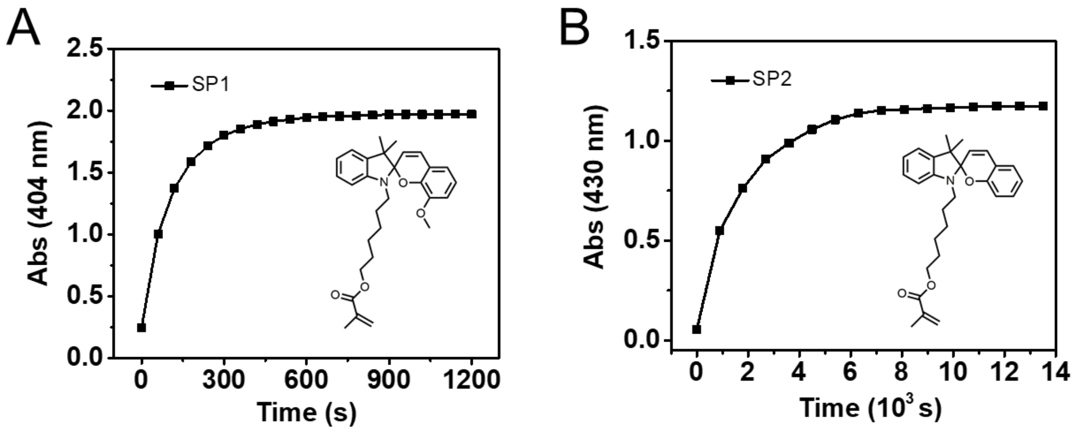

Figure 4.16 Simultaneously ring-opening process of SP1 (a) and SP2 (b) in the dark in a mixture solvent of dioxane/water (4:1, v/v) containing 5 mM of HCl after light irradiation for 30 min (190, 33.0 mW/cm^2 for SP1 and SP2, respectively).

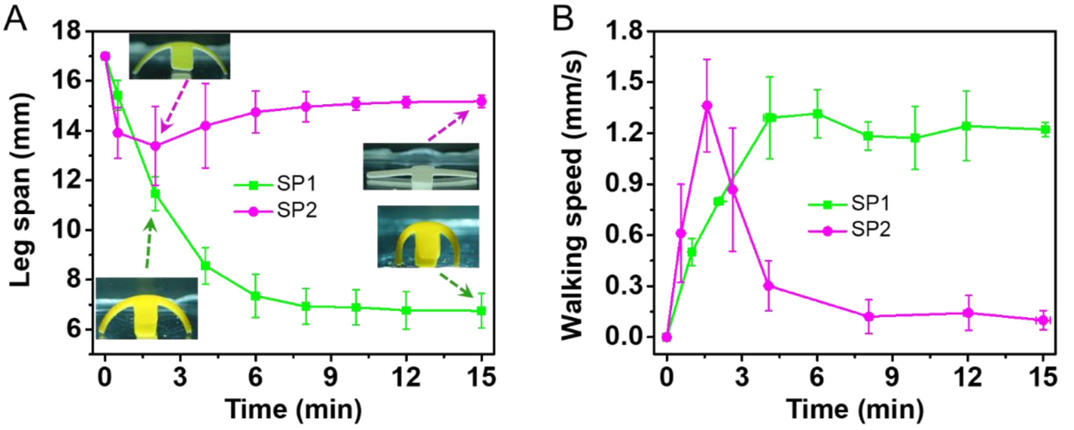

Figure 4.17 (a) Leg span and (b) walking speed under irradiation with 190 mW/cm^2 for SP1 (green) and 33.0 mW/cm^2 SP2 (magenta).

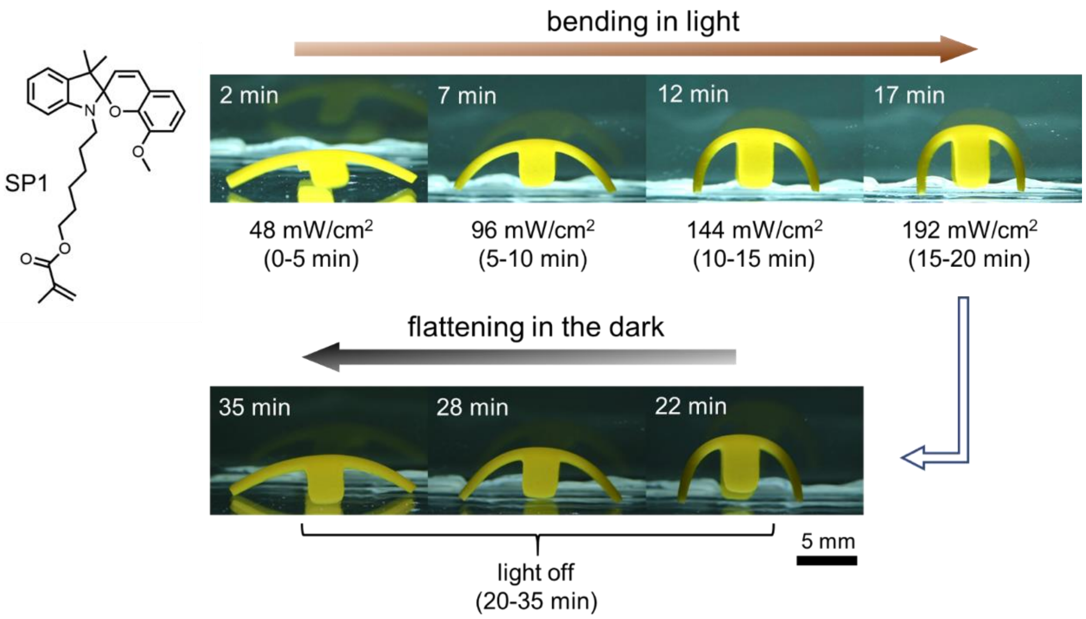

Figure 4.18 Hydrogel objects containing SP1 moiety bend up gradually controlled by programmed sequences of light intensity (48-192 mW/cm^2) irradiating from the bottom and flatten when light is off.

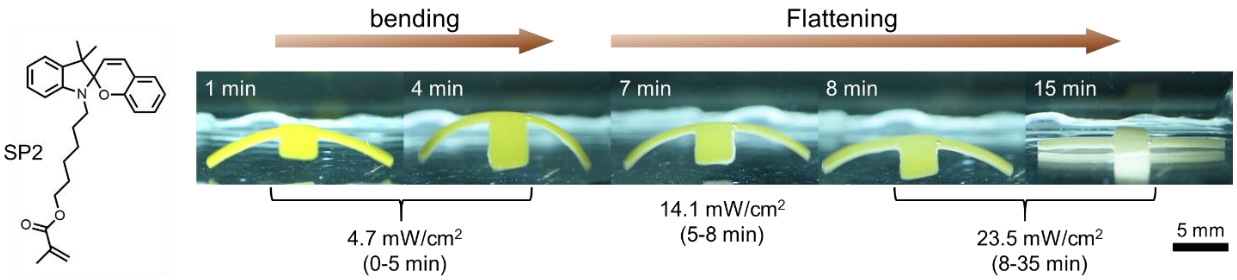

Figure 4.19 Hydrogel objects containing SP2 moiety bend up in 5 min when irradiating with a bottom light (4.7 mW/cm^2) and gradually flatten when irradiating with stronger light (14.1, 23.5 mW/cm^2) due to the elimination of hydrophobicity gradient.

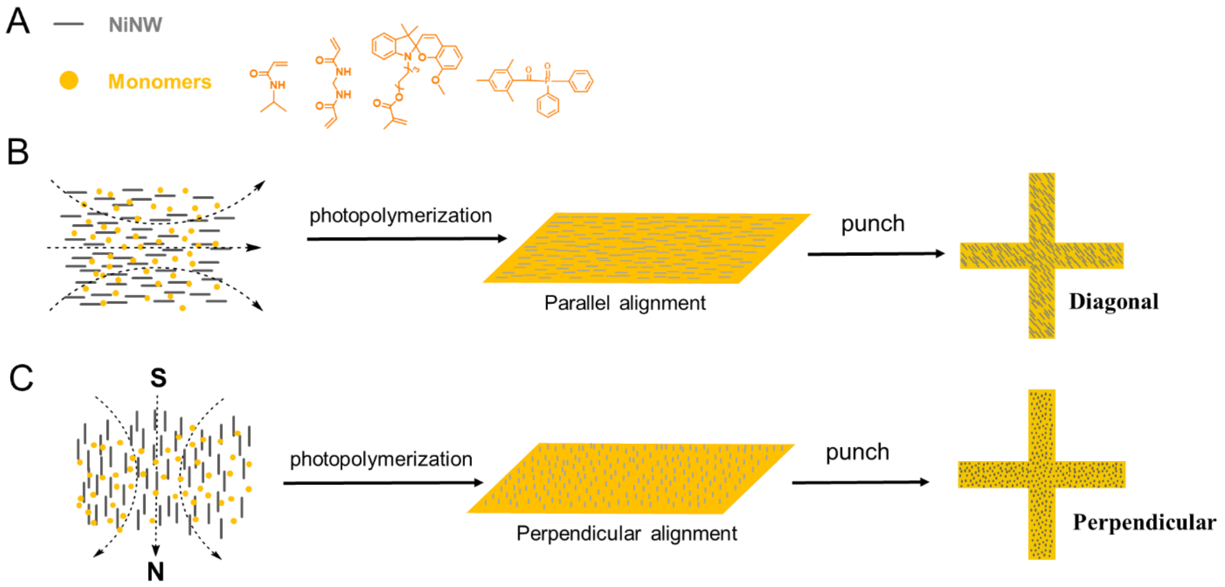

Figure 4.20 Preparation of hydrogel objects with different alignment directions. (a) Molecular structures used for free-radical photopolymerization. (b) Preparation of cross-shaped hydrogel objects with diagonal alignment of Ni nanowires. (c) Preparation of cross-shaped hydrogel objects with perpendicular alignment of Ni nanowires.

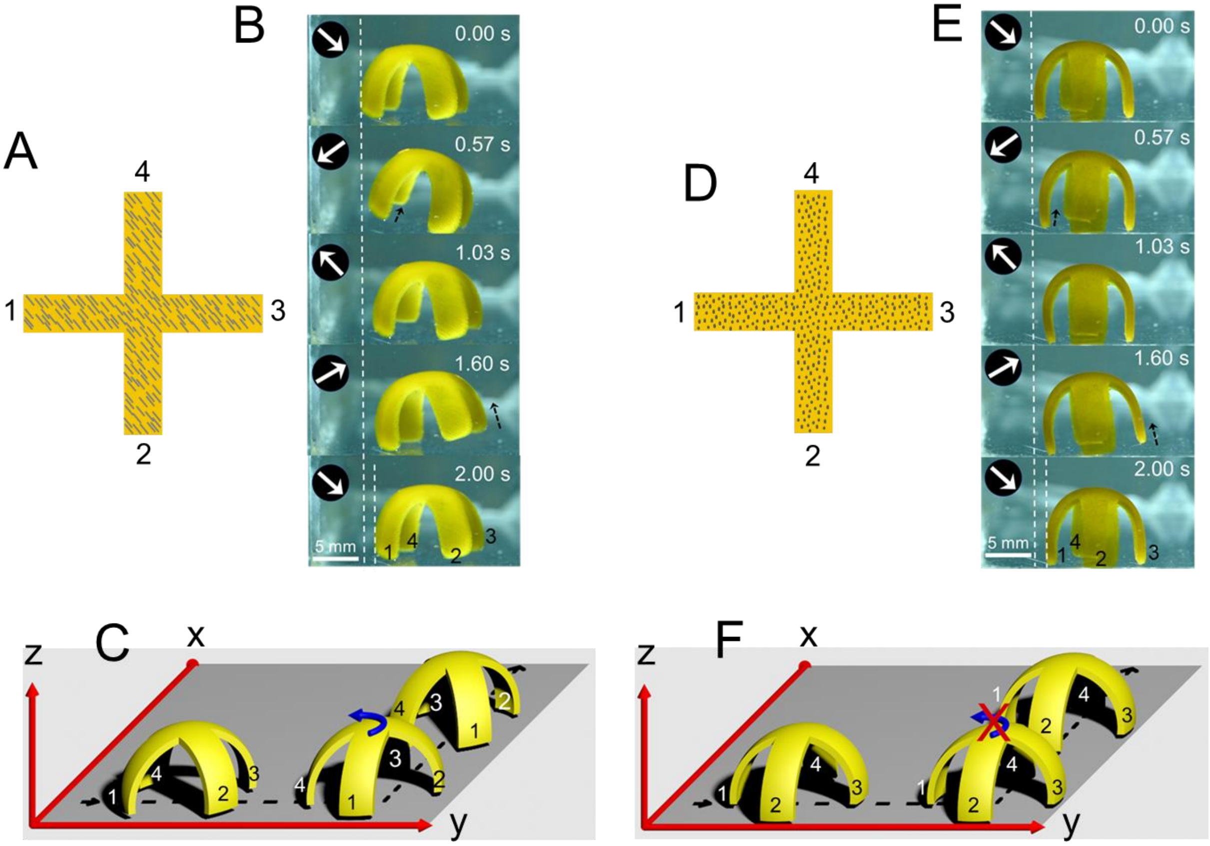

Figure 4.21 (a) Schematic representation of a diagonal cross-shaped hydrogel object (top view). (b) Photographs of the diagonal hydrogel object with bottom light induced bending geometry walking from left to right for one cycle by lifting two legs simultaneously (1, 4) or (2, 3). White arrows indicate direction of the magnetic fields. Black arrows indicate the lifting of legs. (c) The diagonal hydrogel object rotates its body 90° counterclockwise for turning when the rotation direction of magnetic fields changes from y-z plane to x-z plane. (d) Schematic representation of a perpendicular cross-shaped hydrogel object (top view). (e) Photographs of the perpendicular hydrogel object with bottom light induced bending geometry walking from left to right for one cycle by lifting leg 1 or 3 alternately. White arrows indicate direction of the magnetic fields. Black arrows indicate the lifting of legs. (f) The perpendicular hydrogel object does not rotate its body for turning when the rotation direction of magnetic fields changes from y-z plane to x-z plane.

The hydrogel–metal hybrid samples can transport and release cargos by light and magnetic field exposure. Irradiating samples with high intensity light (4800 mW/cm^2) from below caused it to curl into a spheroidal object, wrapping around an alginate hydrogel bead (cargo) that had been placed underneath it (Figure 4.14g, top). Under a rotating magnetic field, the ball-like object can roll to an arbitrary destination bringing its cargo with it (Figure 4.14g, middle). By shining light on the convex side of the object, we can eliminate the photoisomerization gradient, causing the object to gradually flatten and release its cargo (Figure 4.14g, bottom, Video 4.10). In a similar way, samples can be programmed to transport cargo, adhered to its "shoulder" through electrostatic attractions, which can be subsequently released by fast spinning (Figure 4.22, Video 4.10). These results offer proof-of-concept on the use of programmed light and magnetic fields to externally and remotely stimulate materials to transport and release cargo.

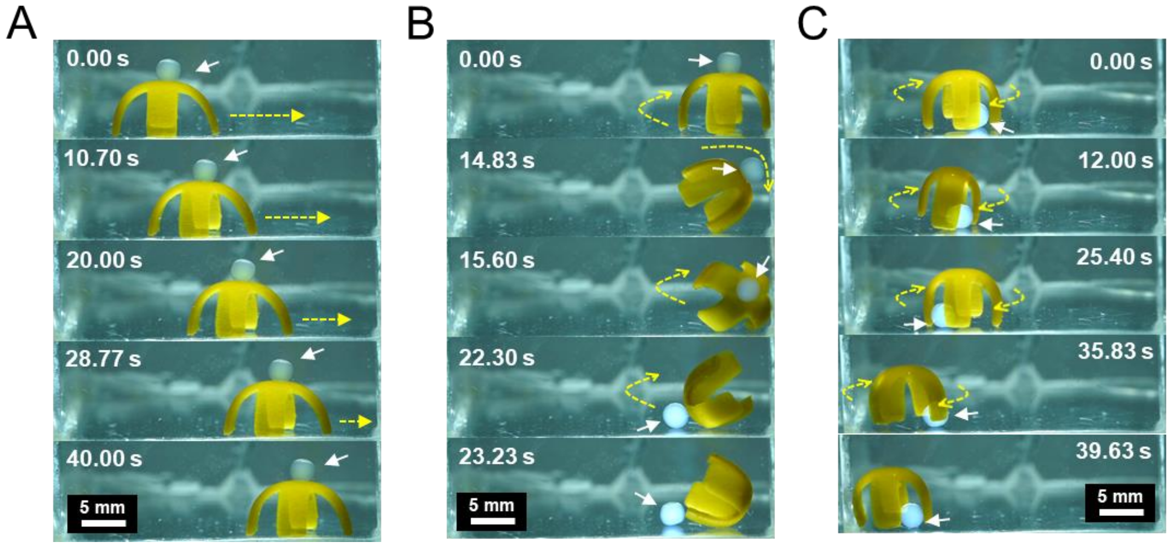

Figure 4.22 (a) Hydrogel object containing of SP1 walks with an alginate bead cargo stick to its shoulder from left to right under a magnetic field rotating in y-z plane. White arrows indicate the alginate bead. Yellow arrows indicate the walking direction. (b) The sticky cargo was released by a fast spin motion of the hydrogel robot. (c) The hydrogel object can play soccer (alginate bead) under a magnetic field rotating in x-y plane.

4.4 CONCLUSIONS

In this work we have investigated the design of highly hydrated soft matter with the capability to respond to both light and magnetic fields in order to emulate locomotion and other functions observed in living organisms. This coupling is achieved by embedding rigid ferromagnetic components in a soft photoactive hydrogel. We conclude that light exposure can create 3D non-uniform magnetization profiles and enable programmable robotic functions in these materials such as walking, climbing, steering, and delivering cargo. By theoretically integrating magnetoelasticity, polymer physics, and photochemical kinetics, we learned how to control locomotion and shape changes in soft materials using light and magnetic fields. Further work on actuation in high-water-content materials will help us understand the autonomous behaviors of living matter, and possibly allow us to emulate or surpass some of its remarkable functions.

4.5 MATERIALS AND METHODS

4.5.1 MATERIALS

All chemicals used for spiropyran synthesis were purchased from Sigma Aldrich, Thermo Fisher or other commercial companies and used directly without any purification unless mentioned. Anodic alumina (AAO) membranes were purchased from Whatman Anodisc (filter membranes, 0.02 μm pore size, 47 mm diameter, polypropylene support ring, GE Healthcare 68095502). Nickel electroplating solution was purchased from Alfa Aesar (2026 Nickel plating solution, semi-bright finish). Nickel nanoparticles (200 nm diameter, 99.5% purity) were purchased from US Research Nanomaterials, Inc and used as received. The UV curable resin was purchased from Loon Outdoors (UV Clear Fly Finish Thick).

4.5.2 EQUIPMENT

The white light LEDS were purchased from Chanzon (6000-6500K color temperature, Amazon ASIN B01DBZHUXA). The NdFeB rare earth magnets used during hydrogel preparation were purchased from Applied Magnets (6"×2"×1" NdFeB Grade N42 block, model # NB085-5). The gaussmeter was purchased from AlphaLab (Model VGM). The power and energy meter were purchased from Thorlabs (Digital Handheld Optical Power and Energy Meter Console, Model PM100D). A custom triaxial Helmholtz coil system was designed and fabricated by Micro Magnetics, Inc. for all magnetic actuation and locomotion experiments (see Section 4.5.7 for more details). Front and side-view videos and photographs of photoactuation and locomotion experiments were taken using a Nikon D5600 DSLR camera with a macro lens (Sigma 105mm f/2.8 EX DG OS HSM Macro). Top view videos and photographs were taken using an endoscopic camera (Dylviw 3 Meter Cable USB C Endoscope Inspection Camera, Amazon ASIN B075D52H7M) inserted into the magnetic chamber.

4.5.3 SYNTHESIS OF METHACRYLATE-SPIROPYRAN MONOMER

Spiropyrans were synthesized following the procedure described in Scheme S1 and purified using an automatic column machine (CombiFlash® EZ Prep). ^{1}H nuclear magnetic resonance (NMR) spectra were taken on an Agilent DD 600 MHz with an HCN cryoprobe. Electrospray ionization mass spectrometry (ESI-MS) were carried out using an Agilent 6510 quadrupole time-of-flight (Q-TOF) instrument.

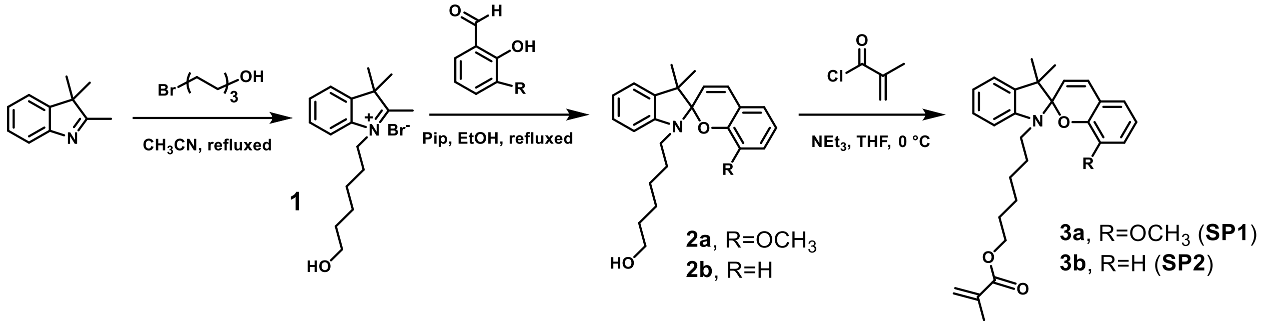

Scheme S1. Synthesis of methacrylate-spiropyran **SP1** and **SP2**.

*Synthesis of 1-(6-hydroxyhexyl)-2, 3, 3-trimethyl-3H-indole-1-ium bromide (**1**).* 2, 3, 3-trimethyl-3*H*-indolenine (2.0 g, 12.4 mmol) and 6-bromo-1-hexanol (2.9 g, 16.2 mmol) were dissolved in 20 mL acetonitrile, followed by stirring for 24 h at 85 °C under reflux. Afterwards the mixture is slowly cooled to room temperature and acetonitrile was removed under reduced pressure to produce a dark red oil. After complete drying under high vacuum overnight, the product was dissolved in 50 mL dichloromethane and extracted three times with DI water (3×50 mL). The aqueous phase was carefully concentrated by rotary evaporation at 60 °C to remove water, followed by complete drying under high vacuum to afford a red dark salt (3.3 g, 78%).

^{1}H-NMR (400 MHz, d_6-DMSO) δ (ppm): 7.99 (m, 1H), 7.85 (m, 1H), 7.63 (m, 2H), 4.46 (t, 2H), 3.39 (t, 2H), 2.85 (s, 3H), 1.84 (m, 2H), 1.55 (s, 6H), 1.33-1.48 (m, 6H).

MS-ESI (m/z): [M] calc. for $C_{17}H_{26}NOBr$ 340.31; found $[M\text{-}Br]^-$ 260.09.

*Synthesis of 6-(3, 3'-dimethyl-8- methoxyspiro [chromene-2, 2'-indoline]-1'-yl) hexan-1-ol (**2a**).* 2,3,3-Trimethylindoleninalcohol (**1**, 9.6 g, 33.6 mmol) and 2-hydroxy-3-methoxybenzaldehyde (7.8 g, 51.4 mmol) were added to 50 mL of ethanol, followed by addition of Piperidine (3.64 mL, 36.4 mmol). The reaction mixture was stirred at 80 °C under reflux for 24 h. After cooling to room temperature, the solvent was removed under reduced pressure and the crude product was purified via silica column chromatography by using DCM/methanol (100:4) as eluent. After complete drying under vacuum overnight, 8.07 g (20.5 mmol) of a dark green solid (**2a**) was obtained.

^{1}H-NMR (400 MHz, $CDCl_3$) δ (ppm): 7.10-7.14 (m, 1H), 7.02-7.06 (m, 1H), 6.76-6.80 (m, 2H), 6.73-6.75 (m, 2H), 6.66-6.70 (m, 1H), 6.50 (d, 1H), 5.66 (d, 1H), 3.66 (s, 3H), 3.08-3.28 (m, 2H), 1.48-1.60 (m, 4H), 1.31-1.40 (m, 4H), 1.30 (s, 3H), 1.15 (s, 3H).

MS-ESI (m/z): [M] calc. for $C_{25}H_{31}NO_3$ 393.53; $[M+H]^+$ found 394.33.

*Synthesis of 6-(3', 3'-dimethyl-spiro [chromene-2,2'-indoline]-1'-yl) hexan-1-ol (**2b**).* **2b** was synthesized following the same protocol as **2a**.

^{1}H-NMR (400 MHz, $CDCl_3$) δ (ppm): 7.32-7.15 (m, 2H), 7.12-7.03 (m, 3H), 6.84 (t, 2H), 6.70 (d, 1H), 6.55 (d, 1H), 5.69 (s, 1H), 3.62 (t, 2H), 3.29-3.06 (m, 2H), 1.72-1.41 (m, 8H), 1.31 (s, 3H), 1.18 (s, 3H).

MS-ESI (m/z): [M] calc. for $C_{24}H_{29}NO_2$ 363.50; $[M+H]^+$ found 364.22.

*Synthesis of 6-(3', 3'-dimethyl-8-methoxyspiro [chromene-2,2'-indolin]-1'-yl) hexyl methacrylate (**3a**).* 6-(3, 3'-dimethyl-8-methoxyspiro [chromene-2, 2'-indoline]-1'-yl) hexan-1-ol (**2**, 3.1 g, 7.87 mmol, 1 equiv.) was dissolved in 40 mL of THF, followed by addition of Et_3N (2.25 mL, 15.75 mmol, 2 equiv.) in one portion. The reaction mixture was cooled to 0 °C followed by drop-wise addition of methacryloyl chloride (1.57 mL, 15.75 mmol, 2 equiv.). After keeping the reaction at 0 °C for an additional hour, the mixture was stirred at room temperature for 4 h. After filtered, the solution was purified by column chromatography (3:2 DCM/hexanes) to afford **3** (1.64 g, 3.56 mmol, 45%) as a brown solid.

^{1}H-NMR (400 MHz, $CDCl_3$) δ (ppm): 7.10-7.15 (m, 1H), 7.04-7.06 (m, 1H), 6.77-6.81 (m, 2H), 6.73-6.76 (m, 2H), 6.66-6.70 (m, 1H), 6.50 (d, 1H), 6.09 (d, 1H), 5.67 (d, 1H), 5.54 (m, 1H), 4.10 (m, 2H), 3.66 (s, 3H), 3.08-3.29 (m, 2H), 1.94 (s, 3H), 1.59-1.67 (m, 4H), 1.32-1.39 (m, 4H), 1.30 (s, 3H), 1.16 (s, 3H).

MS-ESI (m/z): [M] calc. for $C_{29}H_{35}NO_4$ 461.60; $[M+H]^+$ found 462.33.

*Synthesis of 6-(3', 3'-dimethyl-spiro[chromene-2,2'-indolin]-1'-yl) hexyl methacrylate (**3b**).* Compound **3b** was synthesized following the same protocol as described for **3a**, yield 48%.

^{1}H-NMR (400 MHz, $CDCl_3$) δ (ppm): 7.95 (dd, 1H), 7.70-7.65 (m, 1H), 7.18 (dd, 1H), 7.05 (d, 1H), 6.86-6.80 (m, 2H), 6.70 (d, 1H), 6.55 (d, 1H), 6.45 (t, 1H) 6.12-6.08 (m, 1H), 5.87 (t, 1H), 5.56 (t, 1H), 4.13 (m, 2H), 3.29-3.07 (m, 2H), 1.96 (s, 3H), 1.71-1.59 (m, 4 H), 1.44-1.33 (m, 4H), 1.31 (s, 3H), 1.18 (s, 3H).

MS-ESI (m/z): [M] calc. for $C_{28}H_{33}NO_3$ 431.58; $[M+Na]^+$ found 454.38.

4.5.4 SYNTHESIS OF NICKEL NANOWIRES

Ni nanowires were synthesized as adapted from a protocol described by Bentley *et al*[45]. Anodic alumina (AAO) membranes (Whatman Anodisc filter membranes, 0.02 μm pore size, 47 mm diameter, polypropylene support ring, GE Healthcare 68095502) were coated with 250 nm of silver by thermal evaporation at a rate of 1 angstrom/second on the side of the membrane with the 0.02 μm pores (side with wider portion of polypropylene support ring), using a Lesker NANO 38 deposition system. Copper electrical tape (3M 1181 tape) was adhered to the edge of the AAO coated with silver. The entire backside coated with silver was lightly covered with clear acrylate-based nail polish (Wet N Wild, wildshine© Clear Nail Protector) to prevent deposition of nickel on the backside of the silver coating. Thicker coatings would result in penetration and blocking of the porous silver layer. After complete drying of the nail polish, nickel nanowires were deposited within the AAO using a commercial nickel electroplating solution (Alfa Aesar, 42026 Nickel plating solution, semi-bright finish) and potentiostatic deposition at -1.0 V vs. Ag/AgCl (BASi model RE5B) for 50 minutes with a nickel plate counter-electrode. Before deposition was started, the AAO membrane was soaked in the nickel-plating solution for 2 minutes to allow full wetting of the AAO membrane, and a steel alligator clip was clipped onto the copper tape at the point of contact with the AAO membrane to apply pressure and ensure electrical contact.

After deposition, AAO membranes were rinsed with milli-Q water and soaked in acetone for 10 minutes to remove the nail polish and adhesive tape residue. The membranes were rinsed with fresh acetone and allowed to dry. The silver contact layer was removed by wiping with cotton swabs soaked in concentrated nitric acid (68%). The AAO was quickly rinsed with water to avoid dissolution of the Ni nanowires and soaked in milli-Q water for 10 minutes to ensure full removal of silver and nickel ions. The cotton swabs were also rinsed with water before disposal to prevent formation of nitrocellulose.

AAO was subsequently dissolved around the nanowires by shaking in aqueous 6 M NaOH for 15 minutes. The suspension of nickel nanowires was rested for one minute to allow for settling of larger aggregates of nickel. The supernatant containing suspended individual nanowires was collected by pipetting into a separate vial. The nanowires from this supernatant was then washed by consecutive 1 minute bath sonication, collection by magnetic separation (large NdFeB magnet used), decanting of supernatant (cloudy from small 20 nm wide chunks of nickel deposited at the bottom of the AAO membrane), and refilling with fresh milli-Q water. This process was continued five times until the supernatant water was clear. The process was repeated three times with absolute ethanol to remove water from the Ni nanowires. The Ni nanowires were then concentrated with magnetic separation before transferring by pipette to a dry tared glass vial. The Ni nanowires were dried at 60 °C in a convection oven for three hours and weighed, with typical batches resulting in ~3 mg/AAO membrane. Ni nanowires were re-dispersed by sonication at 10 mg/mL concentration in absolute ethanol and aliquoted into centrifuge tubes in 1 mg Ni nanowire portions using a displacement pipette. Each portion was dried at 60 °C and stored dry at room temperature until use in fabrication of the hydrogel composite.

4.5.5 HYDROGEL COMPOSITE PREPARATION

Thin films of hydrogel composite were prepared by photopolymerization of a solution containing monomers and Ni nanowires within glass molds. The thickness of hydrogel films (350-580 μm) is controlled by the thickness of plastic spacers adhered to the glass slides using a UV curable resin (Loon Outdoors, UV Clear Fly Finish Thick). The polymerization solution is prepared in ethanol by adding N-isopropylacrylamide monomer (10 wt%), *N*, *N*'-methylenebisacrylamide cross-linker (0.68 wt%), diphenyl(2,4,6-trimethylbenzoyl) phosphine oxide photoinitiator (0.5 wt%) and the spiropyran molecule (1.0 wt%). Polymerization solutions were centrifuged prior to use. An appropriate amount of solution was added to Ni nanowire portions and sonicated to disperse the Ni nanowires in a 5 mg/mL concentration prior to pipetting into glass molds. The headspace of the mold was sparged for 10 minutes with Argon gas saturated with ethanol vapor by passing through a bubbler filled with ethanol, mitigating any evaporation of the monomer solution. The molds were sealed with the UV curable resin and briefly sonicated and shaken before immediately placing in the photopolymerization setup. The photopolymerization set-up consists of a room-temperature transparent water bath that hold the molds upright between a pair of 100 watt white light LEDS (Chanzon, 6000-6500K color temperature, Amazon ASIN B01DBZHUXA) mounted on aluminum fan-cooled heat sinks and 44 mm 60° lens (TX, Amazon ASIN B01D1LD68C). Perpendicular to the LEDs, a pair of NdFeB rare earth magnets (Applied Magnets, 6"×2"×1" NdFeB Grade N42 block, model # NB085-5) were mounted at an appropriate distance to yield a 25 mT magnetic field strength at the location of the water bath. The field strength was measured using a 3-axis gaussmeter (AlphaLab, Inc. Model VGM). Samples with Ni nanowires aligned parallel to the plane of the films were placed in the photopolymerization setup with the plane of the films oriented parallel to the direction of the magnetic field and were photopolymerized for 110 seconds to increase solution viscosity before brief sonication and vigorous shaking. Samples were immediately placed back into the photopolymerization setup and allowed to fully polymerize for an additional eight minutes and ten seconds. After polymerization, the gels were gently de-molded using a razor blade and exchanged to methanol for 10 minutes to wash out excess monomer and photoinitiator. Samples containing SP1 (or SP2) photoactive moiety were exchanged to 5 mM aqueous HCl for 40 minutes (or 90 minutes) in the dark to swell the hydrogels prior to actuation experiments. Samples were punched to the desired shape and Ni nanowire orientation in the swollen state using a printed puncher. The hydrogel film with chained Ni nanoparticles aligned parallel to the film was prepared following the same protocol above.

Samples with Ni nanowires aligned perpendicular to the films was prepared by orienting the molds perpendicular to the magnetic field between the NdFeB magnets. Unaligned samples were prepared following the same protocol but without the presence of the magnets.

4.5.6 HYDROGEL CHARACTERIZATION

Optical microscopy. Optical microscopy was performed using bright-field imaging on a Nikon Eclipse TE200 microscope with 10x/0.25 Ph1 Dl and LWD 20x/0.40 Ph1 D1 objectives.

Scanning electron microscopy (SEM). Hydrogel samples were thoroughly swollen in water and lyophilized. After sputter coating with a 9 nm thick Au/Pd film, the sample was observed by SEM. SEM imaging of Ni nanowires were conducted on bare Ni nanowires cast on a gold-plated glass substrate. All SEM imaging was performed using a Hitachi SU8030 SEM.

Two-dimensional small angle X-ray scatting (SAXS). SAXS measurements were performed at beamline 5-ID-D of the DuPont-Northwestern-Dow Collaborative Access Team (DND-CAT) Synchrotron Research Center at the Advanced Photon Source, Argonne National Laboratory. Samples were soaked in milli-Q water before sealing between Kapton sheets in silicone isolators with double-sided adhesive. Data was collected using an energy of 17 keV using a CCD detector positioned 245 cm behind the sample. Scattering intensities were recorded within a q range of $0.0024 < q < 0.40$ Å^{-1}, where the wave vector q is defined as $q = (4\pi/\lambda)\ sin(\theta/2)$ where θ is the scattering angle. For the plot of integrated intensity vs. azimuthal angle "Fit2D" software was used to subtract the background from measured 2D SAXS patterns using a solvent-containing well with the same path length. A radial integration in the q range of $0.0024 < q < 0.0135$ Å^{-1} with an azimuthal angle range of 270 degrees to exclude the beam stop was performed.

Permeability calculation. The differential susceptibility was estimated from the hysteresis loops and obtained a value of 6×10^{-5} emu/Oe. To get the volume susceptibility, we divided this value with the total mass of the nanowires in grams (2.44×10^{-4} g). To pass from CGS to SI units, we multiplied the mass susceptibility by the density of Ni, ρ=8.9 g/cm^3, and by a factor of 4 multiply by the number Pi (susceptibility (SI)+4×Pi×ρ×susceptibility(cgs)). With the susceptibility in SI units we compute the magnetic permeability along the nanowire axis as mu=mu0× (1+susceptibility (SI)) and obtained a value of 3.58164×10^{-5} H/m.

Vibrating sample magnetometry (VSM) measurement. VSM measurements were performed on hydrated samples of 0.55 mm thickness as polymerized. After polymerization, the sample (containing 2 mg Ni nanowires in total) was transferred to DI water and completely swollen. The total area of this sample was calculated by multiplying the length and width (L × W). The sample was cut to 7.5 × 7.5 mm squares and the mass of Ni nanowires (0.25 mg) in the square was calculated by area ratio (7.5 × 7.5)/(L × W). Squares samples were then swollen in dark conditions in 5 mM aqueous HCl for 30 minutes placing in the centers of 15 × 15 mm squares of microscope slide glass. Excess water was carefully removed by wicking with a tissue wipe prior to sandwiching with another identical square of glass and sealed around the edges with UV curable resin (Loon Outdoors, UV Clear Fly Finish Thick).

Superconducting quantum interference device (SQUID) measurements. A small sapphire wafer (University Wafer, 430 μm thickness) was cut into a piece approximately 3 × 5 mm using a diamond file as a sample stage. The hydrogel sample containing aligned Ni nanowires was prepared using the same protocol as the VSM experiment and incubated in DI water was cut into the same shape and size, then deposited onto the sapphire, frozen in liquid nitrogen and lyophilized. The mass of Ni nanowires (0.033 mg) in the sample was calculated by the area ratio compared to that before cutting. The sapphire wafer with the dried sample deposited was affixed to the stage of a Quantum Design horizontal sample rotator using a small amount of Apezion M grease. SQUID magnetometry measurements were performed on a Quantum Design MPMS-XL SQUID magnetometer at 300 K under fields of both 0 Oe and 160 Oe. Sample rotation was achieved using a Quantum Design horizontal rotation sample rod and an automated sample rotation motor. The sample was assumed to be normal to the z-direction at 60° and 240° rotation angle, meaning that at 0° as recorded by the software controlling the motor, the sample was at -60° relative to z. This miscalibration is due to a misalignment of the sample rod 0° starting point with that recorded by the motor. Samples containing unaligned Ni nanowires (0.104 mg) or aligned chains of Ni nanoparticles (0.087 mg) were measured following the same protocol above. The mass of magnetic component was calculated by area ratio. The magnetization showed at 300 K under 0 Oe of magnetic field is attributed to the pre-magnetization of our sample during hydrogel preparation process. The magnetization measured using SQUID (~132 emu/cm^3) was lower in relative to that measured using VSM (~260emu/cm^3). The reason might be the dried sample used for SQUID contracted during drying process which disturbs the alignment of Ni nanowires.

Note that the sample containing aligned chains of Ni nanoparticles showed almost zero magnetization under 0 Oe of magnetic field. However, this sample exhibited superparamagnetism under 160 Oe of magnetic field. We did not observe any superparamagnetism for the Ni nanowire samples.

Rheological measurements. Rheological properties of hydrogels were measured using an Anton Paar Modular Compact Rheometer (MCR 302). Three types of rheological experiments were performed in 8 mm parallel-plate geometry with a gap size of 0.4 mm: i) oscillatory strain sweep (0.05-500%) and were conducted with a fixed angular frequency of 10 rad/s at 25 ºC. ii) angular frequency sweep (0.05-500 rad/s) was carried out with a fixed strain of 1 % at 25 ºC; and iii) time-scan tests were done at a fixed angular frequency of 10 rad/s and strain of 1%, respectively, at 25 ºC for a specific time.

Dynamic mechanical analysis (DMA). Stress–strain curves were obtained using TA Instruments RSA G2 instrument. Samples were tested at 25 ºC in 8 mm parallel-plate geometry using a compression mold with a compression rate of 0.48 mm/min.

4.5.7 PHOTOACTUATION

Photoactuation by irradiation with light from top was conducted using gooseneck fiber optics combined with a white light LED source. Photoactuation from underneath was conducted using a 100-watt white LED (Bridgelux LED COB Vero 29 5000K round, product #BXRC-50C10K1-D-74) driven at different variable currents directly underneath the sample chamber. Specifically, for walking motion study, 48-192 mW/cm^2 were applied from below the hydrogel objects containing the SP1 moiety and 4.7-33.0 mW/cm^2 were applied from below the hydrogel objects containing the SP2 moiety. For cargo capture, 4800 mW/cm^2 was applied from below the hydrogel objects containing the SP1 moiety for 10 s. For cargo release, 282 mW/cm^2 was applied on the convex side of the bending object to flatten the object. After photoactuation was complete, illumination for photography and videography was performed using the Bridgelux LED driven at 1 mA (~4.7 mW/cm^2) to minimize photoisomerization.

4.5.8 LIGHT RESPONSIVE HYDROGEL THEORY

4.5.8.1 Photo-chemical reaction

Upon light radiation, the spiropyran chromophores grafted on the polymer chains of the hydrogels undergo a reaction from hydrophilic merocyanine form (MCH$^+$) to hydrophobic spiropyran form (SP):

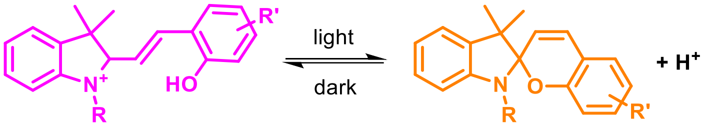

Merocyanine (MCH$^+$)   ***Spiropyran (SP)***

The reaction rate equation can be solved to compute the concentration of SP moiety:

$$\frac{\partial r_{SP}}{\partial t} = k_L(I)r_{MCH} - k_D r_{SP} \tag{S1}$$

where r_{MC} and r_{SP} are the fractions of chromophores in MCH^+ and SP forms respectively. Ring-opening reaction rate coefficient, k_D is usually a constant value at a given substituent, temperature and pH[146], and the ring-close reaction rate coefficient, k_L is dependent on the incident light intensity, I. At equilibrium the rate $\frac{\partial r_{SP}}{\partial t} = 0$, which gives the equilibrium concentration of chromophores.

$$r_{SP} = \frac{k_L(I)}{k_L(I) + k_D} \tag{S2}$$

For a unidirectional and monochromatic light source with frequency ν, an expression for k_L can be written as[147]:

$$k_L = \frac{\Psi_{\nu,\mathrm{MCH}}}{h\nu} \epsilon_{\nu,\mathrm{MCH}} I \tag{S3}$$

where, $\Psi_{\nu,\mathrm{MCH}}$ is the quantum yield of MCH^+ chromophore which is defined as the number of reactions per photon, $\epsilon_{\nu,\mathrm{MCH}}$ is the molar absorptivity and h is the Planck's constant.

4.5.8.2 Light propagation

The decay of the light intensity in the photoresponsive gels has two contributions: the absorption of light by the photo-chemical reaction and the absorption of light by the gel's polymer matrix. The absorption coefficient k_ν can therefore be written as[147]:

$$k_\nu = \frac{k_{\nu,1}}{J} + k_{\nu,2} \tag{S4}$$

where $k_{\nu,1}$ denotes the absorption of light by the dry polymer matrix, which is then rescaled by $J = \det \boldsymbol{F}$ due to the volumetric changes, and $k_{\nu,2}$ is the absorption of light due to the photo-chemical reaction. The term, $k_{\nu,2}$ can be written as

$$k_{\nu,2} = \epsilon_{\nu,\mathrm{MCH}} c_{\mathrm{MCH}} = \epsilon_{\nu,\mathrm{MCH}} r_{\mathrm{MCH}} \left(\frac{f \phi}{v_m N_A} \right) \tag{S5}$$

where, c_{MCH} is the concentration of MCH^+ chromophore; f is the fraction of monomers containing a chromophore; ϕ is the volume fraction; v_m is the volume of a chromophore and N_A

is Avogadro's constant. Using Beer-Lambert law, the differential equation for light intensity distribution can be written as (light propagating in the +z direction):

$$\frac{\mathrm{d}I}{\mathrm{d}z} + \left(\frac{k_{\nu,1}}{J} + \epsilon_{\nu,\mathrm{MCH}} r_{\mathrm{MCH}} \left(\frac{f\phi}{v_m N_A}\right)\right) I = 0 \tag{S6}$$

4.5.8.3 Free energy density

The free energy density of polymer hydrogels consists of an elastic term U_{el}, which models the elastic behavior of the polymer matrix and a mixing term U_{mix}, which models the interaction between the polymer chains and the solvent molecules. The elastic energy is often written as[148]:

$$U_{\mathrm{el}} = \frac{1}{2}\frac{k_B T}{v_m N_x}\phi(I_1 - 3) \tag{S7}$$

Where v_m is the volume of the gel monomer; N_x is the average number of segments between two crosslinking junctions of the polymer network. ϕ is the volume fraction of the monomers and I_1 is the trace of the deformation gradient tensor F.

The mixing free energy term is given by the Flory–Huggins energy[148]:

$$U_{\mathrm{mix}} = \frac{k_B T}{v_m}\left[(1-\phi)\ln(1-\phi) + \chi\,\phi(1-\phi)\right] \tag{S8}$$

Where χ describes the interaction between monomers and water molecules and can be derived using a lattice model.

$$\chi = \frac{z}{k_B T}\left(u_{pw} - \frac{(u_{pp} + u_{ww})}{2}\right) \tag{S9}$$

Where z is the coordination number, u_{pw} is the interaction energy between monomer and water molecule, u_{pp} is the self-interaction of monomers and u_{ww} is the self-interaction of water molecules.

To include the free energy contribution from chromophores, we need to make a correction to the χ parameter. This can be done by solving the lattice model by replacing a fraction f of monomers with chromophores. In the limit of small f, a new parameter, χ' can be given by:

$$\chi' = \frac{z}{k_B T}\left[\left(u_{pw} - \frac{(u_{pp} + u_{ww})}{2}\right) + f(u_{sw} - u_{mw})r_{SP}\right] \tag{S10}$$

Where u_{sw} and u_{mw} are the interaction energies of SP and MCH^+ moieties with water respectively. Substituting eq. (S10) in eq. (S8), we can split U_{mix} as:

$$U_{\text{mix}} \rightarrow U_{\text{mix}} + U_{\text{photo}}$$

Where U_{photo} is the additional contribution due to the hydrogel's interaction with light which is given by:

$$U_{\text{photo}} = \frac{zf}{v_m} r_{SP}(u_{sw} - u_{mw})\phi(1 - \phi) \tag{S11}$$

4.5.9 CONTINUUM MODELING OF FIBER-REINFORCED MAGNETOELASTIC MATERIALS

In order to get the magnetic field contributed by both the Ni nanowires and the external magnetic field, we solve the Maxwell's equations for the magnetostatics:

$$\begin{gathered}\mathbf{H} = -\nabla\Phi_{\mathrm{m}} + \mathbf{H}_{\mathrm{b}} \\ \nabla \cdot \boldsymbol{B} = 0\end{gathered} \tag{S12}$$

where $\boldsymbol{H}$ is the total magnetic field strength and $\boldsymbol{H}_b$ is the external magnetic field strength, which is explicitly split up for convenience; Φ_{m} is the magnetic scalar potential and $\boldsymbol{B}$ is the total magnetic flux density.

To complete the system of equations for magnetics, we measured the hysteresis curve of Ni nanowires (cross symbols in **Figure 4.23**) to establish the corresponding magnetic material model, i.e. $\boldsymbol{B} = \boldsymbol{B}(\boldsymbol{H})$. Since the imposed external magnetic field strength is relatively weak (<=16 mT), we assume a linear response of Ni nanowires in the parallel direction (red dash line in **Figure 4.23**):

$$\boldsymbol{B} = \mu(\boldsymbol{H} + \boldsymbol{M}_0) \tag{S13}$$

Where μ is the magnetic permeability of the Ni nanowires (3.58164×10^{-5} H/m, see permeability calculation in Section 4.5.5) and $\boldsymbol{M}_0$ is the residual magnetization. We treat each nickel nanowire as a hard magnet, which translates and rotates with the hydrogel matrix.

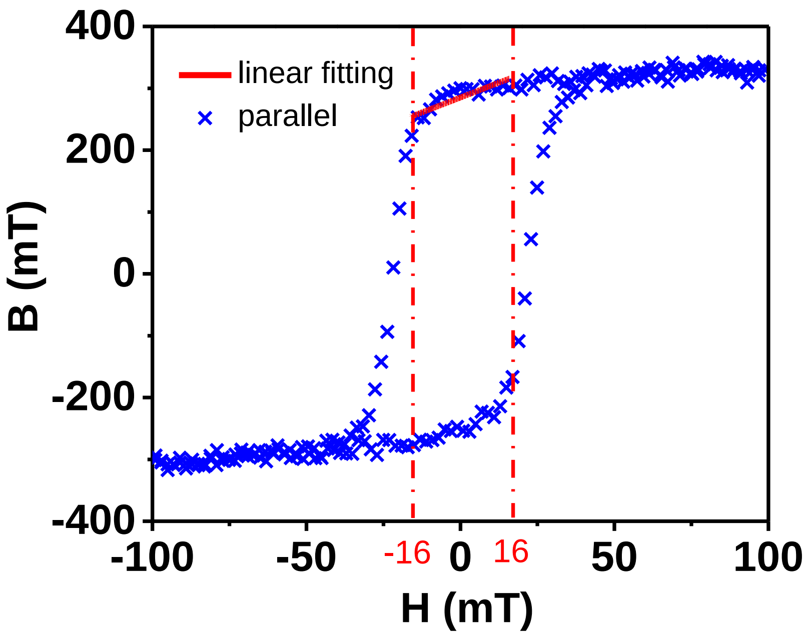

Figure 4.23 Hysteresis curve parallel to the alignment of Ni nanowires (blue cross). A linear fitting is shown by red line within the operational range (between two vertical red lines) of the magnetic field strength.

Solving eq. (S12) and eq. (S13) together give us the distribution of the magnetic flux density $\boldsymbol{B}$, which couples with the magnetization of Ni nanowires and creates magnetic torques on the nanowires. Because the nanowires are fixed within the hydrogel, these magnetic torques cause stresses on the hydrogel matrix and result in macroscopic deformations. Therefore, it's important to develop a material model for the fiber-reinforced magnetoelastic materials. Rheology measurement shows that the viscoelastic effect of this material is not significant ($G'' \ll G'$ see **Figure 4.8**a). Therefore, we will develop the material model under the framework of the hyperelasticity.

In order to describe the anisotropic elastic response of the hydrogel, we assume that the hydrogel is transversely isotropic[145] and its elastic response can be described by the standard reinforcement mode.[149] Then, corresponding elastic energy density function W_{el} in the reference configuration can be written as:

$$W_{el} = \frac{1}{2}\mu(\overline{I_1} - 3) + \frac{1}{2}\mu\gamma(\overline{I_4} - 1)^2 + \frac{\kappa}{2}(J - 1)^2 \tag{S14}$$

Where μ and κ are shear modulus and bulk modulus, respectively; γ is a stiffness parameter which characterizes the Ni nanowires reinforcement $(\gamma > 0)$; $J = \det\boldsymbol{F}$ characterizes volumetric changes with respect to the initial state; $\overline{I_1} = J^{-2/3}I_1 = J^{-2/3}\mathrm{Tr}\boldsymbol{C}$ is the first isochoric invariant[150] of the right Cauchy-Green tensor $\boldsymbol{C} = \boldsymbol{F}^T\boldsymbol{F}$; $\overline{I_4} = J^{-2/3}I_4 = J^{-2/3}\boldsymbol{a} \cdot (\boldsymbol{Ca})$ is the fourth isochoric invariant[149] constructed for transversely isotropic materials [151] with the direction of Ni nanowires specified by a vector field $\boldsymbol{a}$.The initial distribution of $\boldsymbol{a}$ is obtained from the simulation of photo-actuation (see Section 4.5.10.1 for details).

To include the coupling between elasticity and magnetics, a magnetic energy density function W_m is also required. It is important to realize that the magnetic energy density W_m should depend on the orientation of the system. Since the right Cauchy-Green tensor $\boldsymbol{C}$ does not contain any information about rotation ($\boldsymbol{C} = \boldsymbol{F}^T\boldsymbol{F} = \boldsymbol{U}^2$, where $\boldsymbol{U}$ is the right stretch tensor), the magnetic energy density should be a function of the deformation gradient tensor $\boldsymbol{F}$ and the magnetic flux density $\boldsymbol{B}$, i.e. $W_m = W_m(\boldsymbol{F}, \boldsymbol{B})$. We assume that Ni nanowires move with the hydrogel matrix without slipping and the magnetization in the deformed configuration is $\boldsymbol{FM}/J$, where $\boldsymbol{M}$ denotes the magnetization in the reference configuration. Ignoring the higher order energy contributions from $\boldsymbol{M}$ and $\boldsymbol{B}$, the magnetic energy density in the deformed configuration can be written as $-(\boldsymbol{FM}/J) \cdot \boldsymbol{B}$. Therefore, W_m in the reference configuration can be expressed as[133]:

$$W_m = -J[(\boldsymbol{FM}/J)\cdot\boldsymbol{B}] = -\boldsymbol{FM}\cdot\boldsymbol{B} \tag{S15}$$

Combining eq. (S14) and eq. (S15) together, the total energy density W in the reference configuration is:

$$W = W_{el} + W_m = \frac{1}{2}\mu(\overline{I_1} - 3) + \frac{1}{2}\mu\gamma(\overline{I_4} - 1)^2 + \frac{\kappa}{2}(J-1)^2 - (\boldsymbol{FM})\cdot\boldsymbol{B} \tag{S16}$$

This energy density function defines the constitutive law of the fiber-reinforced magnetoelastic materials. This can be shown explicitly by calculating corresponding stresses[152]. For the elastic stress, corresponding second Piola–Kirchhoff stress tensor $\boldsymbol{S}_{el}$ can be calculated as following:

$$\begin{aligned}\boldsymbol{S}_{\mathrm{el}} = 2\frac{\partial W_{el}}{\partial \boldsymbol{C}} = \mu J^{-2/3}\left(-\frac{\boldsymbol{C}:\boldsymbol{I}}{3}\boldsymbol{C}^{-1} + \boldsymbol{I}\right) \\ + 2\mu\gamma J^{-2/3}(\boldsymbol{C}:\boldsymbol{a}\otimes\boldsymbol{a} - 1)\left(-\frac{\boldsymbol{C}:\boldsymbol{a}\otimes\boldsymbol{a}}{3}\boldsymbol{C}^{-1} + \boldsymbol{a}\right. \\ \left.\otimes\,\boldsymbol{a}\right) + \kappa(J-1)\mathrm{J}\boldsymbol{C}^{-1}\end{aligned} \tag{S17}$$

Where $\boldsymbol{I}$ is the identity tensor; $\otimes$ denotes the dyadic product, i.e. $c_{ij} = a_i \otimes b_j$; The symbol ':' denotes double contraction of two tensors, i.e. $\boldsymbol{A}:\boldsymbol{B} = \sum_{i,j} A_{ij}\, B_{ij}$. The elastic Cauchy stress tensor $\boldsymbol{\sigma}_{el}$ can be obtained via the following transformation:

$$\boldsymbol{\sigma}_{el} = J^{-1}\boldsymbol{F}\boldsymbol{S}_{el}\boldsymbol{F}^{T} \tag{S18}$$

Substituting eq. (S17) into eq. (S18) yields:

$$\boldsymbol{\sigma_{el}} = \mu J^{-5/3}\left[-\frac{\boldsymbol{C}:\boldsymbol{I}}{3}\boldsymbol{I} + \boldsymbol{F}\boldsymbol{F}^{\boldsymbol{T}}\right] + 2\mu\gamma J^{-5/3}(\boldsymbol{C}:\boldsymbol{a}\otimes\boldsymbol{a} - 1)\left[-\frac{\boldsymbol{C}:\boldsymbol{a}\otimes\boldsymbol{a}}{3}\boldsymbol{I} + \boldsymbol{F}(\boldsymbol{a}\otimes\boldsymbol{a})\boldsymbol{F}^{\boldsymbol{T}}\right] + \kappa(J-1)\boldsymbol{I} \tag{S19}$$

Also, the magnetic stress can be derived by the work-conjugation relation (*29*):

$$\boldsymbol{P}_m = \frac{\partial W_m}{\partial \boldsymbol{F}} \tag{S20}$$

Where $\boldsymbol{P}_m$ is the first Piola-Kirchhoff magnetic stress tensor. Note that the relation between Cauchy stress tensor and first Piola–Kirchhoff stress tensor is:

$$\boldsymbol{\sigma}_m = J^{-1}\boldsymbol{P}_m\boldsymbol{F}^T \tag{S21}$$

Substituting eq. (S20) into eq. (S21) gives:

$$\boldsymbol{\sigma}_m = \frac{1}{J}\frac{\partial W_m}{\partial \boldsymbol{F}}\boldsymbol{F}^T = -J^{-1}\boldsymbol{B}\otimes\boldsymbol{F}\boldsymbol{M} \tag{S22}$$

Since the magnetic Cauchy stress tensor $\boldsymbol{\sigma}_m$ is asymmetric, it leads to local magnetic torques ($\boldsymbol{\tau}_\mathrm{m} = J^{-1}\boldsymbol{F}\boldsymbol{M}\times\boldsymbol{B}$). Combining the elastic stress and magnetic stress together gives us the constitutive law of the fiber-reinforced magnetoelastic materials:

$$\boldsymbol{\sigma} = \boldsymbol{\sigma}(\boldsymbol{F}) = \boldsymbol{\sigma}_{el} + \boldsymbol{\sigma}_m \tag{S23}$$

It can be shown that the torque balance is automatically satisfied for the asymmetric total stress tensor $\boldsymbol{\sigma}$. Therefore, solving the force balance equation and the constitutive relation eq. (S23) together gives the time-dependent deformations of the hydrogel object in response to the external time-varying magnetic fields.

4.5.10 IMPLEMENTATION DETAILS OF SIMULATIONS AND BENCHMARK TEST

4.5.10.1 Implementation details of simulations

The continuum model of the hydrogel robot was solved in two steps using the commercial finite-element software COMSOL. The first step calculates the deformation of the hydrogel robot under the influence of light and the second step uses the deformed geometry as the reference configuration to calculate the dynamic behavior of the robot under an external magnetic field.

For the first step, we use COMSOL's solid mechanics module and model the hydrogel as a hyperelastic material to calculate its response to light. Since the photo component, U_{photo} of the free energy density of the material depends on r_{sp} (the concentration of chromophores in SP form), the general form PDE module of COMSOL is also used to calculate the light intensity and hence, r_{sp} in the bulk of the material.

For the second part of the simulation, the magnetic field is solved via the AC/DC module of COMSOL. The developed material model of fiber-reinforced magnetoelastic materials is implemented as a user-defined hyperelastic model in the Structural Mechanics module of COMSOL. The contribution from asymmetric magnetic Cauchy stress tensor $\boldsymbol{\sigma_m}$ is implemented via the weak contribution functionality of COMSOL. The contacts between the hydrogel robot and the floor are assumed to be non-slippery and the contact events are detected via the Events module of COMSOL, which triggers time-dependent non-slippery boundary conditions (See section 4.5.10.2 for details). Besides, both volumetric gravitational force and frictional force are added into the continuum model to take into account the effect of gravity and the viscosity of liquid environment, respectively.

4.5.10.2 Contact boundary conditions

The complete analysis of the contacts between the hydrogel robot and the floor requires the simulation to consider mechanical frictions and contact pressures, which are generally difficult to model in the finite element analysis. In order to keep the essential physics without introducing too much complexities, we assume all contacts are non-slippery during walking. Specifically, it means that once a leg of the hydrogel robot lands on the floor, the landed leg is not allowed to have translational displacement. However, rotational movement around the center of the landed leg is allowed to give its steering capability. Besides, we assume all contacts are perfectly inelastic collisions, which means that the kinetic energy of the hydrogel robot gets dissipated immediately when a leg lands on the ground.

With above assumptions, we track the positions of each legs of the hydrogel robot during the time-dependent simulation and trigger a contact event once any leg hits the floor. For each contact event, the boundary condition of the landed leg is switched as a fixed boundary condition; At the same time, the boundary condition of the other leg is switched as a free boundary condition; The kinetic energy of the hydrogel robot is also dissipated completely during each contact events. This contact event-driven boundary condition allows us to recover the dynamic behaviors of the hydrogel robots observed in the experiment and quantitatively study possible robotic functions of the hydrogel robots.

4.5.10.3 Benchmark test

In order to validate our implementation of the proposed continuum model, we compare our simulation results with analytic solutions. For the benchmark, we consider the fiber-reinforced magnetoelastic materials with a simple cubic geometry. To simplify the problem, we further restrict our considerations to the cases where both the magnetization and the external magnetic field are along the z-axis. Due to the symmetry of the system, the principal stretches of the material (λ_x, λ_y and λ_z) obey the relation $\lambda_x = \lambda_y$. We also assume the material is incompressible (i.e. $J = \lambda_x \lambda_y \lambda_z = 1$). Therefore, the deformation gradient tensor of this system has the following diagonal form:

$$\boldsymbol{F} = \begin{pmatrix} \lambda_z^{-1/2} & 0 & 0 \\ 0 & \lambda_z^{-1/2} & 0 \\ 0 & 0 & \lambda_z \end{pmatrix} \tag{S24}$$

Also note that:

$$\mathbf{C} = \begin{pmatrix} \lambda_z^{-1} & 0 & 0 \\ 0 & \lambda_z^{-1} & 0 \\ 0 & 0 & \lambda_z^2 \end{pmatrix}, \boldsymbol{a} = \begin{pmatrix} 0 \\ 0 \\ 1 \end{pmatrix}, \boldsymbol{M} = M_0 \begin{pmatrix} 0 \\ 0 \\ 1 \end{pmatrix}, \boldsymbol{B} = B_{ext} \begin{pmatrix} 0 \\ 0 \\ 1 \end{pmatrix}$$

where M_0 is the average volumetric magnetization of Ni nanowires and B_{ext} is the amplitude of the external magnetic flux density. Plugging these expressions back into eq. (S23) gives:

$$\sigma_{xx} = \sigma_{yy} = \frac{1}{3}\mu(\lambda_z^{-1} - \lambda_z^2) - \frac{2}{3}\mu\gamma\lambda_z^2(\lambda_z^2 - 1) - p \tag{S25}$$

$$\sigma_{zz} = \frac{2}{3}\mu(\lambda_z^2 - \lambda_z^{-1}) + \frac{4}{3}\mu\gamma\lambda_z^2(\lambda_z^2 - 1) - p - B_{ext}M_0\lambda_z \tag{S26}$$

Where volumetric pressure $p = -\kappa(J - 1)$. The traction-free boundary condition requires that:

$$\sigma_{xx} = \sigma_{yy} = \sigma_{zz} = 0 \tag{S27}$$

Combining with above boundary conditions, eq. (S25) and eq. (S26) yield following dimensionless equation:

$$(\lambda_z - \lambda_z^{-2}) + 2\gamma\lambda_z(\lambda_z^2 - 1) = \frac{B_{ext}M_0}{\mu} \tag{S28}$$

Above relation can serve as a benchmark test of our numeric implementation. For a given set of material properties (μ, γ, M_0) and experiment condition (B_{ext}), the response of the material is characterized by the z-component principal stretch λ_z. As indicated by eq. (S28), λ_z is a nonlinear function of two dimensionless quantities $\frac{B_{ext}M_0}{\mu}$ and γ, which is plotted as solid lines in Figure 4.24. Corresponding finite-element simulation is set up with $\kappa \gg \mu$ to ensure the incompressibility of the materials. Finite element solutions are marked as cross symbols in Figure 4.24, and they match consistently with analytic solutions, which validate our implementations of the continuum model of fiber-reinforced magnetoelastic materials.

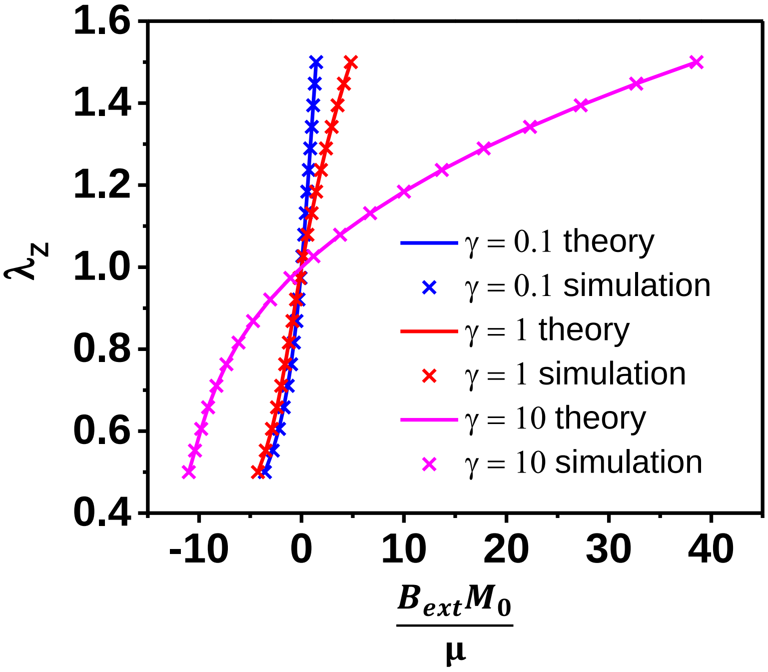

Figure 4.24 Comparison between the numeric solutions (cross symbols) and the corresponding analytic solutions (solid lines) of the fiber-reinforced magnetoelastic materials with a simple cubic geometry.

4.5.10.4 Parameters Calibration

With the established material model as shown in eq. (S16), elastic parameters (μ, κ, γ) need to be calibrated from the experiment measurement. Dynamic mechanical analysis (DMA) is conducted to get the elastic response of the materials via a uniaxial compression (see Figure 4.8b, Dynamic Mechanical Analysis in section 4.5.6). Then, the calibration process is done by the reverse modeling. Basically, we establish the simulation model with the same configurations of the experiment and try to find the optimal parameters which match the simulated responses with the experimental responses best. In the parameter calibration process, we use least square function as the objective function and SNOPT as the optimization solver.

For the calibration purpose, identical circular samples with the diameter of 8 mm and thickness of 0.536 mm are cut by mold for uniaxial compression test. The nominal stresses of samples without Ni nanowires (control sample), samples with Ni nanowires aligned perpendicular to bottom surface (perpendicular sample) and samples with Ni nanowires aligned parallel to bottom surface (parallel sample) are measured with respect to the strain, which are shown as cross symbols in Figure 4.25.

For the control sample, corresponding continuum model reduces as the Neo-Hookean model since it does not contain anisotropic contribution from the Ni nanowires. The best fitting extracts corresponding elastic parameters of the hydrogel are: $\mathrm{\mu} = 3.6\ \mathrm{kPa}, \mathrm{\kappa} = 17.5\ \mathrm{kPa}.$ (see blue solid line in Figure 4.25)

For the perpendicular and parallel samples, we use the same set of elastic parameters to fit experimental data of both samples simultaneously. The continuum model of perpendicular sample only differs at Ni nanowires' orientation with the parallel sample. Since the concentration of the Ni nanowires is low (~0.5 % weight percentage), we assume the bulk modulus of fiber-reinforced materials is roughly the same as the bulk modulus of the control sample. The best fitting extracts corresponding elastic parameters of the fiber-reinforced hydrogel are: $\mu = 5.2\ \mathrm{kPa}, \gamma = 0.9, \kappa = 17.5\ \mathrm{kPa}$ (see red and magenta solid lines in Figure 4.25).

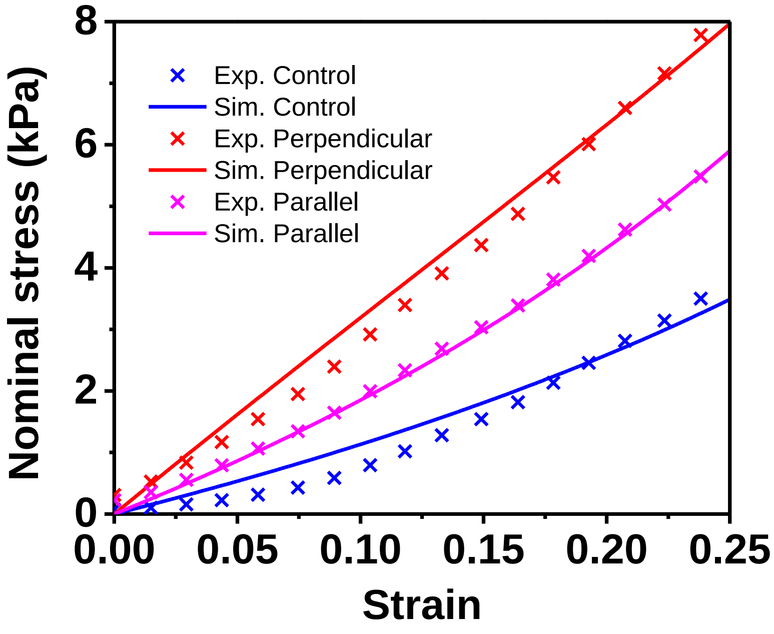

Figure 4.25 Calibration of the elastic parameters from the DMA measurement. The experiment results are shown as cross symbols and the corresponding simulation results are shown as solid lines.

4.5.11 LOCOMOTION UNDER LIGHT AND MAGNETIC FIELD

Magnetic actuation. Magnetic actuation experiments were performed using a custom-designed 6-helmholtz coil 3-axis electromagnetic stage fabricated by Micro Magnetics, Inc. with the following specifications: Triaxial Helmholtz coils with effective diameters of 6, 11.3, and 17.5 inches for the X-, Y-, and Z-axes, respectively; Maximum DC magnetic field +/- 300 Oe for X-axis, +/-250 Oe for Y-axis, +/-160 Oe for Z-axis (working with Controller); Physical dimensions: 19.5 (W) × 19.5 (D) × 14 inches (H). For translational locomotion studies (rolling, flipping and walking), a magnetic field rotating in either the x-z or y-z planes were used, depending on whether translation in the x or y axes was desired, respectively. Rotating magnetic fields were generated by driving perpendicular pairs of Helmholtz coils with sinusoidal current amplitude, with a phase lag of +/- 90° controlling the direction of rotation. x-z and y-z rotating magnetic fields had an amplitude of 16 mT.

Walking speed measurement. The cross-shaped hydrogel film containing aligned Ni nanowires was transferred to a water tank (40 × 40 × 75 mm, L×W×H) followed by placed in the magnetic field. Low intensity of DC field (50 Oe) was applied to align the sample. After that, a rotating magnetic field along y-z axis and light irradiation underneath the film were applied simultaneously, enabling walking along the y-axis of the chamber. The walking direction was reversed periodically to prevent the object from colliding with the walls of the water tank. Video recording was conducted of the entire process using a digital camera. Walking speed for one specific time point was obtained by averaging five walking steps around that time point. For one specific set of experimental conditions (fixed frequency, strength of magnetic field, fixed light intensity), the averages and standard derivations were obtained over three samples.

Gel punches were designed in Autodesk Fusion 360 for reproducible cutting of photopolymerized hybrid gel walkers with precise arm lengths. The punches were 3D printed using a Stratasys Connex 350 printer with high-strength ABS and 30 μm layer height. All punchers were made 11 mm tall with a 1 mm wall thickness to allow for facile handling. The top surface of each puncher has 1 mm tall, 45° beveled edges that result in a sharp inner cutting-edge for punching through the 0.5 mm thick gels. For the punched walkers, the leg width and length were kept constant at 3 mm and 7 mm, respectively, while the stabilizing arm length was varied between 3 and 7 mm.

Walking on slope (9° angle of inclination). The cross-shaped object was irradiated light from bottom first to get the bending geometry, followed by putting in a water tank with a 9° angle of inclination. The rotating magnetic field was applied to enable the walking motion along the inclined surface (ascend). Once the walker touched the wall of the water tank, the rotating direction of the magnetic field was reversed to descend. As a control, the same sample with the same bending geometry was also placed on a flat surface to walk left and right.

UV-Vis spectroscopy. SP1 (or SP2) was dissolved in a mixture solvent of dioxane/water (4/1, v/v) containing 5 mM of HCl to get a final concentration of 0.1 mM and incubated in the dark for 3 h before the measurement. Absorbance spectroscopy of this solution was collected using a 1 mm path length, demountable quartz cuvette on a Shimadzu UV-1800 UV Spectrophotometer. A specific intensity (96, 190 mW/cm^2 for SP1; 23.5, 33.0 mW/cm^2 for SP2) of white LED (Bridgelux LED COB Vero 29 5000K round, product #BXRC-50C10K1-D-74) was applied to this solution, followed by collecting the absorbance spectroscopy every 20 s for SP1 and every 2 s for SP2 until the absorbance did not change. Plotting the absorbance of SP1 at 404 nm (MCH$^+$) and SP2 at 430 nm over irradiation time resulted the photoactuation kinetics.

Sequential light intensity. A light sequence with a stepwise increasing intensity was applied at a flat cross-shape film containing SP1. Each light intensity was irradiated for 5 min. Four different light intensities (48, 96, 144, 192 mW/cm^2) were applied on the same sample until the sample obtained the maximum bending angle. Additional strong light irradiation on the object did not induce any increase on the bending angle as well as the walking speed. For objects containing SP2, three light intensities (4.7, 14.1, 23.5 mW/cm^2) were applied to the cross-shaped sample.

4.5.12 OTHER WALKING MODES BY CONTROL OF THE ALIGNMENT DIRECTION

Diagonal and perpendicular walkers. Diagonal samples were punched from thin films with Ni nanowires aligned parallel to the film plane using a cross-shaped puncher and perpendicular samples were punched from thin films with Ni nanowires aligned perpendicular to the film plane.

Due to the magnetic anisotropy, the diagonal object with a bending geometry induced by bottom light irradiation is able to walk by lifting two front legs simultaneously under the rotating magnetic field in y-z plane. The aligned Ni nanowires tend to follow y direction when the magnetic field in rotating in y-z plane. However, this diagonal object will rotate its body 90° counterclockwise once the magnetic field starts rotating in x-z plane. This rotation behavior is similar to the parallel walker which also has magnetic anisotropy in x-y plane. As a control, the perpendicular object was able to walk and turn under the rotating magnetic field, but there is no rotation of its body observed when changing the rotating plane of the magnetic field. This is because the perpendicular walk lacks magnetic anisotropy in the x-y plane.

4.5.13 CARGO CAPTURE AND RELEASE

Development of a ball-shaped object for cargo capture. A ten-second exposure to 4800 mW/cm^2 of white LED illumination resulted in extremely rapid bending of a cross-shaped sample containing SP1. This bending process was maintained for two minutes after the light was dimmed to 4.7 mW/cm^2, resulting into a round-ball shape. This suggests that the kinetics for isomerizing the population of hydrophilic merocyanine moieties to hydrophobic spiropyran were faster than the rate of water expulsion. There was a corresponding lag between the isomerization and the de-swelling of the hydrogel. A cargo can be wrapped inside the ball-like geometry if it is placed underneath the object prior to photoactuation.

Preparation of alginate sphere cargo. A 2.5 wt% (w/v) solution of high molecular weight sodium alginate (Protanal HF 120) was made by mixing solid sodium alginate with MilliQ. The mixture was then agitated until dispersed and then allowed to sit overnight to allow for full hydration of the alginate polymers. The hydrated mixture was then agitated and mixed via a dual syringe mixing method and centrifuged to remove bubbles. The sodium alginate solution was put into a 10 mL plastic syringe and extruded through varying needle gauges. Needles used had stainless steel circular tips with flat ends. A NE-300 Just Infusion syringe pump was used to extrude the alginate solution into a gelation solution of 1 M $CaCl_2$. The solution immediately gelled into a spherical shape upon contact with the gelation solution. These gels were allowed to soak in the $CaCl_2$ solution for up to 30 minutes or until they sank to the bottom of the solution, implying full ionic crosslinking. The beads were then washed in MilliQ to remove excess ions. Size and shape of alginate beads was determined by extrusion speed and needle gauge. The cargo used in this paper is 2.4 mm in diameter with a density of 1.38 g/cm^3. Fully ionic crosslinked alginate bead is non-charged and non-sticky to the hydrogel objects. The sticky cargo was obtained by soaking this bead in MilliQ water for at least 4 h to remove some cations, resulting in a negatively charged surface, which could stick to the hydrogel objects due the electrostatic interaction with positively charged merocyanines (MCH^+).

5 IMAGING SUPRAMOLECULAR MORPHOGENESIS WITH CONFOCAL LASER SCANNING MICROSCOPY AT ELEVATED TEMPERATURES

5.1 OBJECTIVE AND SIGNIFICANCE

The morphogenesis of supramolecular assemblies is a highly dynamic process that has only recently been recognized and our understanding of this phenomenon will require imaging techniques capable of crossing scales. Shape transformations depend both on the complex energy landscapes of supramolecular systems and the kinetically controlled pathways that define their structures and functions. We report here the use of confocal laser scanning microscopy coupled with a custom-designed variable temperature sample stage that enables *in-situ* observation of such shape changes. The sub-micrometer resolution of this technique allows for real-time observation of the nanostructures in the native liquid environments in which they transform with thermal energy. We use this technique to study the temperature-dependent morphogenic behavior of peptide amphiphile nanofibers and photocatalytic chromophore amphiphile nanoribbons. The variable temperature confocal microscopy technique demonstrated in this work can sample a large volume and provides real-time information on thermally induced morphological changes in solution.

5.2 BACKGROUND

Confocal laser scanning microscopy (CLSM), first reported 60 years ago,[153] has enabled life and materials scientists to obtain three-dimensional spatial information with superior axial resolution.[154] In life sciences, the versatile sample mounting environment allows observation of live cells with multiple sets of fluorophore probes at the micrometer length scale. Use of CLSM and its related techniques, such as fluorescence recovery after photobleaching (FRAP)[155,156], Förster resonant energy transfer (FRET) microscopy[157–159], and super-resolution imaging[160–162], is also useful in materials science, particularly for studying soft matter.[163–169] As one recent example, the effect of ice crystal formation on colloidal assembly processes was carefully studied using controlled temperature gradients under CLSM on a sample stage custom-designed for cooling below room temperature.[170,171]

Formation of supramolecular assemblies are highly pathway dependent, and thermal processing is commonly used to tailor the resulting superstructures.[63,169,172–174] While the characterization of end products can shed light on the energy landscapes associated with the assemblies, real-time observation of structural transformation has been largely achieved using ensemble information such as light or X-ray scattering, partly due to the challenges associated with imaging technique limitations. CLSM can provide direct visual observation of the transformation pathways for meso- and microscale assemblies and has been utilized to observe samples at elevated temperatures, including the formation of supramolecular helical ribbon structures upon cooling from 50°C,[170] as well as a number of food science applications above 55°C.[175–180] However, such use of CLSM has been limited by challenges associated with sample temperature uniformity, heat transfer and damage to the objective lens. Careful sample stage design is essential for enabling *in-situ* heating of liquid samples near microscope objective lenses with short working distances.

In this paper, we describe the use of CLSM to visualize the dynamic nature of supramolecular assemblies at temperatures at which structure transformations have been observed with bulk characterization techniques and ex-situ methods. To enable this technique, we fabricated a custom-designed variable temperature (VT) stage for CLSM. The aluminum enclosure allows for temperature uniformity and spatial stability, and samples can be heated without damaging microscope objectives.

5.3 RESULTS AND DISCUSSION

5.3.1 STAGE DESIGN

We designed a VT stage consisting of commercial thermoelectric modules mounted between a 0.25-inch-thick aluminum heat distribution plate and aluminum water blocks with room temperature circulated water (Figure 5.1). An aluminum sample holder plate with a channel machined to accommodate square cross-section sealed glass capillaries is screwed to the bottom of the heat distribution plate. Due to the short working distance typically employed for high-resolution optical imaging, we designed the holder plate such that the aluminum on the bottom of the sample channel has a thickness of 100 µm. The low emissivity of aluminum and the clearance afforded by this sample holder plate design allows for imaging of samples at elevated temperatures without significant heat transfer to the objective lens. Infrared (IR) imaging of the objective lens after focusing 500 µm deep into a sample (~345 µm separation between the top of the lens and the bottom surface of the sample holder plate) heated to 95°C showed a maximum temperature of 28°C at the lens surface of the Nikon CFI Plan Apochromat VC 20X with a numerical aperture of 0.75 and the working distance of 1.0 mm, which was used throughout the experiments shown in this work (Video 5.1). We note that the use of air objectives limits the numerical apertures of the objective lenses used, and in turn reduces the maximum achievable resolution. A 2 mm diameter viewport is machined through the center of both the heat distribution plate as well as the sample holder to allow for bright-field imaging in addition to fluorescence imaging on an inverted microscope. The VT stage assembly is fixed to a turntable stage bracket, which is then pinned to the outer adapter plate for the microscope by a set of plastic clips (Figure 5.1b). This turntable design allows for easy rotation of samples during the polarized optical microscopy. Capillary sealing is achieved through a UV-cured resin and is compatible with aqueous solutions and heating up to 95°C.

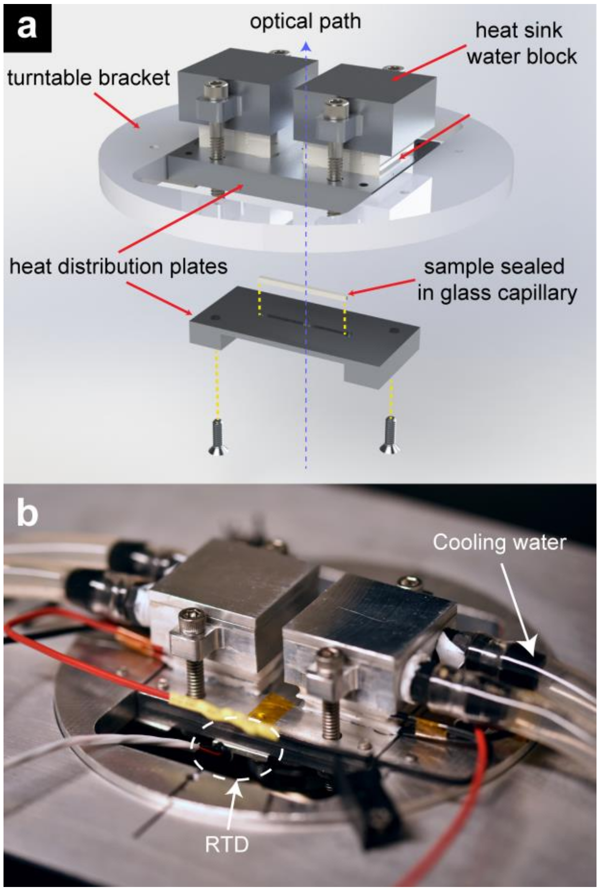

Figure 5.1 Design of variable-temperature stage assembly. a) CAD-rendered schematic. b) Photograph of stage assembly mounted on an inverted confocal laser scanning microscope.

5.3.2 TEMPERATURE PROFILE AND STAGE STABILITY

To characterize the thermal uniformity of the VT stage, we conducted IR imaging of the stage heated to 95°C (Figure 5.2). Due to the low emissivity of the aluminum, we adhered 70 µm thick polyimide tape to the bottom surface of the sample holder plate as an IR emitter. The temperature profile shows a standard deviation in temperature of 0.18°C over a distance of 20 mm (Figure 5.2b). Additionally, the temperature stability of the stage was characterized for a ramp cycle to 95°C with a 1°C/min ramp rate (Figure 5.2c). The deviation from the set point temperature measured by a thermocouple sealed with UV-cured resin in a glass capillary increases with temperature due to a small thermal gradient between the sample and the resistance temperature detector (RTD) used for temperature feedback control. The temporal stability of the stage temperature measured at the RTD is within 0.1°C and is commensurate with the readability of the thermoelectric controller used.

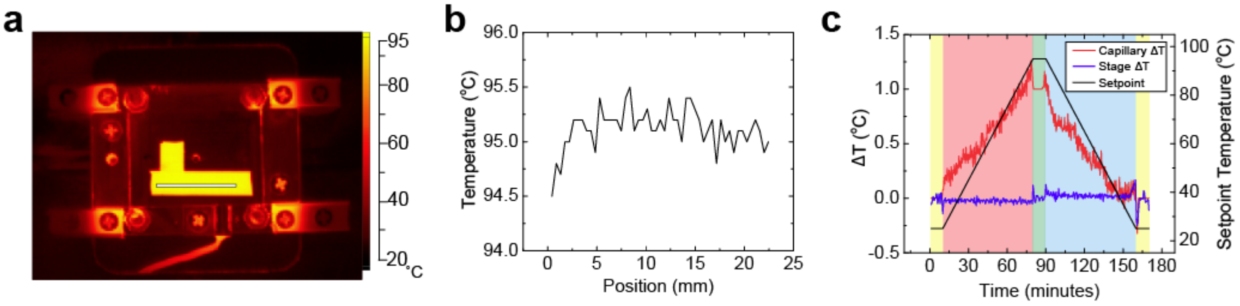

Figure 5.2 Thermal uniformity and stability characterization. a) IR camera image of the bottom of the stage assembly heated to 95 ˚C with polyimide tape adhered to the surface. b) Line cut of temperature profile along line depicted in (a). c) Deviation from the set point temperature measured inside a capillary sample (red) and the resistance temperature detector sensor bolted to the stage (blue). The background color indicates heating (red), cooling (blue), dwelling (green), and isothermal segments (yellow).

The vertical stability of the stage during heating and cooling was measured by recording the objective lens position with the hardware-based autofocus function in the Nikon A1R microscope (Figure 5.3). There is a 10-µm vertical drift over a heating cycle between room temperature and 95°C, which we associate with thermal expansion of the VT stage components and the glass capillary. This drift can be compensated with the use of autofocus systems during observation of our samples.

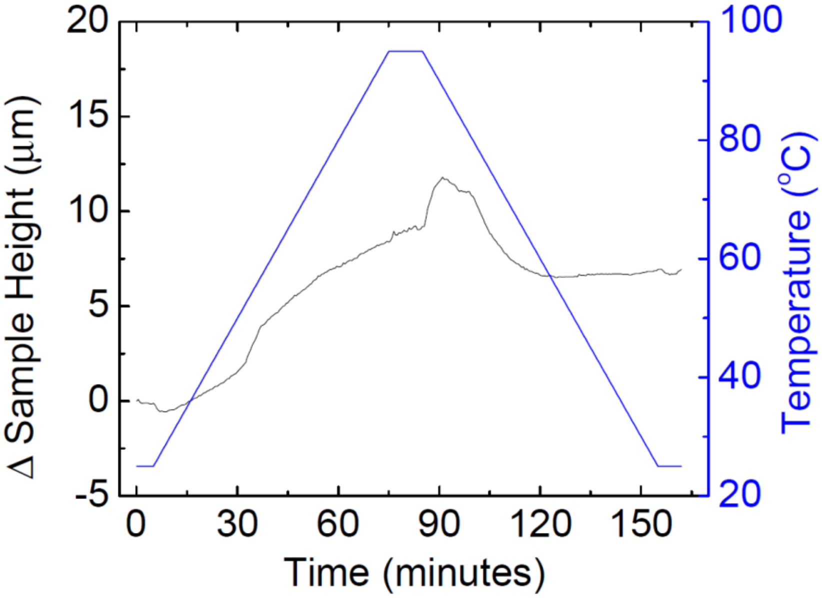

Figure 5.3 Sample height tracked with image metadata during a heating cycle to 95 °C with Nikon's Perfect Focus System enabled.

5.3.3 PATHWAY-DEPENDENT STRUCTURAL TRANSFORMATION OF PEPTIDE AMPHIPHILE SUPRAMOLECULAR ASSEMBLIES

The VT stage allows for *in-situ* observation of supramolecular shape changes in solution at temperature ranges previously not readily accessible by commercial systems. Tantakitti *et al.* have described the pathway-dependent structural transformations of peptide amphiphile (PA) nanofibers upon thermal annealing in solutions of varying ionic strengths.[174] Below a critical ionic strength, the thermodynamically preferred product of the supramolecular assembly is a short nanofiber (~150 nm length). At higher ionic strengths, long PA nanofibers become the thermodynamically stable state, accessible by thermal annealing to 80°C. However, the lengths of these nanostructures have been difficult to measure accurately due to limitations in the field of view for transmission electron microscopy (TEM). A number of bulk characterization techniques have been used to characterize PA assemblies during thermal annealing, but none have been used to directly image PA nanofibers at high temperature. We thus aimed to directly observe the structural transformation of PA nanofibers using VT-CLSM.

To visualize the transition between long nanofibers and short nanofibers, we used the fluorescent dye-labeled analogs of the PAs as the tracer molecules and performed the VT-CLSM. Specifically, we formed the long nanofibers by thermally annealing an 20 mM aqueous solution of the C_{16}-$V_3A_3K_3$-$CONH_2$ PA containing 2 mol% of the same molecule containing 5-carboxy X-rhodamine (5-ROX) as a fluorescent label (C_{16}-$V_3A_3K_4$-(5-ROX)-$CONH_2$) (molecular structures in Figure 5.4). 5-ROX is known to maintain its fluorescence quantum yield at elevated temperature, which arises from the closed ring conformation around the amines that restricts its rotation.[181,182] We then diluted the resulting PA solution to 2 μM, which corresponds to a low ionic strength that favors short fibers or micelles.[174] These small objects are challenging to observe even using the immersion objective lenses in CLSM due to the limited size and their Brownian motion in solution. We then performed VT-CLSM on the diluted sample and analyzed the resulting images with respect to the number of fibers within the field of view (Figure 5.5, Video 5.2a,b). Since the fiber fluorescence intensity is qualitatively distinguishable from the background, it was possible to apply the iterative intermeans automatic segmentation algorithm for this data set to detect the nanofibers.[183] We were able to observe a dilute solution of long fibers upon initially loading the sample at room temperature (Figure 5.5a). After two hours at 80°C, the number of observable fibers decreases (Figure 5.5b). Use of a more temperature-dependent dye such as rhodamine B led to similar observations of steadily decreasing number of fibers upon annealing, although the signal to noise ratio is significantly reduced at higher temperatures (Figure 5.6).[181,184] We note that some long nanofibers do remain after thermal annealing, observed both in CLSM and cryo-TEM (Figure 5.7). Nonetheless, the overall steady decrease in the number of observable long fibers over the course of the heat treatment (Figure 5.5d) indicates that long nanofibers are indeed thermodynamically unfavorable and the transition to short fibers or micelles occurs on the time scale of hours.

(a)

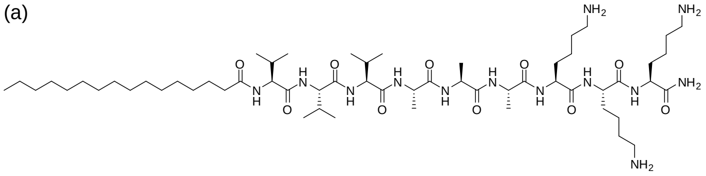
NH2
NH2
O
H
N
NH2
NH2

(b)

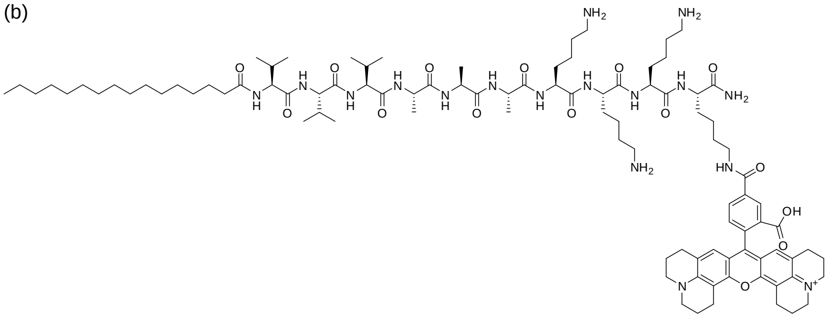
NH2
NH2
NH2
NH2
HN
O
OH
N
N+

(c)

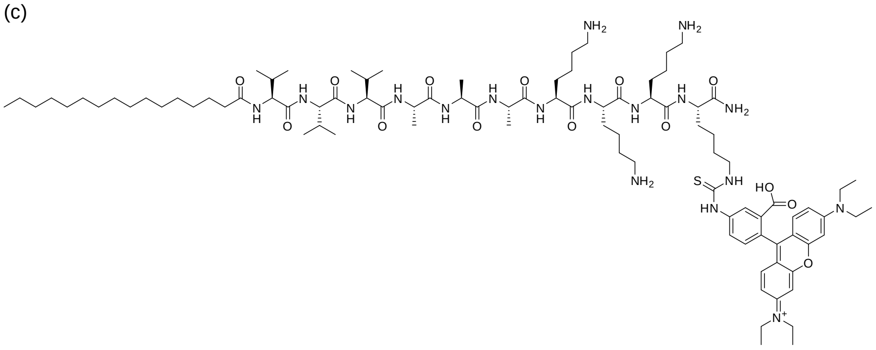
NH2
NH2
NH2
NH2
S
NH
HN
HO
O
N
O
N+

(d)

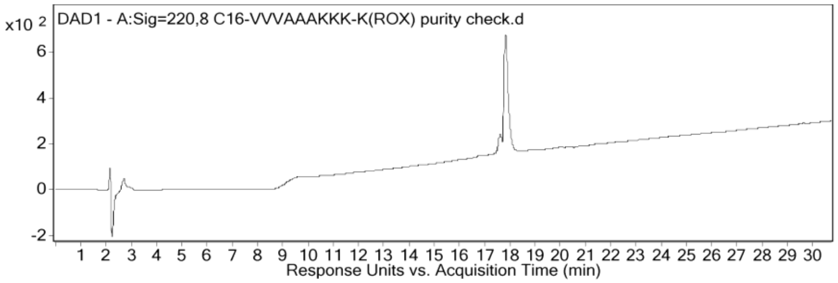
x10 2
DAD1 - A:Sig=220,8 C16-VVVAAAKKK-K(ROX) purity check.d
6
4
2
0
-2
1 2 3 4 5 6 7 8 9 10 11 12 13 14 15 16 17 18 19 20 21 22 23 24 25 26 27 28 29 30
Response Units vs. Acquisition Time (min)

(e)

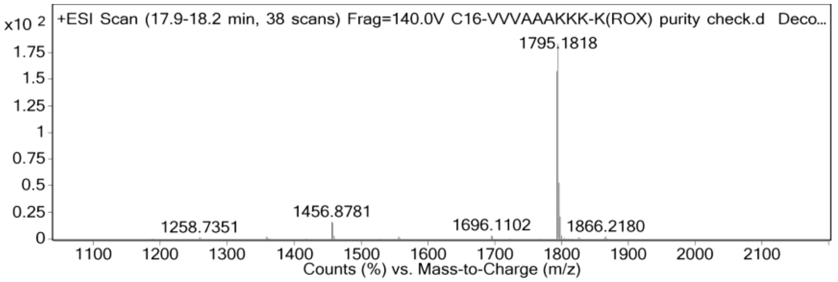
x10 2
+ESI Scan (17.9-18.2 min, 38 scans) Frag=140.0V C16-VVVAAAKKK-K(ROX) purity check.d Deco...
1795.1818
1.75
1.5
1.25
1
0.75
0.5
0.25
0
1258.7351
1456.8781
1696.1102
1866.2180
1100 1200 1300 1400 1500 1600 1700 1800 1900 2000 2100
Counts (%) vs. Mass-to-Charge (m/z)

Figure 5.4 Peptide amphiphile molecular structures. (a) C16-V3A3K3-CONH2. (b) C16-V3A3K4-(5-ROX)-CONH2. (c) C16-V3A3K4-(RBITC)-CONH2. (d-e) LC-MS trace of the C16-V3A3K4-(5-ROX)-CONH2.

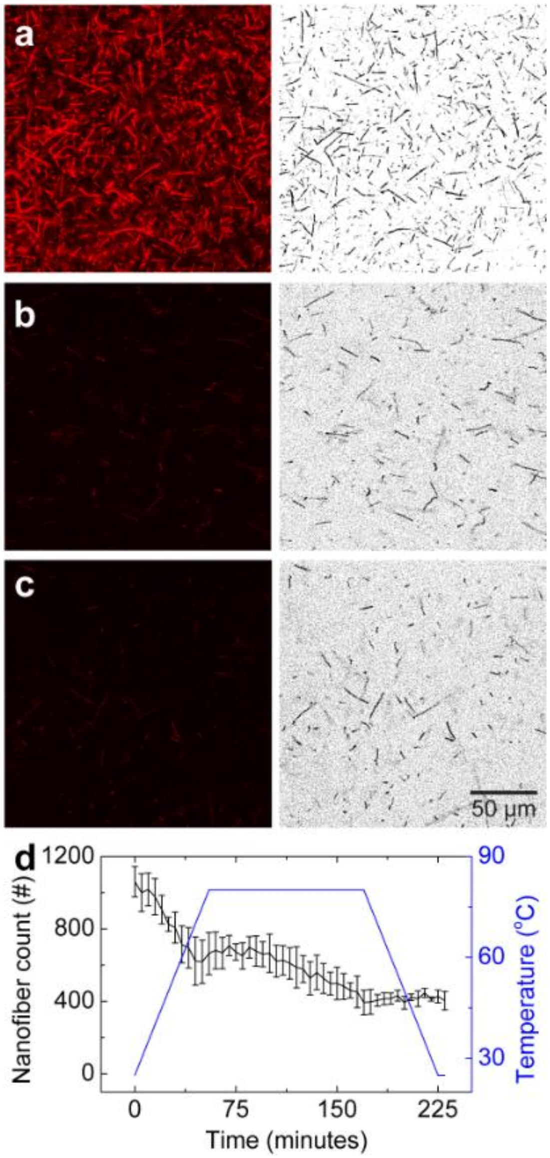

Figure 5.5 Confocal images of 5-ROX fluorophore-labeled peptide amphiphile nanofibers upon thermal annealing. a) Sample in initial state at 25˚C. b) Sample after annealing at 80˚C for two hours. c) Sample after cooling to 25˚C. For (a-c), images on the right show the background-subtracted, thresholded images from the left panels. d) Plot of the annealing temperature profile (blue) plotted with the number of long nanofibers. (black).

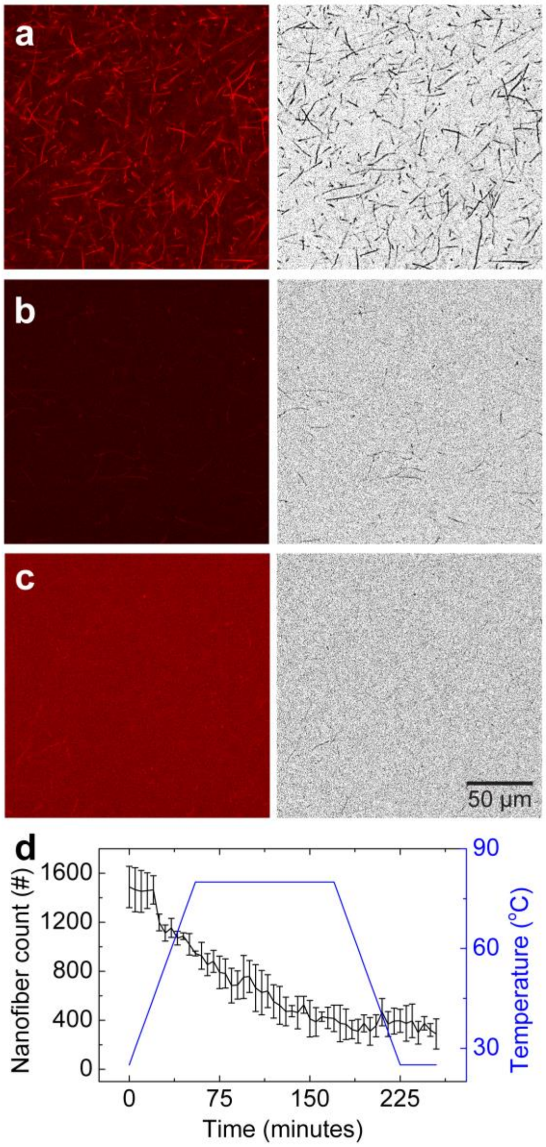

Figure 5.6 Confocal images of rhodamine B fluorophore-labeled peptide amphiphile nanofibers upon thermal annealing. a) Sample in initial state at 25 ˚C. b) Sample after annealing at 80 ˚C for two hours. c) Sample after cooling to 25 ˚C. For (a-c), images on the right show the background-subtracted, thresholded images from the left panels. d) Plot of the annealing temperature profile (blue) plotted with the number of long nanofibers. (black).

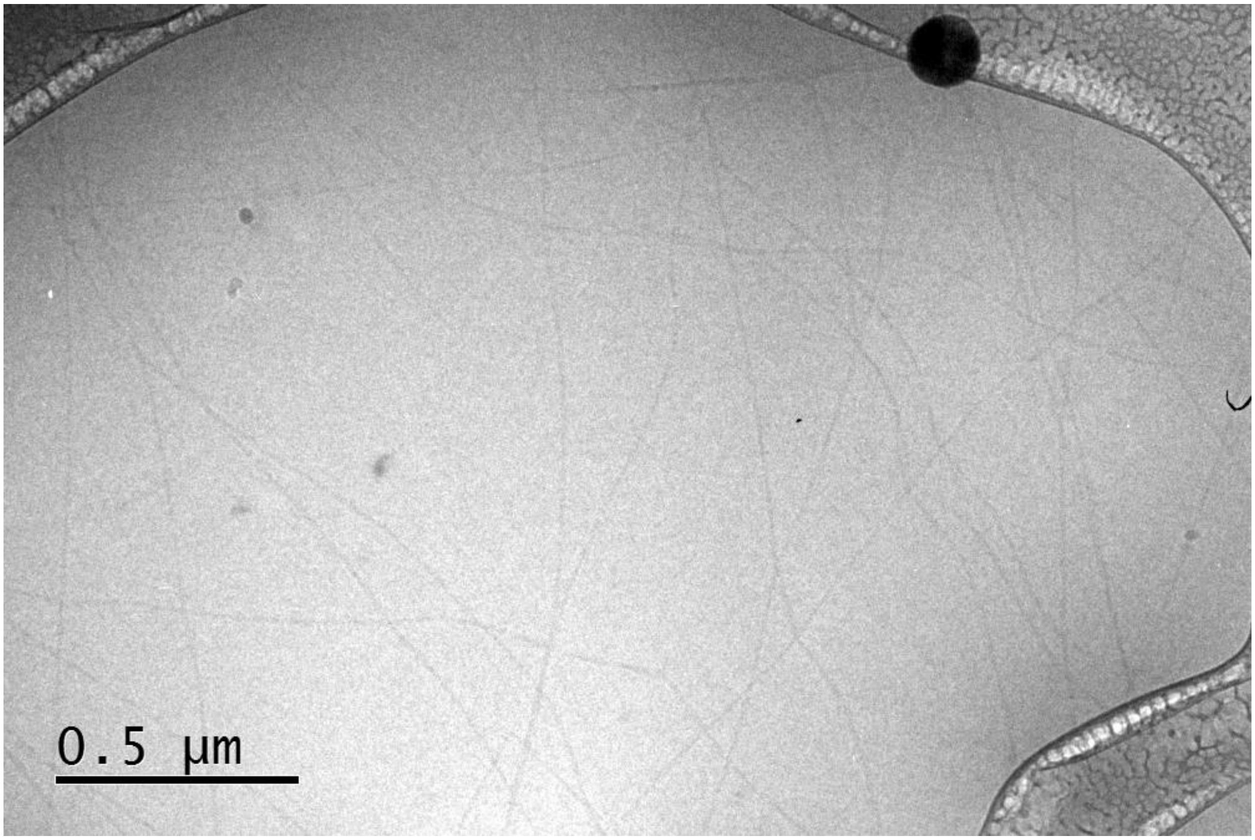

Figure 5.7 Cryogenic TEM image showing existence of some long PA nanofibers after thermal annealing at 80 °C for two hours.

5.3.4 NUCLEATION AND GROWTH OF CHROMOPHORE AMPHIPHILE RIBBON-LIKE SUPRAMOLECULAR ASSEMBLIES

Our group has also recently explored supramolecular shape transformations of chromophore amphiphiles into supramolecular ribbons in water, which have yielded functional three-dimensional scaffolds for photocatalytic reactions.[62,130,185–187] The perylene monoimide chromophore amphiphiles (PMI-CAs) possess large dipole-dipole and π-π interactions, as well as strong amphiphilicity imparted by the conjugation of the hydrophobic perylene core to carboxylated alkyl tails. The interactions and amphiphilicity drive self-assembly of these molecules in water forming crystalline ribbon-like assemblies that are of interest in photocatalysis since they support the diffusion of excitons upon light exposure. We have recently discovered that some PMI-CA derivatives form kinetically trapped amorphous assemblies that crystallize upon heating in the presence of salt.[62,187] Due to the fluorescent nature of the crystalline supramolecular assemblies and large size of the final thermally annealed structures, we expected that our VT confocal stage would provide a unique method to observe heating-induced nucleation and growth behavior of a PMI-CA containing a 3-pentylamino group substituent on the 9 position of the perylene core (PMI-CA-1, Figure 5.8a).[187]

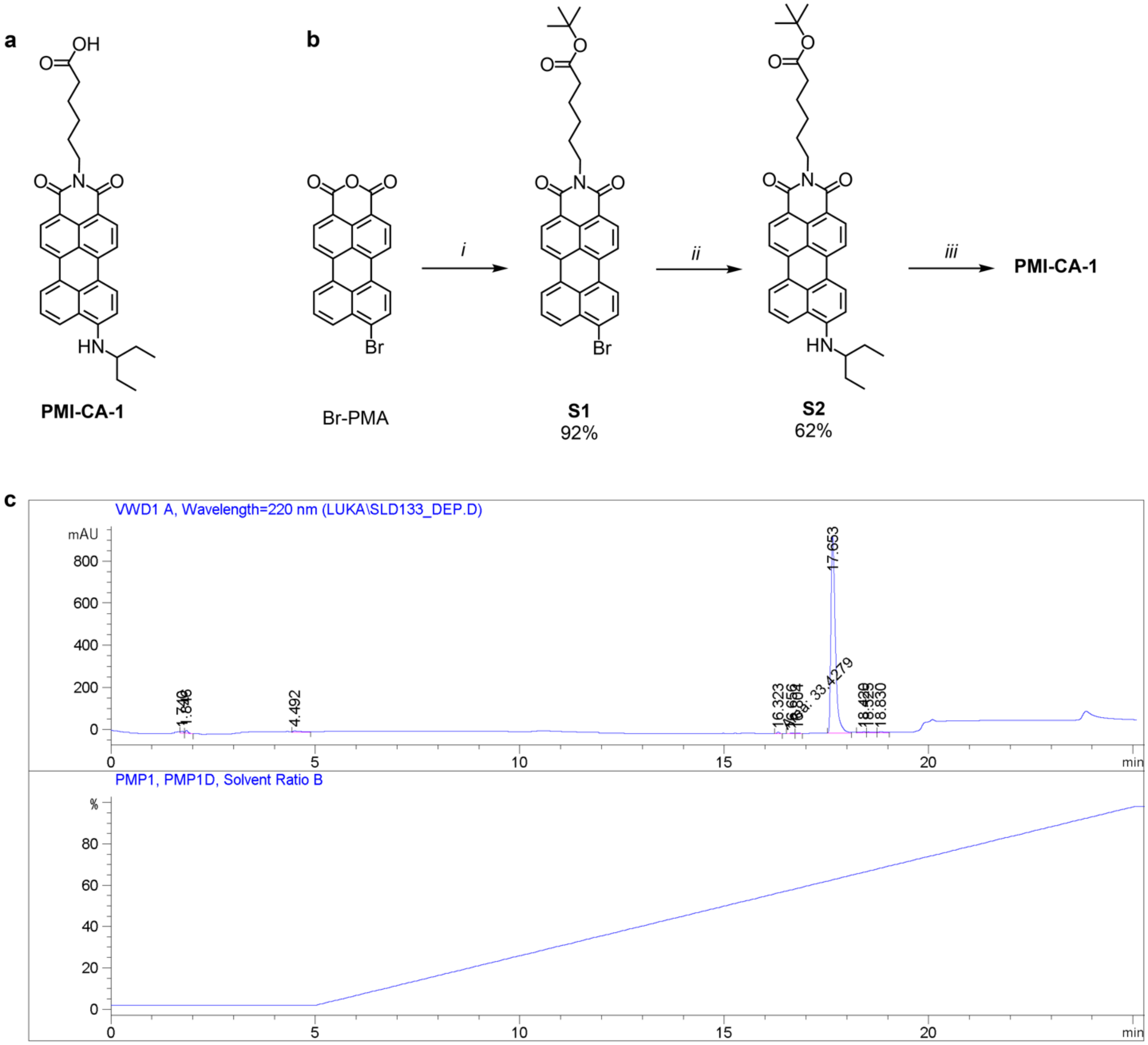

Figure 5.8 Structure, synthesis and purity of PMI-CA-1. a) Chemical structure of PMI-CA with a 3-pentylamino group on the 9-position of the perylene core (PMI-CA-1). b) Synthetic approach for the synthesis of PMI-CA-1. Reagents and conditions: (i) tert-butyl 6-aminohexanoate, tert-butanol, DMF, 100 °C, N2, 16 h; (ii) 3-pentylamine, [Pd2(dba)3], BINAP, NaOtBu, dry toluene, 90 °C, N2, 16 h; (iii) CF3COOH, toluene (1:1 v/v), r.t., 8 h. c) HPLC trace of PMI-CA-1 (eluted using H2O and CH3CN as solvent A and solvent B, respectively, both with 0.1% NH4OH; peaks at 20 and 24 minutes appear in the blank run as well).

While the solution of amorphous PMI-CA-1 is initially non-fluorescent, the crystalline assemblies formed by heating exhibit fluorescence with broad maxima of 790 and 820 nm (Figure 5.9) due to the formation of charge-transfer excitons and the corresponding excimer-like emission. This allows observation of the crystalline assemblies with CLSM as the sample is thermally annealed. We tracked the nucleation and growth of PMI-CA-1 crystalline assemblies utilizing VT-CLSM with a 640 nm laser, observing fluorescence at 700 nm (Figure 5.10, Figure 5.11, Video 5.3). Upon heating to 95°C, we observed the formation of crystalline structures with widths on the order of 1-2 µm and varying lengths (Figure 5.10a). These thin ribbon-like supramolecular structures continue to grow in both length and width, forming bright edges at the narrow ends of the ribbons (Figure 5.10b). After 15 minutes of heating at 95°C, the growth of ribbon widths slows down, indicating the completion of crystallization (Figure 5.10c). Notably, the three-dimensional reconstruction image clearly reveals that the ribbon assemblies are curled and distributed in random orientation (Figure 5.10d, Video 5.4). Close-inspection of individual ribbon assemblies during annealing also shows their growth front forming a curl and an increase in length on the time scale of minutes (Figure 5.10e, Video 5.5). We note that previous work on the PMI-CA-1 showed flat ribbon-like structures that are one molecule thick, as confirmed *via* atomic force microscopy (AFM) and TEM imaging.[187] The three-dimensional nature of these assemblies and their formation is only observable with the combination of a large field of view and sub-micrometer volumetric resolution of the VT-CLSM technique. Figure 5.10f-h compares the same area under multiple optical imaging modalities: the bright field image (Figure 5.10f) and the cross-polarized optical image (Figure 5.10g) both capture the curled ribbons, but they both suffer from signals from out-of-focus planes, and only show qualitative information due to the difference in light absorption depending on the ribbon orientation. In contrast, signals in the CLSM image (Figure 5.10h) are semi-quantitative, allowing for 3D reconstruction. CLSM images of the PMI-CA-1 solution annealed in a vial and subsequently transferred to the glass cover slip exhibit flat ribbon morphologies due to shear-induced uncurling from convection and pipetting during sample preparation (Figure 5.12), consistent with the previous observation that these two-dimensional crystalline materials are one molecule thick and thus mechanically flexible.[187] We do not know at this time why the assemblies curl but speculate that supramolecular packing of the asymmetric molecules substituted in the 9 position might be optimized in this morphology (Figure 5.8a). Similar induction of ribbon curvature was observed in another PMI-CA assembly where the 9-position of the perylene unit was substituted with a propyl group, although the radius of curvature for those ribbons was much smaller and can only be confirmed via AFM and TEM.[186]

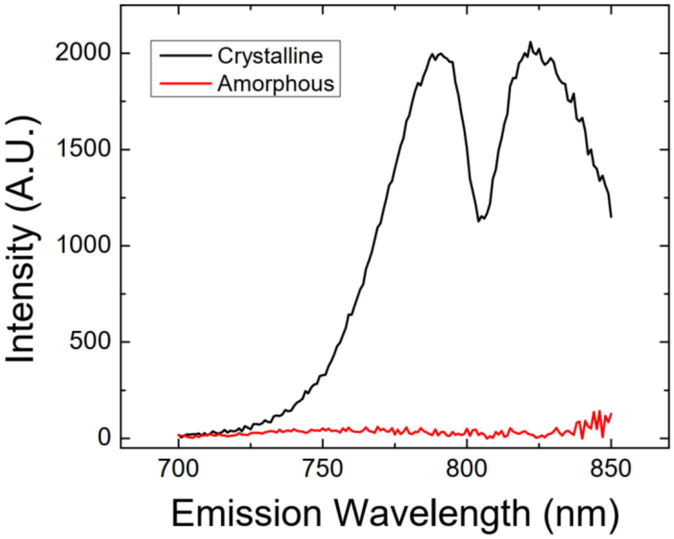

Figure 5.9 Fluorescence emission spectrum of crystalline vs. amorphous PMI-CA-1 with an excitation wavelength of 650 nm.

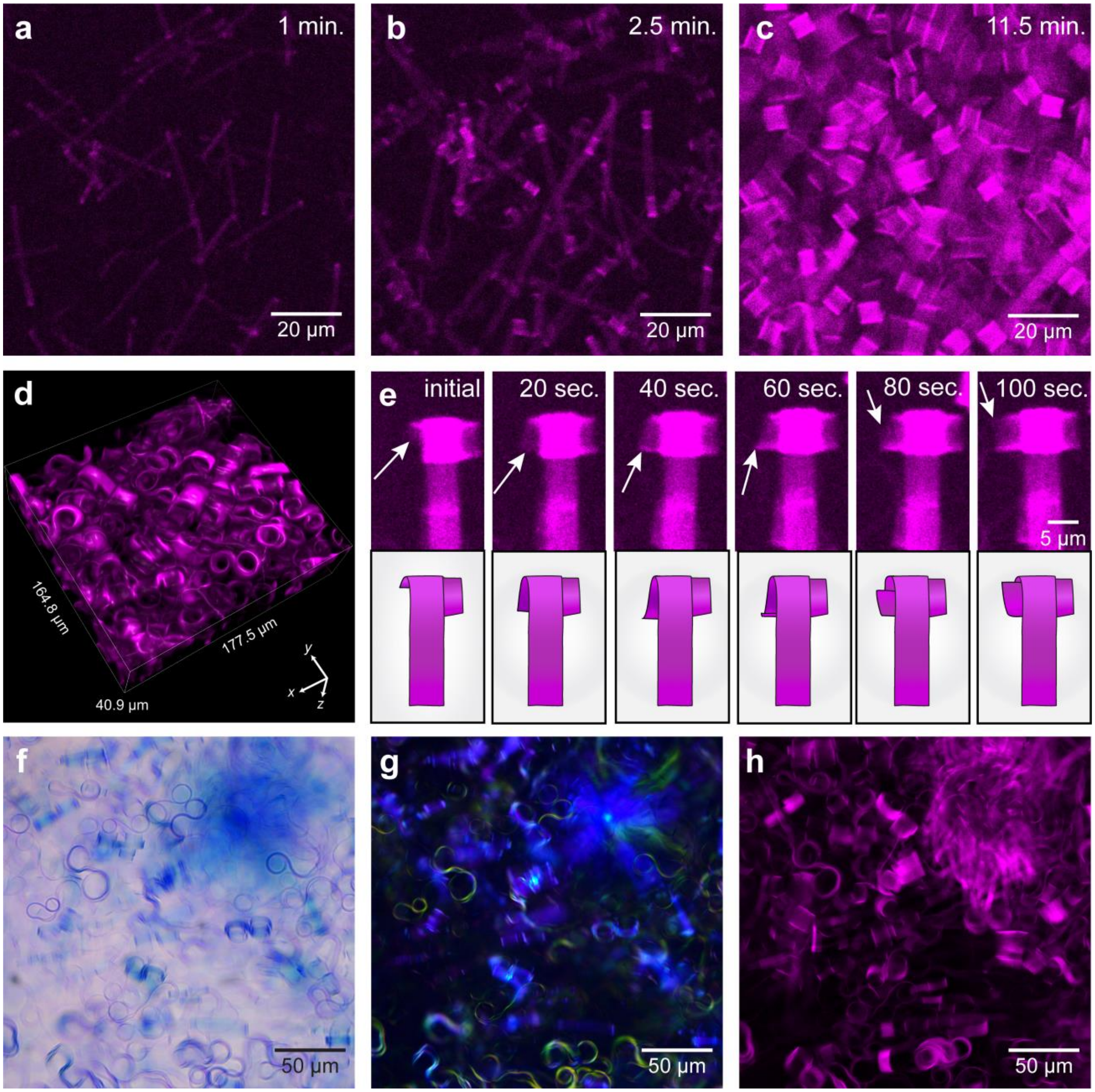

Figure 5.10 Confocal images of chromophore amphiphile nanostructure nucleation and growth under isothermal annealing at 95˚C: a) Initial appearance of fluorescent thin ribbons. b) Short edges of ribbon curl upon continued elongation. c) Final mixture of curled ribbons after 15 minutes of annealing. d) 3D reconstruction of the sample after annealing at 95˚C. e) Growth of ribbon curling front over time at 95˚C (top) and corresponding schematic of curled ribbon supramolecular assemblies (bottom). f-h) Comparison of optical micrographs with different configurations of the sample after annealing at 95˚C. f) Bright field transmission optical micrograph. g) Cross-polarized transmission optical micrograph. h) CLSM image from the same focal plane.

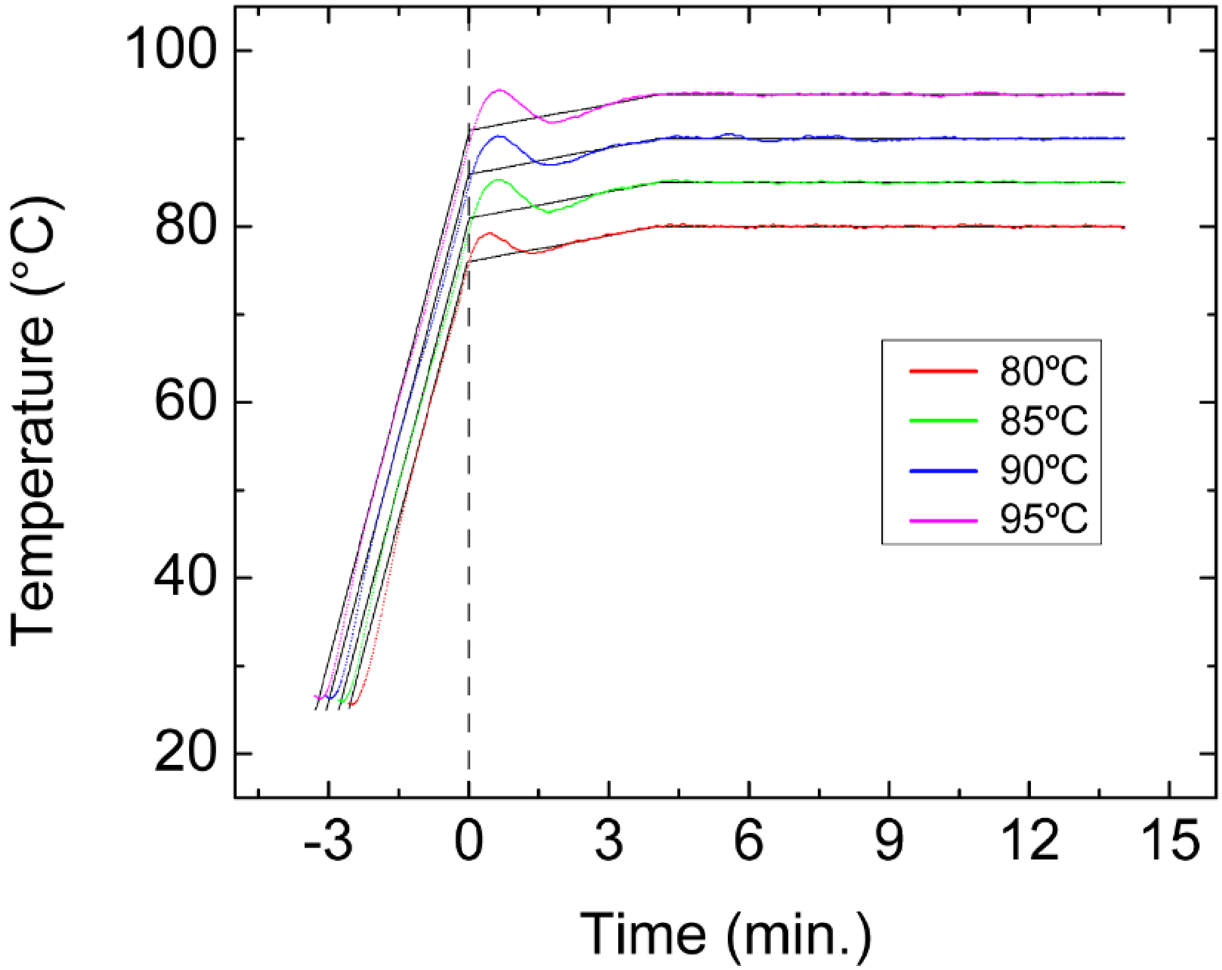

Figure 5.11 Temperature profiles of the PMI-CA-1 annealing steps. In order to minimize the overshoot in the PID controller, we split the heating steps into two segments: the first segment ramps at 20 °C/min, while the second segment ramps at 1 °C/min. The overshoot from the first ramp segment brings the heating stage to the dwell setpoint upon the completion of the first segment, which we take as time 0 for the isothermal heating process.

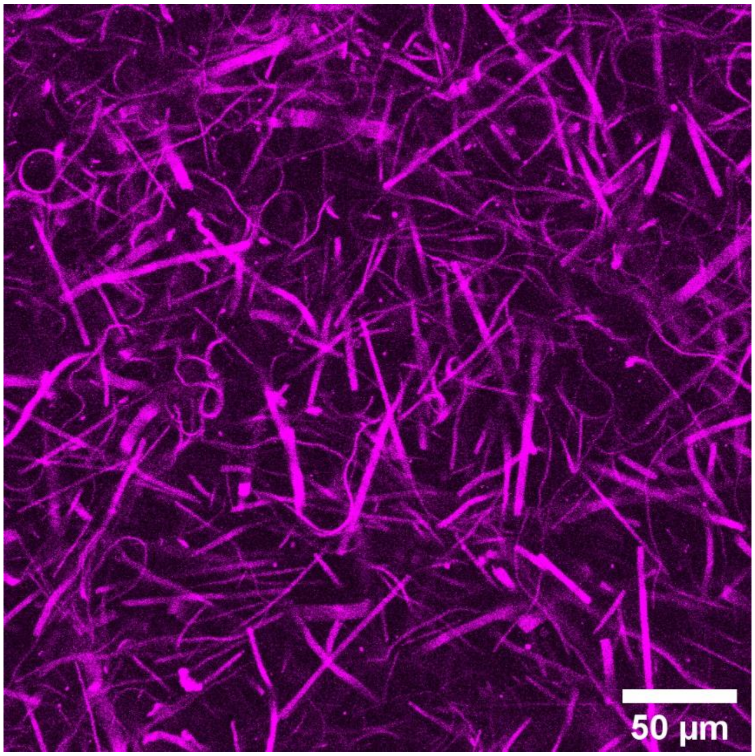

Figure 5.12 Bulk-annealed and crystallized PMI-CA-1 ribbons pipetted onto a glass coverslip.

Having established the ability to observe growth of PMI-CA-1 crystalline nanostructures, we focused our attention on the growth rate of individual ribbon widths as a function of annealing temperature and correlated it with the overall conversion rate to a crystalline phase. In previous studies, the extent of conversion from amorphous to crystalline material for PMI-CA-1 was measured by tracking the absorption peak intensity at 750 nm.[187] A recent study shows for two-dimensional peptide crystals on a molybdenum sulfide surface that the rapid dimerization and adsorption of the monomers lead to a row-by-row crystal growth.[188] While the limited resolution of the CLSM precludes such molecular-scale studies, growth rates in anisotropic objects can reveal dominant growth orientation and key factors that control their shapes. To reduce translational motion and more easily track individual ribbons, the glass capillaries were coated with poly(diallyldimethylammonium chloride) to create positively charged surfaces and electrostatically bind the PMI-CA-1 (Video 5.6). We point out that the rates of growth are not significantly altered by the presence of the polymer-coated surface (Figure 5.13). At 95°C, the ribbon width initially grows linearly with time but begins to plateau after fifteen minutes, indicating depletion of amorphous precursor and completion of crystallization (Figure 5.14a). This plateauing in growth coincides with the completion of crystallization, as observed by UV-Vis spectroscopy while the transformation occurs in the capillary (Figure 5.14a, Figure 5.15). We note that some of the ribbons nucleate later and grow at similar rates but stop growing at a given time point. This is indicative of feed-limited growth conditions. We thus speculate that the initially fibrous assemblies that are observed in cryo-TEM (Figure 5.16) attach to crystalline ribbons in row-to-row fashion. The growth rate of this initial linear regime was tracked at a temperature range between 80 and 95°C and was found to increase from 0.133 to 0.54 µm/min (Figure 5.14b), consistent with our previous study revealing an enthalpy driven amorphous to crystalline transition.[187] The difference in growth rate is reflected in the final widths of the ribbons as well, with wider ribbons forming at 95°C compared to lower temperatures (Figure 5.17, Video 5.7). We have also observed that in addition to homogeneous nucleation of individual ribbons, we see aggregates of ribbons radiating from a single point (Figure 5.18, Video 5.8). This phenomenon is noticeably reduced when the sample is filtered before capillary loading, indicating the presence of heterogeneous nucleation points that may be removed by filtration. The ribbons nucleating from these regions tend to be thinner and less regularly curled, suggesting local depletion of the amorphous starting material and physical crowding effects. We suspect that this heterogeneous nucleation can also occur in bulk annealing, leading to larger polydispersity in ribbon widths. While the overall crystallization kinetics was previously described as thermally activated,[187] this is the first time that we have tracked the growth of these assemblies along a specific dimension using an imaging technique. The current observation that the width growth rate is constant as a function of time satisfies one of the requirements to obtain uniform-size supramolecular ribbons. This mechanism is analogous to a living polymerization in which termination of growth does not happen. We envision that this mechanism, combined with control over nucleation events, may provide a strategy to obtain supramolecular nanostructures with monodisperse width.

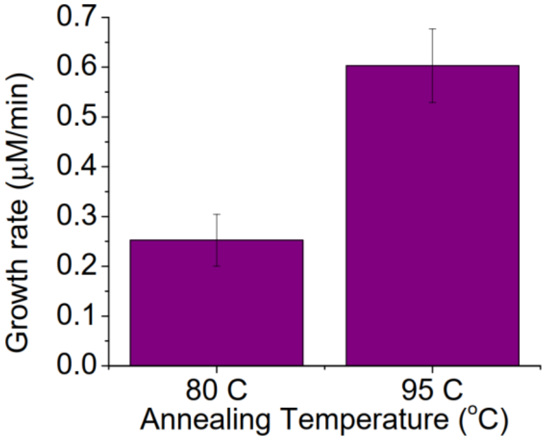

Figure 5.13 Ribbon width growth rate vs. annealing temperature in pristine glass capillaries.

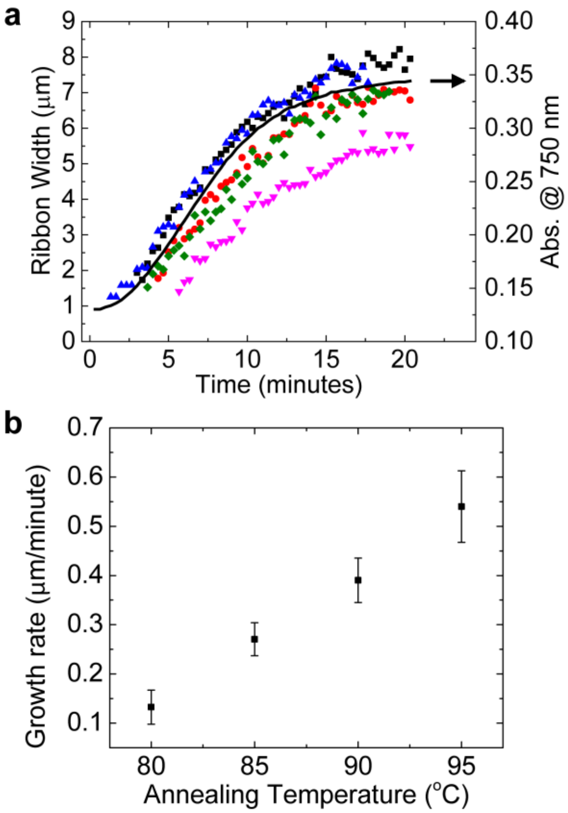

Figure 5.14 Temperature dependence of chromophore amphiphile nanostructure size and growth rate. a) Individual ribbon width tracking during annealing at 95°C (scatter plots, left axis) overlaid with absorbance at 750 nm wavelength (line plot, right axis). b) Growth rate of ribbon widths vs. annealing temperature.

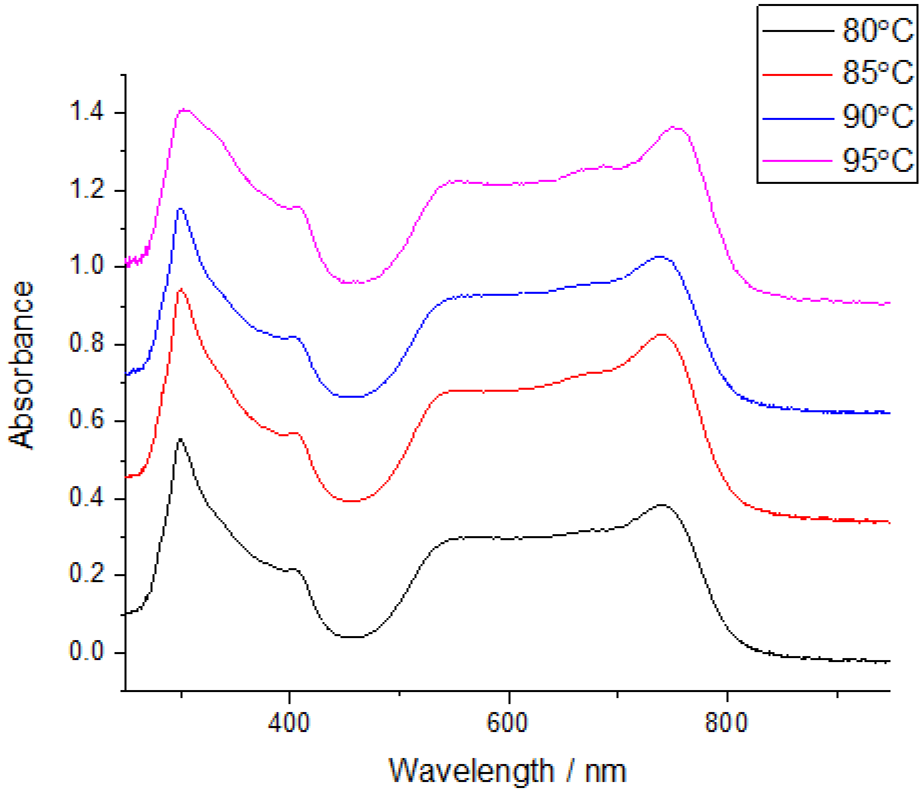

Figure 5.15 UV-Vis spectra of the solutions of of PMI-CA-1 after annealing in capillaries.

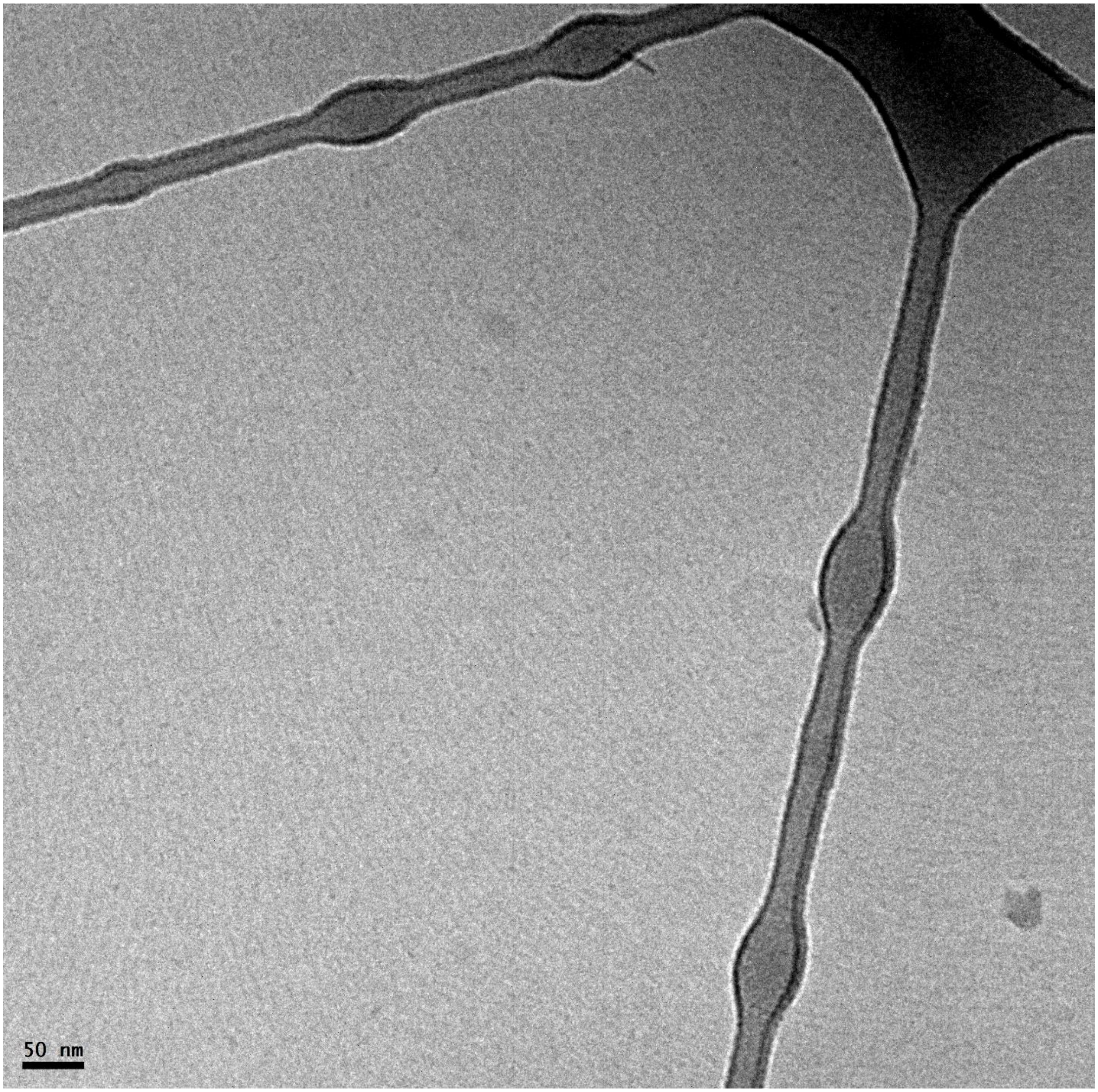

Figure 5.16 Cryo-TEM image of amorphous PMI-CA-1 solution at 6 mM.

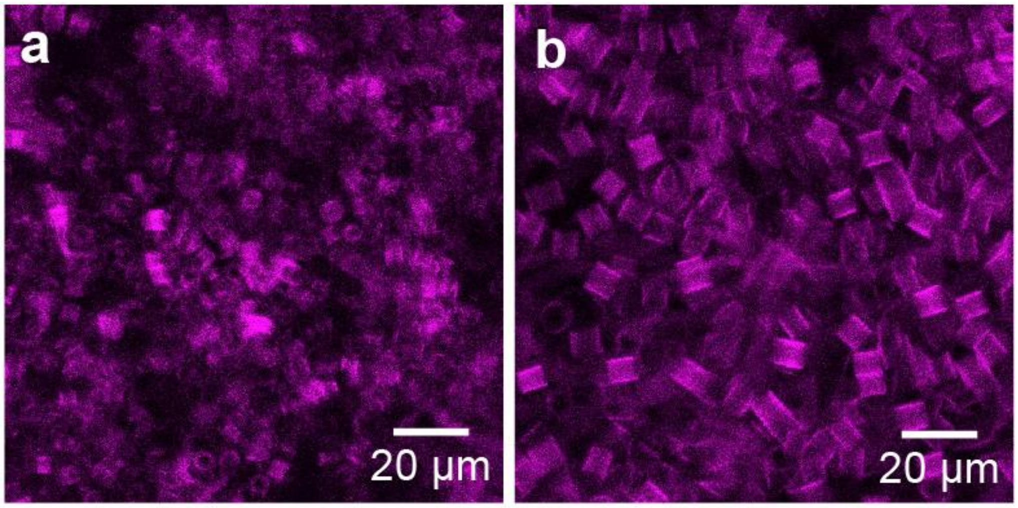

Figure 5.17 PMI crystallites post-annealing at a) 80 °C vs. b) 95 °C.

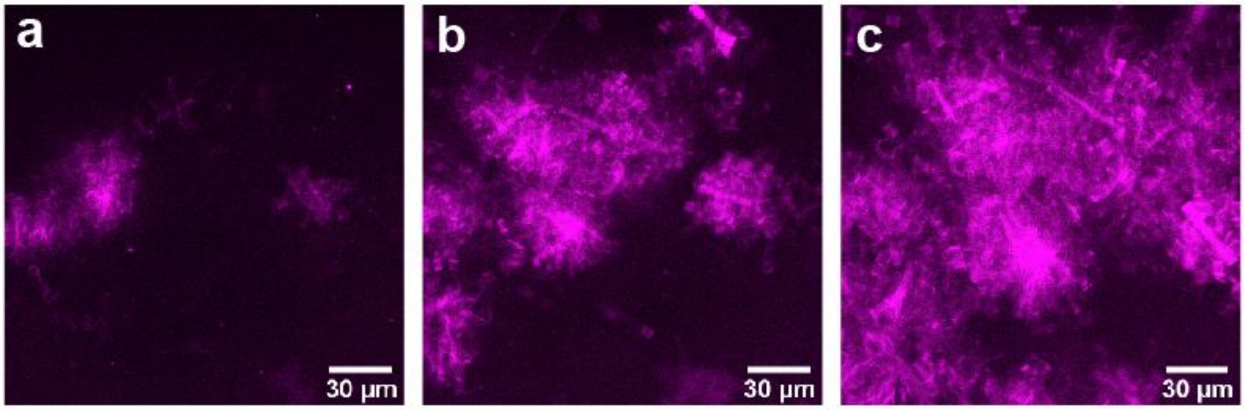

Figure 5.18 Heterogeneous aggregate formation during annealing of PMI-CA-1 at 95 °C. a) Initial formation of aggregate upon nucleation of crystallites, b) continued growth of aggregates over 2 minutes, c) polydispersity of ribbon sizes observed 5 minutes after initial appearance of aggregates.

5.4 CONCLUSIONS

We have developed a variable-temperature stage design for confocal laser scanning microscopy that enables *in-situ* observation of supramolecular transformations of fluorescent assemblies in liquids at elevated temperatures. This technique allowed us to survey a large sample volume with 3D sub-micrometer resolution in real-time. In conjunction with other in-situ characterization methods, including liquid-cell transmission electron microscopy, variable-temperature x-ray scattering and variable-temperature spectroscopic techniques, we anticipate that experiments with this technique will contribute to a better understanding of energy landscapes and dynamic transformation pathways in supramolecular assemblies. We also envision that many well-established CLSM accessories and techniques, such as piezoelectric motors, resonant scanners, FRAP and FRET, can also be applied with the VT stage to reveal temperature-dependent behavior of supramolecular exchange dynamics and photophysics.

5.5 MATERIALS AND METHODS

5.5.1 MATERIALS

The peptide amphiphiles C_{16}-$V_3A_3K_3$-CONH$_2$ and C_{16}-$V_3A_3K_3$-K(RBITC)-CONH$_2$ were synthesized in the Peptide Synthesis Core in the Simpson Querrey Institute at Northwestern University according to previously reported protocols.[189] For the synthesis of C_{16}-$V_3A_3K_3$-K(5-ROX)-CONH$_2$, first C_{16}-V_3A_3K(Boc)$_3$-K(Mtt) (0.0625 mmol) was synthesized. The 4-methyltrityl (Mtt) protecting group was removed by shaking in 15 mL of 1% trifluoroacetic acid (TFA) and 4% triisopropylsilane (TIS) in DCM twice for five minutes each time. The resin was then rinsed twice with DMF and once with DMF with 1 mL of diisopropylethylamine (DIEA). Next, 5-ROX-NHS ester (Lumiprobe) (50 mg, 0.079 mmol, 1.27 eq) was dissolved in 4 mL DMF with DIEA (2 mL, 11.5 mmol, 184 eq.). The solution of 5-ROX was added to the PA on resin and this solution was shaken for 48 h. Upon completion of the reaction, the PA was cleaved of the resin by shaking in a solution of 95% TFA, 2.5% TIS and 2.5% water. After cleavage of the PA, the solvent was evaporated under reduced pressure. The crude product was precipitated out by the addition of cold diethyl ether (~25 mL). This precipitate was filtered and washed with ether before taking it up in 9 mL water with 0.1% TFA. This solution was purified using reversed-phase high-performance liquid chromatography (HPLC, Waters Prep 150) in a water/acetonitrile gradient containing 0.1%

TFA with a starting condition of 2% acetonitrile. The fraction of acetonitrile was increased linearly in 45 min to 65% acetonitrile in water. Purified PAs were lyophilized and stored at −20 °C until further use. The purity of the PAs was confirmed to be >90% by electrospray ionization mass spectrometry in positive mode (ESI-MS, Agilent 6510 Q-TOF) and analytical HPLC (Agilent 1260 Infinity, eluted with a gradient of 0.1% formic acid in water: 0.1% formic acid in acetonitrile from 95:5 to 5:95 in 30 min).LC-MS traces of the final product is shown in Figure 5.4d-e.

The perylene monoimide chromophore amphiphile (PMI-CA-1) used for experiments in Figure 5.9, Figure 5.10a-c, Figure 5.10e, Figure 5.11-Figure 5.18Figure 5.14, and Videos 5.3, Videos 5.5-5.8 was synthesized according to previously reported procedures.[187] PMI-CA-1 used for experiments in Figure 5.10d, Figure 5.10f-h and Video 5.4 were synthesized via a modified route as described below.

N-(*tert*-butyl 6-hexanoate)-9-bromoperylene-3,4-dicarboximide (S1): To a suspension of 9-bromoperylene-3,4-dicarboxylic anhydride[190] (0.60 g, 1.50 mmol) in *tert*-butanol and DMF (50 mL, 1:9 v/v) was added *tert*-butyl 6-aminohexanoate[191] (0.70 g, 3.74 mmol) under N_2 and was stirred at 100 °C for 16 hours. The reaction mixture was then cooled to r.t. and was poured into 0.1 M aq. HCl (250 mL) and the mixture was left stirring for 15 minutes. The suspension was then filtered, washed with 0.1 M aq. HCl (1 × 50 mL), H_2O (3 × 50 mL) and left to dry under vacuum. The solid was recovered with CH_2Cl_2 and purified by column chromatography (SiO_2, CH_2Cl_2 → CH_2Cl_2/MeOH 99:1 *v/v*) to obtain pure product as dark red solid (0.78 g, 92% yield). ^{1}H-NMR (500 MHz, $CDCl_3$): δ 8.41 (d, J = 8.0 Hz, 1H), 8.39 (d, J = 8.0 Hz, 1H), 8.24 (d, J = 7.8 Hz, 1H), 8.18 (d, J = 8.2 Hz, 1H), 8.17 (d, J = 8.2 Hz, 1H), 8.10 (d, J = 8.1 Hz, 1H), 7.97 (d, J = 8.2 Hz, 1H), 7.76 (d, *J* = 8.1 Hz, 1H), 7.60 (t, *J* = 7.8 Hz, 1H), 4.17 (t, *J* = 7.8 Hz, 2H), 2.26 (t, *J* = 7.5 Hz, 2H), 1.77 (p, *J* = 7.6 Hz, 2H), 1.69 (p, *J* = 7.6 Hz, 2H), 1.49 (p, *J* = 7.6 Hz, 2H), 1.44 (s, 9H). ^{13}C-NMR (126 MHz, $CDCl_3$): δ 173.32, 163.82, 163.81, 136.31, 136.17, 132.88, 131.46, 131.38, 131.23, 130.04, 129.51, 129.50, 128.95, 128.92, 128.16, 126.22, 126.18, 124.28, 123.60, 121.35, 121.34, 120.62, 120.34, 80.21, 40.50, 35.75, 29.93, 28.35, 28.05, 26.91, 25.12. HRMS (ESI+): *m/z* for $C_{32}H_{28}BrNO_4$ calcd. 569.1202, found 592.1089 $[M+Na]^+$.

N-(*tert*-butyl 6-hexanoate)-9-((3-pentyl)amino)perylene-3,4-dicarboximide (S2): One day prior to the reaction, 3-pentylamine and toluene were dried (3-pentylamine was dried over KOH pellets and then distilled, while toluene was dried over CaH_2 and then distilled) and were stored over previously activated molecular sieves, under N_2 and dark. An oven-dried Schlenk flask was charged with compound S1 (150.0 mg, 0.26 mmol), tris(dibenzylideneacetone)dipalladium(0) (12.0 mg, 13.1 μmol), BINAP (16.1 mg, 26.2 μmol) and sodium *tert*-butoxide (67 mg, 0.69 mmol) and placed under vacuum for 15 minutes. After introduction of N_2 into the flask, dry 3-pentylamine (153 uL, 1.31 mmol) and dry toluene (40 mL) were added and the flask was degassed by evacuation and purging with N_2 (3 ×). The reaction mixture was stirred for 16 h at 90 °C and then cooled down to r.t. and then passed through a silica plug (CH_2Cl_2/acetone, 97:3 *v/v*). Purification of the mixture by column chromatography (SiO_2, $CH_2Cl_2 \rightarrow CH_2Cl_2$/acetone, 98:1.5 *v/v*) gave pure product as a dark blue solid (93.7 mg, 62% yield). ^{1}H-NMR (500 MHz, DMSO-d_6): δ 8.73 (d, *J* = 7.6 Hz, 1H), 8.60 (d, *J* = 8.5 Hz, 1H), 8.56 (d, *J* = 8.4 Hz, 1H), 8.49 (d, *J* = 8.9 Hz, 1H), 8.39 (d, *J* = 8.1 Hz, 1H), 8.32 (d, *J* = 8.3 Hz, 1H), 8.27 (d, *J* = 8.5 Hz, 1H), 7.65 (t, *J* = 8.0 Hz, 1H), 6.98 (d, *J* = 8.4 Hz, 1H), 6.84 (d, *J* = 9.2 Hz, 1H), 4.05 (t, *J* = 7.4 Hz, 2H), 3.71 – 3.62 (m, 1H), 2.19 (t, *J* = 7.2 Hz, 2H), 1.70 (p, *J* = 7.3 Hz, 4H), 1.64 (p, *J* = 7.5 Hz, 2H), 1.54 (p, *J* = 7.3

Hz, 2H), 1.37 – 1.29 (m, 2H), 1.35 (s, 9H), 0.95 (t, *J* = 7.4 Hz, 6H). ^{13}C-NMR (126 MHz, DMSO-*d*$_6$): δ 172.22, 163.12, 163.00, 148.81, 139.00, 137.76, 131.52, 130.86, 129.94, 128.94, 128.22, 128.19, 125.65, 125.58, 124.98, 122.43, 119.07, 118.89, 116.53, 115.56, 114.73, 105.60, 79.35, 55.45, 34.58, 27.70, 27.25, 26.40, 25.87, 24.41, 10.58. HRMS (ESI+): *m/z* for $C_{37}H_{40}N_2O_4$ calcd. 576.2988, found 577.3068 $[M+H]^+$.

N-(6-hexanoic acid)-9-((3-pentyl)amino)perylene-3,4-dicarboximide (PMI-CA-1): A vial was charged with compound S2 (60.0 mg, 0.10 mmol), trifluoracetic acid and toluene (5.0 mL, 1:1 *v/v*) and the solution was stirred at r.t for 8 h. The solvents were removed under reduced pressure. The solid was then suspended in toluene and dried (2 ×), followed by suspension in CH_3OH and drying again. After drying the solid under high vacuum overnight (54.0 mg, quant.), the analytical purity was checked by HPLC (>97%, Figure 5.8c). ^{1}H-NMR (500 MHz, DMSO-*d*$_6$): δ 11.95 (bs, 1H), 8.65 (d, *J* = 7.5 Hz, 1H), 8.56 (d, *J* = 8.0 Hz, 1H), 8.45 (d, *J* = 8.0 Hz, 1H), 8.41 (d, *J* = 8.9 Hz, 1H), 8.31 (d, *J* = 8.0 Hz, 1H), 8.23 (d, *J* = 8.0 Hz, 1H), 8.16 (d, *J* = 8.0 Hz, 1H), 7.60 (t, *J* = 8.0 Hz, 1H), 6.94 (d, *J* = 7.5 Hz, 1H), 6.79 (d, *J* = 9.0 Hz, 1H), 4.06 (t, *J* = 7.5 Hz, 2H), 3.70 – 3.62 (m, 1H), 2.24 (t, *J* = 7.5 Hz, 2H), 1.69 (p, *J* = 7.5 Hz, 4H), 1.60 (p, *J* = 7.5 Hz, 2H), 1.55 (p, *J* = 7.5 Hz, 2H), 1.39 – 1.36 (m, 2H), 1.35 ppm (d, *J* = 6.5 Hz, 6H). ^{13}C-NMR (126 MHz, DMSO-*d*$_6$): δ 174.89, 163.52, 163.40, 149.22, 139.37, 138.13, 131.87, 131.22, 130.32, 129.30, 128.65, 128.61, 126.06, 125.96, 125.37, 122.88, 119.44, 119.28, 116.91, 115.97, 115.20, 106.02, 55.92, 33.98, 27.79, 26.86, 26.58, 24.75, 11.05 ppm. HRMS (ESI+): *m/z* for $C_{33}H_{32}N_2O_4$ calcd. 520.2362, found 521.2435 $[M+H]^+$. Characterization in accordance with literature.[192]

All other chemicals and solvents were of ACS grade or higher and were purchased from commercial sources. Borosilicate capillaries were purchased from VitroCom, product numbers 8100 (1 mm square ID, 0.2 mm wall thickness, 1.4 mm square OD) and 5010 (rectangular ID, 0.1 mm path length, 1 mm outer width, 0.07 mm wall thickness). UV curable resin was purchased from Loon Outdoors (UV Clear Fly Finish Thick). Syringe filters (0.45 micrometer) were purchased from Tisch Scientific.

6061 aluminum for the VT-stage body and adapter plates were purchased from McMaster-Carr. Thermoelectric modules (item #: 03111-9L31-06CG) and water blocks (item #: WBA-1.00-0.49-AL-01) were purchased from Custom Thermoelectric, LLC. Thermoelectric temperature controller (item #: ATEC302C2BMN) and H-bridge amplifier (item #: FTX300) were purchased from Accuthermo Technology Corp. 15V DC power supply unit (item #: 285-1805-ND) was purchased from Digi-Key Electronics. Surface bolt-on RTD sensor (item # RTD-830) was purchased from Omega Engineering, Inc. The electronic elements were assembled in accordance to the manuals attached to the controller, with four thermoelectric elements in series. Two thermoelectric elements were placed per each pocket of the aluminum block below the water block using the thermal conductive grease, with the hot side facing the aluminum block and the cold side contacting the water block. The computer-aided design (CAD) files for the machined aluminum parts can be downloaded from https://doi.org/10.21985/n2-8z3s-0550.

5.5.2 METHODS

5.5.2.1 PA Solution

Lyophilized powder of C_{16}-$V_3A_3K_3$-$CONH_2$ PA and fluorescently tagged C_{16}-$V_3A_3K_3$-K(5-ROX)-$CONH_2$ or C_{16}-$V_3A_3K_3$-K(RBITC)-$CONH_2$ PA were weighed out in a 100:2.5 mass ratio and subsequently dissolved in 1,1,1,3,3,3-hexafluoroisopropanol (HFIP) to promote co-assembly. HFIP was then removed by evaporation under a stream of nitrogen and subsequent vacuum drying overnight. The resulting dry film was then re-dissolved with ultrapure water to a total PA concentration of 8.8 or 20 mM. This solution was annealed at 80 °C and slow-cooled overnight to form the initial long nanofibers. Solutions were diluted to 1.6-2 μM by volume with water and pH adjusted to 4.5 with HCl_{aq} or $NaOH_{aq}$ before loading into capillaries for VT-CLSM analysis.

5.5.2.2 PMI-CA-1 solutions

PMI-CA-1 powder was dissolved in 4:1 by volume dichloromethane/methanol to make 6 mM solutions and aliquoted into conical microcentrifuge tubes with volumetric pipets and allowed to form dry films by evaporation overnight. Aqueous PMI-CA-1 solutions were prepared freshly before VT-CLSM analysis by dissolving dried films with 6 mM aqueous NaOH solutions and diluted to 5 mM PMI-CA-1 with 300 mM aqueous NaCl. The resulting solution of 5 mM PMI-CA-1 and 50 mM NaCl was filtered through a 0.45 μm pore-size syringe filter at a rate of 100 μL/min using a syringe pump before loading into capillaries for VT-CLSM.

5.5.2.3 Capillary Loading

1 mm × 1 mm square ID capillaries were used for PA solutions and were sealed with UV-cured resin on one end before injecting the sample solutions with a syringe needle. The other end was then sealed in the same manner. For the PMI-CA-1 samples, thinner rectangular ID capillaries were used to reduce assembly motion. PMI-CA-1 solutions were introduced into the capillaries by capillary action and sealed on both ends with UV cured resin. For the thin rectangular capillaries, 1.15 × 1.4 mm rectangular-cross section aluminum spacers were used to fill the inner cavity above the thin capillaries in the sample holder plate of the stage and improve thermal contact with the top heat distribution plate.

5.5.2.4 PDDA-coating of capillaries

1 wt% aqueous PDDA (Sigma-Aldrich, medium molecular weight, average M_w 200,000-350,000, diluted from 20 wt%) solutions were wicked into rectangular ID capillaries and allowed to incubate for one minute before thorough flow-through rinsing with ultrapure water. Capillaries were dried under hot air flow with a heat gun prior to loading with PMI-CA-1 solutions.

5.5.2.5 Confocal Laser Scanning Microscopy (CLSM)

Confocal laser scanning microscopy was performed using a Nikon A1R confocal system fitted on an Eclipse Ti-E inverted microscope. A 20× CFI Plan Apochromat VC objective lens with a numerical aperture of 0.75 and working distance of 1 mm was used to image samples. Where applicable, the Nikon Perfect Focus System (PFS) was used to maintain focus on a specific sample height. Data was acquired using NIS-Elements AR software from Nikon and was analyzed using the Fiji package of ImageJ.[183] For the 3D reconstruction in Figure 5.10d, the images were intensity-corrected and thresholded using NIS-Elements AR software.

5.5.2.6 PA nanofiber disassembly counting analysis

The background was first subtracted using the background subtraction tool with a rolling ball radius of 5 pixels (0.21 micrometer pixel size). The image stack was then thresholded using the default thresholding tool and method, converting the stack to binary images. Finally, the Analyze Particles tool was used to count particles with a size of 2 μm^2 or greater and a circularity of 0.00 to 0.50, yielding hundreds of particles in each time frame with an elongated ellipsoidal shape and a length of ~2 μm or greater (the outlines of thresholded nanofibers was measured to be an average of 1 μm in width). Three separate PA samples were measured and counted with this method to generate the plots in Figure 5.5d.

5.5.2.7 Cryogenic Transmission Electron Microscopy

Cryo-TEM was performed using a JEOL 1230 TEM working at 100 kV accelerating voltage. Samples were plunge frozen using a Vitrobot Mark IV (FEI) vitrification robot at room temperature at 95-100% relative humidity. 7.5 μL of sample solution were placed undiluted on 300-mesh copper grids with lacey carbon support, blotted, and plunge frozen into liquid ethane. Samples were transferred into a liquid nitrogen bath and placed into a Gatan 626 cryo-holder through a cryo-transfer stage. Images were acquired using a Gatan 831 CCD camera.

5.5.2.8 PMI-CA-1 fluorescence measurement

Fluorescence spectroscopy was performed using an ISS PC1 Spectrofluorometer in an L-configuration. Amorphous PMI-CA-1 solution for the fluorescence measurements were prepared by dissolving the PMI-CA-1 in 11 mM in water with 1 molar equivalence of NaOH. Crystalline PMI-CA-1 solution was prepared by taking the amorphous PMI-CA-1 solution and mixing with 300 mM $NaCl_{aq}$ at a volume ratio of 5:1, creating a 9.6 mM PMI-CA-1 solution in 50 mM $NaCl_{aq}$, and subsequently annealing the solution in a sealed vial at 95 °C for 30 min. These solutions were diluted 200 times immediately prior to measurement using water and 50 mM $NaCl_{aq}$, respectively, and were measured in 10 mm quartz cuvettes, excited at 650 nm, and fluorescence intensity recorded between 700 and 850 nm.

5.5.2.9 PMI-CA-1 ribbon width tracking analysis

Images of PMI-CA-1 grown on PDDA were captured at a rate of 3 frames per minute. Measurement of ribbon widths were performed using the Fiji package of ImageJ, with at least five ribbons counted per annealing temperature.

5.5.2.10 PMI-CA-1 VT UV-vis spectroscopy in VT-CLSM stage

The VT-CLSM stage was mounted on a 3D-printed adapter that situates the circular apertures in line with optical fiber ends for a QEPro UV-Vis spectrometer equipped with a DH-2000-BAL balanced deuterium tungsten source (Ocean Optics). The dark reference and baseline spectra were obtained with water-filled rectangular capillaries (solution thickness 100um), followed by real time data collection as the samples in rectangular capillaries underwent thermal treatment. The spectra were recorded on the OceanView (Ocean Optics) software with dark reference and baseline subtraction.

6 SUMMARY AND FUTURE OUTLOOK

6.1 SUMMARY

The work presented in this thesis describes the development and transformation of shape in soft and hybrid materials from the nano- to macroscale. Analogous to morphogenesis in biological organisms, the novel materials investigated in this work changed shape across scales as a function of their designed molecular precursors, external stimuli such as light and magnetic fields, chemical environment, or temperature. The bio-inspired approaches highlighted in this work provide pathways towards complex architectures across length scales, as well as examples of structural modification with post-synthetic processing and external stimulation. These approaches will have great importance in controlling materials properties and performance in energy storage and conversion applications with nano- to microscale morphologies, as well as novel actuation modes and semi-autonomous response to external stimuli for soft robotic materials.

6.2 FUTURE OUTLOOK

The organic-$Co(OH)_2$ based supercapacitor electrodes described in Chapter 2 have limited commercial potential because of their degradation during cycling and the low energy storage capacity compared to state-of-the-art Li-ion batteries. However, there has been much interest in reducing the size of Li-ion cathode materials to increase surface area for higher discharge-rate capability and improving electrode packing density when mixed with traditional > 5 μm diameter cathode particles. In private correspondence with industry professionals in cathode materials manufacturing, synthesis of nanoscale precursors for metal-oxide based cathode materials (e.g.

lithium cobalt oxide, lithium manganese oxide, lithium nickel manganese cobalt oxide, lithium nickel cobalt aluminum oxide) is cost-prohibitive for use in commodity lithium ion batteries. Utilizing low-cost surfactants during chemical precipitation synthesis of these precursor materials to form nanostructured hybrids may be an effective and scalable route towards higher power and more energy dense lithium ion batteries.

While applications of the hierarchical metallic architectures were not specifically tested and described in this dissertation, NiNWs grown on nickel foam may prove useful as current collectors in both solid-state batteries and photocatalytic electrodes. In future studies, more sophisticated control over NiNW mesh density and formation within the porous nickel foam must be developed to optimize the performance of devices in which they are incorporated.

For composites and soft robots utilizing NiNWs as the magnetically responsive component, further work on complex patterning of the NiNWs (e.g. tri-axial control of orientation combined with stereolithographic 3D printing) may yield even more interesting modes of locomotion. This approach should be guided by the theoretical framework and simulations developed in Chapter 4, as prediction of actuation geometries and locomotion will allow faster and more rational design of both the NiNW patterning and the initial fabricated geometry.

In order to enable locomotion of robotic objects out of water, the design of any robotic object must take into consideration the lack of buoyant forces. The hydrogel objects described in Chapter 4 cannot support their own weight without the assistance of buoyant forces. Two different approaches for solving this problem are increasing elastic modulus of the photoactive matrix surrounding the ferromagnetic NiNW component or reducing the size of the hydrogel objects.

Increasing the modulus of the photoactive matrix can be accomplished either through adding additional stiffening components to the hydrogel such as laponite[193] or changing the matrix completely to photoactive LC elastomers. In the case of the addition of stiffening modifiers to the photoactive hydrogel, care must be taken to ensure that the photoactuation mechanism is not disrupted by adding ionicity that neutralizes the electrostatic charge of the MCH+ moieties. For any increase in stiffness of the object, an increase in NiNW concentration is required in order to produce the larger magnetic torques and deform the stronger surrounding matrix. There is likely a limit to the maximum NiNW concentration that can be incorporated before sensitivity to light stimuli is impaired by the opacity of the NiNWs. Simulations of both photoactuation and magnetic actuation will need to be performed to optimize the concentration of NiNWs, the resulting light attenuation of the material, and the elastic modulus of the material for locomotion out of water. As an alternative approach, reduction in size of the hydrogels may also enable self-support out of water due to scaling laws for volume and length. Reducing the length and thickness of the hydrogels results in a cubic reduction of volume and thus mass of the objects. For the same reason that insects do not require strong internal skeletons to support their own weight in contrast to larger vertebrate animals, a sufficiently small hydrogel object should be self-supporting. Finite element analysis may be useful for determining the maximum size of a self-supporting soft object. In the specific case of hydrogels, a strategy may be necessary to place a water impermeable coating to prevent rapid drying of a sub-millimeter scale object. Adhesive forces should also be considered and movement may be limited to non-stick, low surface energy surfaces.

Besides potentially allowing self-supporting objects and locomotion out of water, shrinking the scale of robots made with magnetic photoactive composites may prove fruitful in fabricating microswimmers and micro-carriers for therapeutic drug delivery,[194] as well as combining phototaxis and magnetotaxis in cooperative motion of swarms of microrobots. 2-photon 3d laser lithography may be useful in forming the microstructures required for these approaches.[195] An important consideration for reducing the size of aquatic robots is that propulsion at the microscale is limited by low Reynolds numbers. At low Reynolds numbers, viscous forces dominate over inertial forces in hydrodynamics, and fin-based flapping propulsion methods are ineffective. Flagellar and rotating helical screw-based designs are the most commonly investigated modes of propulsion for microswimmers.[196] A photoactive hydrogel helical microswimmer could exhibit light-responsive variations in helical pitch and thus swimming speeds under different light environments.

Another requirement for using these hydrogel robots in biomedical applications is non-toxicity and biocompatibility. Studies on degradation rate of the hydrogel and biocompatibility of released spiropyran methacrylate molecules must be performed. Additionally, the NiNWs must be rendered biologically inert, potentially through impermeable polymer or passivating oxide coatings. Atomic layer deposition of silica or alumina may be one approach, but care must be taken to form complete conformal coating while avoiding agglomeration of NiNWs from the coating process.

Finally, the VT stage described in Chapter 5 has already proven to be extremely useful in discovering new phenomena and transformations in supramolecular materials. For example, in unpublished work (manuscript in progress), Stacey Chin and Hiroaki Sai have observed microscale bundling of PA nanofibers into the “plaques” long hypothesized to exist during thermal annealing.[197] Furthermore, the ability to vary the temperature of samples during confocal laser scanning microscopy may lead to exciting studies in supramolecular exchange dynamics of mixed systems and in-situ mechanical measurements from bending fluctuation dynamics. It would also be interesting to observe co-crystallization and other multi-phase transformations in the PMI-CA family of molecules, as well as other fluorescent chromophores. We have also recently shown that hydrothermal processes may be observed in the VT stage, since the glass capillaries can withstand the internal pressure of superheating water up to 150 °C. We observe melting of PMI-CA crystals at these temperatures, potentially enabling the study of classical nucleation and growth when cooling samples slowly down from hydrothermal conditions.

REFERENCES

---

(1) Sanchez, C.; Shea, K. J.; Kitagawa, S. Recent Progress in Hybrid Materials Science. *Chem. Soc. Rev.* **2011**, *40* (2), 471.

(2) Stupp, S. I.; Braun, P. V. Molecular Manipulation of Microstructures: Biomaterials, Ceramics, and Semiconductors. *Science (80-.).* **1997**, *277* (5330), 1242–1248.

(3) Mann, S.; Ozin, G. A. Synthesis of Inorganic Materials with Complex Form. *Nature*. 1996, pp 313–318.

(4) Lehn, J. M. Cryptates: The Chemistry of Macropolycyclic Inclusion Complexes. *Acc. Chem. Res.* **1978**, *11* (2), 49–57.

(5) Israelachvili, J. N.; Mitchell, D. J.; Ninham, B. W. Theory of Self-Assembly of Hydrocarbon Amphiphiles into Micelles and Bilayers. *J. Chem. Soc. Faraday Trans. 2* **1976**, *72* (0), 1525.

(6) Yanagisawa, T.; Shimizu, T.; Kuroda, K.; Kato, C. The Preparation of Alkyltriinethylaininonium–Kaneinite Complexes and Their Conversion to Microporous Materials. *Bull. Chem. Soc. Jpn.* **1990**, *63* (4), 988–992.

(7) Kresge, C. T.; Leonowicz, M. E.; Roth, W. J.; Vartuli, J. C.; Beck, J. S. Ordered Mesoporous Molecular Sieves Synthesized by a Liquid-Crystal Template Mechanism. *Nature* **1992**, *359* (6397), 710–712.

(8) Templin; Franck; Du Chesne A; Leist; Zhang; Ulrich; Schadler; Wiesner. Organically Modified Aluminosilicate Mesostructures from Block Copolymer Phases. *Science* **1997**, *278* (5344), 1795–1798.

(9) Orilall, M. C.; Wiesner, U. Block Copolymer Based Composition and Morphology Control in Nanostructured Hybrid Materials for Energy Conversion and Storage: Solar Cells, Batteries, and Fuel Cells. *Chem. Soc. Rev.* **2011**, *40* (2), 520–535.

(10) Osenar, P.; Braun, P.; Stupp, S. Lamellar Semiconductor–Organic Nanostructures from Self-assembled Templates. *Adv. Mater.* **1996**, No. 12, 1022–1025.

(11) Braun, P. V.; Osenar, P.; Stupp, S. I. Semiconducting Superlattices Templated by Molecular Assemblies. *Nature* **1996**, *380* (6572), 325–328.

(12) Chmelka, B. F.; Zhao, D.; Stucky, G. D.; Margolese, D. I.; Yang, P. Generalized Syntheses of Large-Pore Mesoporous Metal Oxides with Semicrystalline Frameworks. *Nature* **2002**, *396* (6707), 152–155.

(13) Sofos, M.; Goldberger, J.; Stone, D. A.; Allen, J. E.; Ma, Q.; Herman, D. J.; Tsai, W.-W.; Lauhon, L. J.; Stupp, S. I. A Synergistic Assembly of Nanoscale Lamellar Photoconductor Hybrids. *Nat. Mater.* **2009**, *8* (1), 68–75.

(14) Herman, D. J.; Goldberger, J. E.; Chao, S.; Martin, D. T.; Stupp, S. I. Orienting Periodic

Organic-Inorganic Nanoscale Domains through One-Step Electrodeposition. *ACS Nano* **2011**, *5* (1), 565–573.

(15) Bruns, C. J.; Herman, D. J.; Minuzzo, J. B.; Lehrman, J. A.; Stupp, S. I. Rationalizing Molecular Design in the Electrodeposition of Anisotropic Lamellar Nanostructures. *Chem. Mater.* **2013**, *25* (21), 4330–4339.

(16) Lehrman, J. A.; Cui, H.; Tsai, W.-W.; Moyer, T. J.; Stupp, S. I. Supramolecular Control of Self-Assembling Terthiophene–Peptide Conjugates through the Amino Acid Side Chain. *Chem. Commun.* **2012**, *48* (78), 9711.

(17) Lehrman, J. A. Balancing Competitive Non-Covalent Interactions in Water : From Chromophore-Peptide Amphiphiles to Supramolecular Materials, Northwestern University, 2014.

(18) Liu, X.; Ma, R.; Bando, Y.; Sasaki, T. Layered Cobalt Hydroxide Nanocones: Microwave-Assisted Synthesis, Exfoliation, and Structural Modification. *Angew. Chemie - Int. Ed.* **2010**, *49* (44), 8253–8256.

(19) Rayment, I.; Holden, H. M.; Whittaker, M.; Yohn, C. B.; Lorenz, M.; Holmes, K. C.; Milligan, R. A. *Structure of the Actin-Myosin Complex and Its Implications for Muscle Contraction*; 1993; Vol. 261.

(20) Chin, S. M.; Synatschke, C. V.; Liu, S.; Nap, R. J.; Sather, N. A.; Wang, Q.; Álvarez, Z.; Edelbrock, A. N.; Fyrner, T.; Palmer, L. C.; et al. Covalent-Supramolecular Hybrid Polymers as Muscle-Inspired Anisotropic Actuators. *Nat. Commun.* **2018**, *9* (1), 2395.

(21) Hines, L.; Petersen, K.; Lum, Z.; Sitti, M.; Hines, L.; Lum, G. Z.; Sitti, M.; Petersen, K. Soft Actuators for Small-Scale Robotics. **2016**.

(22) Huang, C.; Lv, J.; Tian, X.; Wang, Y.; Yu, Y.; Liu, J. Miniaturized Swimming Soft Robot with Complex Movement Actuated and Controlled by Remote Light Signals. *Sci. Rep.* **2015**, *5* (1), 17414.

(23) Iamsaard, S.; Aßhoff, S. J.; Matt, B.; Kudernac, T.; Cornelissen, J. J. L. M.; Fletcher, S. P.; Katsonis, N. Conversion of Light into Macroscopic Helical Motion. *Nat. Chem.* **2014**, *6* (3), 229–235.

(24) White, T. J.; Tabiryan, N. V.; Serak, S. V.; Hrozhyk, U. A.; Tondiglia, V. P.; Koerner, H.; Vaia, R. A.; Bunning, T. J. A High Frequency Photodriven Polymer Oscillator. *Soft Matter* **2008**, *4* (9), 1796.

(25) Erol, O.; Pantula, A.; Liu, W.; Gracias, D. H. Transformer Hydrogels: A Review. *Adv. Mater. Technol.* **2019**, 1900043.

(26) Tomatsu, I.; Peng, K.; Kros, A. Photoresponsive Hydrogels for Biomedical Applications. *Adv. Drug Deliv. Rev.* **2011**, *63* (14–15), 1257–1266.

(27) Satoh, T.; Sumaru, K.; Takagi, T.; Kanamori, T. Fast-Reversible Light-Driven Hydrogels Consisting of Spirobenzopyran-Functionalized Poly(N-Isopropylacrylamide). *Soft Matter* **2011**, *7* (18), 8030.

(28) Ter Schiphorst, J.; Coleman, S.; Stumpel, J. E.; Azouz, A. Ben; Diamond, D.; Schenning,

A. P. H. J. Molecular Design of Light-Responsive Hydrogels, For in Situ Generation of Fast and Reversible Valves for Microfluidic Applications. **2015**.

(29) Gelebart, A. H.; Jan Mulder, D.; Varga, M.; Konya, A.; Vantomme, G.; Meijer, E. W.; Selinger, R. L. B.; Broer, D. J. Making Waves in a Photoactive Polymer Film. *Nature* **2017**, *546* (7660), 632–636.

(30) Erb, R. M.; Martin, J. J.; Soheilian, R.; Pan, C.; Barber, J. R. Actuating Soft Matter with Magnetic Torque. *Adv. Funct. Mater.* **2016**, *26* (22), 3859–3880.

(31) Narayan, R. *Biomedical Materials*; 2009.

(32) Erb, R. M.; Libanori, R.; Rothfuchs, N.; Studart, A. R. Composites Reinforced in Three Dimensions by Using Low Magnetic Fields. *Science (80-.).* **2012**, *335* (6065), 199–204.

(33) Laurent, S.; Forge, D.; Port, M.; Roch, A.; Robic, C.; Vander, L.; Muller, R. N. Magnetic Iron Oxide Nanoparticles: Synthesis, Stabilization, Vectorization, Physicochemical Characterizations, and Biological Applications.

(34) Erb, R. M.; Sander, J. S.; Grisch, R.; Studart, A. R. Self-Shaping Composites with Programmable Bioinspired Microstructures. *Nat. Commun.* **2013**, *4* (1), 1712.

(35) Erb, R. M.; Segmehl, J.; Charilaou, M.; Löffler, J. F.; Studart, A. R. Non-Linear Alignment Dynamics in Suspensions of Platelets under Rotating Magnetic Fields. *Soft Matter* **2012**, *8* (29), 7604.

(36) Kwon, S.; Kim, J.; Chung, S. E.; Lee, H.; Choi, S.-E.; Kim, J. Programming Magnetic Anisotropy in Polymeric Microactuators. *Nat. Mater.* **2011**, *10* (10), 747–752.

(37) Garstecki, P.; Tierno, P.; Weibel, D. B.; Sagués, F.; Whitesides, G. M. Propulsion of Flexible Polymer Structures in a Rotating Magnetic Field. *J. Phys. Condens. Matter* **2009**, *21* (20), 204110.

(38) Huang, H. W.; Sakar, M. S.; Petruska, A. J.; Pané, S.; Nelson, B. J. Soft Micromachines with Programmable Motility and Morphology. *Nat. Commun.* **2016**, *7* (1), 12263.

(39) Lum, G. Z.; Ye, Z.; Dong, X.; Marvi, H.; Erin, O.; Hu, W.; Sitti, M. Shape-Programmable Magnetic Soft Matter. *Proc. Natl. Acad. Sci. U. S. A.* **2016**, *113* (41), E6007–E6015.

(40) Hu, W.; Lum, G. Z.; Mastrangeli, M.; Sitti, M. Small-Scale Soft-Bodied Robot with Multimodal Locomotion. *Nature* **2018**, *554* (7690), 81–85.

(41) Kim, Y.; Yuk, H.; Zhao, R.; Chester, S. A.; Zhao, X. Printing Ferromagnetic Domains for Untethered Fast-Transforming Soft Materials. *Nature* **2018**, *558* (7709), 274–279.

(42) Whitney, T. M.; Jiang, J. S.; Searson, P. C.; Chien, C. L. Fabrication and Magnetic Properties of Arrays of Metallic Nanowires. *Science (80-.).* **1993**, *261* (5126), 1316–1319.

(43) Ferré, R.; Ounadjela, K.; George, J. Magnetization Processes in Nickel and Cobalt Electrodeposited Nanowires. *Phys. Rev. B - Condens. Matter Mater. Phys.* **1997**, *56* (21), 14066–14075.

(44) Sergelius, P.; de la Prida, V. M.; Zocher, M.; Fernandez, J. G.; Martens, S.; Böhnert, T.; Martinez, V. V.; Nielsch, K.; Görlitz, D. Statistical Magnetometry on Isolated NiCo

Nanowires and Nanowire Arrays: A Comparative Study. *J. Phys. D. Appl. Phys.* **2016**, *49* (14), 145005.

(45) Bentley, A. K.; Farhoud, M.; Ellis, A. B.; Nickel, A.-M. L.; Lisensky, G. C.; Crone, W. C. Template Synthesis and Magnetic Manipulation of Nickel Nanowires. *J. Chem. Educ.* **2005**, *82* (5), 765.

(46) Aprelev, P.; Gu, Y.; Burtovyy, R.; Luzinov, I.; Kornev, K. G. Synthesis and Characterization of Nanorods for Magnetic Rotational Spectroscopy. *J. Appl. Phys.* **2015**, *118* (7), 074901.

(47) Lapointe, C.; Hultgren, A.; Silevitch, D. M.; Felton, E. J.; Reich, D. H.; Leheny, R. L. Elastic Torque and the Levitation of Metal Wires by a Nematic Liquid Crystal. *Science (80-.).* **2004**, *303* (5658), 652–655.

(48) Lapointe, C. P.; Reich, D. H.; Leheny, R. L. Manipulation and Organization of Ferromagnetic Nanowires by Patterned Nematic Liquid Crystals. *Langmuir* **2008**, *24* (19), 11175–11181.

(49) Anguelouch, A.; Leheny, R. L.; Reich, D. H. Application of Ferromagnetic Nanowires to Interfacial Microrheology. *Appl. Phys. Lett.* **2006**, *89* (11), 111914.

(50) Cappallo, N.; Lapointe, C.; Reich, D. H.; Leheny, R. L. Nonlinear Microrheology of Wormlike Micelle Solutions Using Ferromagnetic Nanowire Probes. *Phys. Rev. E - Stat. Nonlinear, Soft Matter Phys.* **2007**, *76* (3).

(51) Gu, Y.; Kornev, K. G. Ferromagnetic Nanorods in Applications to Control of the In-Plane Anisotropy of Composite Films and for In Situ Characterization of the Film Rheology. *Adv. Funct. Mater.* **2016**, *26* (22), 3796–3808.

(52) Aprelev, P.; McKinney, B.; Walls, C.; Kornev, K. G. Magnetic Stage with Environmental Control for Optical Microscopy and High-Speed Nano- and Microrheology. *Phys. Fluids* **2017**, *29* (7).

(53) Bentley, A. K.; Ellis, A. B.; Lisensky, G. C.; Crone, W. C. Suspensions of Nickel Nanowires as Magneto-Optical Switches. *Inst. Phys. Publ. Nanotechnol. Nanotechnol.* **2005**, *16*, 2193–2196.

(54) Aida, T.; Meijer, E. W.; Stupp, S. I. Functional Supramolecular Polymers. *Science* **2012**, *335* (6070), 813–817.

(55) Stupp, S. I.; Palmer, L. C. Supramolecular Chemistry and Self-Assembly in Organic Materials Design. *Chem. Mater.* **2014**, *26* (1), 507–518.

(56) Korevaar, P. a.; George, S. J.; Markvoort, A. J.; Smulders, M. M. J.; Hilbers, P. a. J.; Schenning, A. P. H. J.; De Greef, T. F. a.; Meijer, E. W. Pathway Complexity in Supramolecular Polymerization. *Nature* **2012**, *481* (7382), 492–496.

(57) Tantakitti, F.; Boekhoven, J.; Wang, X.; Kazantsev, R. V.; Yu, T.; Li, J.; Zhuang, E.; Zandi, R.; Ortony, J. H.; Newcomb, C. J.; et al. Energy Landscapes and Functions of Supramolecular Systems. *Nat. Mater.* **2016**, *15* (4), 469–476.

(58) Zhang, S.; Greenfield, M. a; Mata, A.; Palmer, L. C.; Bitton, R.; Mantei, J. R.; Aparicio, C.;

de la Cruz, M. O.; Stupp, S. I. A Self-Assembly Pathway to Aligned Monodomain Gels. *Nat. Mater.* **2010**, *9* (7), 594–601.

(59) She, M.-S.; Lo, T.-Y.; Ho, R.-M. Long-Range Ordering of Block Copolymer Cylinders Driven by Combining Thermal Annealing and Substrate Functionalization. *ACS Nano* **2013**, *7* (3), 2000–2011.

(60) Aytun, T.; Barreda, L.; Ruiz-Carretero, A.; Lehrman, J. A.; Stupp, S. I. Improving Solar Cell Efficiency through Hydrogen Bonding: A Method for Tuning Active Layer Morphology. *Chem. Mater.* **2015**, *27* (4), 1201–1209.

(61) da Silva, R. M. P.; van der Zwaag, D.; Albertazzi, L.; Lee, S. S.; Meijer, E. W.; Stupp, S. I. Super-Resolution Microscopy Reveals Structural Diversity in Molecular Exchange among Peptide Amphiphile Nanofibres. *Nat. Commun.* **2016**, *XXX* (XXX), XXX.

(62) Kazantsev, R. V.; Dannenhoffer, A. J.; Weingarten, A. S.; Phelan, B. T.; Harutyunyan, B.; Aytun, T.; Narayanan, A.; Fairfield, D. J.; Boekhoven, J.; Sai, H.; et al. Crystal-Phase Transitions and Photocatalysis in Supramolecular Scaffolds. *J. Am. Chem. Soc.* **2017**, *139* (17), 6120–6127.

(63) Chen, C. H.; Palmer, L. C.; Stupp, S. I. Self-Repair of Structure and Bioactivity in a Supramolecular Nanostructure. *Nano Lett.* **2018**, *18* (11), 6832–6841.

(64) Bard, J. Morphogenesis. *Scholarpedia* **2008**, *3* (6), 2422.

(65) Nykvist, B.; Nilsson, M. Rapidly Falling Costs of Battery Packs for Electric Vehicles. *Nat. Clim. Chang.* **2015**, *5* (April), 329–332.

(66) Zhang, Q.; Uchaker, E.; Candelaria, S. L.; Cao, G. Nanomaterials for Energy Conversion and Storage. *Chem. Soc. Rev.* **2013**, *42* (7), 3127.

(67) Yu, G.; Xie, X.; Pan, L.; Bao, Z.; Cui, Y. Hybrid Nanostructured Materials for High-Performance Electrochemical Capacitors. *Nano Energy* **2013**, *2* (2), 213–234.

(68) Simon, P.; Gogotsi, Y. Materials for Electrochemical Capacitors. *Nat. Mater.* **2008**, *7* (11), 845–854.

(69) Wang, G.; Zhang, L.; Zhang, J. A Review of Electrode Materials for Electrochemical Supercapacitors. *Chem. Soc. Rev.* **2012**, *41* (2), 797–828.

(70) Ji, J.; Li, Y.; Peng, W.; Zhang, G.; Zhang, F.; Fan, X. Advanced Graphene-Based Binder-Free Electrodes for High-Performance Energy Storage. *Adv. Mater.* **2015**, *27* (36), 5264–5279.

(71) Shen, G.; Sun, X.; Zhang, H.; Liu, Y.; Zhang, J.; Meka, A.; Zhou, L.; Yu, C. Nitrogen-Doped Ordered Mesoporous Carbon Single Crystals: Aqueous Organic–Organic Self-Assembly and Superior Supercapacitor Performance. *J. Mater. Chem. A* **2015**, *3* (47), 24041–24048.

(72) Simon, P.; Gogotsi, Y.; Dunn, B. Where Do Batteries End and Supercapacitors Begin? *Science* **2014**, *343* (March), 1210–1211.

(73) Augustyn, V.; Simon, P.; Dunn, B. Pseudocapacitive Oxide Materials for High-Rate Electrochemical Energy Storage. *Energy Environ. Sci.* **2014**, *7* (5), 1597.

(74) Lukatskaya, M. R.; Dunn, B.; Gogotsi, Y. Multidimensional Materials and Device Architectures for Future Hybrid Energy Storage. *Nat. Commun.* **2016**, *7*, 12647.

(75) Cao, L.; Xu, F.; Liang, Y.-Y.; Li, H.-L. Preparation of the Novel Nanocomposite Co(OH)2/ Ultra-Stable Y Zeolite and Its Application as a Supercapacitor with High Energy Density. *Adv. Mater.* **2004**, *16* (20), 1853–1857.

(76) Chang, J.-K.; Wu, C.-M.; Sun, I.-W. Nano-Architectured Co(OH)2 Electrodes Constructed Using an Easily-Manipulated Electrochemical Protocol for High-Performance Energy Storage Applications. *J. Mater. Chem.* **2010**, *20* (18), 3729–3735.

(77) Deng, M.-J.; Song, C.-Z.; Wang, C.-C.; Tseng, Y.-C.; Chen, J.-M.; Lu, K.-T. Low Cost Facile Synthesis of Large-Area Cobalt Hydroxide Nanorods with Remarkable Pseudocapacitance. *ACS Appl. Mater. Interfaces* **2015**, *7* (17), 9147–9156.

(78) Wang, L.; Dong, Z. H.; Wang, Z. G.; Zhang, F. X.; Jin, J. Layered α-Co(OH) 2 Nanocones as Electrode Materials for Pseudocapacitors: Understanding the Effect of Interlayer Space on Electrochemical Activity. *Adv. Funct. Mater.* **2013**, *23* (21), 2758–2764.

(79) Zhao, J.; Xu, S.; Tschulik, K.; Compton, R. G.; Wei, M.; O'Hare, D.; Evans, D. G.; Duan, X. Molecular-Scale Hybridization of Clay Monolayers and Conducting Polymer for Thin-Film Supercapacitors. *Adv. Funct. Mater.* **2015**, *25* (18), 2745–2753.

(80) Gao, S.; Sun, Y.; Lei, F.; Liang, L.; Liu, J.; Bi, W.; Pan, B.; Xie, Y. Ultrahigh Energy Density Realized by a Single-Layer β-Co(OH) 2 All-Solid-State Asymmetric Supercapacitor. *Angew. Chemie Int. Ed.* **2014**, *53*, 12789–12793.

(81) Wang, L.; Lin, C.; Zhang, F.; Jin, J. Phase Transformation Guided Single-Layer β-Co(OH)2 Nanosheets for Pseudocapacitive Electrodes. *ACS Nano* **2014**, *8* (4), 3724–3734.

(82) Liu, Z.; Ma, R.; Osada, M.; Takada, K.; Sasaki, T. Selective and Controlled Synthesis of α- and β-Cobalt Hydroxides in Highly Developed Hexagonal Platelets. *J. Am. Chem. Soc.* **2005**, *127* (40), 13869–13874.

(83) Du, Y.; Ok, K. M.; O'Hare, D. A Kinetic Study of the Phase Conversion of Layered Cobalt Hydroxides. *J. Mater. Chem.* **2008**, *18* (37), 4450–4459.

(84) Liu, X.; Ma, R.; Bando, Y.; Sasaki, T. High-Yield Preparation, Versatile Structural Modification, and Properties of Layered Cobalt Hydroxide Nanocones. *Adv. Funct. Mater.* **2014**, *24* (27), 4292–4302.

(85) Braun, P. V.; Osenar, P.; Tohver, V.; Kennedy, S. B.; Stupp, S. I. Nanostructure Templating in Inorganic Solids with Organic Lyotropic Liquid Crystals. *J. Am. Chem. Soc.* **1999**, *121* (32), 7302–7309.

(86) Aizenberg, J.; Weaver, J. C.; Thanawala, M. S.; Sundar, V. C.; Morse, D. E.; Fratzl, P. Skeleton of Euplectella Sp.: Structural Hierarchy from the Nanoscale to the Macroscale. *Science (80-.).* **2005**, *309* (5732), 275–278.

(87) Zhou, L.; Xu, H.; Zhang, H.; Yang, J.; Hartono, S. B.; Qian, K.; Zou, J.; Yu, C. Cheap and Scalable Synthesis of α-Fe2O3 Multi-Shelled Hollow Spheres as High-Performance Anode Materials for Lithium Ion Batteries. *Chem. Commun. (Camb).* **2013**, *49*, 8695–8697.

(88) Zhou, L.; Zhuang, Z.; Zhao, H.; Lin, M.; Zhao, D.; Mai, L. Intricate Hollow Structures: Controlled Synthesis and Applications in Energy Storage and Conversion. *Advanced Materials*. 2017, p 1602914.

(89) Yarger, M. S.; Steinmiller, E. M. P.; Choi, K.-S. Electrochemical Synthesis of Cobalt Hydroxide Films with Tunable Interlayer Spacings. *Chem. Commun.* **2007**, *14* (2), 159–161.

(90) Pralong, V.; Delahaye-Vidal, A.; Beaudoin, B.; Gérand, B.; Tarascon, J. Oxidation Mechanism of Cobalt Hydroxide to Cobalt Oxyhydroxide. *J. Mater. Chem.* **1999**, *9* (4), 955–960.

(91) Ni, B.; Liu, H.; Wang, P.; He, J.; Wang, X. General Synthesis of Inorganic Single-Walled Nanotubes. *Nat. Commun.* **2015**, *6* (May), 8756.

(92) Gido, S. P.; Gunther, J.; Thomas, E. L.; Hoffman, D. Lamellar Diblock Copolymer Grain Boundary Morphology. 1. Twist Boundary Characterization. *Macromolecules* **1993**, *26* (17), 4506–4520.

(93) Read, W.T., J. *Dislocations in Crystals*; McGraw-Hill: New York, 1953.

(94) Bavykin, D. V.; Parmon, V. N.; Lapkin, A. A.; Walsh, F. C. The Effect of Hydrothermal Conditions on the Mesoporous Structure of TiO2 Nanotubes. *J. Mater. Chem.* **2004**, *14* (22), 3370–3377.

(95) Augustyn, V.; Simon, P.; Dunn, B. Pseudocapacitive Oxide Materials for High-Rate Electrochemical Energy Storage. *Energy Environ. Sci.* **2014**, *7* (5), 1597.

(96) Gupta, V.; Kusahara, T.; Toyama, H.; Gupta, S.; Miura, N. Potentiostatically Deposited Nanostructured α-Co(OH)2: A High Performance Electrode Material for Redox-Capacitors. *Electrochem. commun.* **2007**, *9* (9), 2315–2319.

(97) Wang, Y.; Yang, W.; Chen, C.; Evans, D. G. Fabrication and Electrochemical Characterization of Cobalt-Based Layered Double Hydroxide Nanosheet Thin-Film Electrodes. *J. Power Sources* **2008**, *184* (2), 682–690.

(98) Zhou, W.; Zhang, J.; Xue, T.; Zhao, D.; Li, H. Electrodeposition of Ordered Mesoporous Cobalt Hydroxide Film from Lyotropic Liquid Crystal Media for Electrochemical Capacitors. *J. Mater. Chem.* **2008**, *18* (8), 905–910.

(99) Jiang, J.; Liu, J.; Ding, R.; Zhu, J.; Li, Y.; Hu, A.; Li, X.; Huang, X. Large-Scale Uniform Alpha-Co(OH)(2) Long Nanowire Arrays Grown on Graphite as Pseudocapacitor Electrodes. *ACS Appl Mater Interfaces* **2011**, *3* (1), 99–103.

(100) Zhao, T.; Jiang, H.; Ma, J. Surfactant-Assisted Electrochemical Deposition of α-Cobalt Hydroxide for Supercapacitors. *J. Power Sources* **2011**, *196* (2), 860–864.

(101) Li, H. B.; Yu, M. H.; Lu, X. H.; Liu, P.; Liang, Y.; Xiao, J.; Tong, Y. X.; Yang, G. W. Amorphous Cobalt Hydroxide with Superior Pseudocapacitive Performance. *ACS Appl. Mater. Interfaces* **2014**, *6* (2), 745–749.

(102) Vialat, P.; Mousty, C.; Taviot-Gueho, C.; Renaudin, G.; Martinez, H.; Dupin, J. C.; Elkaim, E.; Leroux, F. High-Performing Monometallic Cobalt Layered Double Hydroxide Supercapacitor with Defined Local Structure. *Adv. Funct. Mater.* **2014**, *24* (30), 4831–4842.

(103) Xing, W.; Qiao, S.; Wu, X.; Gao, X.; Zhou, J.; Zhuo, S.; Hartono, S. B.; Hulicova-Jurcakova, D. Exaggerated Capacitance Using Electrochemically Active Nickel Foam as Current Collector in Electrochemical Measurement. *J. Power Sources* **2011**, *196* (8), 4123–4127.

(104) Lee, J. H.; Lee, H. J.; Lim, S. Y.; Chae, K. H.; Park, S. H.; Chung, K. Y.; Deniz, E.; Choi, J. W. Stabilized Octahedral Frameworks in Layered Double Hydroxides by Solid-Solution Mixing of Transition Metals. *Adv. Funct. Mater.* **2016**, 1605225.

(105) Owusu, K. A.; Qu, L.; Li, J.; Wang, Z.; Zhao, K.; Yang, C.; Hercule, K. M.; Lin, C.; Shi, C.; Wei, Q.; et al. Low-Crystalline Iron Oxide Hydroxide Nanoparticle Anode for High-Performance Supercapacitors. *Nat. Commun.* **2017**, *8*, 14264.

(106) Choi, B. G.; Yang, M.; Jung, S. C.; Lee, K. G.; Kim, J.-G. G.; Park, H.; Park, T. J.; Lee, S. B.; Han, Y.-K. K.; Huh, Y. S. Enhanced Pseudocapacitance of Ionic Liquid/Cobalt Hydroxide Nanohybrids. *ACS Nano* **2013**, *7* (3), 2453–2460.

(107) Liu, T.-C. Behavior of Molybdenum Nitrides as Materials for Electrochemical Capacitors. *J. Electrochem. Soc.* **1998**, *145* (6), 1882–1888.

(108) Wang, J.; Polleux, J.; Lim, J.; Dunn, B. Pseudocapacitive Contributions to Electrochemical Energy Storage in TiO2 (Anatase) Nanoparticles. *J. Phys. Chem. C* **2007**, *111* (40), 14925–14931.

(109) Augustyn, V.; Come, J.; Lowe, M. A.; Kim, J. W.; Taberna, P.; Tolbert, S. H.; Abruña, H. D.; Simon, P.; Dunn, B. High-Rate Electrochemical Energy Storage through Li+ Intercalation Pseudocapacitance. *Nat. Mater.* **2013**, *12* (6), 518–522.

(110) Xu, Z. P.; Zeng, H. C. Interconversion of Brucite-like and Hydrotalcite-like Phases in Cobalt Hydroxide Compounds. *Chem. Mater.* **1999**, *11* (1), 67–74.

(111) Feng, C.; Zhang, J.; He, Y.; Zhong, C.; Hu, W.; Liu, L.; Deng, Y. Sub-3 Nm Co 3 O 4 Nanofilms with Enhanced Supercapacitor Properties. *ACS Nano* **2015**, *9* (2), 1730–1739.

(112) Gallagher, K. G.; Trask, S. E.; Bauer, C.; Woehrle, T.; Lux, S. F.; Tschech, M.; Lamp, P.; Polzin, B. J.; Ha, S.; Long, B.; et al. Optimizing Areal Capacities through Understanding the Limitations of Lithium-Ion Electrodes. *J. Electrochem. Soc.* **2016**, *163* (2), A138–A149.

(113) Gogotsi, Y.; Simon, P. True Performance Metrics in Electrochemical Energy Storage. *Science*. 2011, pp 917–918.

(114) Chabi, S.; Peng, C.; Hu, D.; Zhu, Y. Ideal Three-Dimensional Electrode Structures for Electrochemical Energy Storage. *Adv. Mater.* **2014**, *26*, 2440–2445.

(115) Sun, H.; Zhu, J.; Baumann, D.; Peng, L.; Xu, Y.; Shakir, I.; Huang, Y.; Duan, X. Hierarchical 3D Electrodes for Electrochemical Energy Storage. *Nat. Rev. Mater.* **2019**, *4* (1), 45–60.

(116) Lang, X.; Hirata, A.; Fujita, T.; Chen, M. Nanoporous Metal/Oxide Hybrid Electrodes for Electrochemical Supercapacitors. *Nat. Nanotechnol.* **2011**, *6* (4), 232–236.

(117) Zhang, H.; Yu, X.; Braun, P. V. Three-Dimensional Bicontinuous Ultrafast-Charge and -Discharge Bulk Battery Electrodes. *Nat Nanotechnol* **2011**, *6* (5), 277–281.

(118) Zhu, H.; Jia, Z.; Chen, Y.; Weadock, N.; Wan, J.; Vaaland, O.; Han, X.; Li, T.; Hu, L. Tin

Anode for Sodium-Ion Batteries Using Natural Wood Fiber as a Mechanical Buffer and Electrolyte Reservoir. *Nano Lett.* **2013**, *13* (7), 3093–3100.

(119) Yao, H.; Zheng, G.; Li, W.; McDowell, M. T.; Seh, Z.; Liu, N.; Lu, Z.; Cui, Y. Crab Shells as Sustainable Templates from Nature for Nanostructured Battery Electrodes. *Nano Lett.* **2013**, *13* (7), 3385–3390.

(120) Zhu, J.; Shan, Y.; Wang, T.; Sun, H.; Zhao, Z.; Mei, L.; Fan, Z.; Xu, Z.; Shakir, I.; Huang, Y.; et al. A Hyperaccumulation Pathway to Three-Dimensional Hierarchical Porous Nanocomposites for Highly Robust High-Power Electrodes. *Nat. Commun.* **2016**, *7* (1), 13432.

(121) Guo, X.; Wang, L.; Yue, S.; Wang, D.; Lu, Y.; Song, Y.; He, J. Single-Crystalline Organic–Inorganic Layered Cobalt Hydroxide Nanofibers: Facile Synthesis, Characterization, and Reversible Water-Induced Structural Conversion. *Inorg. Chem.* **2014**, *53*, 12841–12847.

(122) Kung, C.-W.; Cheng, Y.-H.; Ho, K.-C. Single Layer of Nickel Hydroxide Nanoparticles Covered on a Porous Ni Foam and Its Application for Highly Sensitive Non-Enzymatic Glucose Sensor. *Sensors Actuators B Chem.* **2014**, *204*, 159–166.

(123) Galwey, A. K. 1152. The Thermal Decomposition of Nickel Benzoate and of the Nickel Salt of Cyclohexanecarboxylic Acid. *J. Chem. Soc.* **1965**, 6188.

(124) Jeangros, Q.; Hansen, T. W.; Wagner, J. B.; Damsgaard, C. D.; Dunin-Borkowski, R. E.; H??bert, C.; Van Herle, J.; Hessler-Wyser, A. Reduction of Nickel Oxide Particles by Hydrogen Studied in an Environmental TEM. *J. Mater. Sci.* **2013**, *48* (7), 2893–2907.

(125) Kawamori, M.; Yagi, S.; Matsubara, E. Formation of Nickel Nanowires via Electroless Deposition Under a Magnetic Field. *J. Electrochem. Soc.* **2011**, *158* (8), E79.

(126) Kawamori, M.; Asai, T.; Shirai, Y.; Yagi, S.; Oishi, M.; Ichitsubo, T.; Matsubara, E. Three-Dimensional Nano-Electrode by Metal-Nanowire-Nonwoven Clothes. *Nano Lett.* **2014**.

(127) Xu, C.; Li, Z.; Yang, C.; Zou, P.; Xie, B.; Lin, Z.; Zhang, Z.; Li, B.; Kang, F.; Wong, C. P. An Ultralong, Highly Oriented Nickel-Nanowire-Array Electrode Scaffold for High-Performance Compressible Pseudocapacitors. *Adv. Mater.* **2016**, 4105–4110.

(128) Wehner, M.; Truby, R. L.; Fitzgerald, D. J.; Mosadegh, B.; Whitesides, G. M.; Lewis, J. A.; Wood, R. J. An Integrated Design and Fabrication Strategy for Entirely Soft, Autonomous Robots. *Nature* **2016**, *536* (7617), 451–455.

(129) Choi, J.-W.; Park, S.-J.; Capulli, A. K.; Gazzola, M.; Lauder, G. V; Ahn, S.; Cho, A.; Campbell, P. H.; Vijaykumar, R.; Deisseroth, K.; et al. Phototactic Guidance of a Tissue-Engineered Soft-Robotic Ray. *Science (80-.).* **2016**, *353* (6295), 158–162.

(130) Weingarten, A. S.; Kazantsev, R. V.; Palmer, L. C.; McClendon, M.; Koltonow, A. R.; Samuel, A. P. S.; Kiebala, D. J.; Wasielewski, M. R.; Stupp, S. I. Self-Assembling Hydrogel Scaffolds for Photocatalytic Hydrogen Production. *Nat. Chem.* **2014**, *6* (11), 964–970.

(131) Dreyfus, R.; Baudry, J.; Roper, M. L.; Fermigier, M.; Stone, H. A.; Bibette, J. Microscopic Artificial Swimmers. *Nature* **2005**, *437* (7060), 862–865.

(132) Cui, J.; Huang, T. Y.; Luo, Z.; Testa, P.; Gu, H.; Chen, X. Z.; Nelson, B. J.; Heyderman, L.

J. Nanomagnetic Encoding of Shape-Morphing Micromachines. *Nature* **2019**, *575* (7781), 164–168.

(133) Kim, Y.; Parada, G. A.; Liu, S.; Zhao, X. Ferromagnetic Soft Continuum Robots. *Sci. Robot.* **2019**, *4* (33), eaax7329.

(134) Xu, T.; Zhang, J.; Salehizadeh, M.; Onaizah, O.; Diller, E. Millimeter-Scale Flexible Robots with Programmable Three-Dimensional Magnetization and Motions. *Sci. Robot.* **2019**, *4* (29).

(135) Zhao, Y.; Xuan, C.; Qian, X.; Alsaid, Y.; Hua, M.; Jin, L.; He, X. Soft Phototactic Swimmer Based on Self-Sustained Hydrogel Oscillator. *Sci. Robot.* **2019**, *4* (33).

(136) Francis, W.; Dunne, A.; Delaney, C.; Florea, L.; Diamond, D. Spiropyran Based Hydrogels Actuators—Walking in the Light. *Sensors Actuators B Chem.* **2017**, *250*, 608–616.

(137) Kim, Y. S.; Liu, M.; Ishida, Y.; Ebina, Y.; Osada, M.; Sasaki, T.; Hikima, T.; Takata, M.; Aida, T. Thermoresponsive Actuation Enabled by Permittivity Switching in an Electrostatically Anisotropic Hydrogel. *Nat. Mater.* **2015**, *14* (10), 1002–1007.

(138) Maeda, S.; Hara, Y.; Sakai, T.; Yoshida, R.; Hashimoto, S. Self-Walking Gel. *Adv. Mater.* **2007**, *19* (21), 3480–3484.

(139) Han, D.; Farino, C.; Yang, C.; Scott, T.; Browe, D.; Choi, W.; Freeman, J. W.; Lee, H. Soft Robotic Manipulation and Locomotion with a 3D Printed Electroactive Hydrogel. *ACS Appl. Mater. Interfaces* **2018**, *10* (21), 17512–17518.

(140) Klajn, R. Spiropyran-Based Dynamic Materials. *Chemical Society Reviews*. Royal Society of Chemistry January 7, 2014, pp 148–184.

(141) Chen, J.; Leung, F. K. C.; Stuart, M. C. A.; Kajitani, T.; Fukushima, T.; Van Der Giessen, E.; Feringa, B. L. Artificial Muscle-like Function from Hierarchical Supramolecular Assembly of Photoresponsive Molecular Motors. *Nat. Chem.* **2018**, *10* (2), 132–138.

(142) Leung, F. K.; Kajitani, T.; Stuart, M. C. A.; Fukushima, T.; Feringa, B. L. Dual-Controlled Macroscopic Motions in a Supramolecular Hierarchical Assembly of Motor Amphiphiles. *Angew. Chemie Int. Ed.* **2019**, *58* (32), 10985–10989.

(143) Wang, J.; Liu, Q.; Gao, B.; Qiao, L.; Li, F.; Feng, J.; Xue, D. Microwave Absorption Properties of the Ni Nanowires Composite. *Artic. J. Phys. D Appl. Phys.* **2008**, *41*, 5.

(144) Kuksenok, O.; Balazs, A. C. Modeling the Photoinduced Reconfiguration and Directed Motion of Polymer Gels. *Adv. Funct. Mater.* **2013**, *23* (36), 4601–4610.

(145) Qiu, G. Y.; Pence, T. J. Remarks on the Behavior of Simple Directionally Reinforced Incompressible Nonlinearly Elastic Solids. *J. Elast.* **1997**, *49* (1), 1–30.

(146) Satoh, T.; Sumaru, K.; Takagi, T.; Takai, K.; Kanamori, T. Isomerization of Spirobenzopyrans Bearing Electron-Donating and Electron-Withdrawing Groups in Acidic Aqueous Solutions. *Phys. Chem. Chem. Phys.* **2011**, *13* (16), 7322–7329.

(147) Dehghany, M.; Zhang, H.; Naghdabadi, R.; Hu, Y. A Thermodynamically-Consistent Large Deformation Theory Coupling Photochemical Reaction and Electrochemistry for Light-Responsive Gels. *J. Mech. Phys. Solids* **2018**, *116*, 239–266.

(148) Doi, M. Gel Dynamics. *Journal of the Physical Society of Japan*. The Physical Society of Japan May 27, 2009.

(149) Dorfmann, L.; Ogden, R. W. *Nonlinear Theory of Electroelastic and Magnetoelastic Interactions*; Springer US, 2014; Vol. 9781461495963.

(150) Attard, M. M. Finite Strain - Isotropic Hyperelasticity. *Int. J. Solids Struct.* **2003**, *40* (17), 4353–4378.

(151) Bustamante, R. Transversely Isotropic Nonlinear Magneto-Active Elastomers. *Acta Mech.* **2010**, *210* (3–4), 183–214.

(152) Bonet, J.; Wood, R. D. *Nonlinear Continuum Mechanics for Finite Element Analysis*; Cambridge University Press, 2008.

(153) Minsky M. Memoir on Inventing the Confocal Scanning Microscope. *Scanning* **1987**, *10* (1 988), 128–138.

(154) Cox, G. Biological Confocal Microscopy. *Mater. Today* **2002**, *5* (3), 34–41.

(155) Axelrod, D.; Koppel, D. E.; Schlessinger, J.; Elson, E.; Webb, W. W. Mobility Measurement by Analysis of Fluorescence Photobleaching Recovery Kinetics. *Biophys. J.* **1976**, *16* (9), 1055–1069.

(156) Sprague, B. L.; McNally, J. G. FRAP Analysis of Binding: Proper and Fitting. *Trends Cell Biol.* **2005**, *15* (2), 84–91.

(157) Förster, T. Zwischenmolekulare Energiewanderung Und Fluoreszenz. *Ann. Phys.* **1948**, *437* (1–2), 55–75.

(158) Jares-Erijman, E. A.; Jovin, T. M. FRET Imaging. *Nat. Biotechnol.* **2003**, *21* (11), 1387–1395.

(159) Piston, D. W.; Kremers, G. J. Fluorescent Protein FRET: The Good, the Bad and the Ugly. *Trends Biochem. Sci.* **2007**, *32* (9), 407–414.

(160) Hell, S. W.; Wichmann, J. Breaking the Diffraction Resolution Limit by Stimulated Emission: Stimulated-Emission-Depletion Fluorescence Microscopy. *Opt. Lett.* **1994**, *19* (11), 780.

(161) Westphal, V.; Blanca, C. M.; Dyba, M.; Kastrup, L.; Hell, S. W. Laser-Diode-Stimulated Emission Depletion Microscopy. *Appl. Phys. Lett.* **2003**, *82* (18), 3125–3127.

(162) Rust, M. J.; Bates, M.; Zhuang, X. Sub-Diffraction-Limit Imaging by Stochastic Optical Reconstruction Microscopy (STORM). *Nat. Methods* **2006**, *3* (10), 793–795.

(163) Hoheisel, W.; Jacobsen, W.; Lüttge, B.; Weiner, W. Confocal Microscopy: Applications in Materials Science. *Macromol. Mater. Eng.* **2001**, *286* (11), 663–668.

(164) Hovis, D. B.; Heuer, A. H. The Use of Laser Scanning Confocal Microscopy (LSCM) in Materials Science. *J. Microsc.* **2010**, *240* (3), 173–180.

(165) Takeno, H.; Iwata, M.; Takenaka, M.; Hashimoto, T. Combined Light Scattering and Laser Scanning Confocal Microscopy Studies of a Polymer Mixture Involving a Percolation-to-Cluster Transition. *Macromolecules* **2000**, *33* (26), 9657–9665.

(166) Lee, W.; Yoon, J.; Lee, H.; Thomas, E. L. Direct 3-d Imaging of the Evolution of Block Copolymer Microstructures Using Laser Scanning Confocal Microscopy. *Macromolecules* **2007**, *40* (17), 6021–6024.

(167) Kiyonaka, S.; Sugiyasu, K.; Shinkai, S.; Hamachi, I. First Thermally Responsive Supramolecular Polymer Based on Glycosylated Amino Acid. *J. Am. Chem. Soc.* **2002**, *124* (37), 10954–10955.

(168) Ogi, S.; Stepanenko, V.; Sugiyasu, K.; Takeuchi, M.; Würthner, F. Mechanism of Self-Assembly Process and Seeded Supramolecular Polymerization of Perylene Bisimide Organogelator. *J. Am. Chem. Soc.* **2015**, *137* (9), 3300–3307.

(169) Onogi, S.; Shigemitsu, H.; Yoshii, T.; Tanida, T.; Ikeda, M.; Kubota, R.; Hamachi, I. In Situ Real-Time Imaging of Self-Sorted Supramolecular Nanofibres. *Nat. Chem.* **2016**, *8* (8), 743–752.

(170) Dedovets, D.; Monteux, C.; Deville, S. A Temperature-Controlled Stage for Laser Scanning Confocal Microscopy and Case Studies in Materials Science. *Ultramicroscopy* **2018**, *195*, 1–11.

(171) Dedovets, D.; Monteux, C.; Deville, S. Five-Dimensional Imaging of Freezing Emulsions with Solute Effects. *Science (80-.).* **2018**, *360* (6386), 303–306.

(172) Aida, T.; Meijer, E. W.; Stupp, S. I. Functional Supramolecular Polymers. *Science (80-.).* **2012**, *335* (6070), 813–817.

(173) Korevaar, P. A.; George, S. J.; Markvoort, A. J.; Smulders, M. M. J.; Hilbers, P. A. J.; Schenning, A. P. H. J.; De Greef, T. F. A.; Meijer, E. W. Pathway Complexity in Supramolecular Polymerization. *Nature* **2012**, *481* (7382), 492–496.

(174) Tantakitti, F.; Boekhoven, J.; Wang, X.; Kazantsev, R. V.; Yu, T.; Li, J.; Zhuang, E.; Zandi, R.; Ortony, J. H.; Newcomb, C. J.; et al. Energy Landscapes and Functions of Supramolecular Systems. *Nat. Mater.* **2016**, *15* (4), 469–476.

(175) Thorvaldsson, K.; Stading, M.; Nilsson, K.; Kidman, S.; Langton, M. Rheology and Structure of Heat-Treated Pasta Dough: Influence of Water Content and Heating Rate. *LWT - Food Sci. Technol.* **1999**, *32* (3), 154–161.

(176) Lorén, N.; Langton, M.; Hermansson, A. M. Confocal Laser Scanning Microscopy and Image Analysis of Kinetically Trapped Phase-Separated Gelatin/Maltodextrin Gels. *Food Hydrocoll.* **1999**, *13* (2), 185–198.

(177) Olsson, C.; Langton, M.; Hermansson, A. M. Dynamic Measurements of β-Lactoglobulin Structures during Aggregation, Gel Formation and Gel Break-up in Mixed Biopolymer Systems. *Food Hydrocoll.* **2002**, *16* (5), 477–488.

(178) Ko, S.; Gunasekaran, S. Error Correction of Confocal Microscopy Images for in Situ Food Microstructure Evaluation. *J. Food Eng.* **2007**, *79* (3), 935–944.

(179) Ko, S.; Gunasekaran, S. In Situ Microstructure Evaluation during Gelation of β-Lactoglobulin. *J. Food Eng.* **2009**, *90* (2), 161–170.

(180) Woo, H.-D.; Moon, T.-W.; Gunasekaran, S.; Ko, S. Determining the Gelation Temperature

of β-Lactoglobulin Using in Situ Microscopic Imaging. *J. Dairy Sci.* **2013**, *96*, 5565–5574.

(181) Karstens, T.; Kobs, K. Rhodamine B and Rhodamine 101 as Reference Substances for Fluorescence Quantum Yield Measurements. *J. Phys. Chem.* **1980**, *84* (14), 1871–1872.

(182) You, Y.; Tataurov, A. V.; Owczarzy, R. Measuring Thermodynamic Details of DNA Hybridization Using Fluorescence. *Biopolymers* **2011**, *95* (7), 472–486.

(183) Schindelin, J.; Arganda-Carreras, I.; Frise, E.; Kaynig, V.; Longair, M.; Pietzsch, T.; Preibisch, S.; Rueden, C.; Saalfeld, S.; Schmid, B.; et al. Fiji: An Open-Source Platform for Biological-Image Analysis. *Nature Methods*. 2012.

(184) Kubin, R. F.; Fletcher, A. N. Fluorescence Quantum Yields of Some Rhodamine Dyes. *J. Lumin.* **1982**, *27* (4), 455–462.

(185) Weingarten, A. S.; Kazantsev, R. V.; Palmer, L. C.; Fairfield, D. J.; Koltonow, A. R.; Stupp, S. I. Supramolecular Packing Controls H2Photocatalysis in Chromophore Amphiphile Hydrogels. *J. Am. Chem. Soc.* **2015**, *137* (48), 15241–15246.

(186) Hestand, N. J.; Kazantsev, R. V.; Weingarten, A. S.; Palmer, L. C.; Stupp, S. I.; Spano, F. C. Extended-Charge-Transfer Excitons in Crystalline Supramolecular Photocatalytic Scaffolds. *J. Am. Chem. Soc.* **2016**, *138* (36), 11762–11774.

(187) Kazantsev, R. V.; Dannenhoffer, A. J.; Aytun, T.; Harutyunyan, B.; Fairfield, D. J.; Bedzyk, M. J.; Stupp, S. I. Molecular Control of Internal Crystallization and Photocatalytic Function in Supramolecular Nanostructures. *Chem* **2018**, *4* (7), 1596–1608.

(188) Chen, J.; Zhu, E.; Liu, J.; Zhang, S.; Lin, Z.; Duan, X.; Heinz, H.; Huang, Y.; De Yoreo, J. J. Building Two-Dimensional Materials One Row at a Time: Avoiding the Nucleation Barrier. *Science (80-.).* **2018**, *362* (6419), 1135–1139.

(189) Boekhoven, J.; Zha, R. H.; Tantakitti, F.; Zhuang, E.; Zandi, R.; Newcomb, C. J.; Stupp, S. I. Alginate-Peptide Amphiphile Core-Shell Microparticles as a Targeted Drug Delivery System. *RSC Adv.* **2015**, *5* (12), 8753–8756.

(190) Chen, L.; Zhang, K.; Zhu, L.; Xiao, Y. New and Efficient Approach to the Versatile Building Block of 3,4-Perylenedicarboxylic Monoanhydride. *Ind. Eng. Chem. Res.* **2015**, *54* (50), 12699–12703.

(191) Ishoey, M.; Chorn, S.; Singh, N.; Jaeger, M. G.; Brand, M.; Paulk, J.; Bauer, S.; Erb, M. A.; Parapatics, K.; Müller, A. C.; et al. Translation Termination Factor GSPT1 Is a Phenotypically Relevant Off-Target of Heterobifunctional Phthalimide Degraders. *ACS Chem. Biol.* **2018**, *13* (3), 553–560.

(192) Kazantsev, R. V; Dannenhoffer, A. J.; Aytun, T.; Harutyunyan, B.; Fairfield, D. J.; Bedzyk, M. J.; Stupp, S. I. Molecular Control of Internal Crystallization and Photocatalytic Function in Supramolecular Nanostructures. *Chem* **2018**, *4* (7), 1596–1608.

(193) Becher, T. B.; Braga, C. B.; Bertuzzi, D. L.; Ramos, M. D.; Hassan, A.; Crespilho, F. N.; Ornelas, C. The Structure-Property Relationship in LAPONITE® Materials: From Wigner Glasses to Strong Self-Healing Hydrogels Formed by Non-Covalent Interactions. *Soft Matter* **2019**, *15* (6), 1278–1289.

(194) Ceylan, H.; Yasa, I. C.; Yasa, O.; Tabak, A. F.; Giltinan, J.; Sitti, M. 3D-Printed Biodegradable Microswimmer for Theranostic Cargo Delivery and Release. *ACS Nano* **2019**, acsnano.8b09233.

(195) Hippler, M.; Blasco, E.; Qu, J.; Tanaka, M.; Barner-Kowollik, C.; Wegener, M.; Bastmeyer, M. Controlling the Shape of 3D Microstructures by Temperature and Light. *Nat. Commun.* **2019**, *10* (1), 232.

(196) Behkam, B.; Sitti, M. Design Methodology for Biomimetic Propulsion of Miniature Swimming Robots. *J. Dyn. Syst. Meas. Control. Trans. ASME* **2006**, *128* (1), 36–43.

(197) Zhang, S.; Greenfield, M. a; Mata, A.; Palmer, L. C.; Bitton, R.; Mantei, J. R.; Aparicio, C.; de la Cruz, M. O.; Stupp, S. I. A Self-Assembly Pathway to Aligned Monodomain Gels. *Nat. Mater.* **2010**, *9* (7), 594–601.

VITA

Garrett Lau

glau@u.northwestern.edu ▪ (305) 302-0441

EDUCATION

Northwestern University (NU) Evanston, IL
PhD Candidate in Materials Science and Engineering, GPA: 3.82/4.0 Spring 2020
Massachusetts Institute of Technology (MIT) Cambridge, MA
Candidate for Bachelor of Science in Materials Science and Engineering, GPA: 4.8/5.0 Jun. 2013

HONORS AND AWARDS

- Selected for ARPA-E Energy Innovation Summit Student Program Feb. 2017
- National Defense Science and Engineering Graduate Fellowship Sept. 2014-Present
- Horace A. Lubin Award for Outstanding Service to the MIT DMSE Community Jun. 2013
- Inducted to Tau Beta Pi Engineering Honor Society Feb. 2013
- 1st place recipient, MIT MADMEC Sustainable Materials Design Competition Oct. 2012
- Alpha Delta Phi Seward Scholarship Fall 2011

EXPERIENCE

Stupp Group (NU) Evanston, IL
PhD Candidate, Safety Designate, Data Server Manager Oct. 2013-Jun. 2019
Research Goal: Investigate synergistic effects of organic and inorganic phases in hybrid and composite materials towards direction of micro- and nanostructures with desired properties

- Synthesized hybrid nanotubular films for asymmetric supercapacitor cathodes, demonstrating the use of organic small-molecules to template the nanostructured growth of the inorganic $Co(OH)_2$ phase.
- Utilize magnetic fields to pattern magnetic nanoparticles to enable light and magnetic-field-sensitive hydrogel robots
- Designed and machined a variable temperature stage with 50-micron precision for in-situ observation of supramolecular self-assembly and dynamics with high-temperature confocal microscopy

Kellogg Management for Scientists and Engineers (NU) Evanston, IL
Jun.-Aug. 2018

- Completed highly competitive certificate program covering a wide range of business and leadership topics at the Kellogg School of Management

Polsky I-Corps Program (University of Chicago) Chicago, IL
Advanced Li-ion battery startup Jun. 2018

- Conducted over twenty interviews with potential customers and partners
- Identified and visited potential partners for scale-up of raw materials and battery prototyping

Kellogg Commercializing Innovations Class (NU) Evanston, IL
Technical Lead Jan.-Mar. 2018

- Performed market analysis, financial forecasting and technical feasibility studies for a Li-ion battery startup originating from an NU lab
- Conducted end-user interviews and identified key upstream raw materials suppliers
- Investigated potential partnership pathways with established battery manufacturers, battery materials suppliers and EV OEMs.

Ambri, Inc. Cambridge, MA
Materials Engineer Intern May-Aug. 2012

- Worked towards the commercialization of an electro-alloying liquid metal battery for grid-scale energy storage
- Performed post-mortem analysis of small-scale battery cells and provided key design recommendations that led to a successfully issued patent
- Managed database of cell performance data, summarizing and logging performance metrics
- Designed specifications and negotiated the order of a custom-built glovebox for battery assembly

Group Sadoway (MIT) Cambridge, MA
Undergraduate Researcher, Liquid Metal Battery Project Jan.-Aug. 2010, Jan.-May 2012
Research Goal: Development and optimization of an electro-alloying liquid metal battery for grid-scale energy storage.

- Assembled small-scale versions of the liquid metal battery for cost and performance optimization
- Cross-sectioned and performed post-mortem analysis on tested battery cells
- Performed phase analysis of cell components using scanning electron microscopy (SEM), energy dispersive x-ray analysis (EDX), and x-ray diffraction
- Co-developed heating apparatus, containment and electrical couples for a transparent liquid metal battery to visually observe charge/discharge processes at operating temperatures of 400-450 °C

Infinium Metals, Inc. (formerly Metal Oxygen Separation Technologies, Inc.) Natick, MA
Materials Engineer Intern, Magnesium Production Team Jun.-Aug. 2011

- Developed an improved inert anode design for long-term high-temperature use in molten oxide electrolysis, which led to a successfully issued patent
- Used Finite Element Analysis to model and optimize anode design for minimum heat and joule losses
- Performed magnesium Solid Oxide Membrane (SOM) electrolysis experiments
- Aided scale-up efforts for magnesium SOM electrolysis process through set-up design and assembly

PUBLICATIONS

- Lau, G.C.*; Sather, N.*; Sai, H.; Waring, E.; Deiss-Yehieley, E.; Barreda, L.; Beeman, E.; Palmer, L.C.; Stupp, S. I.; Oriented multi-walled hybrid organic-$Co(OH)_2$ nanotubes for electrochemical energy storage. *Advanced Functional Materials* **28(3),** (2018) 1702320 *These authors contributed equally to this work
- Sai, H.*; Lau, G.C.*; Dannenhoffer, A.; Chin, S.; Đorđević, L.; Stupp, S. I.; Imaging Supramolecular Morphogenesis with Confocal Laser Scanning Microscopy at Elevated Temperatures. *Nano Letters* (2020) *These authors contributed equally to this work
- Li, C.*; Lau, G.C.*; Yuan, H.*; Aggarwal, A; Lopez Dominguez, V.; Liu, S.; Sai, H.; Palmer, L.C.; Sather, N.A.; Pearson, T.J.; Freedman, D.A.; Khalili Amiri, P.; Olvera de la Cruz, M.; Stupp, S. I.; Fast and Programmable Locomotion of Hydrogel-Metal Hybrids Under Light and Magnetic Fields. *Manuscript under review* *These authors contributed equally to this work

PRESENTATIONS

- Electrolyte additives for stabilizing cobalt hydroxide nanotubular supercapacitor electrodes
  Best Poster Nominee at the Fall 2016 MRS Meeting (Boston, MA) November 30, 2016

PATENTS

- Adam Clayton Powell, IV, Soobhankar Pati, Stephen Joseph Derezinski, Garrett Lau, Uday B. Pal, Xiaofei Guan, Srikanth Gopalan. 2016. Conductor of high electrical current at high temperature in oxygen and liquid metal environment. U.S. Patent 9234288, filed August 31, 2012, and issued January 12, 2016.
- David J. Bradwell, Alex T. Vai, Tom Kinney, Sean Theriault, Garrett Lau. 2016. Electrochemical energy storage devices. U.S. Patent 9520618, filed February 12, 2014, and issued December 13, 2016.

SKILLS

Electrochemical characterization (impedance spectroscopy, cyclic voltammetry, galvanostatic methods), SEM, TEM, EDS, light microscopy, confocal microscopy, TGA/DSC, XPS, powder and thin-film XRD, SAXS/MAXS/WAXS, AFM, FTIR, DLS, UV-vis, Solidworks CAD, precision machining and prototyping, MATLAB

TEACHING

MSE 301 – Introduction to Materials Science and Engineering (NU) Evanston, IL
Teaching Assistant Fall2013, Fall 2014

- Rewrote final exam questions to tie together concepts of diffusion, phase diagrams, mechanical and electronic properties into a single section (copper contamination in silicon)
- Planned and presented a lecture on electronic materials and devices
- Designed lab modules on fabrication of electric double-layer supercapacitors (slurry composition tuning) and effect of temperature on the electrochemical impedance of Li-ion batteries

LEADERSHIP

Northwestern Energy and Technology Group (NU)

- President: Aug. 2016-Aug. 2018
  - Lead fourteen graduate students to organize energy-related career development, networking and outreach events
  - Established partnership with BASF Corporation to fund two annual student travel grants and collaborate on guest lectures

McCormick Graduate Leadership Council Member (NU)

- Co-Chair Sept. 2015 – Sept. 2016
  - Led a council of thirty graduate students to organize social, career development and youth outreach events for the McCormick School of Engineering
- Engineering Grand Prix Challenge Designer Sept. 2014 – May 2016
  - Designed activities for an engineering competition for 60-70 local underrepresented minority middle school students

Society of Undergraduate Materials Scientists (MIT)

- Vice President Aug. 2012 – Jun. 2013
  - Created a student-faculty lunch program where students could personally interact with faculty members and receive direct career advice and mentorship.
  - Organized annual departmental student surveys to solicit feedback on student life and curricula
  - Represented the undergraduate body during departmental Visiting Committee meetings.
- Freshman Pre-Orientation Program Coordinator Jan. – Sept. 2012
  - Organized a week-long pre-orientation program to introduce 20 incoming freshmen to the field of Materials Science and Engineering and the MIT campus.

Alpha Delta Phi Fraternity (MIT)

- House Manager Jan. – Jun. 2013
  - Oversaw and delegated the maintenance and cleaning of the living facilities for the 40 in-house members

  - Worked with building, sprinklers, and fire/egress inspectors to ensure the safety of the fraternity’s members and the annual renewal of the fraternity house’s lodging license.
- President Dec. 2011 – Dec. 2012
  - Oversaw activities and finances of 67 undergraduate members as the chief executive officer and delegate of the chapter
- Vice President Aug. – Dec. 2010
  - Organized a semiformal attended by 67 people with a $5000 budget
  - Organized a faculty dinner at the chapter house that the MIT President, the Dean of Undergraduate Research, and an MIT Institute Professor attended, along with several other faculty members and teaching assistants.